Determination of the Band gap of Metal Oxide Thin Films through Electroreflectance

BY

Hafiz Adil Qayyum

A Dissertation Presented to the
DEANSHIP OF GRADUATE STUDIES

KING FAHD UNIVERSITY OF PETROLEUM & MINERALS

DHAHRAN, SAUDI ARABIA

In Partial Fulfillment of the
Requirements for the Degree of

DOCTOR OF PHILOSOPHY

In

PHYSICS

November 2017

KING FAHD UNIVERSITY OF PETROLEUM & MINERALS
DHAHRAN- 31261, SAUDI ARABIA
DEANSHIP OF GRADUATE STUDIES

This thesis, written by **Hafiz Adil Qayyum** under the direction of his thesis advisor and approved by his thesis committee, has been presented and accepted by the Dean of Graduate Studies, in partial fulfillment of the requirements for the degree of **PhD in Physics.**

Dr. Abdullah A. Al-Sunaidi
Department Chairman

Dr. Salam A. Zummo
Dean of Graduate Studies

31\12\17
Date

Dr. Mohammad F. Al-Kuhaili
(Advisor)

Dr. Sardar Mohammad Ayub Durrani
(Co-Advisor)

Dr. Khalil A. Ziq
(Member)

Dr. Akhtar A. Naqvi
(Member)

Dr. Ibraheem M. Nasser
(Member)

Dedicated to My Loving Parents and Family

Acknowledgment

All Praises to Almighty Allah, the Lord of the entire Universe. With Your prolific praise, I desire to begin. I offer my great and best gratitude to the last Prophet MUHAMMAD (S.A.W), who has given the lesson of altruism, generosity, benevolence and moral values, and also broke the cage of servitude through His golden sayings, to seek knowledge is obligatory for every Muslims.

I express my sincere thanks to my supervisor Prof. Dr. Mohammad F. Al-Kuhaili for his worthy guidance in preparing this report, and his kind and valuable supervision on all the practical work performed. I have always looked up to him for guidance in any problem I faced in my work, and I consider myself privileged to work under his supervision which always prove to me with cogent vision of exploring things and ideas.

I would like to thank Dr. Sardar Mohammad Ayub and Mr. Imran Ali Bakhtiari for their guidance and assistance during the course of my experimental work.

I would like to thank my committee members Prof. Dr. Akhtar A. Naqvi, Prof. Dr. Ibraheem M. A. Nasser, and Prof. Dr. Khalil A. Ziq, for their useful response, advice, and the time they spent reviewing this thesis.

I would like to thank the Chairman of the Physics department Dr. Abdullah A. Al-Sunaidi for providing me a continuous support throughout my studies.

I am very obliged to King Fahd University of Petroleum and Minerals (KFUPM) for providing me an opportunity to pursue my degree. I would also like to appreciate all the support that I received from Physics department in carrying out my research

I would like to thank my Parents and all other family members for their motivational support, without their confidence in me, this work would have never been completed.

I would like to thank all the faculty members, non-teaching staff and my fellow students for the help they provided me at various stages of this work. Special thanks to all my friends for providing me the unforgettable company in KFUPM

Table of Contents

List of Figures

List of Tables

List of Symbols

$\vec{A}(r)$	Magnetic vector potential
A_o	Magnitude of vector potential
A_1	Normalized constant for wave function
a	Distance of the ionic cores
a_o	Lattice constant
b	Number of fitting components in electroreflectance
C	Amplitude of electroreflectance spectrum
C'	Amplitude of transitions
C_1	Parabolic approximation constant
c	Speed of light
D	Crystallite size
d	Thickness of film
d_1	Lattice spacing
E	Energy of the electron
E_c	Energy of the electron in the conduction band
E_v	Energy of the electron in the conduction band
E_F	Electric field
E_g	Band gap
E_o	Energy associated with the free particle system

E_p	Energy of the photon
E_r	Net relative energy
E_z	Energy gained by the electron due to electric field
e	Charge on electron
$\hat{e}$	Polarization vector along electric field
F	Fermi golden function
g	Order of maxima
H	Net Hamiltonian of the system
Ho	Hamiltonian of a free electron system
H'	External perturbation
H_{e-R}	Electromagnetic Hamiltonian
I	Intensity of light
J	Perturbation matrix element
J_1	Perturbation matrix element between initial and final states
K	Extinction coefficient
K_e	Kinetic energy for electron
$\vec{k}$	Wave vector of the electrons
k_s	Sherrer constant
m	Mass of the electron
m_c	Mass of electron in the conduction band

m_v	Mass of electron in the valence band
N	Refractive index
n	Normal refractive index
P	Momentum of the electron
P'	Probability of a system in a specified state
p	Power factor associated with the movement of electrons
q	Charge of the particle
R	Reflectance
R_t	Transition Rate
S	Constant energy surface
S_o	Poynting vector
T	transmittance of the films
t	Time of perturbation
$U(r)$	Periodic potential
V_c	Volume of the unit cell
$V(r)$	Potential due to ionic core
$V_o(r)$	General perturbation
x	Slit width
$\hbar$	Plank's constant
λ_e	Wave length of the electron
$\varphi(r)$	Scalar potential

$\Psi(r)$	General state of a system
$\xi(r)$	wave function for system of electrons and holes
$\xi_e(r)$	Electronic wave function
ω	Angular frequency of electromagnetic radiation
ε	Dielectric function
ε_r	Real part of dielectric function
ε_i	Imaginary part of dielectric function
λ_p	Wavelength of photon
v	Velocity of propagation
μ	Average energy density
ρ	Joint density of states
μ_r	Reduced mass of electron and hole system
η	Spectrophotometric constant
β	Order of transition in Tauc relation
β_o	Airy function constant
θ	Phase factor
θ_B	Bragg's angle
θ_o	Electrooptic Energy
τ	Periodicity of the lattice
τ_1	Interaction time for electrons

λ_x	Wavelength of x-rays
δ	Work function
Γ	Broadening parameter

List of Abbreviations

AFM	Atomic Force Microscopy
ATD	Aspnes Third Derivative Model
BE	Binding Energy
EELS	Electron Energy Loss Spectroscopy
EM	Electromodulation
ER	Electroreflectance
FWHM	Full Width at Half Maximum
IPE	Internal Photoemission Spectroscopy
LMA	Levenberg–Marquardt Algorithm
PL	Photoluminescence
SE	Spectroscopic Ellipsometry
SP	Spectrophotometry
XES	X-ray Emission Spectroscopy
XPS	X-ray photoelectron spectroscopy
XRD	X-ray Diffraction

THESIS ABSTRACT

NAME	Hafiz Adil Qayyum
TITLE OF STUDY	Determination of the Band gap of Metal Oxide Thin Films through Electroreflectance
MAJOR FIELD	Physics
DATE OF DEGREE	November, 2017

This work was concerned with the determination of the band gap of metal oxide thin films using the method of electroreflectance. Currently, there is a considerable variation in the values of the band gaps of metal oxides as determined by indirect techniques such as spectrophotometry and ellipsometry. The selection of the oxides in this study was based on their importance in applications such as optoelectronics, microelectronics, and photovoltaics. The following oxides were investigated in this work: CeO_2, Fe_2O_3, Ga_2O_3, HfO_2, MoO_3, SnO_2, TiO_2, WO_3, ZnO, and ZrO_2. These metal oxides were synthesized using thermal evaporation, electron beam evaporation or radio frequency sputtering, and were characterized using different techniques such as X-ray diffraction, X-ray photoelectron spectroscopy, atomic force microscopy, and spectrophotometry. Moreover, a capacitor-like geometry of metal- oxide- metal configuration was fabricated in order to characterize the oxides through electroreflectance. The obtained electroreflectance spectra were fitted using the critical point model to extract the band gap values. The originality of this work was to set up an electroreflectance system, and provide the band gaps of the above mentioned oxides using the direct electroreflectance technique.

ملخص الرسالة

الإســــــم: حافظ عادل قيوم

عنوان الرسالة: قياس فجوة الطاقة لاغشية رقيقة من أكاسيد المعادن باستخدام الإنعكاس الكهروضوئي

التخصـــص: فـــيزيــــاء

تاريخ التخــرج: نوفمبر 2017م

هذه الدراسة معنية بقياس فجوة الطاقة لأغشية رقيقة من أ كاسيد المعادن شبه الموصلة باستخدام طريقة الانعكاس الكهروضوئي يوجد حاليا تباين كبير في قيم فجوة الطاقة لأكاسيد المعادن المقاسة باستخدام تقنيات غير مباشرة مثل تقنية التحليل الطيفي و مطيافية القطع الناقص)الإليبسومتري .(تم اختيار أكاسيد المعادن في هذه الدراسة بناء على أهميتها في المجال التطبيقي مثل :صناعة الإلكترونيات الضوئية، والالكترونيات الدقيقة، والفولتوضوئية .في هذا العمل البحثي تم دراسة أكاسيد المعادن التالية ،ثنائي أكسيد السيريوم، أكسيد الحديد، أكسيد الجاليوم ، ثنائي أكسيد الهافنيوم، ثنائي أكسيد الموليبدنوم، ثنائي أكسيد القصدير ثنائي أكسيد التيتانيوم، ثالث أكسيد التنغستن، أكسيد الزنك و ثنائي أكسيد الزركانيوم .هذه الأكاسيد المعدنية تم تحضيرها باستخدام التبخير الحراري، التبخير بواسطة الشعاع الالكتروني أو التبخير بواسطة الشعاع الايوني تحت تاثير جهد كهربائي متردد، وتم توصيفها باستخدام تقنيات مختلفة مثل حيود الأشعة السينية، مطيافية الأشعه السينيه الإلكتروضوئية، مجهر القوة الذرية، وتقنية التحليل الطيفي .علاوة على ذلك، تم تصميم نموذج يشبه المكثف الكهربائي من أكاسيد المعادن موضوع الدراسة بغرض توصيفها باستخدام طريقة الانعكاس الكهروضوئي .تم معالجة أطياف الانعكاس الكهروضوئي التي تم الحصول عليها باستخدام نموذج النقطة الحرجة لايجاد قيم فجوة الطاقة .هدف هذا العمل البحثي هو تصميم جهاز يعمل على مبدأ الانعكاس الكهروضوئي لقياس فجوة الطاقة للأكاسيد المذكورة أعلاه بطريقة مباشرة.

CHAPTER 1

Introduction

1.1 Metal Oxides

Metal oxides constitute a class of materials in which a metal atom is bonded to oxygen atoms. Based on their structure and properties, they provide ample applications in scientific and industrial fields. They are chemically stable and exist in various crystalline forms. Optically, they are transparent to most of the visible region, and their electrical nature varies from insulating to superconducting. The applications of metal oxides are so enormous that, even on the basis of their uses in different scientific domains, they can be categorized into various classes. The main classes of metal oxides are:

1) **Photochromic oxides** that show rapid changes in their optical properties under light interaction. They have found their uses in chemical sensors, radiation controlling industries, secondary lithium ion batteries, smart windows and in building large-area devices like dynamic windows in solar industries and enclosures in spacecraft industries [1–3].

2) **Transparent conducting oxides or TCOs** possess wide band gaps, high transmittance, and optimum electrical conductivity. They are used in flat panel displays, solar cells, ultra-sensible gas devices and in biotechnological applications like human body detection systems, and in deep ultra violet (DUV) technology for the detection of DNA molecules [4, 5].

3) **High dielectric constant oxides** are wide band gap oxides with a high dielectric constant. They are considered as the future replacement of silicon oxide in the next generation electronic devices [6–8].

4) Photocatalytic oxides have suitable band gaps for light-to-current conversion. They are extensively used as catalysts to increase the rate of photo chemical reactions [9].

Besides the above-mentioned oxides, which are the prime materials for many scientific and technological fields, there are many examples of other oxides that play crucial roles in many scientific fields due to their peculiar nature. Examples of such oxides are magnetic oxides, superconductor oxides and anti-corrosion oxides.

1.2 The Need for Accurate Band Gaps

The crystalline structures and properties of an oxide depend upon the number of oxygen and metal atoms within the unit cell, the sharing of electrons between the atoms, and the nature of bonding between the electrons of the atoms. On the other hand, the optical and electronic properties of oxides heavily depend upon their electronic structure. Therefore, knowledge of the electronic structure of an oxide is a core demand in order to investigate its electrical, optical and other physical and chemical properties.

When the electrons in the atoms of a solid come close to each other, their wave functions overlap and interact with each other. As a result, the energy levels of the electrons split up. For a solid which consists of a number of atoms of the order of Avogadro's number ($\sim 10^{23}$), the splitting of the energy levels of the electrons is so closely spaced that they form a continuous band. The electronic distribution in these closely-spaced energy levels is governed by the Pauli exclusion principle. Thus, at a temperature $T = 0$ K, these levels are either filled by electrons or remain empty. The highest filled band is called the valence band. Above the valence band, there is an empty band called the conduction band. The forbidden energy levels, that separate the valence band from the conduction band, constitute the band gap of the material. Materials are classified on the basis of their band gap values as conductors, semiconductors, and insulators. In conductors, the band gap value is too small, and the valence and conduction bands overlap with each other. Semiconductors possess intermediate band gaps (0.1- 6 eV) while insulators possess large band gaps ($E_g > 6$ eV).

The band gap of a semiconductor plays a vital role in defining the material's electrical and optical properties. Therefore, measuring the correct band gap of a material is a basic demand in order to test its performance and uses. Despite the fact that the properties of a material rely heavily on correct determination of its band gap, there are not sufficient experimental techniques available for accurately measuring the band gap. Moreover, the techniques which are available are not direct and rely on assumed theoretical models. Despite the fact that the properties of a material rely heavily on correct determination of its band gap, there are not sufficient experimental techniques available for accurately measuring the band gap. Moreover, the techniques which are available are not direct and rely on measured theoretical models. For example, spectrophotometry is widely used to find the band gaps of materials. However, this indirect technique relies on a graphical method called the Tauc plot that needs extrapolation to find the absorption edge. On the other hand, spectroscopic ellipsometry is a rather sophisticated technique as compared to spectrophotometry regarding the band gap calculations. It measures the amplitude ratio and the phase change of a polarized light beam that is reflected from the surface. However, this technique is critical to the nature of the surface, requires extrapolation, and is affected greatly by light polarization. Electron energy loss spectroscopy (EELS) is another important technique to find the fundamental transitions in metal oxides. However, the spectra of EELS are severely affected by the influence of noise on them [10].

A direct method to find the band gap of semiconductors is modulation spectroscopy. In this technique, the changes in optical parameters, rather than absolute values, are measured. Modulation spectroscopy is a powerful technique for characterizing thin film or bulk materials, nanostructures, superlattices, quantum wells, hatero-structures and interfaces of the materials [11]. The basic principle of this technique is to provide a periodic perturbation to the sample to obtain sharp derivative-like features in the optical response of the material. These derivative features correspond to the critical points of the band structure of the semiconductor. The perturbations are created by an external modulation. The common external modulation methods are (1) thermomodulation or thermoreflectance (in which heat changes are produced by passing current pulses across the heater on which the material is mounted); (2) piezoreflectance (which produces changes in the lattice constant, and as a result, band gap modulation is produced); (3) electromodulation (affects the band structure of the sample); and (4) magnetic field modulation (causes changes in the electron energy levels) [12]. Out of the above mentioned techniques, the most sophisticated and widely used modulation technique is electromodulation.

In electromodulation, an electric field is induced externally across the surface of the sample to produce changes in its optical parameters. There are three basic ways to create the electric field. The first is to use the electric field component of a laser beam. Since light is electromagnetic radiation that consists of electric and magnetic field components, its electric part is used to produce the electric field. This method is called photoreflectance [11]. The use of this method is restricted to those materials which have their band gaps below the photon energy of the laser. The second method is electrolytic electroreflectance, in which an electrolytic solution is used to produce the electric field in the sample [11]. The third method is electroreflectance, in which the electric field is produced using electrical contacts on the surface of the sample. This technique is more robust since it provides the freedom to produce strong magnitudes of the perturbing electric field and it can, in principle, determine the band gap of any material [11,12]. Due to the insulating nature of metal oxides, this technique may be more applicable to metal oxides in thin film form since an intense electric field can be created in a thin film layer using a moderate potential difference.

1.3 Motivation

The aim of this work is to set up an electroreflectance system and subsequently use it to accurately determine the band gaps of metal oxide thin films. The selection of metal oxides in this work is dictated by their applications. The top ten most investigated and used oxides in different fields are analyzed in this work. Even though these oxides are used extensively on the basis of their optical and electrical properties, the variations in their band gaps are significant. The oxides are CeO_2, Fe_2O_3, Ga_2O_3, HfO_2, MoO_3, SnO_2, TiO_2, WO_3, ZnO, and ZrO_2. The aim of this work is the direct determination of band gap. This work can serve as a reference to check the exact value of the band gap of different oxides and can indicate the correctness of the models used in theoretical band gap calculations.

1.4 Literature Review

1.4.1 Cerium Oxide (CeO_2)

Cerium oxide (CeO_2) is an insulating, non-magnetic rare-earth oxide which exists in a cubic structure [13]. In its band structure, Ce 5d and O 2p orbitals respectively form the conduction and valence bands of CeO_2 [14]. Optically, this material has high transmittance in the infrared (IR) and in the visible regions. It owns high thermal stability, diffusivity and electrical conductivity [15,16]. These properties enable CeO_2 to be used as an interface material for SOI (silicon on insulator) applications. CeO_2 is also used in metal finishing coatings and in corrosion resistance applications due to its least mismatch properties with the metals [17].

1.4.2 Iron Oxide (Fe_2O_3)

Iron oxide is highly stable, low cost and nontoxic material. It exists in different crystalline and stoichiometric forms like FeO, Fe_2O_3 and Fe_3O_4. Out of these forms, Fe_2O_3 is the most common and widely used. Fe_2O_3 exists in two different phases. These are known as hematite (α-Fe_2O_3) and maghemite (γ-Fe_2O_3). Optically, this material has a high refractive index and its band gap lies well within the visible region. So, it is considered as an efficient material for optoelectronic applications [18]. The α-phase of Fe_2O_3 is widely used as photo electrodes and as humidity sensors [18]. The γ-Fe_2O_3 shows high ferromagnetic nature and is used in magneto-optic recordings [18–20].

1.4.3 Gallium Oxide (Ga_2O_3)

Gallium oxide (Ga_2O_3) exhibits polymorphism and exists in several crystalline structures. Its stable form at higher temperature is β-Ga_2O_3. β-Ga_2O_3 is a wide band gap material and, intrinsically, it is an insulator. However it can be changed to an n-type semiconductor at a temperature of 500 °C under the reduction of oxygen [21]. Its common crystalline structure is the monoclinic [22]. In its band structure, the top of the valence band is constituted by the 2p orbitals of oxygen, while the bottom of the conduction band is formed by gallium 4s orbitals [23]. Optically this material is transparent from the visible to ultraviolet (UV), and therefore it can be used in optoelectronic devices and as textured dielectric coatings in the field of solar cells. β- Ga_2O_3 is thermally and chemically stable but, unlike most of the wide band gap semiconducting materials, it still shows variations in its conductivity when it is exposed to a redox atmosphere. Due to these kind of characteristics, this material is used as a high temperature oxygen sensor and as a luminescent phosphor [24–26].

1.4.4 Hafnium Oxides (HfO_2)

HfO_2 is a wide band gap semiconductor that exists in three different crystal structures. Its monoclinic structure exists at room temperature, while its tetragonal and cubic structures require high temperature (∼1777 °C for tetragonal and ∼2530 °C for cubic) [27]. The valence band of HfO_2 consists of oxygen states, while the 5d states of hafnium form its conduction band [28]. Optically, this material has a wide band gap and it shows a transparent nature from the UV to mid IR. So, it can be used in optical applications like high reflective mirrors, beam splitters and filters [29]. HfO_2 has several important characteristics associated with technological fields. It has a high dielectric constant, good thermal stability, and great compatibility with other metal oxide semiconductors. These properties have focused the attention to use HfO_2 as a substitute material for SiO_2 in electronics to create a tremendous downscaling in the dimensions of complementary metal oxide semiconductor (CMOS) devices [30]. Alloys of high dielectric materials like HfO_2 and ZrO_2 with SiO_2 and Al_2O_3 are being considered to replace SiO_2 in future CMOS devices [31].

1.4.5 Molybdenum Oxide (MoO_3)

MoO_3 is a transition metal oxide. It exists in orthorhombic, hexagonal and monoclinic structures. The monoclinic structure of MoO_3 ($\beta -$ phase) is a perovskite-like structure [32]. It also has an orthorhombic structure (α-phase) in the bulk form. In its band structure, the 4d bands of Mo in MoO_3 are considered empty and constitute the conduction band while the valence band of MoO_3 consists of 2p states of oxygen atoms [33]. MoO_3 exhibits strong properties of intercalation, high stability and unique two dimensional layered structures in its orthorhombic phase (α-MoO_3) [34]. These layers are held together by weak Van der Waals forces. The dimensionality and the nature of forces in these layered structures of MoO_3 has enabled its use in high energy density secondary lithium batteries as an electro-active material [35]. The carrier diffusion coefficients in MoO_3 are many orders of magnitude less as compared to other familiar non-organic compounds like V_2O_5 or WO_3. This property makes MoO_3 a vital candidate for storing information over a long period [36]. MoO_3 also demonstrates a photochromic nature and it is widely used in many technological fields. These include radiation intensity control, chemical sensors and self-developing photography [36].

1.4.6 Tin Oxide (SnO_2)

SnO_2 is an n-type semiconductor which exists in a rutile structure. Its unit cell is tetragonal and contains two tin and four oxygen atoms [37]. In its geometry, each of the anions has a bonding with cations and they form planar trigonal structures. These structures are oriented in such a way that the p_x and p_y orbitals of oxygen define the bonding plane, while the p_z orbitals have nonbonding nature. These non-bonded p_z orbitals form the valence band in SnO_2 [38]. The stoichiometric form of SnO_2 is insulating, while its non-stoichiometric form exhibits interesting optical and electrical nature. For example, from an optical point of view, it is transparent in the visible region while showing reflecting nature in a wide range of the IR. Its electrical properties are enhanced greatly when it is sufficiently doped. Its high chemical and mechanical stability, inertness towards acids and bases and good adhesive nature towards many common materials like glass, oxides, and metals has increased its importance in the fields optoelectronics and solar cells fabrication [39,40]. SnO_2 thin films show significant variations in their electrical conductivity during the chemisorption process. The atmospheric gases like oxygen are chemisorbed on the oxide surface of SnO_2. This results in the alteration of the band structure of SnO_2, and band bending occurs at its surface. Hence, the conductivity of SnO_2 changes. Due to this, the gas sensing property SnO_2 is widely used in manufacturing semiconductor gas sensors [41].

1.4.7 Titanium Oxide (TiO_2)

Titanium oxide is among the class of wide-band gap transition metal oxides. It possesses high chemical stability, large dielectric constant, nontoxic nature, and strong electron-phonon coupling [42,43]. It exhibits many polymorphs. The common ones are anatase, rutile and brookite. The oxygen 2p states, hybridized with titanium 3d states, make the valence band in the electronic structure of TiO_2, while the conduction band consists of unoccupied 3d states of titanium [44]. Because of its high refractive index and transparency, TiO_2 is used in optical applications as an anti-reflecting coating on SiO_2. This material is an efficient photocatalyst because of its nontoxic nature, good stability and large quantum yield [42,43].

1.4.8 Tungsten Oxide (WO_3)

Tungsten oxide (WO_3) is a transition metal oxide with an indirect band gap. It is an n-type semiconductor. Structurally, this material exists in various structures like simple cubic perovskite, monoclinic, orthorhombic and triclinic [45]. The phases of WO_3 are considered to be temperature-dependent. A low temperature monoclinic phase occurs within the temperature range of -140 ºC to -50 ºC. With the increase in temperature from -50 ºC to 17 ºC, the triclinic phase takes place. At the room temperature, the stable form of WO_3 is monoclinic, which remains up to 330 ºC. Higher temperatures up to about 740 ºC create the orthorhombic phase of WO_3 , while above that temperature, the common phase of WO_3 is tetragonal [45]. In its band structure, the valence band consists of the 2p states of oxygen atoms while the conduction band consists of tungsten 5d states [46]. It shows transparency in the UV and visible regions [47]. The amorphous films of WO_3 exhibit photochromic behavior, and received considerable interest in many technological applications like smart windows, erasable optical storage devices and large area displays [48]. Moreover, because of its optimum band gap, research is being carried out to use this material as a photocatalytic material [49].

1.4.9 Zinc Oxide (ZnO)

ZnO is a wide band gap semiconductor material. It has a large excitation binding energy of about 60 meV. Naturally, ZnO exists as the mineral zincite with a hexagonal wurtzite crystal structure [50]. In its electronic structure, the valence band consists of two parts. The upper part of the valence band comes from the 3d states at the Zn sites while the lower part of the valence band consists of the oxygen 2p states. On the other hand, the 4s states of zinc form the conduction band in ZnO [51]. Optically, this material is highly transparent in the visible and IR spectral regions, and the transmission is higher than 90% in the range 350–1000 nm [52]. It can be doped to increase the free electron density and thus lower the resistivity. Moreover, because of high exciton binding energy and wide band gap, it can be used in a variety of applications which need high temperature stability. Such applications involve automation, aerospace, deep well drilling and other industrial systems [53–55].

1.4.10 Zirconium Oxide (ZrO_2)

Zirconium oxide is a transition metal oxide which possesses a peculiar high dielectric constant. This material shows three important geometrical phases: monoclinic, tetragonal and cubic. All of these phases are temperature dependent [56]. In its band structure, the valence band consists largely of oxygen 2p states with slight contribution from Zr 4d states. This contribution is due to the hybridization of oxygen 2p and Zr 4d orbitals. This hybridization constitutes almost 24% of the bonding in ZrO_2. The conduction band is mainly formed by the Zr 4d states [57]. Optically, this material has a wide band gap, high index of refraction, high transparency in the visible and near IR, and low optical loss [58]. Due to its suitable optical properties, it is used widely in optical applications like broadband interference filters, and high reflectivity mirrors [58]. Like HfO_2, ZrO_2 is also considered for replacing SiO_2 in electronics industries because of its high dielectric constant. Moreover, the alloys of zirconium are also used in anticorrosion industries because of their corrosion resistive abilities [59].

1.4.11 Scattering of the Band Gap Values of Metal Oxides

The variations in the band gap values of metal oxides is an important issue which arises while measuring their band gaps using different experimental techniques. Table 1 summarizes the scattering of the band gap values of metal oxide thin films as measured with different experimental techniques.

Table 1. 1: A brief survey of the reported band gap values of thin films of wide band gap metal oxides obtained through different experimental methods

Material	**Band gap value (eV)**	**Technique**	**Ref.**
Cerium Oxide (CeO_2)	3.1–3.53	SP	[15,60–63]
Iron Oxide (Fe_2O_3)	2.18–2.97	SP	[18,64–68]
	2.2	XES	[69]
Gallium oxide (Ga_2O_3)	4.46–4.74	SE	[70]
	4.5–4.6	EELS	[71]
	4.51–5.30	SP	[4,21–23,25,72–79]
Hafnium oxide (HfO_2)	5.15– 5.7	EELS	[31,80–82]
	5.27–5.82	SE	[83]
	5.45–5.82	SP	[84–92]
	5.6	IPE	[93]
Molybdenum Oxide (MoO_3)	3.15–3.98	SP	[94–98]
Tin Oxide (SnO_2)	3.22–4.42	SP	[99–105]
	4.18	PL	[103]
Titanium Oxide (TiO_2)	3.1–3.7	SP	[106–110]
Tungsten Oxide (WO_3)	2.29–3.78	SP	[47,111-118]
	3.15–3.25	SE	[119,120]
Zinc Oxide (ZnO)	3.20–3.48	SP	[121–131]
	3.42	SE	[128]
Zirconium oxide (ZrO_2)	3.85–6.07	SP	[56,88,132–135]
	4– 5.3	EELS	[82,136]
	4.93–5.2	SE	[137]

SP: spectrophotometry, **XES**: X-ray emission spectroscopy, **SE**: spectroscopic ellipsometry, **EELS**: electron energy loss spectroscopy, **IPE**: internal photoemission spectroscopy, **PL:** Photoluminescence

The common problem faced by most of the experimental techniques, while measuring the band gap, is the absence of the singularity in the optical response of the material. Optical transitions related to the band gap or defect level transitions appear as a sharp edge or a singularity in the optical response of a material, and they are also known as the critical points of the material. In the case of experimental methods like spectrophotometry or ellipsometry, these critical points do not have any physical location in the optical spectra, and hence, the extraction of such critical points is graphical or model-dependent. In fact, it was found by Feng *et. al* [138] that the model of finding the band gap is itself adjusted to find the location of the critical point (band gap in this case) in the absorption coefficient of the material. The EELS based techniques can reveal these critical points in terms of sharp edges or peaks on their optical spectrum [139]. However, these points are extremely suppressed by the background of the spectrum [140,141]. Moreover, in some cases, the observed EELS spectra of the wide band gap oxides spread over wider energies [142,143]. This leads to the problem of indistinguishability of the fundamental transition from the defect level transition that may exist close to it.

1.4.12 Electroreflectance of Metal Oxides

Electromodulation (EM) has been used as an independent technique for the direct observation of the optical transitions involved in a material, and hence extracting the band gaps of the materials.

The preliminary work on the electromodulation of the metal oxides was performed by Cardona *et al.* [144], who performed the electrolytic electroreflectance study of the ZnO. The electroreflectance analysis revealed the two band transitions at 3.30 eV and 3.34 eV. Moreover, the effect of a high electric field on the electroreflectance of ZnO was also observed in terms of oscillatory features towards the high energy side of the electroreflectance spectrum. Kudrawiec *et al.* [145] performed contactless electroreflectance analysis of ZnO thin films grown by atomic layer deposition on different substrates. They found a broad resonance at a value of 3.4 eV for the ZnO polycrystalline phase deposited on a glass substrate, which was attributed to the band transition peaks. Moreover, the exciton transition peak was also observed at a value of 3.32 eV for the ZnO film deposited on a GaN substrate. Welna *et al.*[146] observed the optical transitions in bulk and thin film forms of ZnO. They found well resolved ER spectra of exciton, and band transition at the values of 3.3 eV and 3.4 eV for the bulk phase of zinc oxide. On the other hand, the electroreflectance spectrum showed a broad peak feature at a value of 3.3 eV in the case of thin films, where the two transitions were quite indistinguishable. The main factors behind this distortion were the large scattering, large surface roughness of the films, and light interference effects at the metal and oxide interfaces.

The ER analysis of TiO_2 was first performed by Vos *et al.* [147], who used gold as a field electrodes to induce the surface barrier electroreflectance in TiO_2 single crystals. They found the indirect transition in TiO_2 at a value of about 3.13 eV. Moreover, the effect of temperature on the ER spectrum of TiO_2 was also studied in that work. It was found that decreasing the temperature down to 25 K displaces the ER spectra from 3 to 7 meV. Kulak *et al.*[148] performed the ER analysis of pure and metal modified TiO_2 thin films using electrolytic electroreflectance technique. They observed multiple ER peaks due to the appearance of surface states in the metal modified TiO_2 films. These surface states enhanced the charge exchange between the metal and the conduction band of the semiconductor.

The electroreflectance analysis of In_2O_3 was performed by Pan *et al.* [149] based on electrolytic ER technique. They observed both the direct and indirect transitions of In_2O_3 at values of 3.56 eV and 2.69 eV, respectively.

Although many of the materials have been investigated using electroreflectance technique, a large class of metal oxides still lacks the electroreflectance analysis. This is because of the high resistive nature of the metal oxides, which requires a high electric field to elucidate the optical transitions involved in the metal oxide thin films.

1.5 Scope of the Study

The scope of this work includes:

1- The synthesis of metal oxides is performed with thermal evaporation and RF sputtering. Moreover, to induce the electric field across the oxide, an MOM (metal- oxide- metal) configuration is fabricated.

2- The films are investigated using different characterization methods. Their structural properties are examined through x-ray diffraction, surface morphology through atomic force microscopy, chemical analysis through x-ray photoelectron spectroscopy and optical properties through spectrophotometry

3- The electroreflectance experiments are carried out for these oxides.

4- The electroreflectance spectra of each oxide are analyzed with the help of Aspnes third-derivative modulation spectroscopy [150].

CHAPTER 2

Quantum Theory of Optical Properties of Solids

2.1 Bands Formation in Semiconductors

The formation of bands in semiconductors is a consequence of the nearly free electron model. This model describes the motion of electrons as they move in a solid under the interaction of the nuclei of the atoms. Its basic assumptions are:

1) The ionic cores of the atoms are considered to be fixed in their positions in a solid. This assumption is called the adiabatic approximation [151].

2) During the motion of electrons, they cannot interact with each other (independent electron approximation) [151].

3) The nuclei of the atoms in a solid provide a weak perturbation to the motion of electrons as they move in a crystal [151].

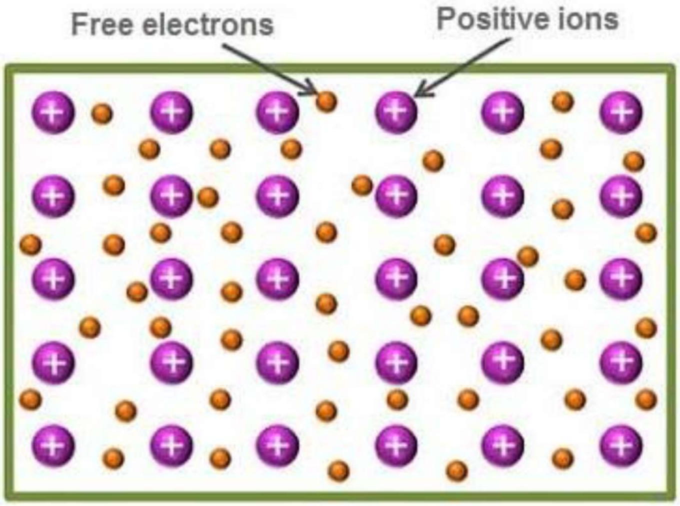

Fig 2.1. Schematic representation of arrangement of atoms in a solid

The electrons are not supposed to be confined to any of the atoms of the solid, and can move though the solid. The energy, E, of the electrons, while moving in the solid, is associated with the momentum of the electrons and is described as

$$E = \frac{\hbar^2 k^2}{2\,m} \tag{2.1}$$

where $\vec{k}$ is the wave vector of the electron, $\hbar$ is Plank's constant, and m is the mass of the electron. The dispersion relation described in eq. (2.1) is a continuous parabola, as shown in figure 2.2

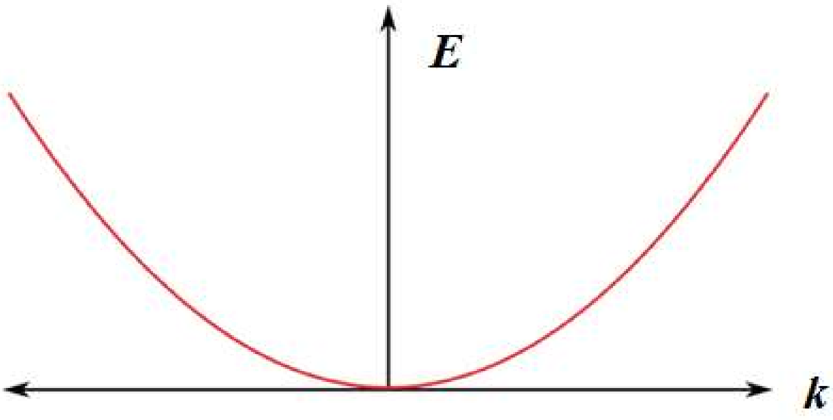

Fig 2. 2. *E* vs *k* relation for the free electron model

Basically, a solid consists of a large number of atoms. The corresponding large number of ionic cores always creates a weak periodic perturbation to the passage of electrons. Hence, the motion of the electrons in a crystal is no more associated with the parabola described in figure 2.2. Electrons, moving in the crystals, always have discrete values of their wave vector $\vec{k}$. These discrete values of wave vector are described as

$$k = \frac{2\pi}{a} \tag{2.2}$$

where *a* is the distance between the ionic cores. The energy dispersion relation of an electron, moving in a lattice under the interaction of the ionic cores, is described in $\vec{k}$ space. A $\vec{k}$ space is a space system which is used to draw the dispersion curves for the electrons moving in the crystal [152]. In $\vec{k}$ space, the values are described by $\frac{2\pi}{\lambda_e}$, where λ_e corresponds to the wavelength of the electron. The wavelengths of the electrons moving in a lattice are assumed to be equal to the size of the atom, so the intervals in the k space are described by $\frac{2\pi}{a}$.

2.2 Bragg’s Planes and Brillouin Zone

The interactions between the ionic cores and the electrons lead to the diffraction of the electrons around these ionic cores. The planes in the $\vec{k}$ space where this diffraction phenomena occur are known as the Bragg’s planes. Whenever a wave vector associated with the motion of an electron touches the Bragg’s plane, the plane wave becomes stationary and a distortion occurs at the Bragg’s plane. Such a distortion causes the creation of a gap, which is a region where electrons cannot occupy a state without an external force. The region in electron dispersion relation in the $\vec{k}$ space where the Bragg’s condition is satisfied is called the Brillouin zone [153]. Thus, the Brillouin zone is an important parameter in finding the diffraction of electrons under the Bragg's condition. Figure 2.3 shows the creation of the Brillouin zones in electron dispersion phenomena.

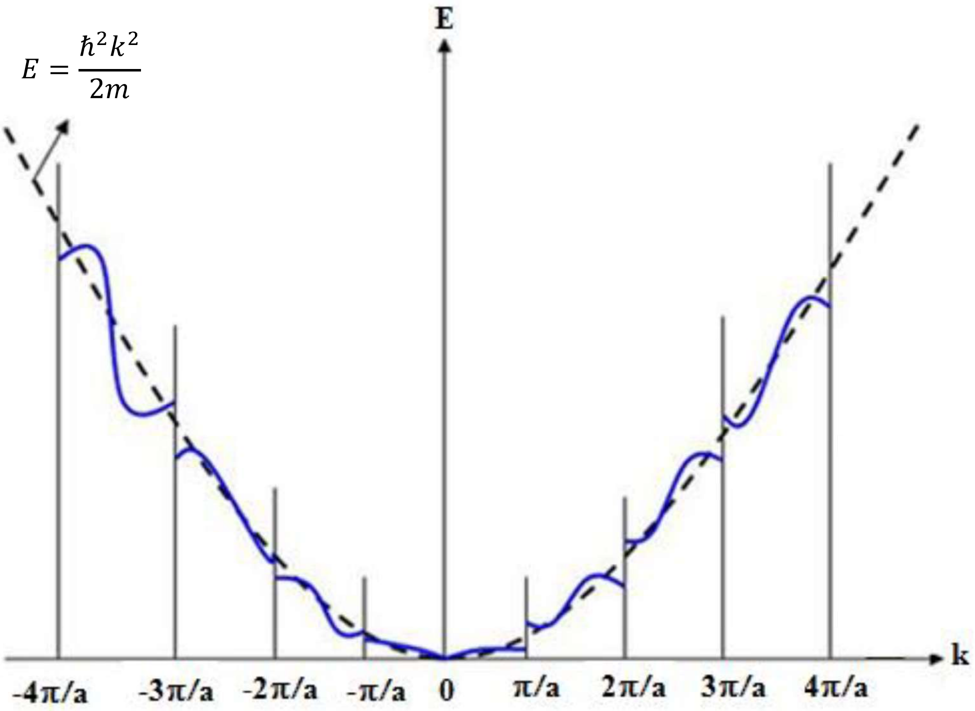

Fig 2.3. *E* vs *k* relation for nearly free electron model

The Brillouin zones schemes are classified into three different schemes. These are extended zone scheme, repeated zone scheme and reduced zone scheme. All of these schemes are shown in figure 2.4. The simplest scheme is the reduced zone scheme in which the extended zone scheme is folded to the first Brillouin zone [154]

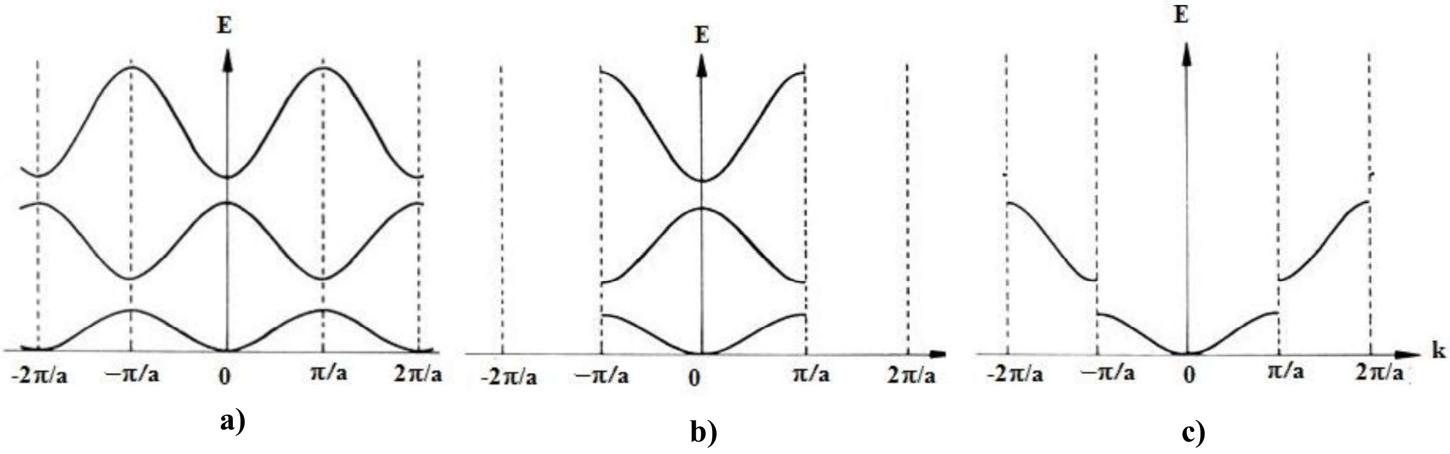

Fig 2.4.Schematic representation of Brillouin zone schemes: a) Extended b) reduced c) repeated zone

.

2.3 Classification of Materials on the Basis of Band Gap

The formation of gaps in the dispersion curves gives a new classification to materials. In this classification, materials are categorized as conductors, semiconductors or insulators on the basis of their dispersion relations. Such a characterization is called the band gap characterization or electronic characterization of materials. In order to do electronic structure characterization, a constant energy surface is always assumed in the band structure of materials. This constant energy surface separates the filled levels from the unoccupied levels and is called the Fermi surface. On the basis of their electronic structure, the materials are classified as: 1) metals where the valence band overlaps with the conduction band, 2) Semiconductors and insulators: there exists a definite band gap due to the diffraction of plane waves at the boundary of the Brillouin zone. Electrons cannot cross these gaps without any external perturbation. In semiconductors, this gap lies within the range of 0.1 to 6 eV, while in insulators, it is above 6 eV. The characterization of materials on the basis of their band structure is shown in figure 2.5

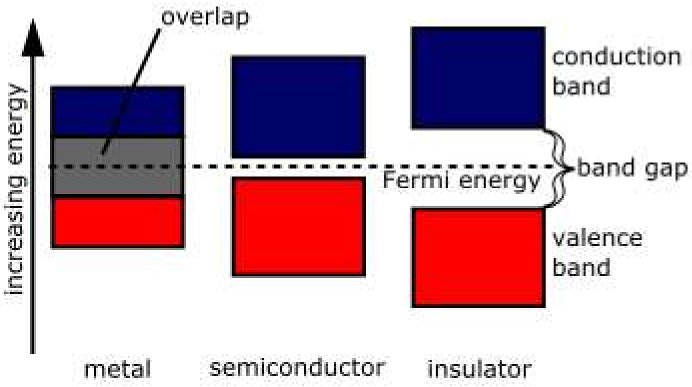

Fig 2.5. Classification of materials on the basis of band structure

2.4 Nature of Band Gaps in Semiconductors

The creation of band gap due to the diffraction of electrons at the zone boundaries is a characteristic feature present in semiconductors. Due to the formation of these gaps, electrons reside in the valence bands and cannot cross the gap until an external perturbation is applied. When the external force is applied, electrons can leave their respective valence bands and enter into the conduction bands by crossing their energy gaps. The most common example of perturbation applied to semiconductors, in order to analyze their band gap, is the interaction of electrons with light. When light of sufficient frequency interacts with a solid, it transfers its energy to the valence electrons. If the energy transferred to the electrons is higher than the band gap value, the electrons make a transition from valence to conduction band. Whenever the valence electrons absorb energy, they make transitions to the conduction bands in different directions in $\vec{k}$ space. A transition in which the wave vector $\vec{k}$ remains the same is called a direct transition. The materials in which direct transitions occur are called direct band gap semiconductors. On the other hand, there is also a possibility for the electrons to make an indirect transition. In these transitions, the excess momentum of photons is transferred to phonons since a phonon can absorb less energy but a large amount of momentum as compared to electrons [155]. As a result, the wave vector $\vec{k}$ changes, and such transition is called an indirect transition. The schematic diagrams of direct and indirect transitions are shown in the figure 2.6.

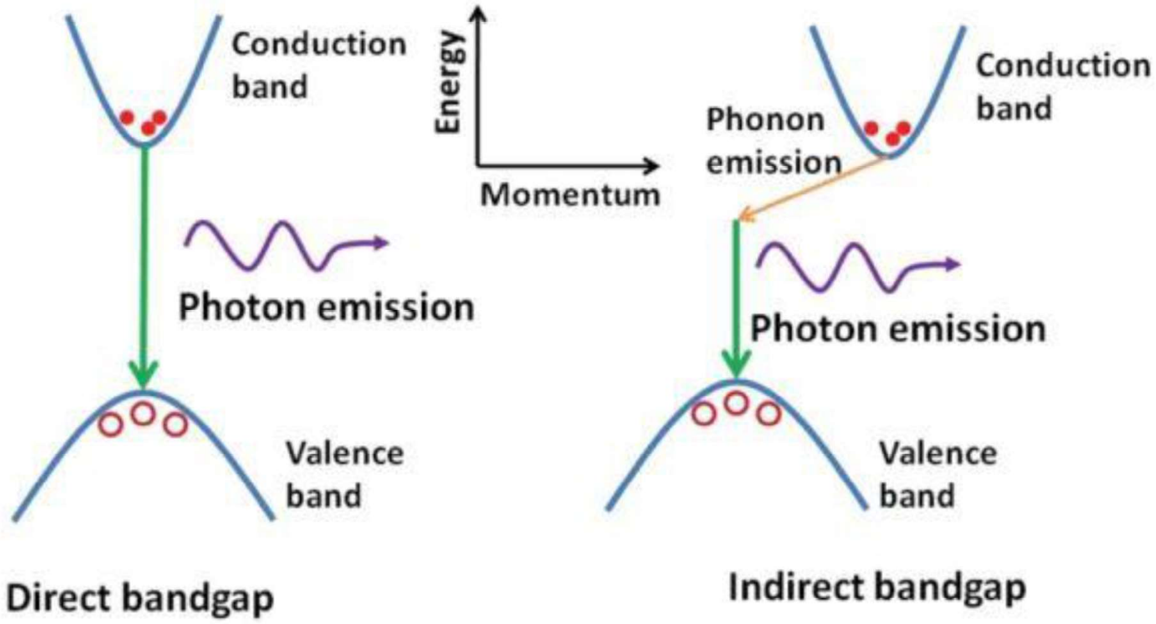

Fig 2.6. Direct and indirect band gaps in semiconductors

2.5 Band Structure of Gallium Arsenide

The band structure is the physical visualization of the energy of the electrons as a function of its momentum in a crystal. In a band structure, the momentum of electrons is given along specific directions in the crystal. These directions are denoted by the symbols Γ, Δ, X, Λ, and L. According to the nearly free electron model, the interaction of electrons with the ionic cores creates the band gap due to the diffraction of electrons at the zone boundaries. The presence of the band gap can be visualized in the band structure diagram of crystal. As a simple case, consider the example of GaAs [66]. The crystal structure GaAs is shown the figure 2.7. It has a face centered cubic (FCC) structure with gallium atoms located at the corners and at the center of the faces of the lattice. On the other hand, 4 arsenic atoms are inside the cell forming a zinc blende type crystal structure. Electrons in gallium arsenide reflect the symmetry of the crystal structure. Their wavefunctions are given by Bloch wave functions. Moreover, in order to reflect the symmetry of the crystal, the minimum wavelength of the electron should be less than the lattice constant of the crystal, which is the smallest periodicity length. This is due to the fact that the same electron state could be described as well by a function with a longer wavelength. As a consequence of the minimal wavelength, the wavevectors have a maximal length, and all possible wavevectors exist within a geometrical shape, which is called the Brillouin zone. The Brillouin zone of the gallium arsenide crystal is shown in figure 2.8. The center of the Brillouin zone corresponds to the wavevector $k = 0$. This point is denoted by Γ. On the other hand, the points L and X denote the centres of the hexagonal and quadratic faces of the Brillouin zone. These are corresponding to the maximal wavevectors in the Brillouin zone of the GaAs. The points Λ and Δ just denote half of these maximal wavevectors.

Figure 2.9 shows the band structure of GaAs which represents the dispersion relation for electrons between the centre and the border of the Brillouin zone. Close to the Γ point, the energy of the electrons is well described by a parabola. However, it is not true for the whole of the Brillouin zone. Moreover, there exists a certain energy region which is not occupied by any wavevector in the Brillouin zone. This empty region is known as the band gap. There are no states available at these energies. The states below the band gap are called states in the valence band, while the states above the gap are in the conduction band. The electrical behavior of a material depends on whether the electrons exist in its conduction band or not. For metals, electrons can easily go through the conduction band. On the other hand, in case of insulators, a large band gap exists between the valence and the conduction band. In case of semiconductors like gallium arsenide, the valence band is filled, and few electrons are usually thermally excited to the conduction band.

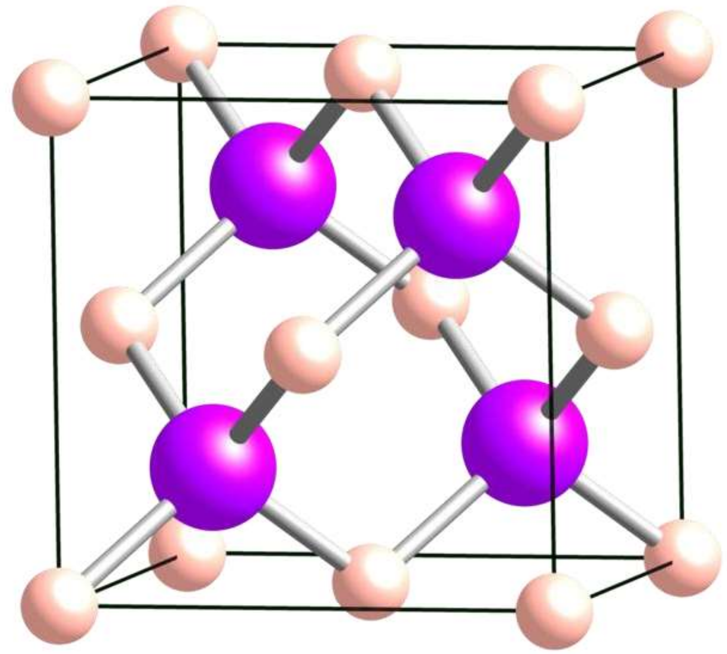

Fig. 2. 7. Crystal structure of GaAs. The small solid circles represents the gallium atoms, the big solid circles represents the arsenic atoms

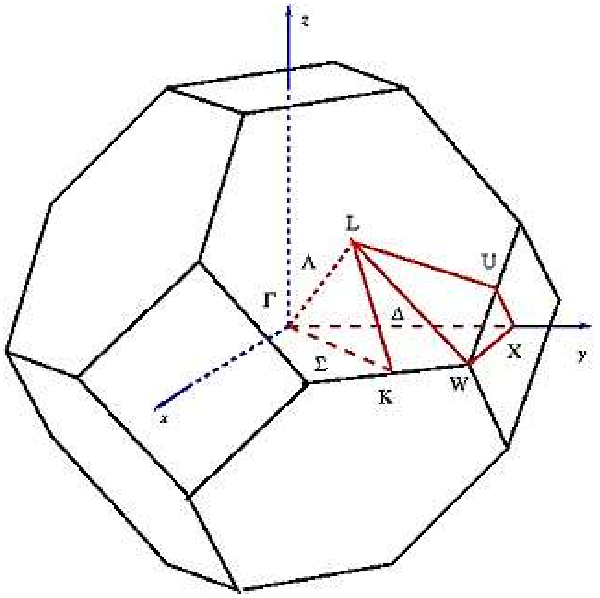

Fig 2. 8. Brillouin zone related to the GaAs.

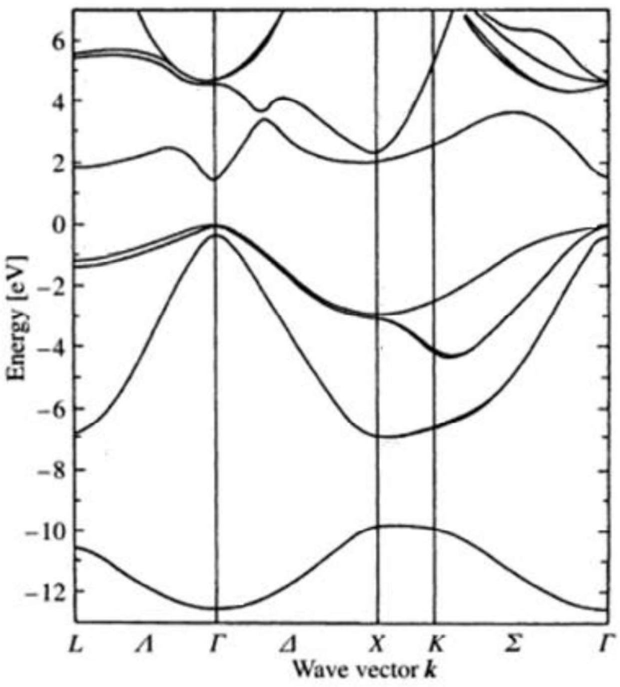

Fig 2. 9. Band structure of GaAs.

2.6 Interaction of Light with Matter

The basic way to analyze the optical properties of a material, such as its band gap, is to study the interaction of its valence electrons with light. So, the basic interaction of electromagnetic radiation with matter should be known in order understand the electroreflectance process [156].

Consider the system of an electron moving in a solid under the interaction of electromagnetic radiation. The Hamiltonian (H_o) of the system is described as

$$H_o = \frac{P^2}{2m} + V(r) \qquad (2.3)$$

where P is the momentum of the electron and $V(r)$ is the potential. In order to introduce the electromagnetic radiation in the system, a scalar potential $\varphi(r)$ and a magnetic vector potential $\vec{A}$(r) are introduced in the system. Under the Coulomb gauge transformation, the electric and magnetic fields are described as

$$\vec{E}_F = \frac{-1}{c}\frac{\partial \vec{A}}{\partial t} \quad \text{and} \quad \vec{B} = \nabla \times \vec{A}$$

where $\vec{B}$ is the magnetic field, $\vec{E}_F$ is the electric field, and c is the speed of light. Since the momentum of a charged particle in the electromagnetic radiation is described as

$\vec{P} \to \vec{P} - \frac{q\vec{A}}{c}$, where q is the charge of the particle. The Hamiltonian for the electron moving in an electromagnetic filed is

$$H = \frac{1}{2m}(\vec{P} + \frac{e\vec{A}}{c})^2 + V(r) \qquad (2.4)$$

The factor $\frac{1}{2m}(\vec{P} + \frac{e\vec{A}}{c})^2$ can be splitted as

$$\frac{1}{2m}(\vec{P}+\frac{e\vec{A}}{c})^2=\frac{1}{2m}(P^2+\frac{e^2A^2}{c^2}+\frac{e\vec{P}.\vec{A}}{c}\quad\frac{e\vec{A}.\vec{P}}{c})$$

$\because \vec{P}=-i\hbar\nabla$ and $\nabla.\vec{A}=0$ $\Rightarrow \vec{P}.\vec{A}=\vec{A}.\vec{P}$

Thus, equation (2.4) becomes

$$H=\frac{1}{2m}(\vec{P}+\frac{e\vec{A}}{c})^2+V(\mathrm{r})=\frac{P^2}{2m}+\frac{e^2A^2}{2mc^2}+\frac{e\vec{A}.\vec{P}}{mc}+V(r)$$

Neglecting the terms which depends quadratically on $\vec{A}$, we have

$$H=H_o+\frac{e\vec{A}.\vec{P}}{mc} \tag{2.5}$$

where the term, $\frac{e\vec{A}.\vec{P}}{mc}$, arises due to interaction of electrons of the solids with the radiation. Hence, we can describe the interaction Hamiltonian as

$$H_{e-R}=\frac{e\vec{A}.\vec{P}}{mc} \tag{2.6}$$

2.7 Theory of Perturbation

Whenever light of suitable energy is introduced to the electrons of a material, it creates a perturbation to the system. The theory of perturbation is important in describing the effects of light on the electrons. Under the influence of light, electrons make a transition. This transition is governed by the difference of energy between their initial and final states. For a general perturbation $V_o(\mathrm{r})$ which is switched on at $t = 0$ and off at $t' > t$, the Hamiltonian for the system is

$$H'=\begin{cases} H_o & t'<0\, and\, t'>t \\ H_o+V_o(\mathrm{r}) & 0<t'<t \end{cases} \tag{2.7}$$

If the system is in the state defined by $\Psi_i^o(r)$ at the time $t' < 0$ and we apply the perturbation V_o(r) to the system, then, the amplitude of the system to be in the state $\Psi_k(r)$, after making a transition from the state $\Psi_i(r)$, is

$$C'_{ki} = \frac{V_{ki}}{i\hbar}\int_0^t e^{i\omega_{ki}t'}dt' \tag{2.8}$$

where ω is the angular frequency of radiation, $\omega_{ki} = \omega_k - \omega_i$, and V_{ki} is the perturbation matrix which lifts the system from state *i* to state *k* and is described by

$$V_{ki} = \int \Psi_k^* V_o(\mathrm{r})\Psi_i dr \tag{2.9}$$

Equation (2.9) just gives a number, so eq. (2.8) can be simplified as

$$C'_{ki} = \frac{V_{ki}}{\hbar\omega_{ki}}(1-e^{i\omega_{ki}t}) \tag{2.10}$$

The corresponding probability of the electrons moving from state $\Psi_i(r)$ to state $\Psi_k(r)$ is

$$P'_{ki}(t) = \left|C'_{ki}(t)\right|^2 = \frac{V_{ki}^2}{\hbar^2\omega_{ki}^2}((1-e^{i\omega_{ki}t})(1-e^{-i\omega_{ki}t})) \tag{2.11}$$

Simplifying the expression, we get

$$P'_{ki}(t) = \frac{4V_{ki}^2}{\hbar^2\omega_{ki}^2}[\sin^2(\frac{\omega_{ki}t}{2})] \tag{2.12}$$

2.8 Fermi Golden Rule

Fermi golden rule connects the transition probability of the electrons, from their initial state *i* to their final state *k*, with the criteria required for a transition to take place. The probability for such a transition is described in equation (2.12) as

$$P'_{ki}(t) = \frac{2V_{ki}^2}{\hbar^2} F(\omega_{ki}, t) \qquad (2.13)$$

where

$$F(\omega_{ki}, t) = \frac{1}{2}\left[\frac{\sin(\frac{\omega_{ki} t}{2})}{\frac{\omega_{ki}}{2}}\right]^2 \qquad (2.13\text{a})$$

The function $F(\omega, t)$ is an important function. The behavior of this function with respect to both frequency ω and time t follows the rule

$$F(\omega, t) = \begin{cases} \frac{t^2}{2} & \omega \to 0 \\ \pi t \delta(\omega) & t \to \infty \end{cases} \qquad (2.14)$$

where $\delta(\omega)$ is the frequency dependent Dirac delta function. For a continuous interaction with matter, we have $t \to \infty$ and the transition probability in eq. (2.13) can be described as

$$\lim_{t\to\infty} P'_{ki}(t) = \frac{2V_{ki}^2}{\hbar^2} \lim_{t\to\infty} F(\omega_{ki}, t)$$

$$\Rightarrow \lim_{t\to\infty} P'_{ki}(t) = \frac{2V_{ki}^2}{\hbar^2} \pi t \delta(\omega_{ki}) \qquad (2.15)$$

Similarly, using the properties of Dirac delta function $\delta(\mathrm{b\,x}) = \frac{1}{b}\delta(\mathrm{x})$ and the photon energy $E_p = \hbar\omega$, we have the transition probability as

$$\lim_{t\to\infty} P'_{ki}(t) = \frac{2V_{ki}^2}{\hbar^2}\pi t\delta(E_k - E_i) \tag{2.16}$$

The transition rate can be described as

$$R_t = \lim_{t\to\infty}\frac{P'_{ki}(t)}{t} = \frac{2V_{ki}^2}{\hbar^2}\pi\delta(E_k - E_i) \tag{2.17}$$

Equation (2.17) is the general expression of Fermi golden rule. The significance of the Fermi golden rule is the appearance of Dirac delta function in its expression which gives a sharp peak only when the difference of the two energy states is zero thus indicating the physical condition of transitions. For an energy value other than the difference between the two transition states, the Dirac delta is 0 by its definition. So, no transitions are possible [157].

2.9 Matrix Elements of Perturbation

Although the Fermi golden rule, described in equation (2.17) gives the dependence of the transition probability on the initial and final state energies, it does not provide any necessary information about the perturbation used to make such transitions. So, knowledge of perturbation matrix elements should be introduced into the expression of Fermi golden rule. For a plane wave form of incident radiation, the perturbation is given by

$$V_{ki}(\mathrm{t}) = V_{ki}(\mathrm{r})e^{i\omega t'} + V_{ki}{}^{\dagger}(\mathrm{r})e^{-i\omega t'} \tag{2.18}$$

where the perturbation matrix elements are defined by

$$V_{ki}(\mathrm{r}) = \left\langle \Psi_k \middle| \mathrm{V}(\mathrm{r}) \middle| \Psi_i \right\rangle \tag{2.19}$$

and the transition amplitude is described in eq. (2.8)

For $k \neq i$, we have the transition amplitude as

$$C'_{ki} = \frac{1}{i\hbar}\int_0^t (\mathrm{V}_{ki}\, e^{i\omega_{ki}t'} + V_{ki}{}^{\dagger} e^{-i\omega_{ki}t'})e^{i\omega t'}dt'$$

$$\Rightarrow C'_{ki} = \frac{V_{ki}}{i\hbar}\int_0^t e^{i\omega_{ki}t'} e^{i\omega t'} + \frac{V_{ki}^{\dagger}}{i\hbar}\int_0^t e^{-i\omega_{ki}t'} e^{i\omega t'} dt'$$

Solving the integration

$$\Rightarrow C'_{ki} = \frac{V_{ki}}{\hbar}\left[\frac{1-e^{i(\omega+\omega_{ki})t}}{\omega+\omega_{ki}}\right] + \frac{V_{ki}^{\dagger}}{\hbar}\left[\frac{1-e^{i(\omega_{ki}-\omega)t}}{\omega_{ki}-\omega}\right] \qquad (2.20)$$

The corresponding probability is described as

$$P'_{ki}(t) = \left|C'_{ki}(t)\right|^2 \qquad (2.21)$$

From equations (2.20) and (2.21), the probability of the system to be found in the state 'k' is maximum only if

$$\omega_{ki} - \omega = 0 \qquad (2.22)$$

or

$$\omega + \omega_{ki} = 0 \qquad (2.23)$$

But they both can't be true simultaneously. So, the two cases are considered separately. Considering the case described by equation (2.22) and neglecting the first component of equation (2.20), we have:

$$C'_{ki} = \frac{V_{ki}^{\dagger}}{\hbar}\left[\frac{1-e^{i(\omega_{ki}-\omega)t}}{\omega_{ki}-\omega}\right] \qquad (2.24)$$

and

$$P'_{ki}(t) = \frac{\left|V_{ki}^{\dagger}\right|^2}{\hbar^2(\omega_{ki}-\omega)^2}\left[(1-e^{i(\omega_{ki}-\omega)t})(1-e^{-i(\omega_{ki}-\omega)t})\right]$$

$$\Rightarrow P'_{ki}(t) = \frac{\left|V_{ki}^{\dagger}\right|^2}{\hbar^2(\omega_{ki}-\omega)^2}\left[2-(e^{i(\omega_{ki}-\omega)t} - e^{-i(\omega_{ki}-\omega)t})\right]$$

$$\Rightarrow P'_{ki}(t)=\frac{\left|V_{ki}^{\dagger}\right|^2}{\hbar^2}\frac{\sin^2\frac{(\omega_{ki}-\omega)t}{2}}{(\frac{\omega_{ki}-\omega}{2})^2}$$

Let $\omega_{ki}-\omega=\omega'$

$$\Rightarrow P'_{ki}(t)=\frac{\left|V_{ki}^{\dagger}\right|^2}{\hbar^2}\frac{\sin^2\frac{(\omega')t}{2}}{(\frac{\omega'}{2})^2}=\frac{2\left|V_{ki}^{\dagger}\right|^2}{\hbar^2}F(\omega',t) \qquad (2.25)$$

where $F(\omega',t)=\frac{1}{2}\frac{\sin^2\frac{(\omega')t}{2}}{(\frac{\omega'}{2})^2}$ is the same function as described in eq. (2.13a) with the properties described in equation (2.14). So, for a continuous perturbation, we have from equation (2.25)

$$\lim_{t\to\infty}P'_{ki}(t)=\frac{2\left|V_{ki}^{\dagger}\right|^2}{\hbar^2}\lim_{t\to\infty}F(\omega',t)=\frac{2\left|V_{ki}^{\dagger}\right|^2}{\hbar^2}\pi t\delta(\omega') \qquad (2.26)$$

Using the properties of Dirac delta function $\delta(\mathrm{ax})=\frac{1}{a}\delta(\mathrm{x})$ and the photon energy $E=\hbar\omega$

$$\lim_{t\to\infty}P'_{ki}(t)=\frac{2\pi t\left|V_{ki}^{\dagger}\right|^2}{\hbar}\delta(E_k-E_i-\hbar\omega) \qquad (2.27)$$

By the definition of Dirac delta function in eq.(2.27), the probability is significant only if

$$E_k-E_i-\hbar\omega=0\Rightarrow E_k-E_i=\hbar\omega \qquad (2.28)$$

An important physical insight can be extracted from eq. (2.27) and eq. (2.28). The light impinging on the material can excite the electrons from the state *i* to state *k* only if the energy of the photons, interacting with the electrons, is equal to the difference of the energy states ‘i’ and ‘k’. The case considered in equation (2.22) is equivalent to the absorption of light. Following the same lines, the relation of the emission of light can also be calculated as

$$\lim_{t\to\infty} P'_{ki}(t) = \frac{2\pi t\left|V_{ki}{}^{\dagger}\right|^2}{\hbar}\delta(E_k - E_i + \hbar\omega) \tag{2.29}$$

Physically, this equation describes the emission of photons as the electrons make a transition from the higher state k to lower energy state i. Considering the absorption process in materials in which the electrons make a transition from their valence band with energy E_v to the conduction band with energy E_c we have

$$\lim_{t\to\infty} P'_{cv}(t) = \frac{2\pi t\left|V_{cv}{}^{\dagger}\right|^2}{\hbar}\delta(E_c - E_v - \hbar\omega) = \frac{2\pi t\left|V_{cv}{}^{\dagger}\right|^2}{\hbar}\delta(E_g - \hbar\omega) \tag{2.30}$$

The corresponding transition rate is described as

$$R_t = \lim_{t\to\infty} P'_{cv}(t) = \frac{2\pi\left|V_{cv}{}^{\dagger}\right|^2}{\hbar}\delta(E_g - \hbar\omega) \tag{2.31}$$

where E_g is the band gap of the material. Equation (2.31) describes the general form of transition rate. We can convert this into the form describing the interacting form of Hamiltonian and the electronic states. The Hamiltonian related to the interaction of radiation with the electrons is described in eq.(2.6) as

$$H_{e-R} = \frac{e\vec{A}.\vec{P}}{mc} \tag{2.6}$$

and the perturbation matrix element for the electron making a transition from the valence to conduction band is

$$V_{cv} = \left\langle \Psi_c \middle| V_o(\mathrm{r}) \middle| \Psi_v \right\rangle$$

$$\Rightarrow V_{cv} = \left\langle \Psi_c \middle| H_{e-R} \middle| \Psi_v \right\rangle = \frac{e}{mc}\left\langle \Psi_c \middle| \vec{A}.\vec{\mathrm{P}} \middle| \Psi_v \right\rangle \tag{2.32}$$

For a given radiation with frequency ω, the vector potential is described as

$$\vec{A} = \hat{e}A_o e^{i(\vec{k}.\vec{r}-\omega t)} + c.c \tag{2.33}$$

where $\hat{e}$ the polarization vector along electric field and c.c is the complex conjugate of the first part. Using these definitions into equation (2.31), we have

$$R_t = \frac{2\pi}{\hbar}\left(\frac{eAo}{mc}\right)^2 \left|\left\langle \Psi_c \middle| e^{ik.r}\hat{e}.\vec{P} \middle| \Psi_v \right\rangle\right|^2 \delta(E_c - E_v - \hbar\omega)$$

$$\Rightarrow R_t = \frac{2\pi}{\hbar}\left(\frac{eAo}{mc}\right)^2 \left|\hat{e}.f_{cv}(\mathrm{k})\right|^2 \delta(E_k - E_i - \hbar\omega) \tag{2.34}$$

where

$$\hat{e}.\vec{f}_{cv}(\vec{\mathrm{k}}) = \left\langle \Psi_k \middle| \hat{e}.\vec{\mathrm{P}} \middle| \Psi_i \right\rangle = \hat{e}.\left\langle \Psi_k \middle| -i\hbar\nabla \middle| \Psi_i \right\rangle = \hat{e}.\int \Psi_k^*(r)(-i\hbar\nabla)\Psi_i(r)d\vec{r}$$

The total number of allowed transitions per unit time per unit volume is the sum of all possible states per unit volume. This includes sum over all the *k* points, sum over all the spin states and sum over all the band indices v and *c*. If the density of allowed vectors $\vec{\mathrm{k}}$ within the Brillouin zone is described by $\frac{V_c}{(2\pi)^3}$, where V_c is the volume of the unit cell, then the total k points within the Brillouin zone is

$$\sum_k \rightarrow \int \frac{1}{(2\pi)^3} dk$$

Also, there are two possible states of spins present, so

$$\sum_s \rightarrow 2$$

So, the transition rate is

$$R_t = \frac{2\pi}{\hbar}\left(\frac{eAo}{mc}\right)^2 \sum_{v,c}\int_{BZ} \frac{2\,d\vec{k}}{(2\pi)^3} \left|\hat{e}.f_{cv}(\mathrm{k})\right|^2 \delta(E_k - E_i - \hbar\omega) \tag{2.35}$$

where the integration is over the first Brillouin zone.

2.10 Connection of Fermi Golden Rule with the Dielectric Function

Equation (2.35) describes the transition rate of electrons from their respective valence bands to the conduction bands under interaction with light. Perhaps the most sophisticated way is to connect such transitions with the basic optical parameters of the materials. The dielectric function is a basic optical parameter in terms of which one can describe most of the optical properties of materials. The dielectric function of a material is a complex quantity described as

$$\varepsilon = \varepsilon_r + i\varepsilon_i \tag{2.36}$$

The dielectric function ε is related to the refractive index as

$$\varepsilon = N^2 \tag{2.36a}$$

the refractive index of a material is also described as

$$N = n + iK \tag{2.37}$$

where *n* is the normal refractive index of the material and *K* is the extinction coefficient. Now, squaring the refractive index, we have

$$N^2 = n^2 - K^2 + i2nK \tag{2.38}$$

Comparing (2.38) with (2.36) we have

$$\varepsilon_r = n^2 - K^2 \tag{2.39}$$

$$\varepsilon_i = 2nK \tag{2.40}$$

Whenever light of a specific intensity passes through the material, it loses its intensity due to the absorbance of light by the material. The absorption coefficient α of a material can be described as

$$\alpha = \frac{4\pi K}{\lambda_p} \tag{2.41}$$

where λ_p is the wavelength of light. Using the expression (2.40) we have

$$\Rightarrow \alpha = \frac{\omega}{n\,c}\varepsilon_i \tag{2.42}$$

Similarly, the reflectance of a material can be described in terms of the refractive index as

$$R = \left|\frac{N-1}{N+1}\right|^2 \tag{2.43}$$

Using eq. (2.37), we have

$$R = \frac{(n-1)^2 + K^2}{(n+1)^2 + K^2} = \frac{n^2 + K^2 + 1 - 2n}{n^2 + K^2 + 1 + 2n} \tag{2.44}$$

Since,

$$n^2 + K^2 = \sqrt{(n^2 + K^2)^2} = \sqrt{(n^2 - K^2)^2 + 4n^2K^2} = \sqrt{\varepsilon_r^{\,2} + \varepsilon_i^{\,2}} \tag{2.45}$$

and

$$2n = \sqrt{4n^2} = \sqrt{2(n^2 + K^2 + n^2 - K^2)^2} = \sqrt{2(\sqrt{\varepsilon_r^{\,2} + \varepsilon_i^{\,2}} + \varepsilon_r)} \tag{2.46}$$

Using Eq. (2.45) and (2.46) in Eq. (2.44), we have the expression of reflectance in terms of the dielectric function of the material.

$$R = \frac{\sqrt{\varepsilon_r^{\,2} + \varepsilon_i^{\,2}} + 1 - \sqrt{2(\sqrt{\varepsilon_r^{\,2} + \varepsilon_i^{\,2}} + \varepsilon_r)}}{\sqrt{\varepsilon_r^{\,2} + \varepsilon_i^{\,2}} + 1 + \sqrt{2(\sqrt{\varepsilon_r^{\,2} + \varepsilon_i^{\,2}} + \varepsilon_r)}} \tag{2.47}$$

Now,

If, $R_t(\omega) =$ transition rate per unit time, then

$\hbar\omega\, R_t(\omega) =$ energy absorbed per unit time

Also, if v = velocity of propagation of radiation then, $\mu v = \mu(\frac{c}{n})$ is the energy flux per unit time where μ is the average energy density of the material.

So, the absorption coefficient is the energy absorbed per unit time per unit volume divided by the energy flux. That is

$$\alpha(\omega) = \frac{\hbar\omega R_t(\omega)}{\mu v} = \frac{\hbar\omega R_t(\omega)}{\mu\frac{c}{n}} \tag{2.48}$$

Using equations (2.35) and (2.48), we have

$$\alpha(\omega) = \frac{2\pi\omega n}{\mu c}\left(\frac{eA_o}{mc}\right)^2 \sum_{v,c}\int_{BZ}\frac{2d\vec{k}}{(2\pi)^3}\left|\hat{e}.f_{cv}(\vec{\mathrm{k}})\right|^2 \delta(E_k - E_i - \hbar\omega)$$

Using equation (2.42), we have

$$\varepsilon_i(\omega) = \frac{2\pi\ n^2}{\mu}\left(\frac{eA_o}{mc}\right)^2 \sum_{v,c}\int_{BZ}\frac{2d\vec{k}}{(2\pi)^3}\left|\hat{e}.f_{cv}(\vec{\mathrm{k}})\right|^2 \delta(E_k - E_i - \hbar\omega) \tag{2.49}$$

Equation (2.49) is the basic expression which associates the band structure of a material with its dielectric function. Once we know one part of the dielectric function, we can find out its other part with the help of Kramers Kronig relationship (KKR). So, the real part of the dielectric function from equation (2.44) can be written, with the help of Kramers Kronig relation, as

$$\varepsilon_r(\omega) = 1 + \frac{2}{\pi} Z\int_0^\infty y\varepsilon_i(y)\frac{1}{y^2-\omega^2}dy \tag{2.50}$$

where y is the frequency defined in a certain range, Z is the principle part of the integral [153]. The two equations (2.49) and (2.50) are the general form of the real and imaginary parts of the dielectric function, and can be used to describe all the optical properties of the material.

2.11 Joint Density of states

The main contribution in the dielectric function, as shown in eq. (2.49), is coming from the factor $\int_{BZ} \frac{2d\vec{k}}{(2\pi)^3}\delta(E_c - E_v - \hbar\omega)$ (since all other factors are constant). This term is called the joint density of states. That is

$$\rho_{c-v} = \int_{BZ} \frac{2d\vec{k}}{(2\pi)^3}\delta(E_c - E_v - \hbar\omega) \qquad (2.51)$$

The joint density of states is defined as the total number of states which are available per unit energy and per unit time with in the energy range of (E_c-E_v) and within $k+dk$,where E_c and E_v are the conduction and valence bands energies, respectively [158]. Since the density of states refers the number of states with in the energy scale at each *k*-point, we should introduce a constant energy surface at each *k*-point. If *S* is the constant energy surface at each *k*-point then eq. (2.51) can be written as

$$\rho_{c-v} = \int \frac{2\,dS}{(2\pi)^3 \left|\nabla(\mathrm{E_c}(\vec{\mathrm{k}}) - \mathrm{E_v}(\vec{\mathrm{k}}))\right|_{E_c - E_v = \hbar\omega}} \qquad (2.52)$$

where we used the property of the Dirac delta function

$$\int \delta f(\mathrm{x}) g(\mathrm{x}) dx = \sum_{x_o} g(\mathrm{x_o}) \left.\frac{dx}{df}\right|_{x=x_o}$$

2.12 Van-Hove Singularities

The joint densities of states, in eq. (2.52), shows strong discontinuities at specific values of *E*. These discontinuities are called the critical points or Van Hove singularities. From eq. (2.52), the critical points appear when

$$\nabla \mathrm{E_c} - \nabla \mathrm{E_v} = 0 \text{ or } \nabla \mathrm{E_c} = \nabla \mathrm{E_v} \qquad (2.53)$$

In the band structure calculations, the first condition appears at any k-point of the Brillouin zone while the second condition appears only at the higher symmetry points. In order to find the real picture of joint density of states at the Van Hove singularities, consider a simple transition in which a photon with energy $\hbar\omega$ excites the electrons from the valence band to the conduction band. Using a simple parabolic expression, we can define the valence and conduction band energies as [159]:

$$E_c(\mathrm{k}) = \mathrm{E_g} + \frac{\hbar^2 k^2}{2m_c} \tag{2.54}$$

$$E_v(\mathrm{k}) = -\frac{\hbar^2 k^2}{2m_v} \tag{2.55}$$

where E_g is the energy difference between valence and conduction bands, m_c and $\mathrm{m_v}$ are the masses of electron and hole in the conduction and valence band respectively.

From eq. (2.54) and (2.55) we have

$$\Rightarrow E_c(\mathrm{k}) - E_v(\mathrm{k}) = \hbar\omega = \mathrm{E_g} + \frac{\hbar^2 k^2}{2\mu_r} \tag{2.56}$$

where μ_r is the reduced mass of the system defined as

$$\frac{1}{\mu_r} = \frac{1}{m_c} + \frac{1}{m_v} \tag{2.57}$$

Using this expression in the joint density of states we have

$$\rho_{c-v} = \int \frac{2\,dS}{(2\pi)^3 \left| \nabla(\mathrm{E_g} + \frac{\hbar^2 k^2}{2\mu_r}) \right|_{E_c - E_v = \hbar\omega}}$$

$$\rho_{c-v} = \frac{2}{(2\pi)^3} \left(\frac{4\pi k^2}{\frac{\hbar^2 k}{\mu}} \right) = \frac{\mu_r k}{\pi^2 \hbar^2} \bigg|_{E_c - E_v = \hbar\omega} \tag{2.58}$$

Using eq. (2.56), we have $k = \frac{2\mu_r}{\hbar^2}\sqrt{\hbar\omega - E_g}$

So, the joint density of states is defined as

$$\rho_{c-v} = \begin{cases} \frac{1}{\left(2\pi^2\right)}\left(\frac{2\mu_r}{\hbar^2}\right)^{3/2}\sqrt{\hbar\omega - E_g} & \hbar\omega > E_g \\ 0 & \hbar\omega < E_g \end{cases} \tag{2.59}$$

Equation (2.59) represents the mathematical description of critical points in the joint density of states for a three-dimensional crystal structure. The discontinuities that appear in the expression represent the Van Hove singularities. Physically, they show the critical points associated with the optical transitions in a material.

2.13 The Spectrophotometric Method

The quantum theory can be utilized to derive a relationship between the absorption coefficient α and the incident photon energy $(\hbar\omega)$. The relation is called the Tauc relation and is written as [160]

$$\left(\alpha\hbar\omega\right)^{1/\beta} = \eta^2\left(\hbar\omega - E_g\right) \tag{2.60}$$

Details of the derivation of this equation are given in Appendix A.

In this equation, η is a constant, and β has different values for different optical transitions described as

$\beta = 1/2$	for direct allowed transition
$\beta = 3/2$	for direct forbidden transition
$\beta = 2$	for indirect allowed transitions
$\beta = 3$	for indirect forbidden transition

The Tauc relation is employed extensively to calculate the band gap of a material. However, the major requirement for this method to work is that the photon energy should not exceed the band gap energy and the absorption phenomena should not be very strong. On the other hand, a less value of the absorption coefficient (α) might behave exponentially rather than square or square-root nature [161]. So, values of the absorption coefficient in the range of 10^2 to 10^3 might not be sufficient to compute the band gap of a material.

Experimentally, the band gap of a material depends on certain fabrication parameters. These include the synthesis of a material with different techniques like electron beam (EB) or sputtering, substrate temperature and post deposition conditions like annealing. In order to illustrate how an experimental parameter affects the band gap of a material, consider the example of WO_3 thin films fabricated at different substrate temperatures. WO_3 is an indirect band gap semiconductor having its band gap in the visible region. Figure 2.10 shows the determination of the band gap of WO_3 deposited on an unheated substrate and a substrate heated to a temperature of 400 °C. The band gap of WO_3 deposited on a heated substrate was less than the one deposited on the unheated substrate. A heated substrate normally provides a well oriented uniform deposition of the films with less surface roughness as compared to the unheated one. In case of thin films, some surface phenomena might have profound effects during the optical transitions. A common example of this is the scattering of light due to the surface roughness and grain boundaries which might lead to the inaccurate determination of the absorption coefficient and ultimately affects the band gap measurement [138].

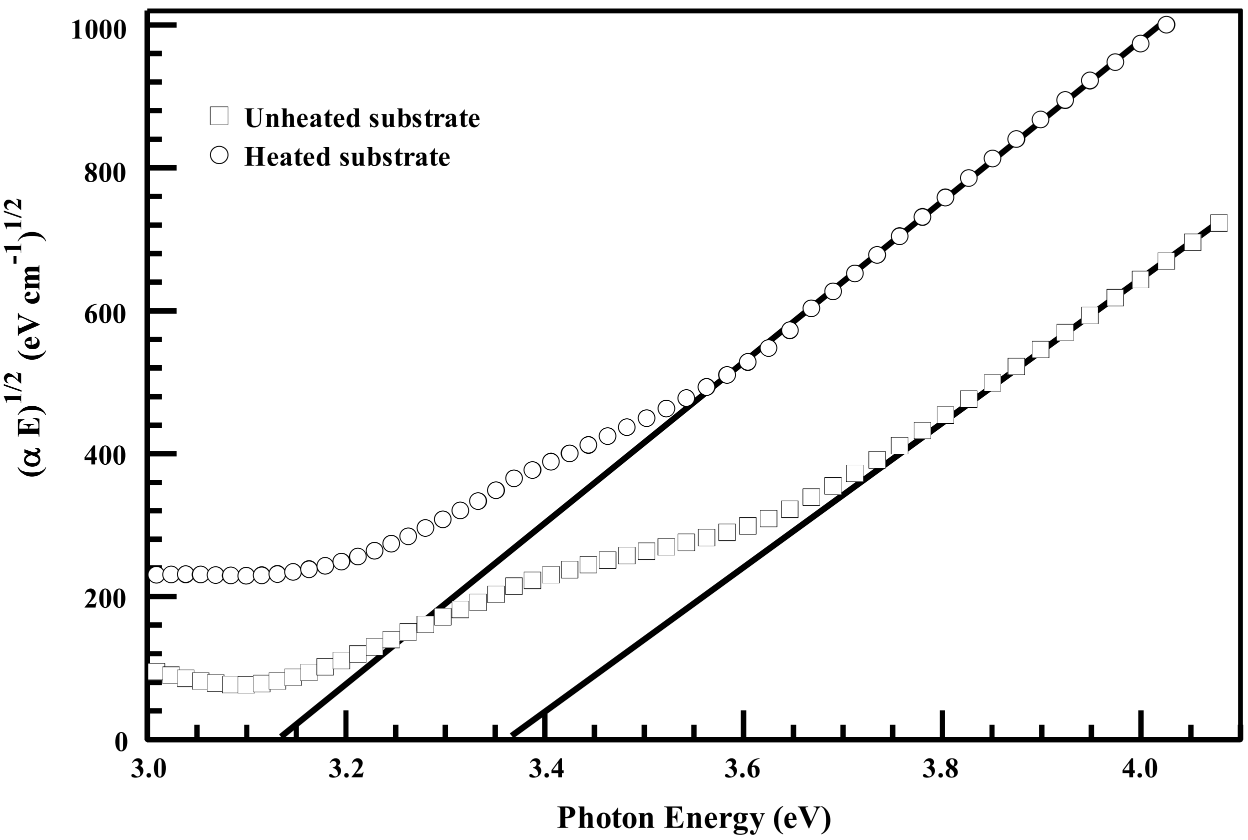

Fig 2. 10. Band gap of WO_3 thin films with heated and non -heated substrates

Besides the experimental conditions, the choice the power factor β in Tauc equation may lead to variations in the band gap of the material. A typical example is the band gap of SnO_2. Tin oxide is a wide band gap semiconductor with a band gap value of 3.88 eV [72]. However, it can be seen from figure 2.11 that the standard direct band gap method (that is choosing β =1/2 in Tauc plot equation) cannot provide us the correct band gap. This is due to the fact that in the downward direction, the Tauc plot is curved rather than linear so, the extrapolation significantly overestimates the band gap. On the other hand, the selection of power factor to β =2 leads to an underestimation of the band gap.

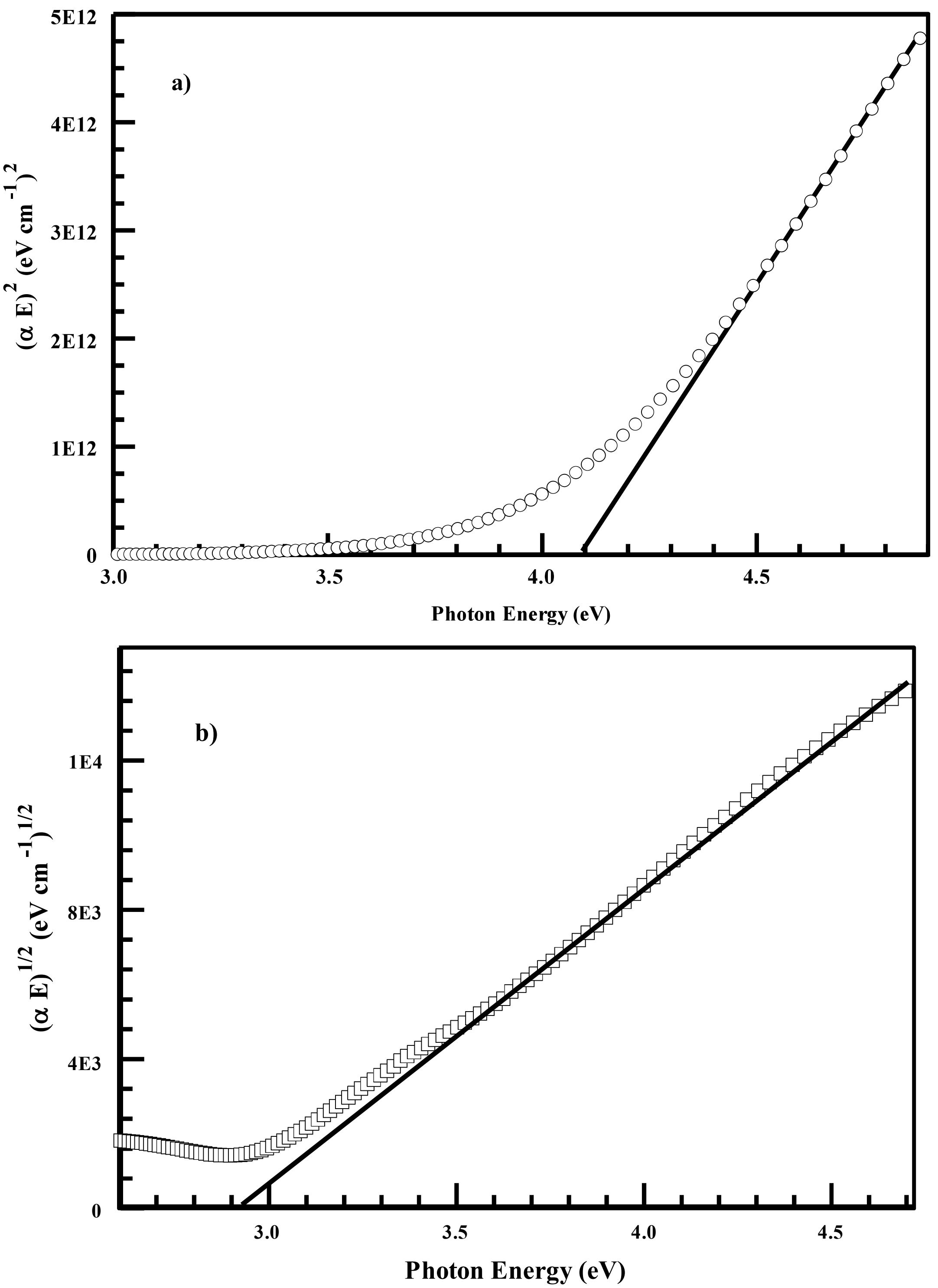

Fig 2. 11. Tauc plots of SnO_2 thin films: a) Direct b) Indirect

In summary, for nano crystals or thin films, the absorption spectrum deviates from its bulk nature. This causes the deviation of squared power law for direct transitions. Hence, the Tauc plot, which is helpful in studying the band gaps of bulk materials, might not be an appropriate choice of selection for calculating the band gaps of direct band gap semiconductors and the low dimensional crystal structures.

CHAPTER 3

Modulation Spectroscopy

3.1 Introduction to Modulation Spectroscopy

Modulation spectroscopy is a direct method to find the band gap of semiconductors. In modulation spectroscopy, the changes in optical parameters, rather than absolute values, are measured. The basic principle of this technique is to provide a periodic perturbation to the sample and to obtain sharp derivative-like structures in the optical response of the material. These peaks, which correspond to sharp changes in the optical spectra, are associated with the critical points of the band structure of the semiconductor.

Modulation spectroscopy is a powerful technique in characterizing thin film or bulk materials, nanostructures, super lattices, quantum wells, heterostructures and interfaces of the materials [11,72]. Some of the advantages of using this technique are

1- The modulated spectrum of an optical quantity is superior to its absolute value. This is because of the fact that a modulated response of a material always originates around the known critical points in the Brillouin zone. Contrary to it, the absolute response of a material always appears in the extended Brillouin zone region [72,73]

2- With the help of modulation spectroscopy, the inter band transition energies can be found within meV range even at room temperature [163].

3- The observed changes in the modulation spectroscopy are so sharp that they behave like a derivative of the absolute spectrum with respect to the modulated parameter. This derivative like nature suppresses the featureless background of the material and emphasizes the regions of inter band transitions. Moreover, due to its derivative like nature, the weak features of the crystal can also be enhanced in modulation spectroscopy [156]. In order to emphasizes the significance of the modulation spectroscopy, the example of absolute reflectance and the modulated reflectance of GaAs is shown in figure 3.1. Both spectra were taken at a temperature of 300 K. The absolute reflectance of GaAs is characterized by broad features. On the other hand, the electroreflectance (ER) spectrum revealed a series of sharp lines. The featureless background of the absolute spectrum was absent in the ER spectrum. The uninteresting background of the spectra is eliminated in favor of the intense sharp lines which are associated with the transitions involved in the material.

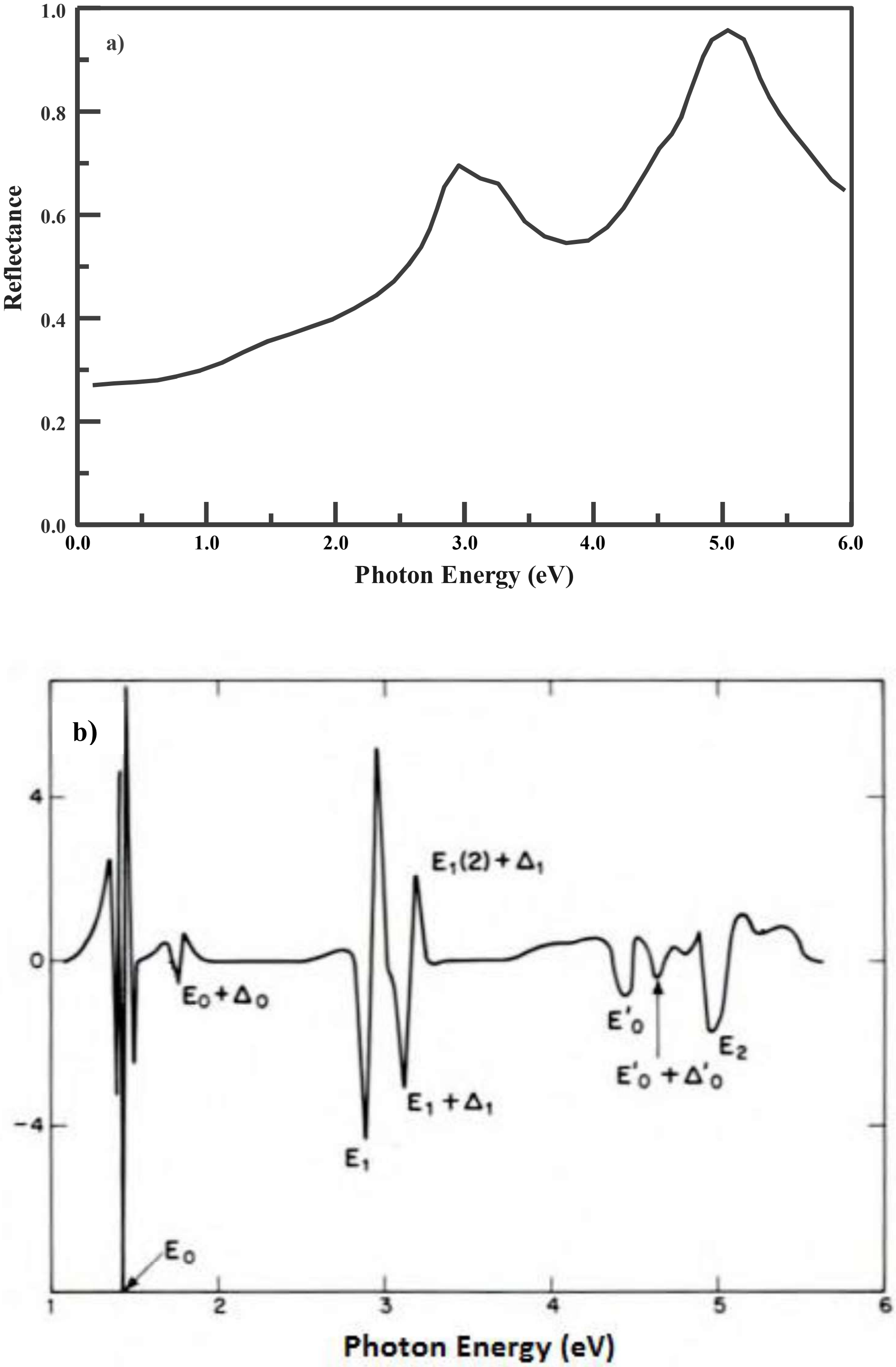

Fig 3. 1.a) Reflectance and b) Electroreflectance spectra of GaAs.

The sharp intense peaks $E_o, E_o + \Delta_o, E_1, E_1 + \Delta_1, E_o^{'}, E_2$ are the critical points associated with optical transitions in GaAs

3.2 Modes of Modulation Spectroscopy

3.2.1 Temperature Modulation

In thermomodulation or thermoreflectance, the heat changes are produced as a periodic perturbation across the heater on which the material is mounted. These heat changes are produced by applying current pulses through the sample. This is applicable only if the sample has a heat-conductive nature. For non-conductive materials, the perturbation is produced by applying a periodically chopped laser light [11]. The periodic change in the temperature causes the variations in the energy E and the broadening parameter Γ around the critical point of the crystal while preserving the crystal symmetry. That is, the resulted spectrum of thermomodulation remains independent to the direction of polarized light [164]. As a result of these changes, the band structure of the material alters, and these alterations are detected in terms of changes in the dielectric function of the material. The shift in the energy gap near a critical point is associated with the singularity point and is defined in terms of changes in the dielectric function as

$$\frac{\partial \varepsilon}{\partial T} = \frac{\partial \varepsilon}{\partial E}\frac{\partial E}{\partial T} \tag{3.1}$$

Besides the inter band transitions, other optical phenomena can also be analyzed with the help of this modulation technique. These include exciton effect and plasma resonance.

3.2.2 Wavelength Modulation

In this technique, the wavelength of the light is used as a periodic perturbation to create changes in the optical parameters of a sample. A wavelength modulation is different from other modulation techniques in a sense that no external modulation is applied to the sample to extract its optical transition information. The wavelength modulated spectrum is simply the first derivative of the normal spectrum of a sample. The multiple structures can be identified easily in the derivative spectrum as compared to the normal spectrum of an optical quantity. For example, if a change of slope is corresponding to a structure in the normal spectrum, it will be a step function in the first derivative of that spectrum [165].

Wavelength modulation can be produced by using a monochromatic beam whose wavelength is modulated periodically. Such a change is produced either by the mechanical vibration of exit or entrance slits of the monochromator or the vibration of a mirror inside the monochromator [166]. The response spectrum obtained in this way will be the derivative of reflected or incident light intensity I with respect to the distance x covered by the slit. So, the wavelength λ derivative of the intensity can be extracted as

$$\frac{dI}{d\lambda_p} = \frac{dI}{dx}\frac{dx}{d\lambda_p} \tag{3.2}$$

The wavelength modulation technique was successfully applied in obtaining the derivative spectrum of many semiconductor materials like Si, GaAs and GaSb [165]. However its use is limited within a specific wavelength range. Normally, it works from the visible to infrared region and cannot be applied in the UV region because of the non-uniformity of light and the appearance of several spectral lines in that region [144]. Moreover, as compared to the other modulation techniques, wavelength modulation spectra usually suffer a huge noise background issue. The elimination of such background is also a challenge in wavelength modulation spectroscopy.

3.2.3 Piezo Modulation

In this technique, a uniaxial stress is applied as a periodic perturbation to the sample. Such perturbation causes a change in the optical parameters (such as reflectance or transmittance) of the sample. These changes are more dominant near the onset of the optical transitions of the material and hence provide information about the transitions involved in the sample under study. Like the temperature modulation, stress modulation also preserves the symmetry and hence its resulted spectra are similar to those obtained from thermal modulation. With the help of this technique, it is possible to obtain not only the energy positions of the transitions but also the locations of these transitions in the Brillouin zone [79, 80]. Moreover, the magnitude of the response spectrum of a piezo modulation can also give information about the deformation of bands which undergo stress effects [169]. However, the use of this technique is limited because of the fact that a piezo modulation method requires a large value of strain induced into the sample (of the order of 10^{-2}) in order to obtain the optical transitions information. Only a few materials can undergo up to such severe strains. Piezo modulation is usually applied to metals and noble metals, in the form of their evaporated thin films, to calculate their optical transitions [80, 82, 83].

3.2.4 Electroreflectance

Electroreflectance is a complex form of modulation spectroscopy in which an electric field is applied across the sample and the changes in its optical reflectance are observed. Further, these changes in the optical reflectance are used to investigate the material under study. Electroreflectance is perhaps the most sophisticated technique in a sense that its spectra are well oriented and intense. However, they rely heavily on the magnitude of the induced electric field. On the basis of electric field strength, an electroreflectance technique can be classified as

1) Low regime electric field: in which the electropotic energy θ_o obeys the following inequality relation with the broadening parameter Γ

$$\left|\hbar\theta_o\right| \le \Gamma \qquad \text{where} \quad \theta_o = \left(\frac{e^2\hbar^2 E_F{}^2}{2\mu_r}\right)^{1/3}$$

where E_F is the electric field, μ_r is the inter band reduced mass in the direction of the field, and e is the electronic charge.

2) High field regime: for which $\left|\hbar\theta_o\right| \ge \Gamma$ and $qE_F a_o > E_g$, where a_o is lattice constant, q is the charge, Γ is the broadening parameter associated with an ER peak, and E_g is the band gap of the material.

3) High field regime: for which $qE_F a_o \sim E_g$

All of the three electric field regimes result in different physical processes. For example, the low field regime is associated with the optical transitions; the intermediate regime shows the optical transitions along with Franz-Keldysh (FK) oscillations. The FK effect is described as the change in the optical response of a material due to the applied electric field. This effect appears in terms of periodicd oscillations whenever the strength of the electric field changes the band structure of a material; the higher field regime is responsible for the phenomenon of Stark shifts [11].

3.3 Theory of Electroreflectance

The fundamental difference between electroreflectance and other forms of modulation spectroscopy is that the electric force is not lattice periodic. It is the net force which accelerates the electrons and, as a result, the translational invariance of the Hamiltonian is completely destroyed in the electric field direction.

The role of translational invariance, in determining the optical properties and the response of a modulation technique, can be understood from the simple free electron model. In the case of a free electron system, the Hamiltonian preserves the translational symmetry and is described by

$$H = \frac{P^2}{2m} \qquad (3.3)$$

The band structure of the system is a continuous parabola and the momentum of this system remains conserved. If a photon with energy $E_p = \hbar\omega$ is absorbed by the electron, it creates a large momentum change. The momentum and energy of the system cannot be conserved simultaneously and electrons cannot make any transition in such a system. The optical transitions are described in terms of the dielectric function of the system. The complex part of the dielectric function ε_i is identically zero for a free electron system. For the electrons which move in a crystal, their Hamiltonian is described as:

$$H = \frac{P^2}{2m} + V(\mathrm{r}) \qquad (3.4)$$

The motion of the electrons which move in a periodic lattice, with periodicity τ, is provided by

$$\psi_k(r) = U_k(\mathrm{r})e^{i\vec{k}.\vec{r}} \qquad (3.5)$$

where *U(r)* is the periodic potential given as

$$U(\mathrm{r}+\tau) = U(\mathrm{r}) \qquad (3.6)$$

The band structure for such a system is not a continuous parabola. It is distorted where the electrons encounter the potential of the ionic cores of the lattice. So, the free electron energy parabola splits up to energy bands. Here, the Hamiltonian is invariant only to those classes of translations which bring the crystal back to itself. As a result, the momentum of the system remains conserved only to a certain wave vector $\vec{k}_n$ of the reciprocal space. The imaginary part of the dielectric function for such a system always has a square root form. For the electrons that move in the crystal, if the external perturbation is applied, the Hamiltonian of the system is described as

$$H = \frac{P^2}{2m} + V(\mathrm{r}) + H' \qquad (3.7)$$

where H' is the external perturbation. If such a perturbation preserves the symmetry of the system (such as in the case of wavelength, temperature or stress modulation) then, the momentum of the system remains conserved within the reciprocal space. Although the symmetry is lowered, the optical transitions remain vertical. Such perturbations change the dielectric function and are analyzed using first order line shape analysis.

If the external perturbation, applied to the electrons which move in a crystal with lattice periodicity τ, is electric field then the Hamiltonian of the system is described as

$$H = \frac{P^2}{2m} + V(\mathrm{r}) + e\vec{E}_F.\vec{r} \qquad (4.8)$$

In such a case, the electric field completely destroys the translational symmetry and accelerates the electrons. As a result, the momentum of the system changes and it is not a good quantum number. The Bloch wave functions of the crystal mix up and the optical transitions, instead of occurring at the same point in the $\vec{k}$ space, spread over a finite range of initial and final states. For a low magnitude of electric field, the mixing occurs only for those Bloch wave functions which are near the original optical transitions. As a result of this, the shape of the original optical transition spectra smears out. The resulted spectrum due to the influence of electric field has a complicated shape having changes in its signs. Such a spectrum which has two zero crossings is the characteristic of a third derivative. So, the changes in the spectrum of the dielectric function because of the electric field are attributed to third order derivatives with respect to electric field [150].

3.4 Mathematical Description of Electroreflectance Phenomena

In order to obtain a quantitative description of the electroreflectance phenomenon, consider the effect of an electric field $\vec{E}_F$ on the electrons moving in a crystal. The Hamiltonian of the system is described as;

$$\left(-\frac{\hbar^2}{2\mu_r}\nabla_r^2 + eE_F z - \mathrm{E}\right)\xi(\mathrm{r}) = 0 \qquad (3.9)$$

Where E is the energy of the electron, $\xi(\mathrm{r})$ is the solution of eq. (3.9). The direction of the electric field is along the z axis. Equation (3.9) can be split into two parts. One corresponds to x-y plane, where the electric field does not have any effect, while the other is the z-component which is parallel to the electric field. So, for the x-y plane, the Schrodinger equation is described as

$$\left(-\frac{\hbar^2}{2\mu_r}\nabla_{x,y}^2 - E\right)\xi(\mathrm{x},\mathrm{y}) = 0 \qquad (3.10)$$

The solution for such an equation is in the form of a plane wave described as [172]

$$\xi(\mathrm{x},\mathrm{y}) = A_1 e^{i(\mathrm{k_x x} + \mathrm{k}_y y)} \qquad (3.11)$$

and the net relative energy E_r is the sum of free electron Hamiltonian energy E_o, the kinetic energy of the electrons along the x,y plane, and the energy of the electrons along the z direction due to electric field. A_1 is the normalization constant

$$E_r = E_o + E_z + \frac{\hbar^2}{2\mu_r}(\mathrm{k}_x^2 + \mathrm{k}_y^2) \qquad (3.12)$$

Along the z-axis, taking the electric field effect, the Hamiltonian of the system is defined by

$$\left(-\frac{\hbar^2}{2\mu}\frac{d^2}{dz^2} + eE_F\,\mathrm{z} - \mathrm{E_z}\right)\xi(\mathrm{z}) = 0 \qquad (3.13)$$

Rearranging equation (3.13)

$$\frac{d^2\xi(z)}{dz^2}+(\frac{2\mu_r E_z}{\hbar^2}-\frac{2\mu_r eE_F\,z}{\hbar^2})\xi(z)=0$$

Converting the equation into a dimensionless reducible form, we define

$$\beta_o=\frac{E_z}{\theta_o}-z(\frac{2\mu_r eE_F}{\hbar^2}) \qquad (3.14)$$

$$\text{where } \theta_o=\left(\frac{e^2E_F^2\hbar^2}{2\mu_r}\right)^{1/3} \qquad (3.15)$$

Equation (3.13) becomes

$$\frac{d^2\varphi_z(\beta_o)}{d\beta^2}+\beta_o\varphi(\beta_o)=0 \qquad (3.16)$$

The solution for equation (3.16) is the Airy function described as [173]

$$\varphi_z(\beta_o)=\frac{eE_F}{\theta_o}Ai(\beta_o) \qquad (3.17)$$

The general form of the dielectric function is

$$\varepsilon_i(\omega)=\frac{4\pi^2e^2}{m^2\omega^2}\sum_k\left|J_{cv}\right|^2\delta(E_k-E_i-\hbar\omega) \qquad (3.18)$$

where J_{cv} is the force oscillator strength. It is the perturbation matrix element in moving the electrons form their initial state to final state under the electromagnetic interaction. That is

$$J_{cv}=\langle f|H_{e-h}|0\rangle \qquad (3.19)$$

where H_{e-h} is the Hamiltonian due to the external field, $|0\rangle$ and $|f\rangle$ are the initial and the final states of the system. Under the interaction of electric field and electromagnetic radiation, when electrons make transitions form their valence band to their conduction band, holes are created in the valence band. The net effect on the dielectric function due to such transitions consists of two parts. One is due to the bound states of valence bands while the other one is due to the continuum states of conduction bands. For the bound states, the case is similar to the hydrogen atom. We can express the wave functions in terms of spherical harmonics where the radial part contributes to the oscillator strength. So, the net contribution of J_{cv} is described as [174]

$$|J_{cv}|^2 = |\xi_e(\mathrm{r})|^2 \left|\langle f | H_{e-r} | 0 \rangle\right|^2 \tag{3.20}$$

where 'r' is the relative position of hole and electron described as $r = R_\mathrm{e} - R_h$, where R_e and R_h are the positions of electrons and holes with respect to some origin. Now, for $r = 0$, we have $R_\mathrm{e} = R_h$ and $|\xi_e(\mathrm{r})|^2 = |\xi_e(0)|^2$ which represents the probability of finding the electrons and the holes within the same primitive cell. So,

$$|P_{cv}|^2 = |\xi_e(0)|^2 \left|\langle f | H_{e-r} | 0 \rangle\right|^2 \tag{3.21}$$

The total density of states of the system can be found by considering the density of states along the x-y plane and integrating over E_z. A two dimensional density of states can be described by [175]

$$\rho(E_{\mathrm{x,y}}) = \begin{cases} \dfrac{\mu}{\pi\hbar^2} & E_{x,y} > E_o \\ 0 & E_{x,y} < E_o \end{cases} \tag{3.22}$$

Based upon the relations defined in equations (3.17), (3.21) and (3.22), the complex dielectric function can be written as

$$\varepsilon_i(\omega, E_F) = \frac{4\pi^2 e^2 J_1^2}{m^2\omega^2} \frac{\mu_r}{\pi\hbar^2} \frac{eE_F}{\theta_o} \int_{\beta_1}^{\infty} Ai^2(\beta_o)\, d\beta_o \tag{3.23}$$

where $J_1 = \xi_e(0)\left|\langle f | H_{e-r} | 0 \rangle\right|$, $\beta_1 = \dfrac{E_o - E}{\theta_o}$ and $E_p = \hbar\omega$. In order to simplify the expression, consider

$$\theta_o = \left(\frac{e^2 E_F^2 \hbar^2}{2\mu_r}\right)^{1/3} \Rightarrow eE_F = \frac{(2\mu_r)^{1/2}}{\hbar}\theta_o^{\,3/2}$$

So, the dielectric function in the presence of an electric field can be written as

$$\varepsilon_i(\omega, E_F) = \frac{2\pi\, e^2 J_1^2}{m^2 E_F^2 \hbar}(2\mu_r)^{3/2}\theta_o^{\,1/2}\int_{\beta_1}^{\infty} Ai^2(\beta_o)\,d\beta_o \tag{3.24}$$

Since the quantity of interest is the change in the dielectric function due to the electroreflectance, it can be described as [156]

$$\Delta\varepsilon = \varepsilon_i(\omega, E_F) - \varepsilon_i(\omega, 0) = \frac{2\pi\, e^2 J_1^2}{m^2 E_F^2 \hbar}(2\mu_r)^{3/2}\theta_o^{\,1/2}\int_{\beta_1}^{\infty} Ai^2(\beta_o)\,d\beta_o - \frac{4\pi^2 e^2}{m^2\omega^2}\sum_k \left|J_{cv}\right|^2 \delta(E_k - E_i - \hbar\omega) \tag{3.25}$$

This is the expression for the change in the dielectric function as a result of the electroreflectance phenomenon.

3.5 Third Derivative Modulation Spectroscopy

An electroreflectance spectrum is generally intense and well resolved in the energy scale. However, it depends heavily on the experimental conditions and specifically on the magnitude of the electric field. For a low value of electric field where $\left|\theta_o\right| \le \Gamma$, an electroreflected spectrum is drastically simplified. It was found by Aspnes that within the low field limit, these spectra correspond to the third derivative of the optical spectra with respect to energy. Such observation is confirmed both theoretically and experimentally [88, 89]. Keeping in view the importance of the third derivative nature of electroreflectance, an empirical formula of it can be deduced in the following way.

Starting from the simple expression of the real part of the dielectric function, and employing the parabolic approximation as described by Yu *et al.* [156], we have

$$\varepsilon_r - 1 = C_1 E^{-2} \sum_k \frac{1}{E_c - E_v - E} \tag{3.26}$$

where C_1 is a constant. Under the interaction with an electric field, the electrons in the conduction band move for a time τ_1 before going into a collision. This time can be defined using the uncertainty relation

$$\tau_1 = \frac{\hbar}{E_c - E_v - E} \tag{3.27}$$

The distance z covered by the conduction electrons under the influence of the electric force is given by

$$z = v\tau_1 = (\frac{-eE_F}{m}\tau_1)\tau_1$$

$$\text{Thus, } z = \frac{-eE_F}{m_c}\frac{\hbar^2}{\left(E_c - E_v - E\right)^2} \tag{2.28}$$

This displacement is due to the influence of electric force (eE_F) on the electrons. As a result of such force, a change in the conduction band energy of the electrons occurs. That is

$$\Delta E_c = -e\vec{E}_F.\vec{d} = -eE_F z = \frac{e^2E_F^2}{m_c}\frac{\hbar^2}{\left(E_c - E_v - E\right)^2} \tag{3.29}$$

Similarly, a change in the valence band energy occurs due to the effect of the electric field on the holes in the valence bands

$$\Delta E_v = -\frac{e^2E_F^2}{m_v}\frac{\hbar^2}{\left(E_c - E_v - E\right)^2}$$

The net shift in the energy of the system is described by

$$\Delta(E_c - E_v) = \frac{e^2E_F^2}{\mu_r}\frac{\hbar^2}{\left(E_c - E_v - E\right)^2} \tag{3.30}$$

where $\frac{1}{\mu_r} = \frac{1}{m_c} + \frac{1}{m_v}$ is the reduced mass of the system

The change in the energy of the system is related to the change in the dielectric function as

$$\Delta\varepsilon_r = \frac{d\varepsilon_r}{d(E_c - E_v)} \cdot \Delta(E_c - E_v) \tag{3.31}$$

Using equation (3.26) and (3.31), we can write

$$\frac{d\varepsilon_r}{d(E_c - E_v)} = -C_1 E^{-2} \sum_k \frac{1}{\left(E_c - E_v - E\right)^2} \tag{3.32}$$

So,

$$\Delta\varepsilon_r = \frac{-C_1 E^{-2} e^2 E_F^2 \hbar^2}{\mu_r} \sum_k \frac{1}{\left(E_c - E_v - E\right)^4} \tag{3.33}$$

The expression of equation (3.33) is more significant since it can be written in terms of third derivative forms. For this, we can write (3.33) as

$$\Delta\varepsilon_r = \frac{-e^2 E_F^2 \hbar^2}{6E^2 \mu_r} \sum_k \frac{6C_1}{\left(E_c - E_v - E\right)^4} \Rightarrow \Delta\varepsilon_r = \frac{-e^2 E_F^2 \hbar^2}{6E^2 \mu_r} \frac{\partial^3 (E^2 \varepsilon_r)}{\partial E^3} \tag{3.34}$$

Or more simply

$$\Delta\varepsilon_r = -\frac{1}{3} \frac{\theta_o^{\,3}}{E^2} \frac{\partial^3 (E^2 \varepsilon_r)}{\partial E^3} \tag{3.35}$$

where $\theta_o = \left(\frac{e^2 E_F{}^2 \hbar^2}{2\mu_r} \right)^{1/3}$ is the electro-optic energy.

Equation (3.35) is the general form of the change in the dielectric function with respect to a third order derivative of the energy. The expression described in equation (3.35) has two important outcomes: 1) It describes the quadratic dependence of electro reflected spectrum on the electric field; and 2) The line shapes are closely related to the third derivative of the absolute dielectric function. From a spectroscopic point of view, third derivative line shapes always have significantly enhanced critical points and strongly suppress backgrounds. Such signals are well localized and even the degenerate critical points are also well resolved [178]. Moreover, the uniformity and localization of the spectra enable one to analyze the actual band structure directly from the experimental low field spectra without any extra analysis technique like Kramers Kronig relations.

3.6 Advantages of Electroreflectance

In case of electroreflectance technique, the optical response of the material, in the presence of the electric field, exhibits sharp third derivative-like features, with strongly enhanced critical points and highly suppressed featureless background. This property makes ER more robust as compared to other techniques in a sense that the observed spectra correspond to the optical transitions around the critical points, with no background interference. Moreover, the electroreflectance avoids complications related to the passage of light through the material, especially when opaque metallic electrodes are used to apply the perturbing electric filed. The sensitivity of this technique to the surface of the material is eliminated by the fact that the electric field is only efficient at the critical points. The high resistive nature of the metal oxides creates an additional difficulty in calculating their band gaps by the spectrophotometric method, where only light is used as an external perturbation, and might not be as efficient to lift the electrons from the valence band into the conduction band. If an electric field is combined with the photon energies as a source of perturbation, it accelerates the electrons against the high resistive nature of the material to enable the optical transitions. Therefore, a large amplitude of the electric field is an important requirement to measure the band gap of the metal oxides. In case of ER, the different geometries, which are designed to achieve different modes of electroreflectance such as transverse electroreflectance or surface barrier electroreflectance, provide high flexibility for achieving the necessary strength and direction of the electric field. Moreover, the requirement of high electric field can also be achieved using the reduced dimensional forms of the materials like thin films, which enable high magnitudes of the electric field of the order of $10^4 - 10^5$ V/cm. Such a large electric field can also be used as an efficient perturbation for revealing the optical transitions associated with the wide band gap oxides, which have their band gaps in the ultraviolet region.

CHAPTER 4

Experimental Techniques

4.1 Fabrication of Oxides

The oxides in this study were fabricated using either thermal evaporation or sputtering in order to maintain the purity of the films and to avoid unnecessary diffusion between different materials. The metal oxides were deposited on a substrate and their band gaps were investigated by the electroreflectance technique. In order to avoid any signal coming from the substrate structure in the electroreflectance, the substrate should have the following characteristics: 1) Its reflection should be minimum; 2) It should not have any structure within the used wavelength range of light; and 3) it should be electrically and chemically inert with respect to the oxide. Based upon these requirements, the choice of substrate was glass and a metal-oxide- metal (MOM) configuration was fabricated in this work. The metals served as electrodes to provide the external AC voltage to the sample. These metals were deposited in such a way that the oxide was sandwiched between them and a capacitor-type geometry was obtained. The selection of the metals was governed by the same conditions as described above for the substrate. Moreover, Au, Ag, Ni and Al metals were analyzed for optimum choice of the electrodes. The thickness of these metals was optimized in order to avoid unnecessary results like maximum utilization of light, metal oxide surface barrier, contact resistance or Schottky barrier. The basic diagram of an MOM configuration in shown in figure 4.1 below.

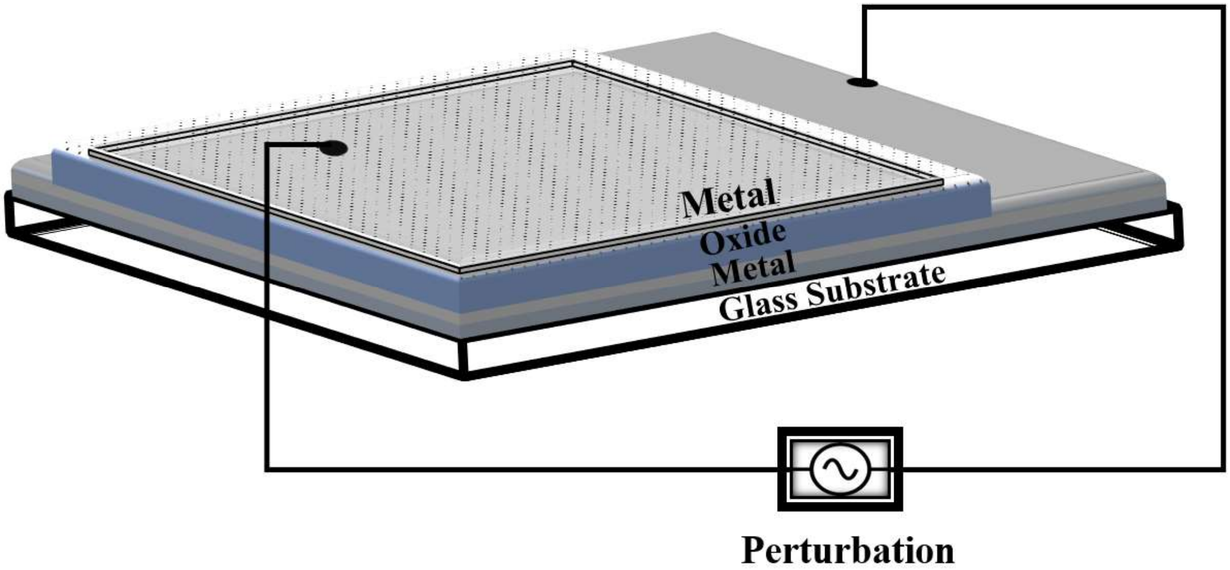

Fig 4. 1. Metal oxide metal configuration

The fabrication of an MOM configuration was done by using thermal evaporation technique except for ZnO where the oxide was prepared using RF sputtering. A brief description of each technique along with the experimental details of material deposition is described below.

4.1.1 Thermal evaporation

Thermal evaporation is one of the common methods of physical vapor deposition (PVD). In this technique, the material undergoes either sublimation or evaporates. The material is heated in a high vacuum chamber up to a temperature which produces some vapor pressure. Since a high vacuum is applied, a low vapor pressure is enough to produce a vapor cloud of the material inside the chamber. These vapors then impinge on the substrate and stick to form thin film. There are two ways in which a thermal evaporation process can proceed: 1) Resistive evaporation; in which a high current is utilized to produce the heat and to evaporate the sample; and 2) Electron beam or e-beam evaporation, in which electrons are emitted from a hot filament and accelerate under a high voltage of 4 kV to eject the material upon bombardment. Thermal evaporation has several advantages over other PVD techniques. It ensures high purity during film deposition. Also, deposition of different materials in multiple layers is easily obtained since there is less chance of film diffusion [179].

4.1.2 RF Sputtering

Sputtering is a sophisticated technique used to deposit thin films. The basic mechanism involves the ejection of atoms of the material by a gas discharge plasma under high voltage. In sputtering, a large negative potential is applied at the cathode while the anode remains grounded. When an inert gas is inserted between the two electrodes, a gas discharge plasma is created. The positive and negative ions move toward the cathode and anode, respectively. As the positive ions move toward the cathode, they hit on the surface of the cathode and the higher potential at the cathode drops down. The material whose fabrication is required is used as a target material on the cathode side. The bombardment of the ions with the surface of the atoms of the target ejects the material atoms which then settle on the substrate. Normally, an inert gas like argon is used to create the gas discharge plasma. For a gas discharge plasma to be created and sustained, a pressure of 3 to 300 Pa and a voltage of 1000 to 2000V are required. The sputtering process operates in various modes. The common modes are radio frequency (RF) magnetron sputtering and direct current magnetron sputtering. The mode used in this work is the RF magnetron sputtering, which is used for nonmetallic targets like oxides or insulators. It uses an AC power supply and prevents the accumulation of positive ions which are produced during the gas discharge on the negative plate.

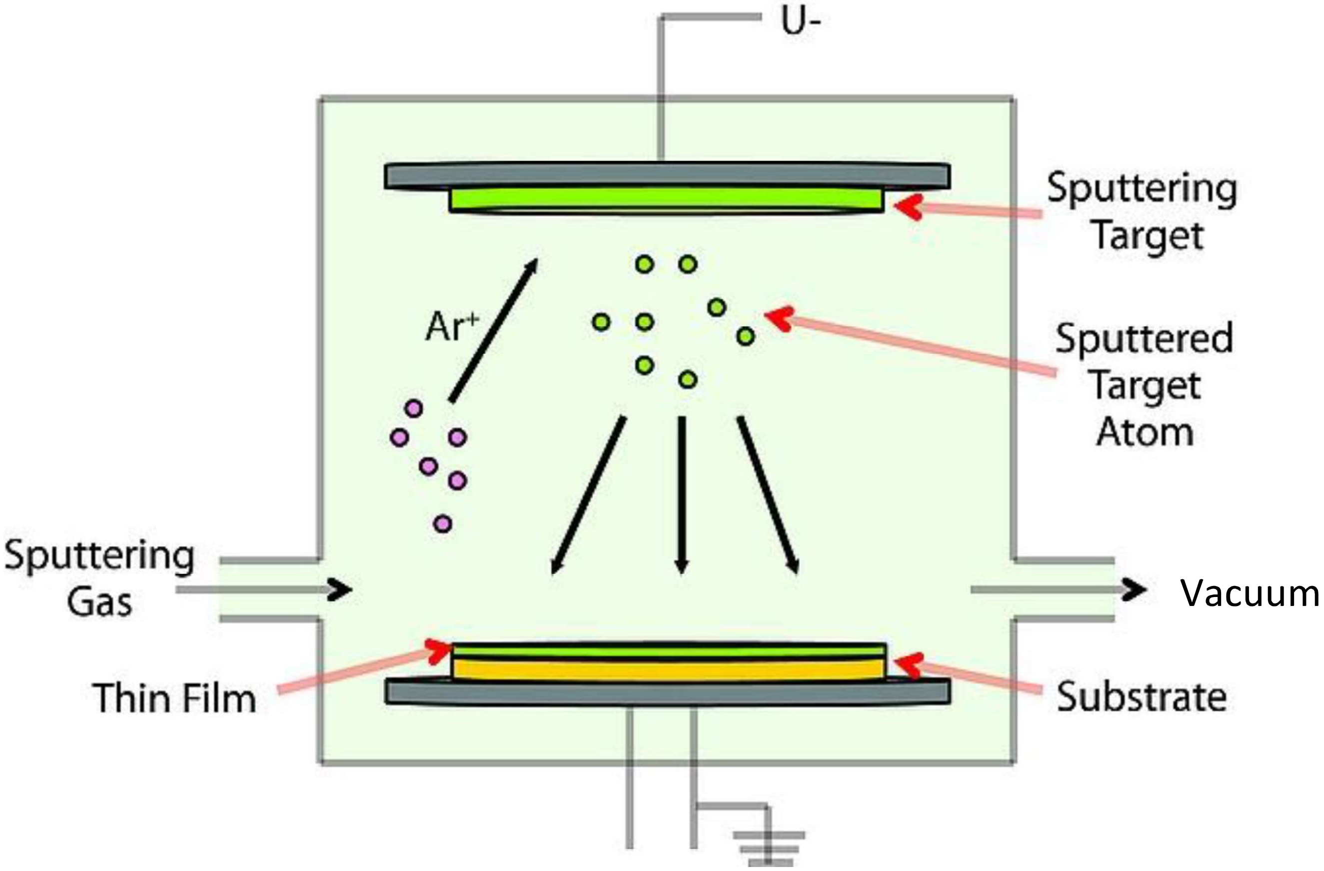

Fig 4. 2. Schematic diagram of RF sputtering

4.2 Optimization of Front Contact for AC Perturbation

In order to create the electroreflectance phenomenon in a metal- oxide- metal configuration (MOM), the basic requirement is to provide an AC modulation to the sample which is exposed to light. Since the aim of this technique is to show the critical points of the oxide under study and not to influence the metals which are used as electrodes for perturbation, the selection of metals used as electrodes is very important. The selection of the metals is governed by the same conditions as described for the substrate. Keeping in view these conditions, metals like Au, Ag, Ni and Al were analyzed both optically as well as electrically.

The thicknesses of these metals were optimized on the basis of their transmittance, reflectance and resistance values. The graphs of reflection and transmittance for four different metals: silver, gold, aluminum and nickel, are shown in figures 4.3 – 4.6, while the resistance of different metals with different thicknesses is shown in table 4.1. It can be seen that both silver and gold show a definite structure in their transmittance and reflectance spectra. For silver, it spans from 300 to 400 nm, while for gold, it was from 475 to 600 nm. Since most of the oxides have their band gaps in the visible region, using silver as a front contact may cause the influence of silver structure on the band gap signals. Similarly, gold cannot be used as a front contact especially when dealing with low band gap semiconductors like Fe_2O_3. The same is true for nickel with films 10 and 15 nm in thickness. Their structures in the UV region make them less efficient in calculating the band gaps of oxides like HfO_2 or ZrO_2. On the other hand, films of 5 nm thickness show a high resistance value which may act as a barrier to the flow of AC voltage, so they were avoided. The metal of choice for making the front contact electrode was aluminum which did not have any structure in the entire wavelength of light of interest. A 10 nm thick aluminum film is quite useful in making the front contact. A 5 nm Al film is highly resistive, while a 15 nm thick Al film, if used as a front contact, reflects more than 30% of light and less intensity reaches the oxide under study.

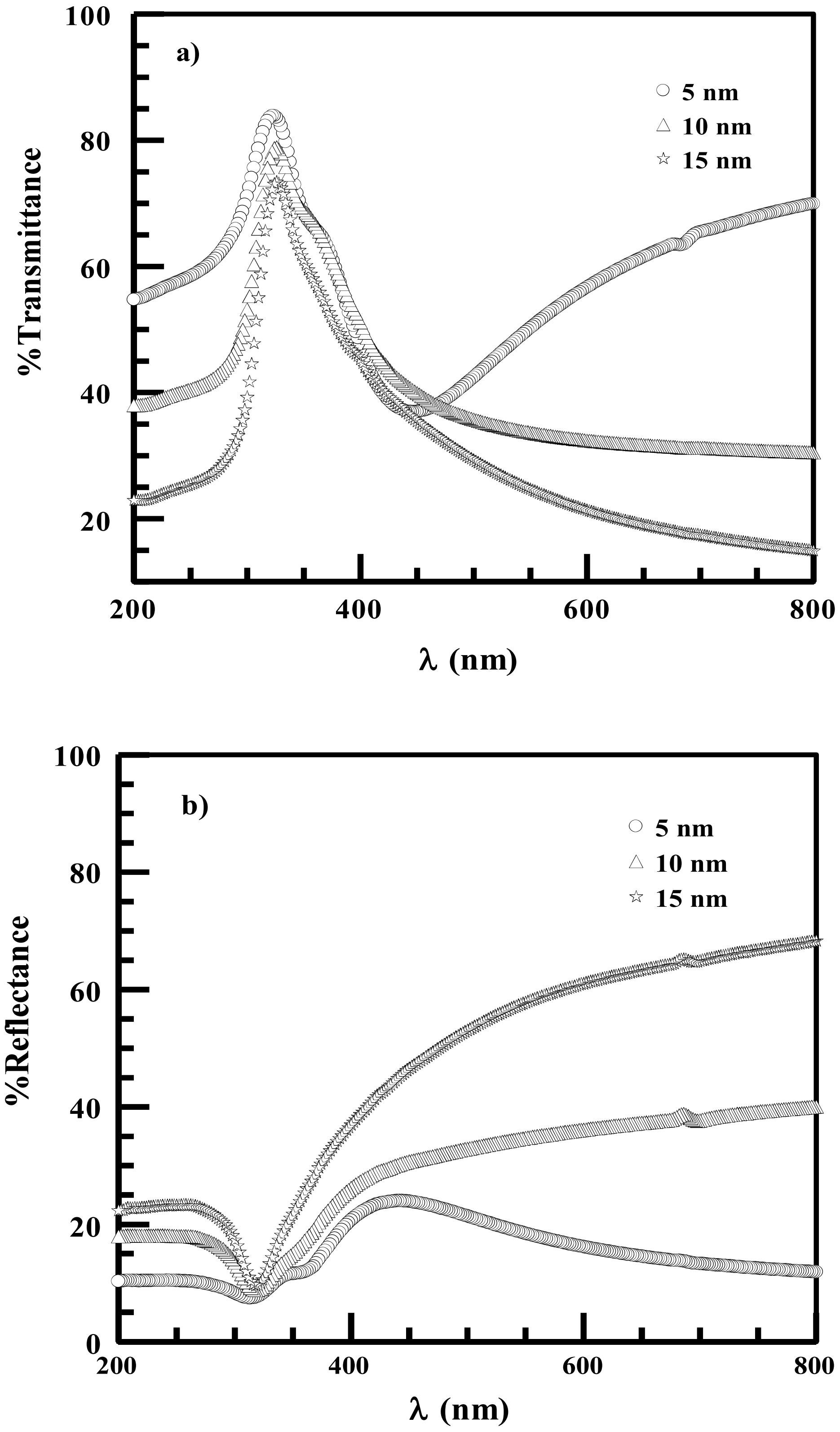

Fig 4. 3. a) Transmittance and b) reflectance spectra of silver for different thickness values

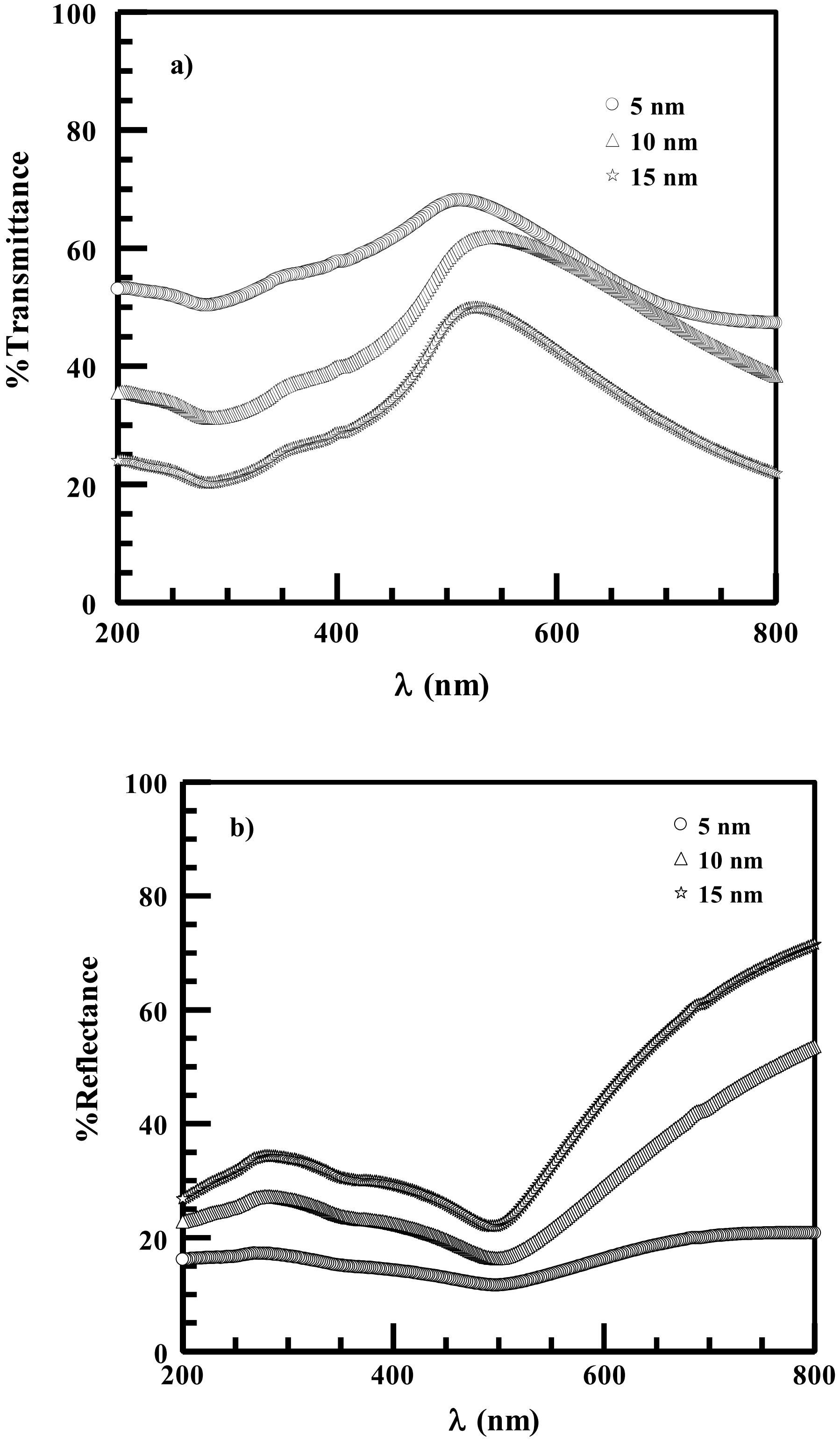

Fig 4. 4 a) Transmittance and b) reflectance spectra of gold for different thickness values

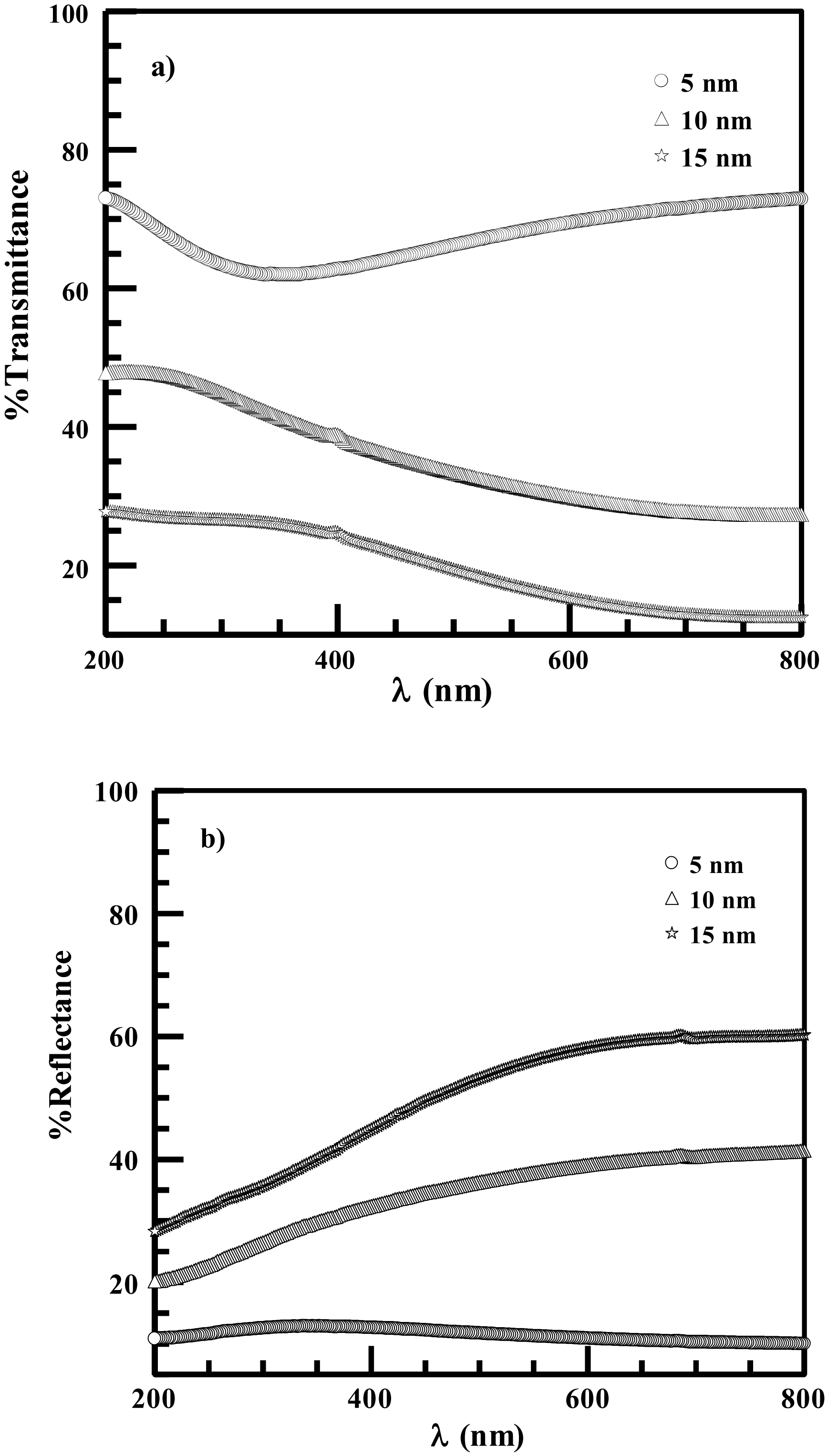

Fig 4. 5 a) Transmittance and b) reflectance spectra of aluminum for different thickness values

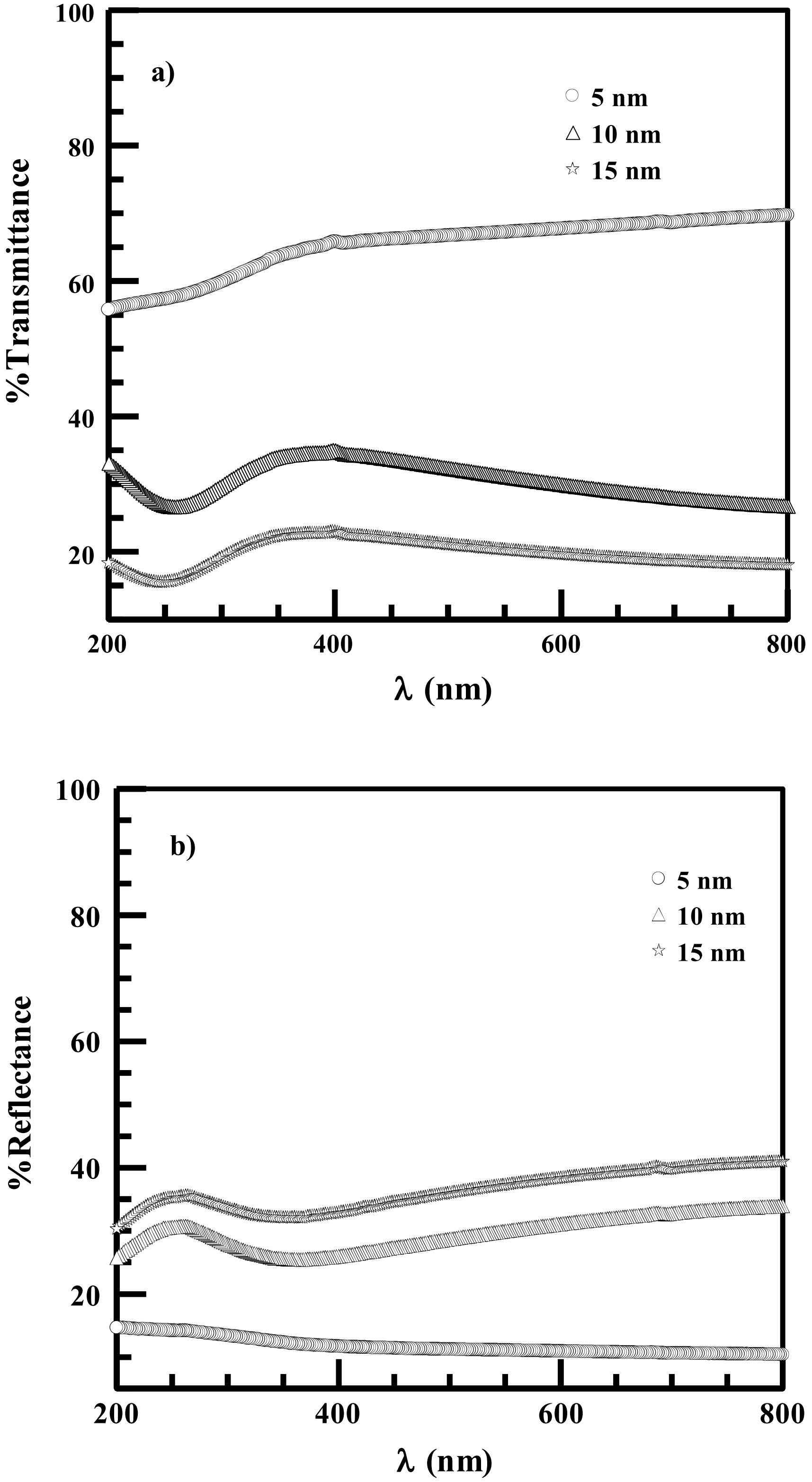

Fig 4. 6 a) Transmittance and b) reflectance spectra of nickel for different thickness values

Thickness (nm)	**Ag (Ω)**	**Au (Ω)**	**Al (Ω)**	**Ni (Ω)**
5	--	154.8	--	2.4E+3
10	45.2	22.1	121.8	81.7
15	8.5	12.1	35.2	96.5

Table 4. 1 Resistance of different metal films with respect to their thicknesses

4.3 Sample Preparation

In thermal evaporation of oxides, the deposition was carried out in a Laybold L560 box coater. Before any deposition, the system was pumped down to a base pressure of 4×10^{-5} mbar. Before starting the deposition, the material was slowly outgassed. A shutter was introduced during the outgassing process in order to block the vapors from reaching the surface of the substrate. All the films were deposited on unheated substrates.

In each metal-oxide-metal configuration, the deposition proceeded as follows

1) Deposition of metal on the substrate. A thick layer of aluminum was deposited on the substrate which acts as the bottom contact. The thickness of the bottom contact was set at 100 nm in order to achieve high conductivity so that an AC signal can pass through the electrode easily.

2) Deposition of the oxide layer on top of the bottom metallic contact.

3) Deposition of the second metal layer on the oxide. A thin layer of metal was deposited on the oxide to act as a front contact. The requirement of a thin layer was due to the fact that the light should transmit through the front contact up to a maximum value and should reflect from the oxide whose band gap is investigated.

During the deposition of metals, the substrate was made stationary because the deposition of the metals is uniform in nature. However, the substrates were rotated during the deposition of the oxides in order to achieve a uniform deposition. The source to substrate distance was 40 cm. The evaporation rate was set to 4 Å/s and the thickness of the oxides was fixed to 300 nm. Both the evaporation rate and the thickness of the oxides were monitored using a quartz crystal thickness monitor. Ga_2O_3, MoO_3, and WO_3 films were deposited using a molybdenum boat and with the help of thermal evaporation. Fe_2O_3 thin films were synthesized via reactive thermal evaporation of iron in the presence of oxygen. The evaporation of granular solid iron was carried out via electron beam deposition using a 4 kW electron gun under an oxygen pressure of 7×10^{-4} mbar. Metal oxides like CeO_2, HfO_2, SnO_2, TiO_2, and ZrO_2 were deposited using e-beam evaporation.

Besides the deposition of metal oxide thins films with thermal evaporation, the deposition of ZnO thin films was performed with the help of RF sputtering. In this case, an RF power of 120 W was applied to a ZnO sputtering target. The ZnO target had 99.99% purity and it was 3 inch in diameter. The system was evacuated to a base pressure of 8.5×10^{-6} mbar prior to any deposition. Then, argon was introduced as a sputtering gas into the chamber at a flow rate of 10 sccm and a chamber pressure of 1.8×10^{-2} mbar was maintained. The ZnO thin film was deposited at room temperature. The source to substrate distance was 11 cm and the substrate was rotating in order to obtain uniform film deposition. The deposition was performed for two hours.

4.4 Characterization Techniques

The properties of metal oxide films were investigated using different characterization methods. Their structural properties were examined through X-ray diffraction (XRD), surface morphology through atomic force microscopy (AFM), chemical analysis through X-ray photoelectron spectroscopy (XPS), and optical properties through spectrophotometry. Besides these characterization techniques, the band gap spectrum of oxides was obtained and analyzed using the electroreflectance technique. A brief description of each technique is provided below.

4.4.1 X-ray Diffraction

XRD is a widely used technique for the characterization of the structure of a material. It can be used for both the liquid and the solid phase of a material. The basic principle of this technique lies on the interaction of X-rays with the atoms of a material. Each material has a different crystal structure due to the arrangement of atoms in it. When X-rays interact with these atoms, they diffract and create a unique diffraction pattern. This diffraction pattern can be used as a finger print to identify the material. The diffraction phenomenon is governed by Bragg's law. It states that constructive interference will occur if the path difference of two rays, interacting with the atoms of the lattice planes, is an integral multiple of their wavelength. The constructive interference in a certain direction and the production of diffracted X-rays is governed by the Bragg's equation.

$$2d_1 \, sin \, \theta_B = g \, \lambda_x \tag{4.1}$$

where d_1 is the lattice spacing, λ_x is the wavelength of x-rays, and g is the order of maxima. The basic diagram of diffraction in Bragg's law is shown in figure 4.7 [180]. With the help of x-ray diffraction, several interesting properties of the material can be analyzed using the diffraction pattern. These include phase of a sample (amorphous or crystalline), structure of the sample (how atoms are arranged in the sample), size and shape of the material and defects, strain, and dislocation. The XRD machine used in this study was the Rigaku Ultima diffractrometer. A CuK$_\alpha$ X-ray source of wavelength 1.5406

Å was employed. The scanning speed of the data collection was set to 2°/ min, while the scanning range ($2\theta_B$) was set to 20°-80°.

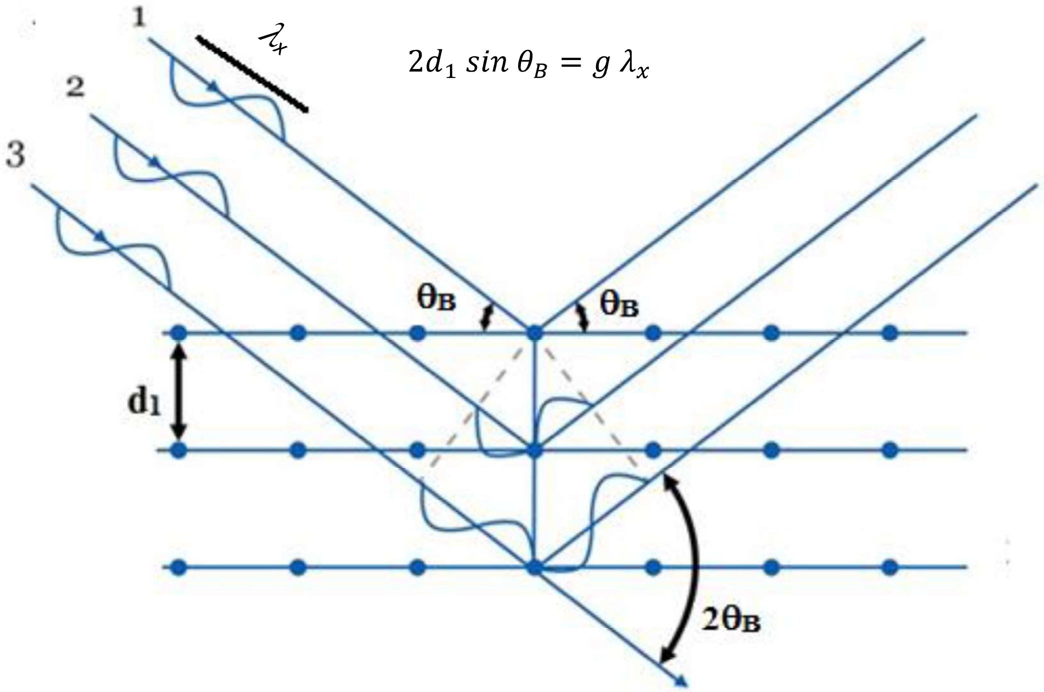

Fig 4. 7. Schematic diagram of Bragg's condition of diffraction

4.4.2 X-ray Photoelectron Spectroscopy

X-ray photoelectron spectroscopy (XPS) is a commonly used surface technique which operates under an ultra high vacuum. It is used for the chemical analysis of a material. The main principle of this technique lies on the ejection of electrons from the valence and core levels of an atom when high energy photons interact with a sample. The kinetic energy (K) of the ejected electrons gives vital information about the atoms and the chemical state of the elements of the sample. The basic diagram of the working principle of XPS is shown in the figure 4.8 [181]. When high energy photons such as x-rays interact with the sample under study, they transfer their energy to the electrons bound to the nuclei of the atoms which reside on or near the surface of the material. If the energy of the photons ($h\nu_p$) is greater than the work function (δ) of the surface (the amount of energy required to remove an electron from the valence band to the continuum state), the electrons leave their bands and accelerate with a definite value of kinetic energy K_e. The same is true for the electrons residing in the lower laying orbitals where a certain binding energy (BE) has also to be overcome to eject the electrons. This decreases the kinetic energy of the ejected electrons from the core levels. The binding energy (BE) of the electrons ejected from the core level is described by the equation

$$BE = h\nu_p - \delta - K_e \qquad (4.2)$$

Any small variation in the core energy levels results in variations in the photoelectron peaks. These variations are generally of the order of 1-5 eV and they are detected by XPS. The peak variations are associated with the bonding of the atoms and the oxidation state of the species. In XPS, the peaks are labeled after the core levels from which the electrons make transitions. For example, the peak coming from the 1s orbital of oxygen are described as O1s.

XPS can be used for the chemical analysis of a sample. This includes identification of the elements present in the sample, their oxidation state and their stoichiometry. In this work, a Thermoscientific Escalab 250Xi spectrometer equipped with a monochromatic Al Kα (1486.6 eV) X-ray source, and with the energy resolution of 0.5 eV, was used to perform the chemical analysis. The pressure inside the spectrometer was 7×10^{-10} mbar. The binding energy of the spectra was calibrated with the reference peak of C1s positioned at 284.5 eV

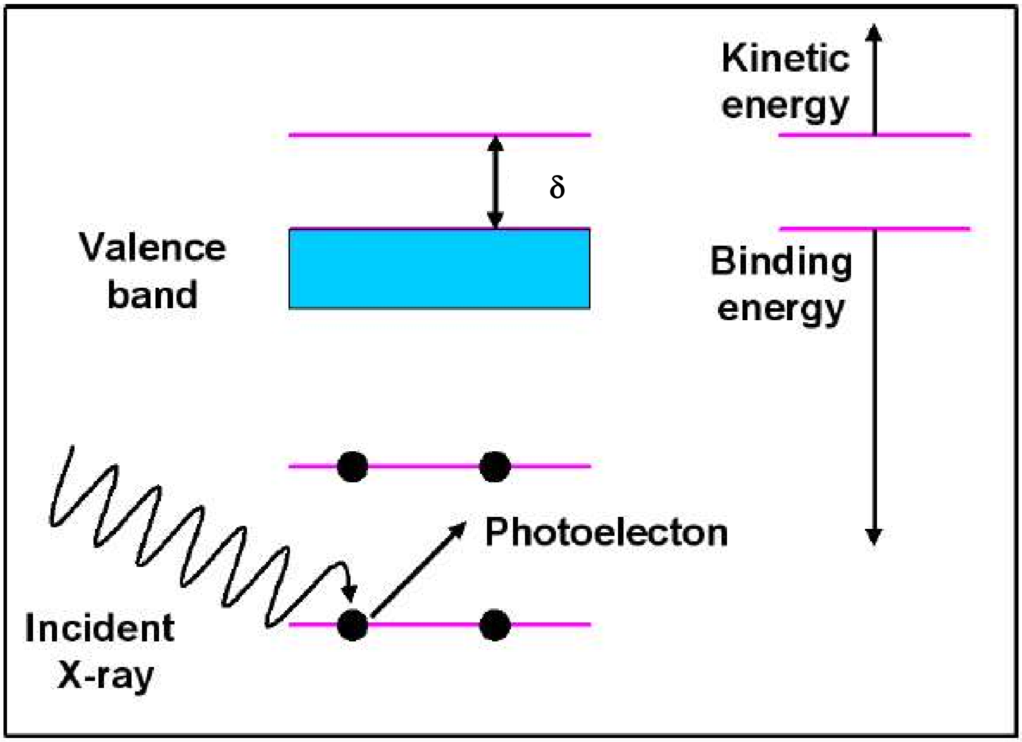

Fig 4. 8. Working principle of x ray photo electron spectroscopy

4.4.3 Atomic Force Microscopy

Atomic force microscopy (AFM) is a surface analysis technique which investigates the topology of the surface of a sample. The basic principle which is used in AFM is Hook's law, which measures the force between the sample and a sharp tip fixed at the end of a cantilever. The cantilever, operating in the raster scan mode, moves over the surface of the sample and bends as a result of the force between the surface and the tip. In order to monitor the bending of the cantilever, an optical lever technique is employed. The basic diagram of an atomic force microscope is shown in the figure 4.9 [182]. Under the normal working conditions, a laser light is continuously reflected from the cantilever and recorded by a position sensitive detector. As the cantilever bends, due to the force felt by the sharp tip, a change in the reflection of light occurs. This change in reflection is further analyzed to calculate the force between the sample and the tip and in this way the surface morphology of the sample is obtained. There are two modes associated with AFM. These include contact and tapping modes. In the contact mode, the tip remains continuously in close contact with the sample. This mode provides a three dimensional image of a sample without causing much damage to it. For the scanning of soft and rather mobilized materials, the tapping mode is preferred. Here the tip remains oscillating with a certain resonant frequency and interacts with the sample during its oscillations. The information which can be extracted about a sample by employing AFM includes the grain size, nature of the surface (granular, columnar or flat) and surface roughness. In this study, the AFM analysis was performed using a Veeco Innova diSPM atomic force microscope operating in the contact mode. A silicon tip of radius 10 nm, and oscillating at a frequency of 300 kHz was used to probe the surface of the films. The scanning area of the sample was set to 2×2 μm^2 and the scan rate was 2 Hz.

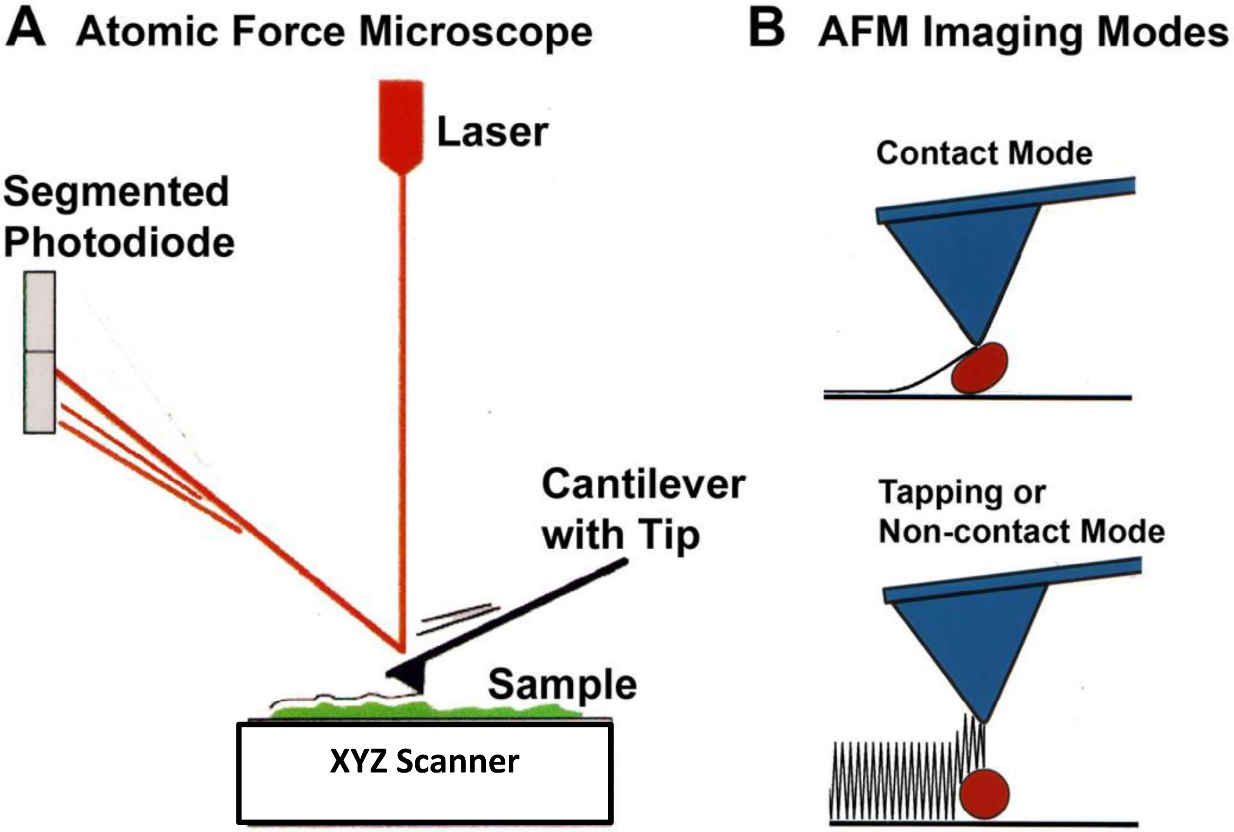

Fig 4. 9. Working principle of atomic force microscopy

4.4.4 Spectrophotometry

Spectrophotometry is a method to measure the optical properties of a sample like transmittance, reflectance and absorbance. The basic principle of a spectrophotometer lies in the fact that each material can absorb, transmit or reflect light up to a certain wavelength. When light of specific intensity passes through a sample, its intensity changes. The initial and final intensities (coming through the sample) are then related to each other to obtain the optical properties of the sample. There are two basic modes under which a spectrophotometer can be operated. These include transmittance/ absorbance mode and the reflectance mode. In the transmittance mode, the transmittance (*T*) can be calculated as the ratio of light I_t which transmits through the sample to the initial intensity I_o incident on the sample.

$$T = \frac{I_t}{I_o} \tag{4.3}$$

The other mode of operation in spectrophotometry is the reflectance mode, which is used to measure the reflectance properties of opaque or shiny surfaces. It is defined as the ratio of light I_r, which reflects from the surface of the sample to the initial intensity I_o incident on the material. There are lots of information that can be extracted from the optical knowledge of transmittance, absorbance and reflectance. Typical examples include the composition of the material that can be found from the Beer Lambart's law once the absorbance is known, thickness of the sample and optical parameters like refractive index, extinction coefficient and the dielectric function [183]. The spectrophotometer used in this study was a Jasco V-570 double beam spectrophotometer which is capable of operating from the ultra violet to near infrared regions. It was used to measure the transmittance spectra of the samples over the wavelength range of 200 to 2000 nm.

4.4.5 Electroreflectance

An electroreflectance setup was developed in the lab in order to carry out the electroreflectance analysis of the metal oxide thin films. The electroreflectance setup is shown schematically in figure 4.10. A 75W xenon lamp was used as a light source. The light coming from the lamp is diffracted by a McPherson 218 monochromator and allowed to fall on the sample at near normal incidence. The scan controller of the monochromator provides the desired wavelength range of light and the delay between the wavelengths increment. It is controlled by a data acquisition system. The intensity of light is controlled by widening or closing the entrance or the exit slits of the monochromator. After passing through the monochromator, the light falls on a beam splitter that divides the light into two beams of equal intensities. One beam is collected by a Hamamatsu 33098 photomultiplier tube (PMT) and can be served as the reference signal. The second beam hits the sample which has the AC voltage across it. The parameters of the AC signal were controlled by a Keysight-Agilent 33210A function generator coupled with the voltage amplification mode of a Trek 615-3 high voltage function generator. The function generator can vary the voltage in magnitude as well as in shape like sinusoidal, square and tiangular. Normally, the selection of the voltage shape is done by studying the shape of the electroreflectance spectra. However, the square shape is preferred in electroreflectance spectroscopy. This AC voltage induces a huge electric field across the surface of the sample. This results in modulated reflection when the second beam hits the sample. The modulated reflection is collected by the second PMT, which transmits the modulated signal to a Stanford Research SR830 DSP lock-in amplifier. The lock-in amplifier is a phase sensitive device. It is controlled by the data acquisition system and it detects the extremely small modulation signals. The lock-in amplifier was used to extract the electroreflectance signal ($\frac{\Delta R}{R}$) as a function of wavelength (λ_p) of light, and the whole acquisition process was controlled through Labview.

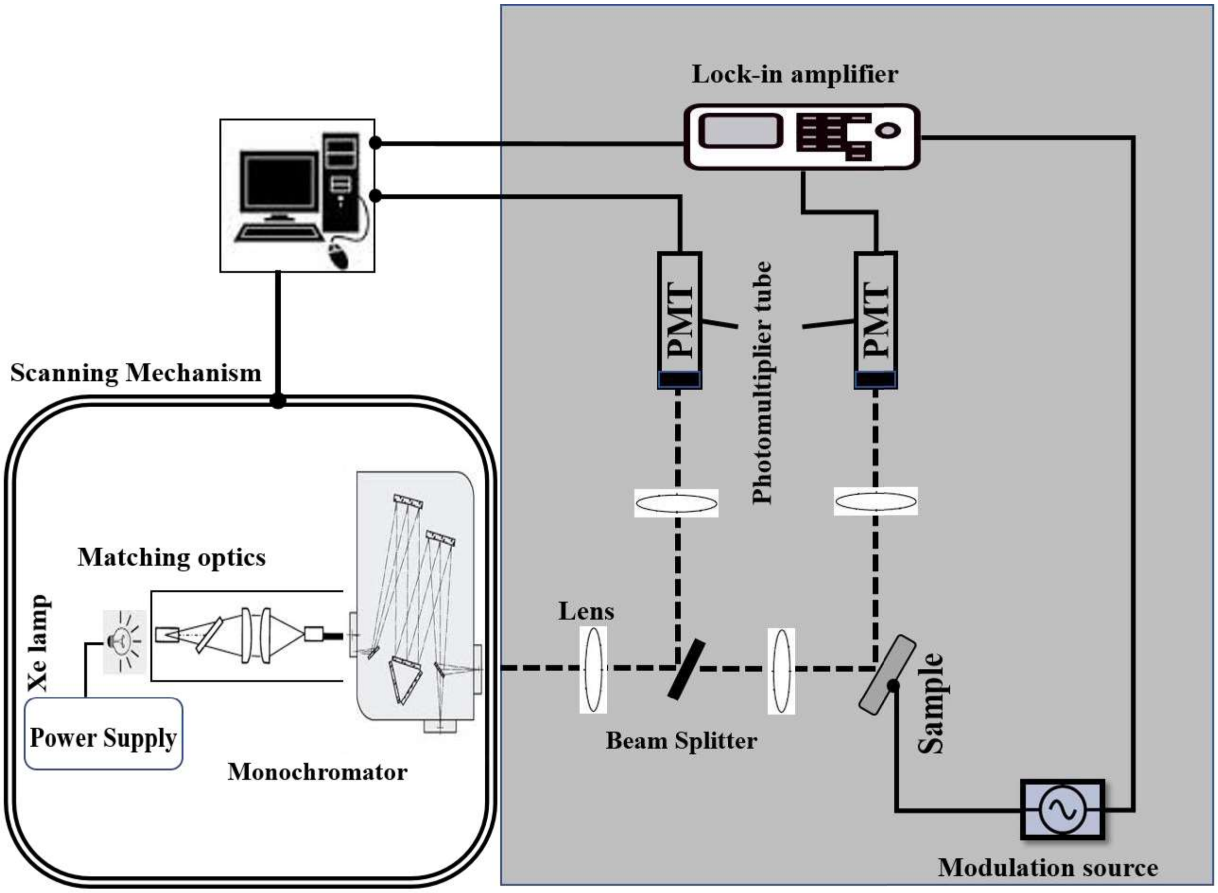

Fig 4. 10. Schematic diagram of the electroreflectance Setup

CHAPTER 5

Characterization

In this chapter, the properties of pure oxide films are presented

5.1 XRD Analysis

X-ray diffraction was used to investigate the crystalline structure of the films. Most of the films exhibited an amorphous structure, which is characterized by the presence of a broad peak centered at $2\theta_B = 20^\circ$ that is attributed to the fused silica substrate as shown in figure 5.1. While most of the metal oxide films exhibited amorphous nature, few films (CeO_2, Fe_2O_3, and ZnO) exhibited polycrystalline structures.

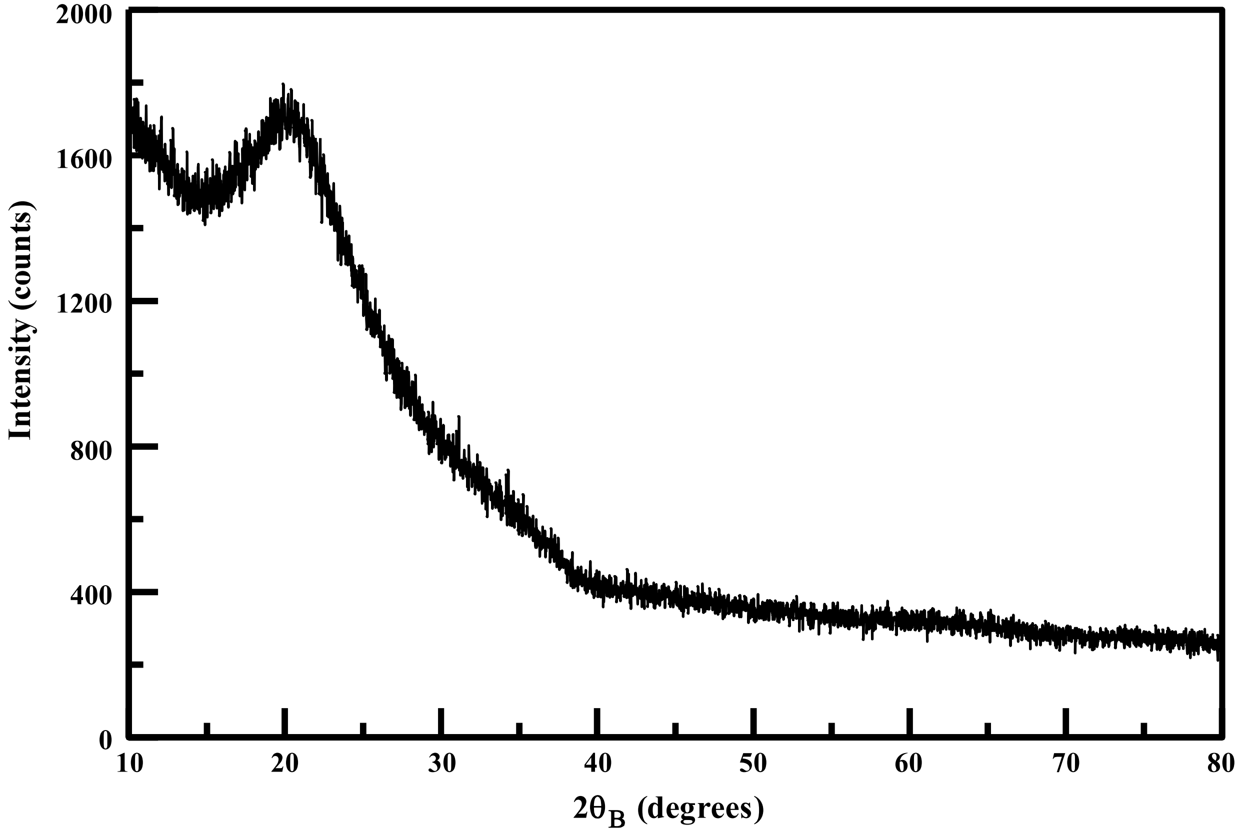

Fig 5. 1 XRD spectrum of amorphous films

Figure 5.2 shows the XRD spectrum of a CeO_2 thin film. CeO_2 exists in cubic phase with a fluorite structure. It had a polycrystalline structure. The preferred growth orientations, as revealed by the location of the intense peaks at angles ($2\theta_B$) of 27° and 45°, respectively, were along (111) and (311) planes. Some low intense peaks associated with (200) and (220) planes were also observed at angles of 32° and 56°, respectively. The crystallite size was calculated by using the Scherrer's formula defined as

$$D = \frac{k_s \lambda_x}{B Cos \theta_B} \tag{5.1}$$

where k_s is the Sherrer constant, λ_x is the wavelength of the x-ray, B is the full width at half maximum and θ_B is the Bragg's angle. The values of the FWHM (B) and angle (θ_B) were taken along the most intense peak (that is along (111) plane). The crystallite size of CeO_2 thin film was found to be 8.5 nm. The lattice constant for CeO_2 was computed using the relation of cubic fluorite structure given as

$$a_o^2 = \frac{\lambda_x^{\ 2}}{4 Sin^2 \theta_B}(h^2 + k^2 + l^2) \tag{5.2}$$

where a_o is the lattice constant, θ_B is the Bragg's angle, and (h k l) are the Miller indices of lowest intense peak. The lattice constant parameter was found to be 0.32 nm.

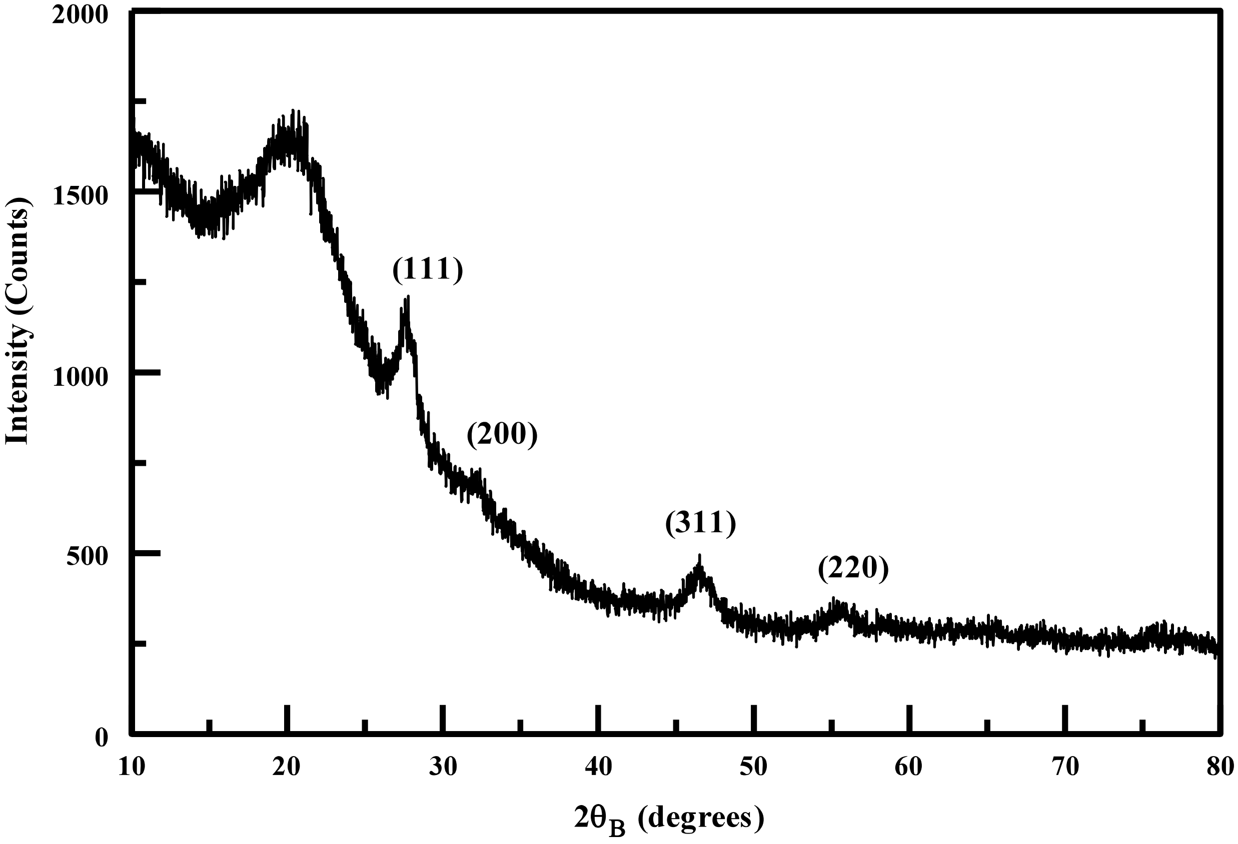

Fig 5. 2 XRD spectrum of CeO_2 film

The XRD spectrum of an Fe_2O_3 film is shown in figure 5.3. The film showed α- Fe_2O_3 phase and exhibited a polycrystalline nature. The peaks located at $2\theta_B$ values of 34.5°, 48.5° and 63.0° were associated with the (110), (024) and (300) planes. The sharp intense peak at 34.5° indicated that the preferred growth of Fe_2O_3 thin film was along the (110) plane. The crystallite size of the film was calculated using the Sherrer formula and was found to be 26.2 nm.

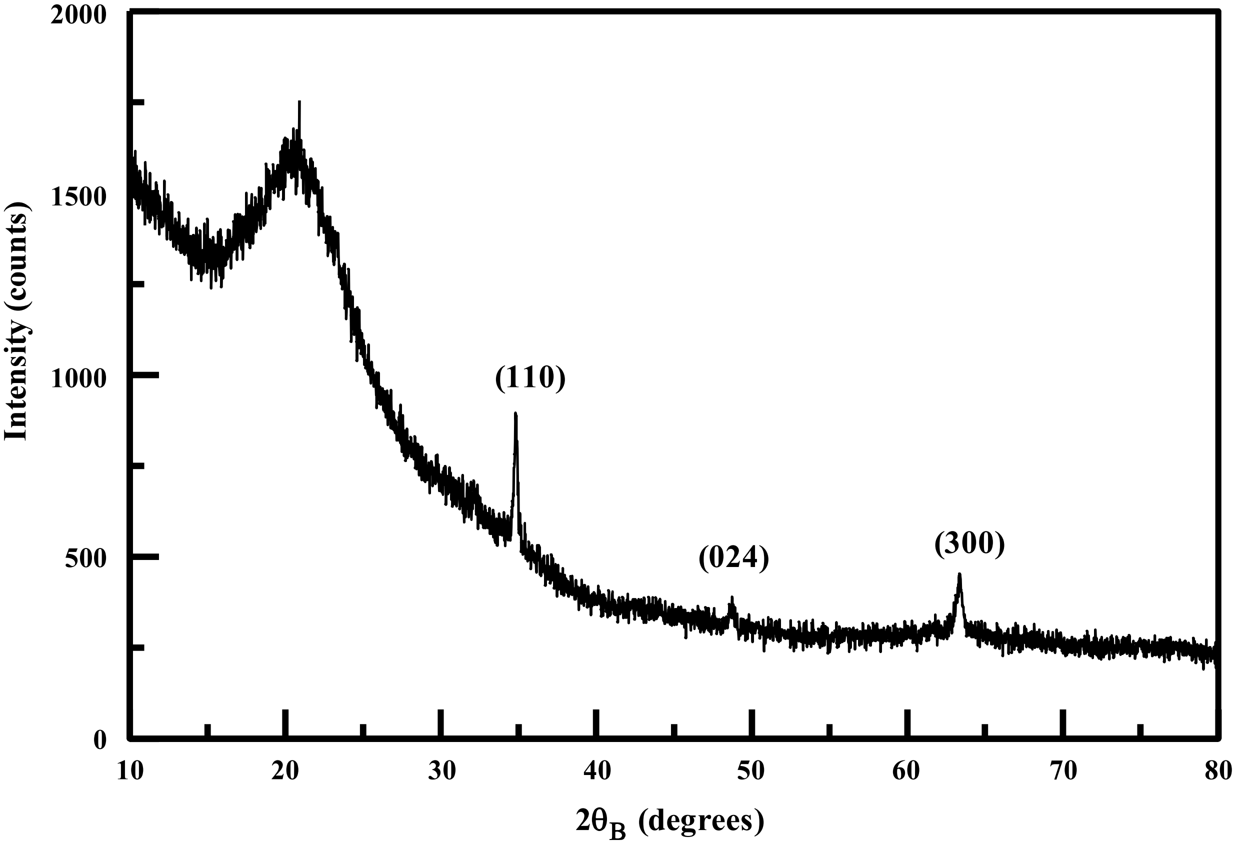

Fig 5. 3 XRD spectrum of Fe_2O_3 film

Figure 5.4 shows the XRD spectrum of a ZnO thin film. The film exhibited a single peak located at a $2\theta_B$ value of 34° and was associated with the (002) plane. The presence of this peak confirms a wurtzite hexagonal crystal structure of ZnO. Moreover, the preferred growth orientation was along the c-axis. The crystallite size of the films was found to be 5.0 nm.

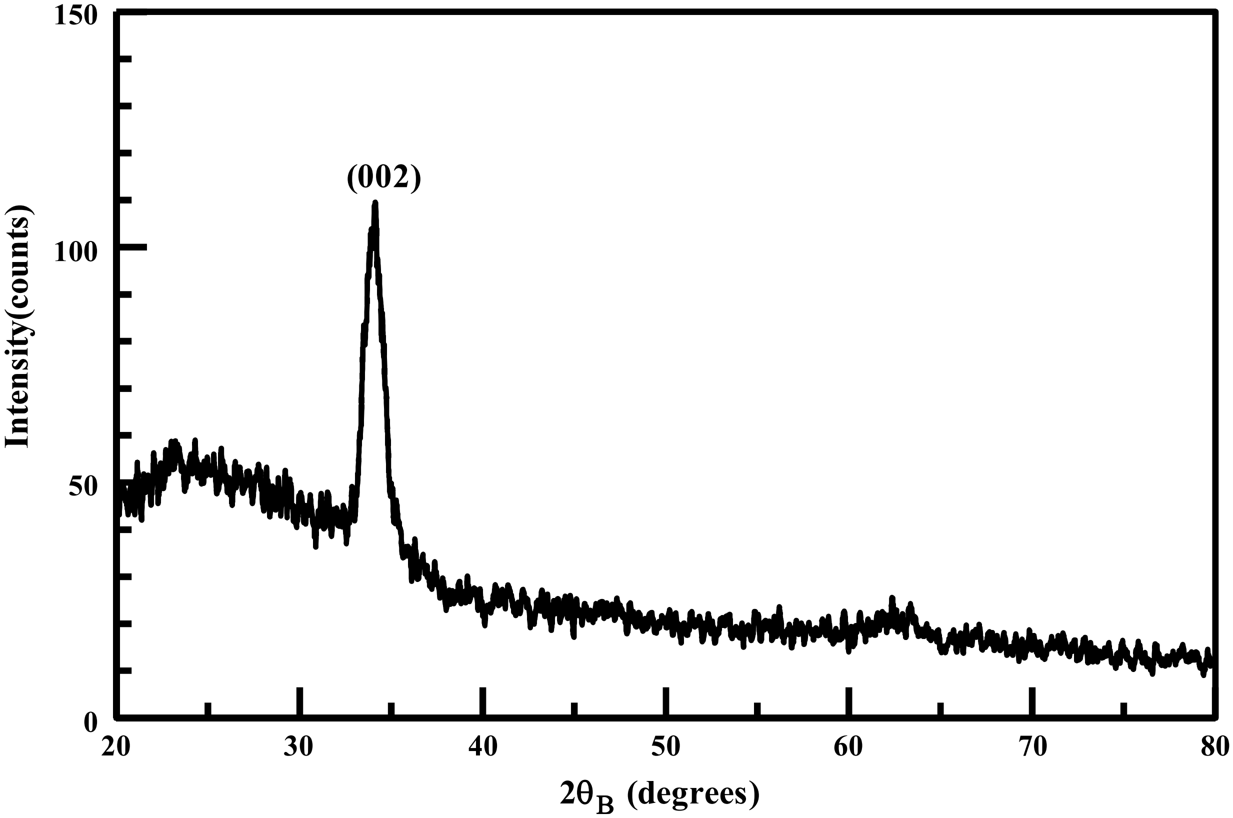

Fig 5. 4. XRD spectrum of ZnO film

The crystallinity in the above mentioned films was governed by the changes in the thermodynamic parameters like temperature and pressure. For example, the e-beam deposition of CeO_2 increases the temperature of the evaporation process, which results in a transformation into a crystalline phase. Similarly, iron oxide thin films were deposited in the presence of oxygen at a pressure of 7×10^{-4} mbar. So, the pressure in this case might be considered as an important parameter for the crystallinity in Fe_2O_3. The ZnO oxide thin film was depostie using RF sputtering which gives layer by layer deposition, and as a result, improves the crystallinity of the film. The existence of the amorphous nature of the other films might attributed as a small crystallite sizes which do not show required coherency length for Bragg’s diffraction.

5.2 Surface morphology

The surface morphology of the films was analyzed using atomic force microscopy (AFM). The surface scan area of $2 \times 2\ \mu m^2$ was taken to account for this purpose. Almost all the films showed a uniform columnar structure with different grain size and surface roughness values. Figure 5.5 shows three dimensional AFM images of the films, while table 5.1 shows the values of the lateral grain size and the root-mean-square surface roughness R_{rms} obtained from statistical analysis of the AFM images.

The AFM analysis shows the films deposited with thermal evaporation possess high grain size. The thermally evaporated films were deposited using molybdenum boat, which has a uniform and symmetric opening. This allows smooth deposition of the film on the substrates. So, a high deposition rate (4 Å/s) was fixed, which increases lateral grain size of the films. On the other hand, films obtained using electron beam deposition shows small lateral grain size. The is because of the less deposition rate (2 Å/s), that was fixed to avoid the spilling of the oxide materials from the boats.

The statistical analysis shows high root-mean-square surface roughness R_{rms} values in case of Fe_2O_3 and ZnO. Since these two films were obtained under the environment of Oxygen (Fe_2O_3) and Argon (ZnO). So, the interaction of these gases on the surface might deteriorated the smoothness of the films.

a) CeO_2

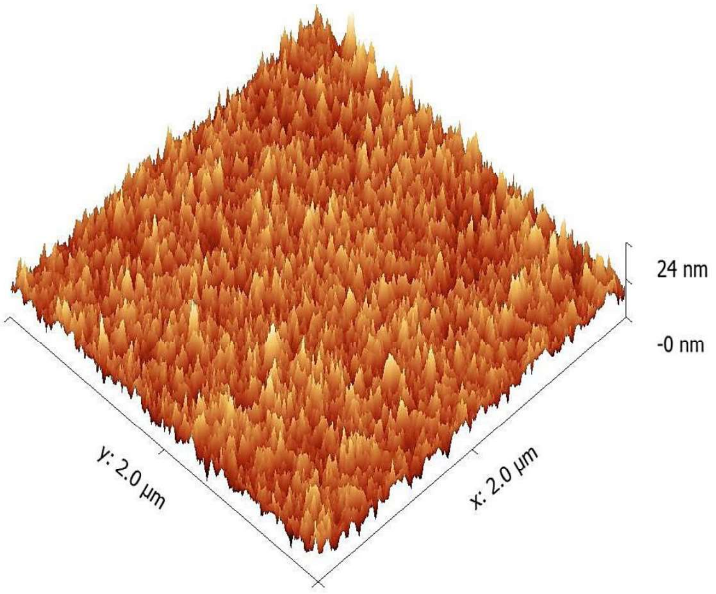

b) Fe_2O_3

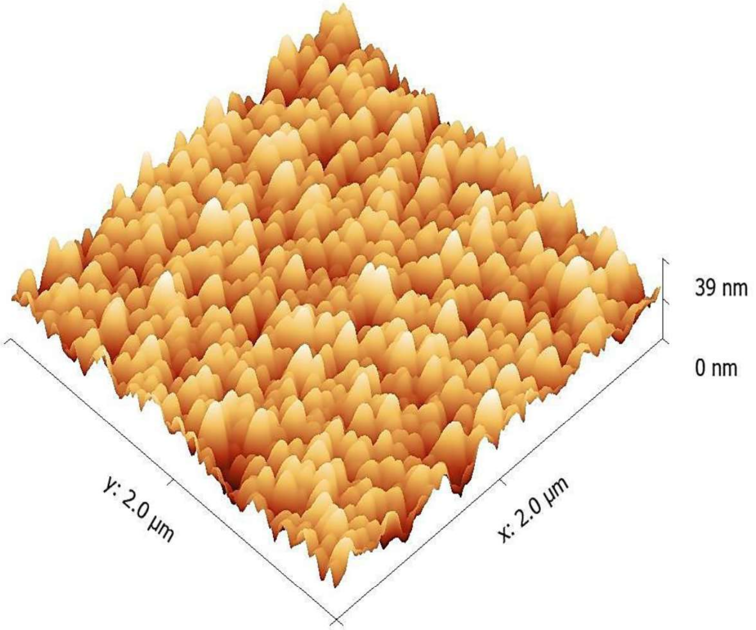

c) Ga_2O_3

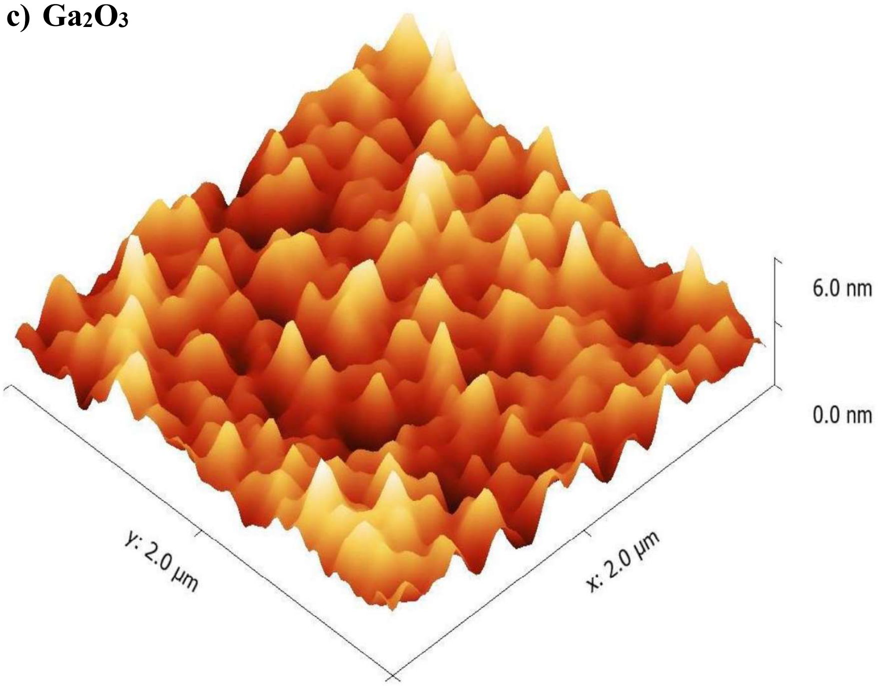

d) HfO_2

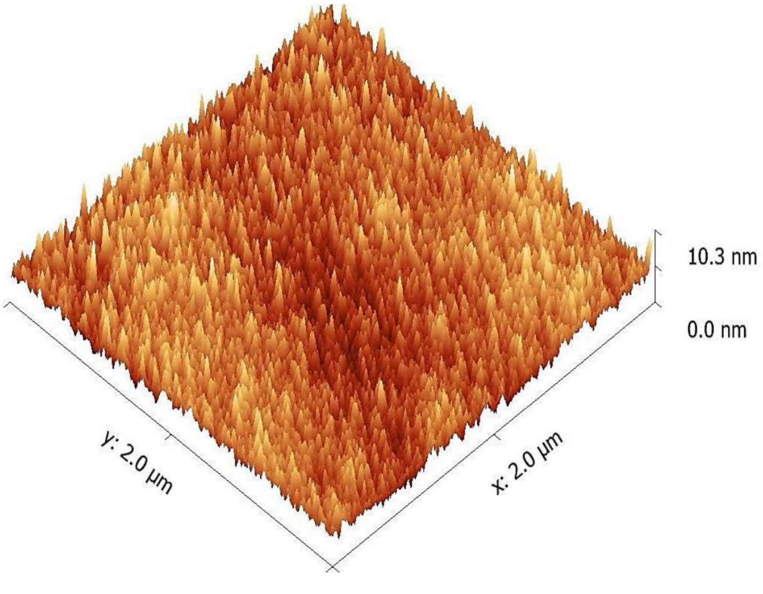

e) MoO_3

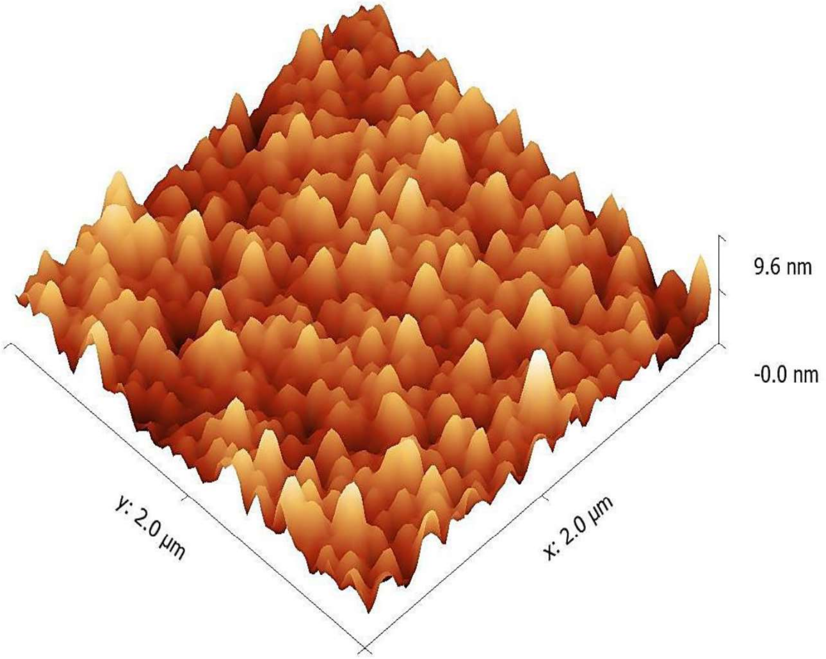

f) SnO_2

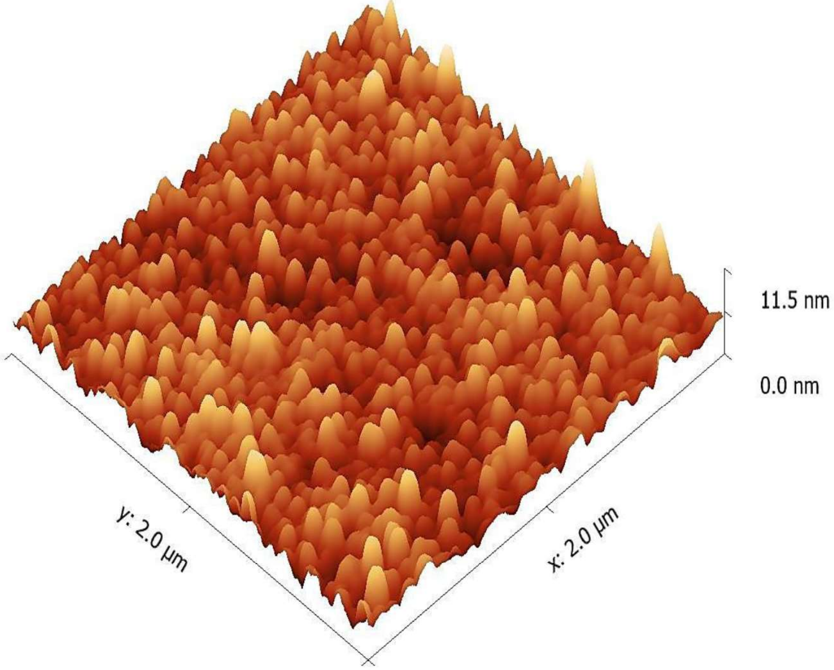

g) TiO_2

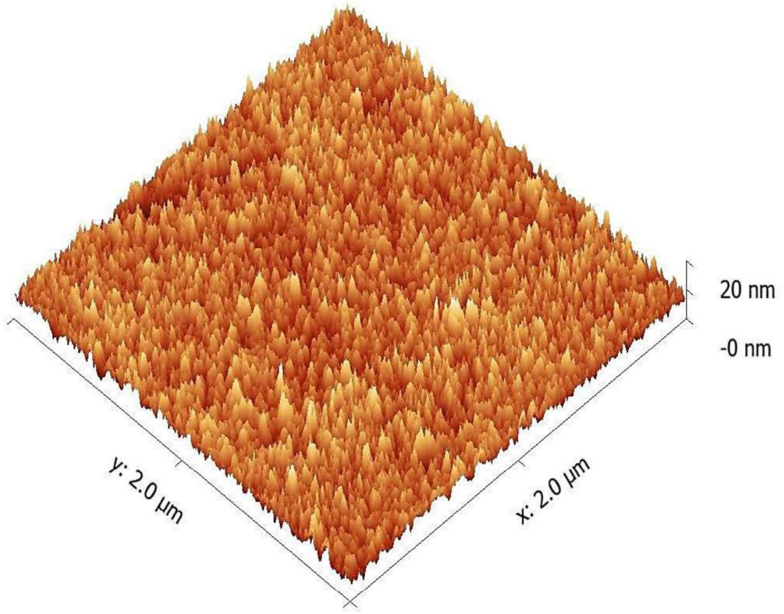

h) WO_3

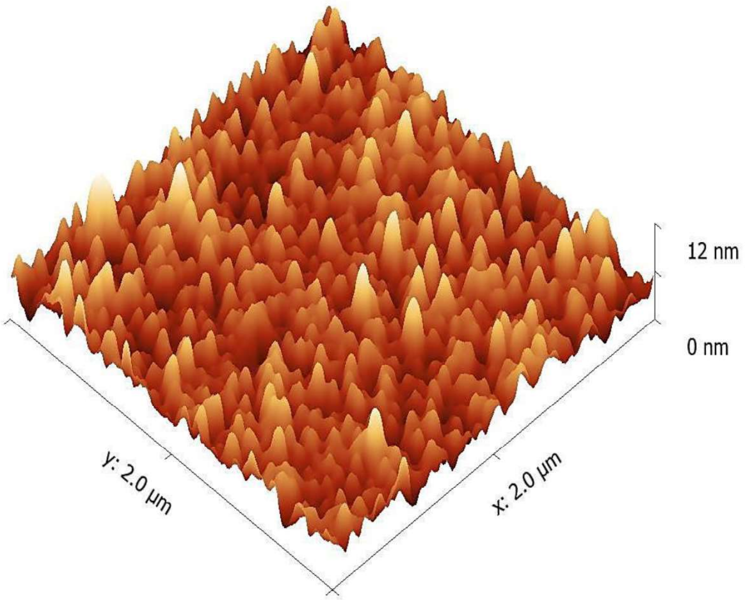

i) ZnO

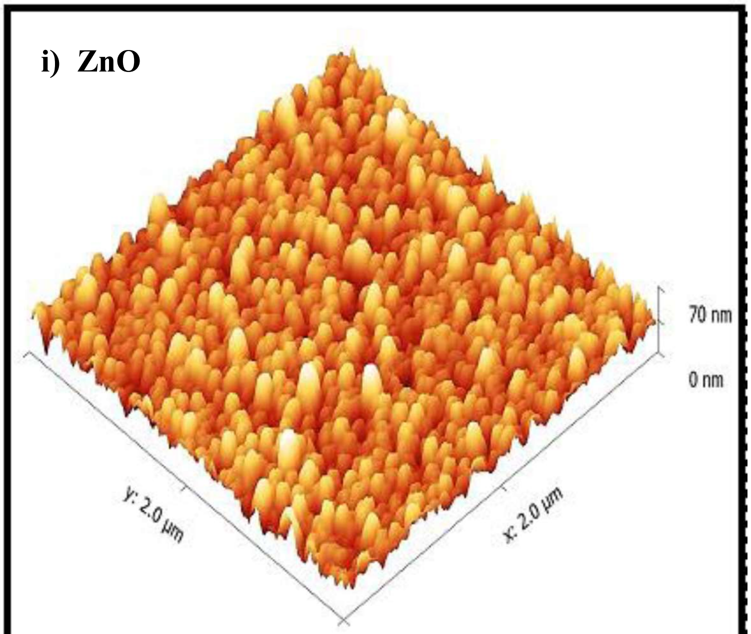

j) ZrO_2

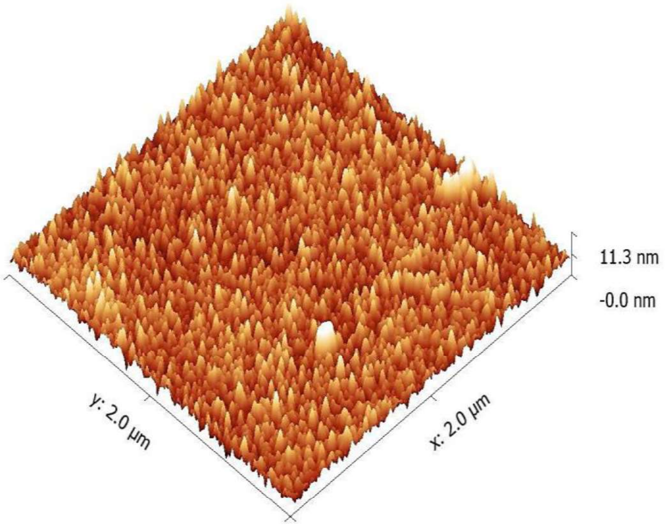

Fig 5. 5. a – j. Three-dimensional AFM images of metal oxide thin films

Sample	**Grain size (nm)**	**Roughness RMS (nm)**
CeO_2	14.6	2.3
Fe_2O_3	41.0	5.2
Ga_2O_3	55.0	0.8
HfO_2	15.6	1.1
MoO_3	46.0	1.2
SnO_2	39.0	1.2
TiO_2	12.8	2.0
WO_3	42.0	1.4
ZnO	30.0	7.8
ZrO_2	18.6	1.4

Table 5. 1. Lateral grain size and surface roughness values of metal oxide thin films

5.3 Optical Properties

The optical properties of the metal oxide thin films were investigated using spectrophotometry. The films were transparent throughout the visible and infrared regions of the electromagnetic spectrum. These spectra were characterized by the presence of maxima and minima that arose from interference of light beams reflected at different interfaces of the films. These extrema were used to estimate the thickness *d* of the films according to the equation.

$$d = \frac{\lambda_{max} \times \lambda_{min}}{4\,n\,|\lambda_{max} - \lambda_{min}|} \qquad (5.3)$$

where λ_{max} is the wavelength corresponding to a maximum in transmittance, λ_{min} is the wavelength corresponding to the adjacent minimum, and *n* is the refractive index of the film estimated using the empirical relation:

$$n = 4.22 - 2.94T_{min} \qquad (5.4)$$

where T_{min} is transmittance of the films corresponds to λ_{min}. The optical band gaps of the films were estimated using the Tauc relation

$$\alpha\, E_P = \eta\left(E_P - E_g\right)^{\beta} \qquad (5.5)$$

where α is the absorption coefficient, E_P is the photon energy, η is a constant, and E_g is the band gap value. The index β associates with the nature of the optical absorption. It has a value of ½ for direct transitions and 2 for indirect transitions. The absorption coefficient was obtained using the equation $\alpha = \frac{1}{d}\ln(\frac{1}{T})$, where T is the transmittance of the film. The band gap was obtained by plotting $\left(\alpha\, E_p\right)^{1/\beta}$ versus photon energy to get a linear relationship that is extrapolated to the energy axis to obtain the band gap. The values of the band gaps obtained from these spectra, along with the thickness of the films are listed in Table 5.2

Oxide	**Thickness (d) (nm)**	**Direct E_g (eV)**	**Indirect E_g (eV)**
CeO_2	296	3.60	3.12
Fe_2O_3	314	2.70	1.80
Ga_2O_3	261	4.80	3.10
HfO_2	193	5.85	5.05
MoO_3	341	4.18	3.05
SnO_2	193	4.08	2.90
TiO_2	318	3.95	3.38
WO_3	315	4.11	3.35
ZnO	467	3.30	3.12
ZrO_2	135	5.80	4.95

Table 5. 2 Values of the thickness, direct band gap and indirect band gap values of metal oxides

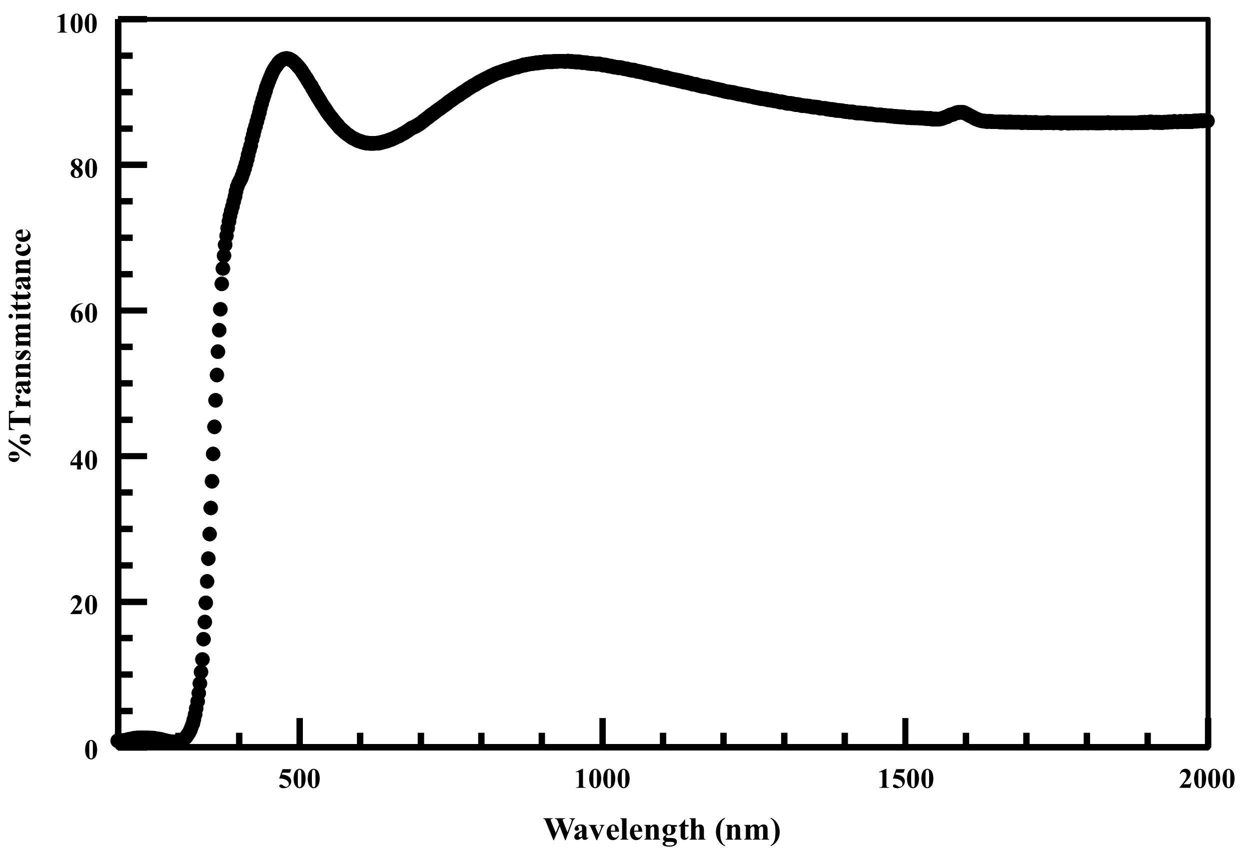

Fig 5. 6. Transmittance spectrum of CeO_2

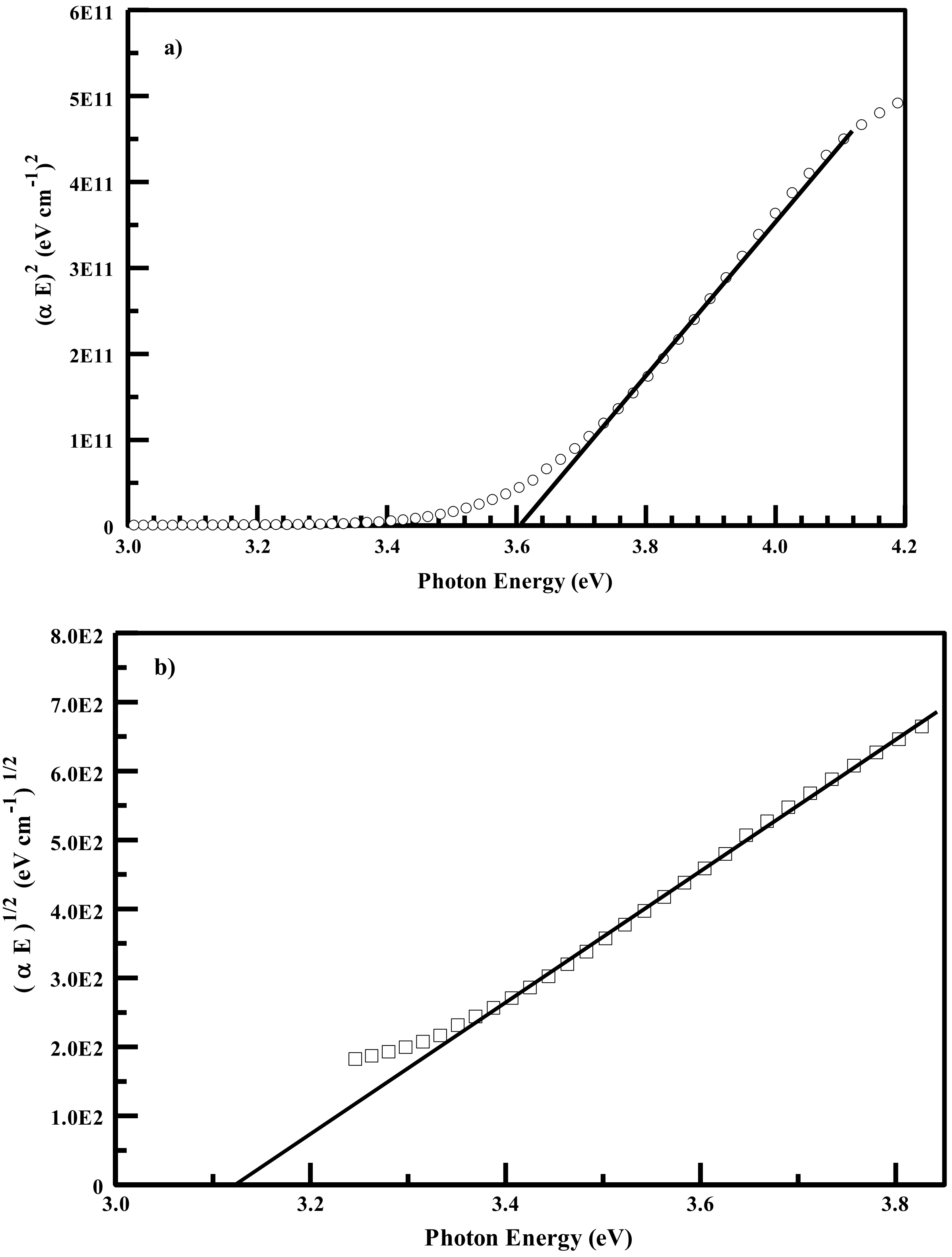

Fig 5. 7. a) Direct and b) Indirect band gap of CeO_2

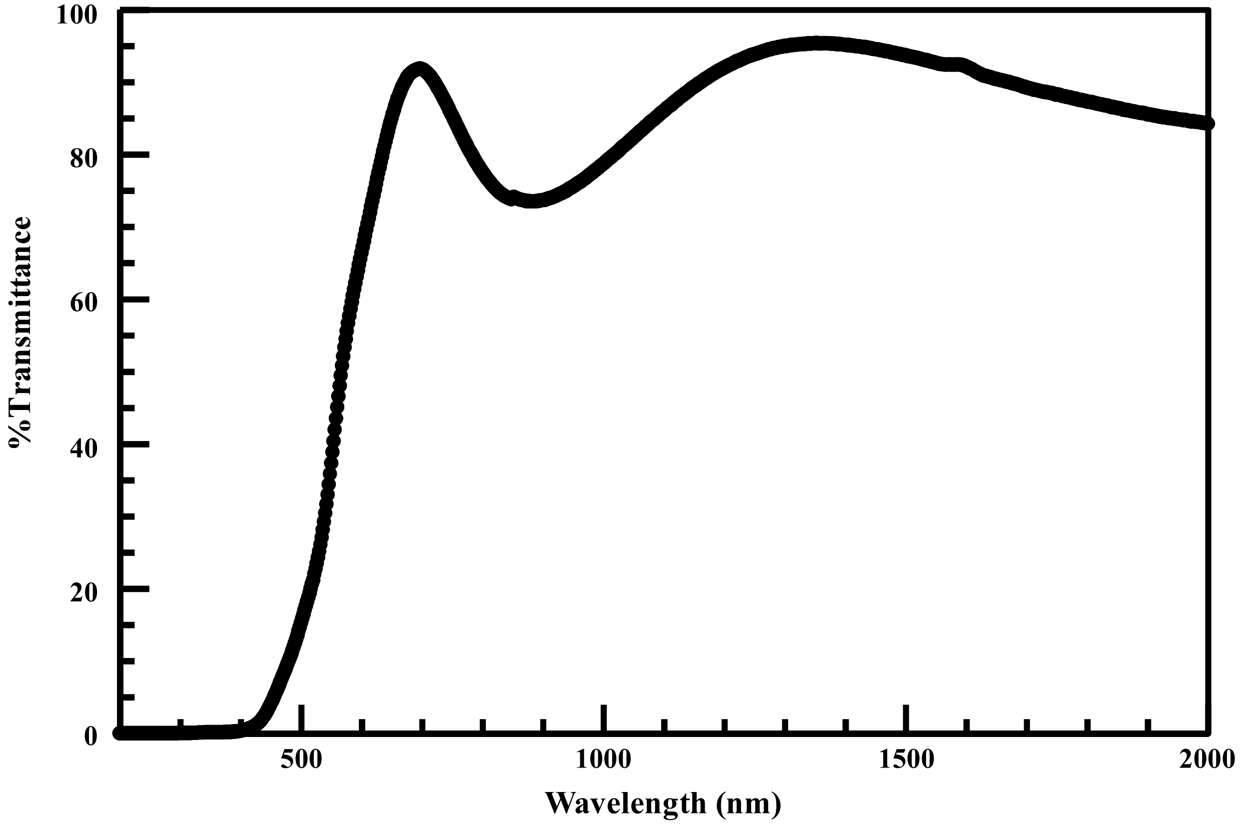

Fig 5. 8 Transmittance spectrum of Fe_2O_3

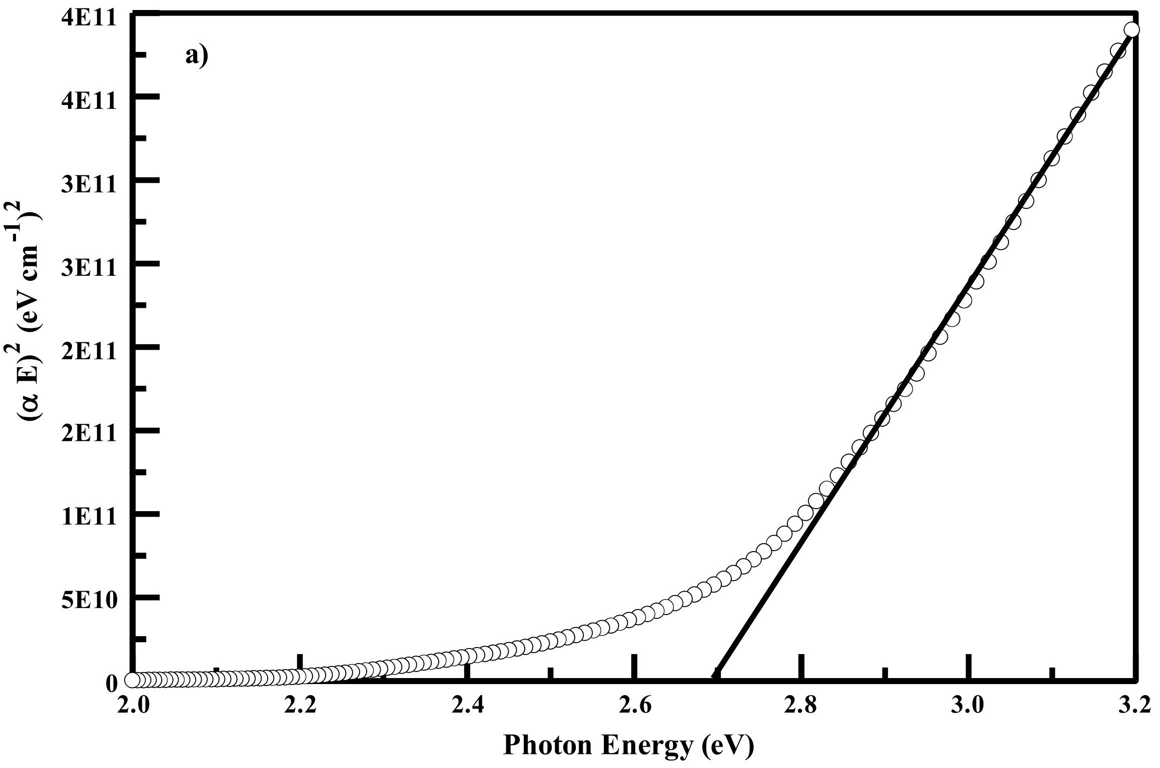

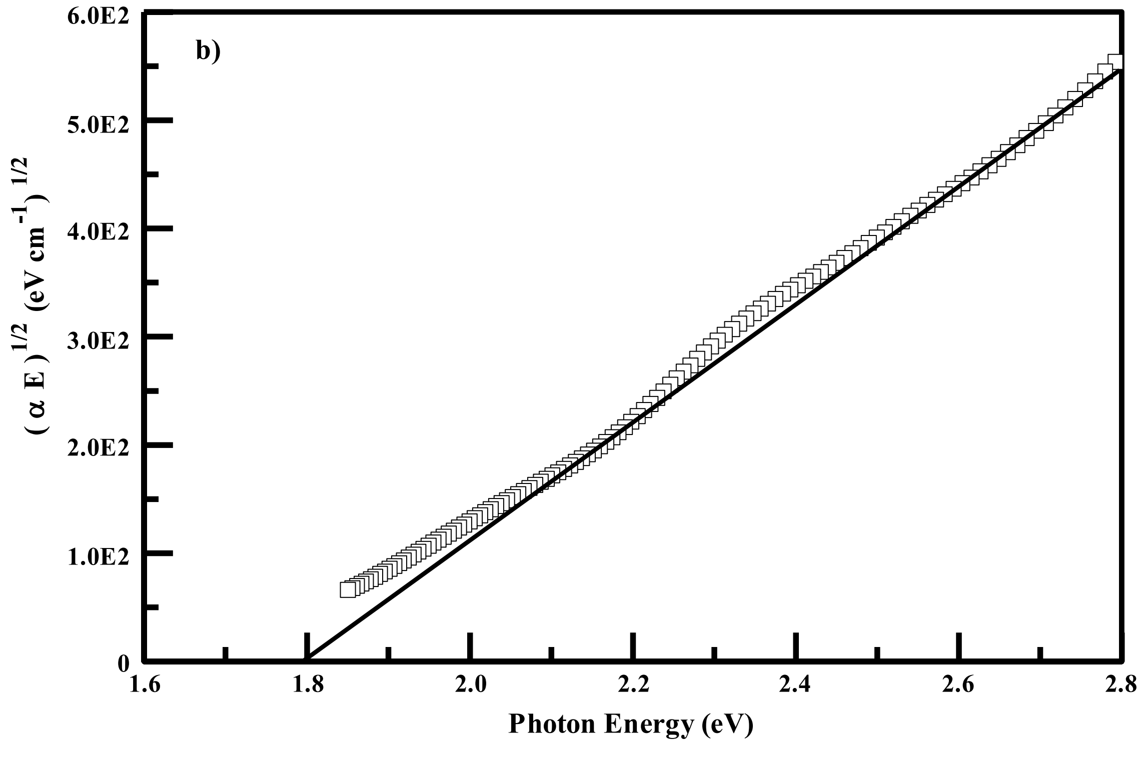

Fig 5. 9. a) Direct and b) Indirect band gap of Fe_2O_3

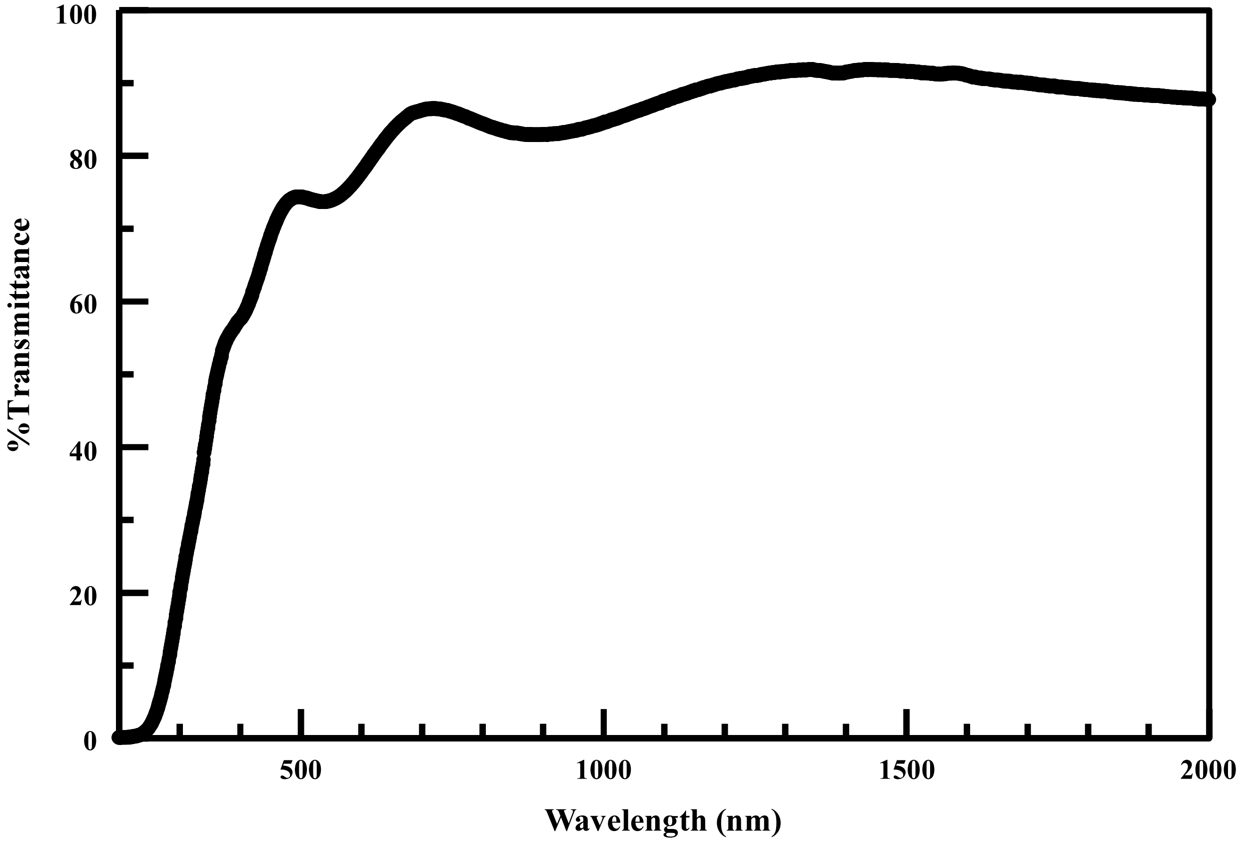

Fig 5. 10 Transmittance spectrum of Ga_2O_3

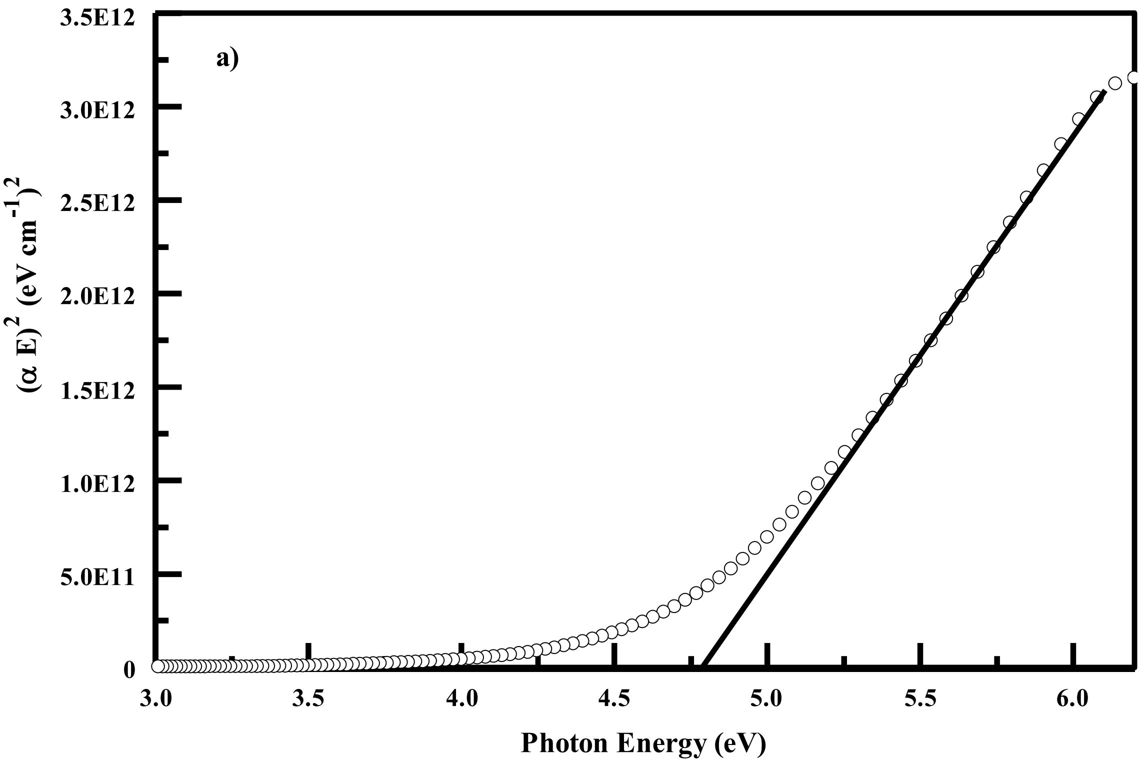

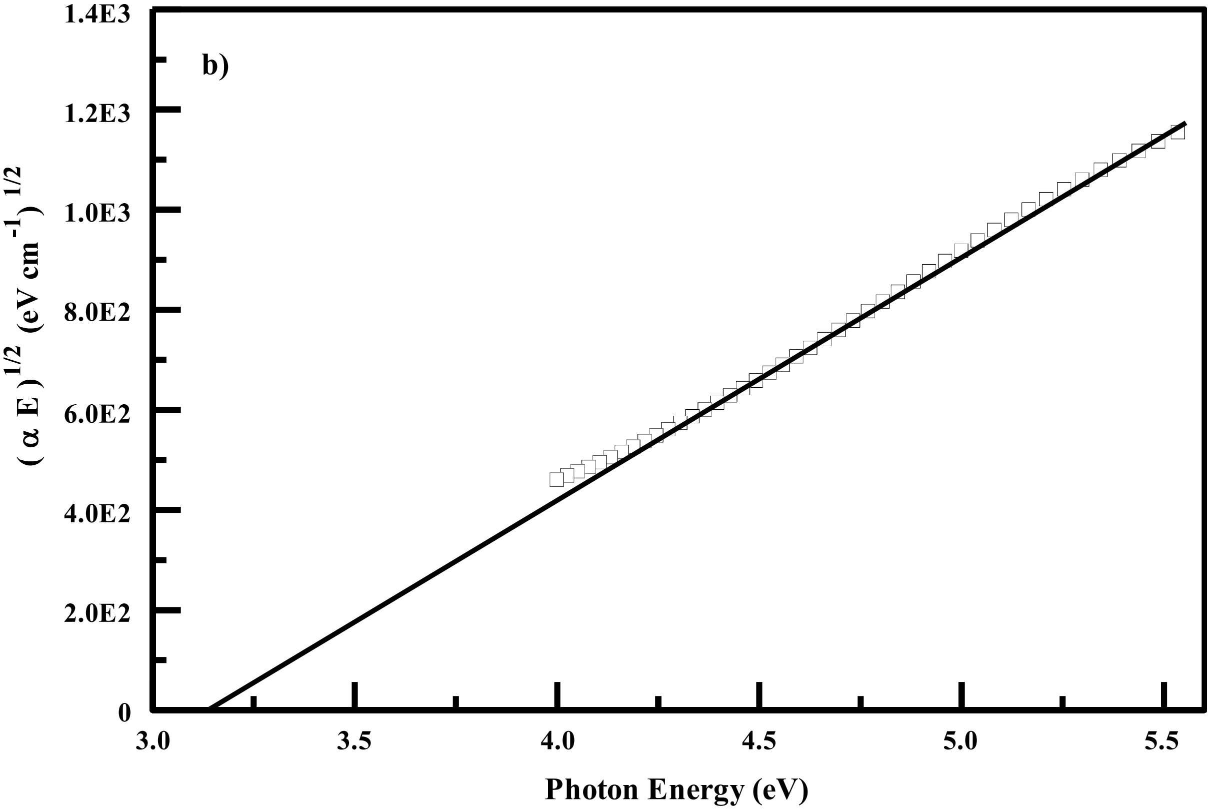

Fig 5. 11. a) Direct and b) Indirect band gap of Ga_2O_3

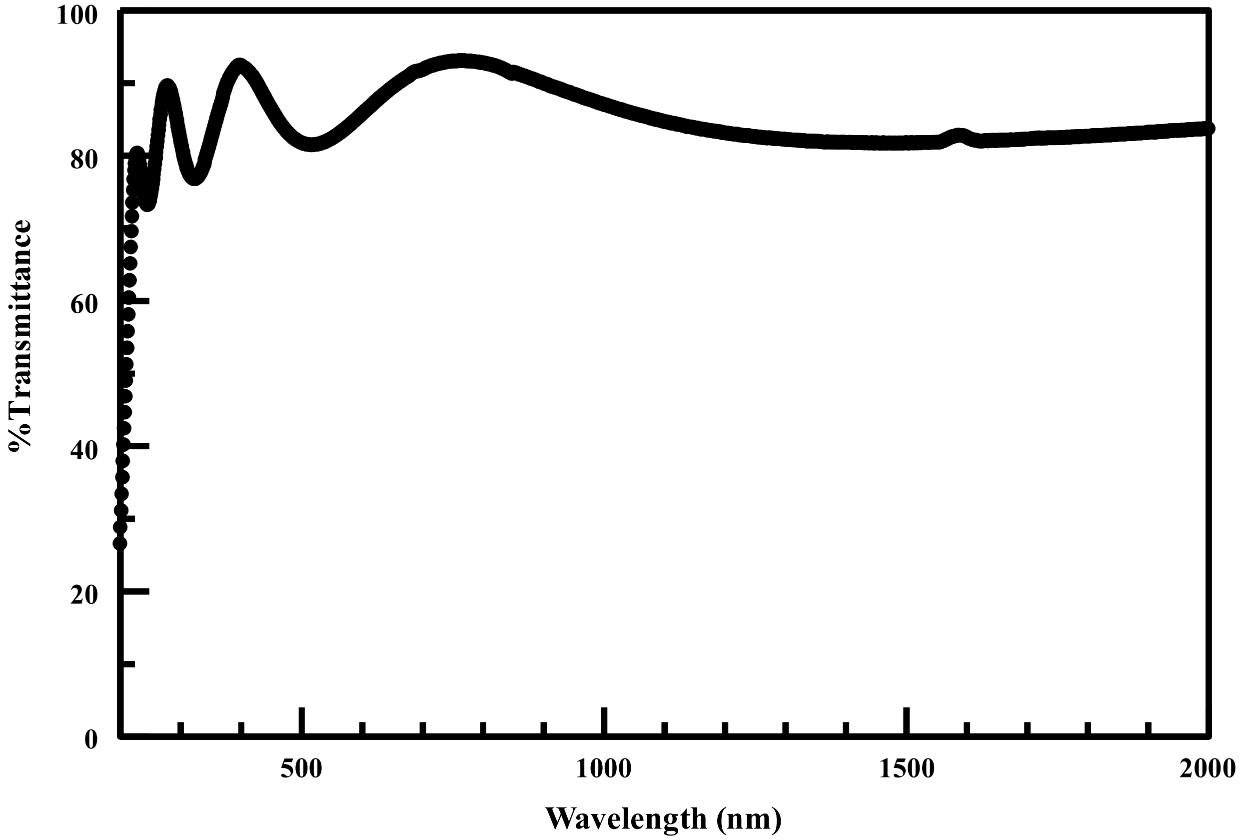

Fig 5. 12 Transmittance spectrum of HfO_2

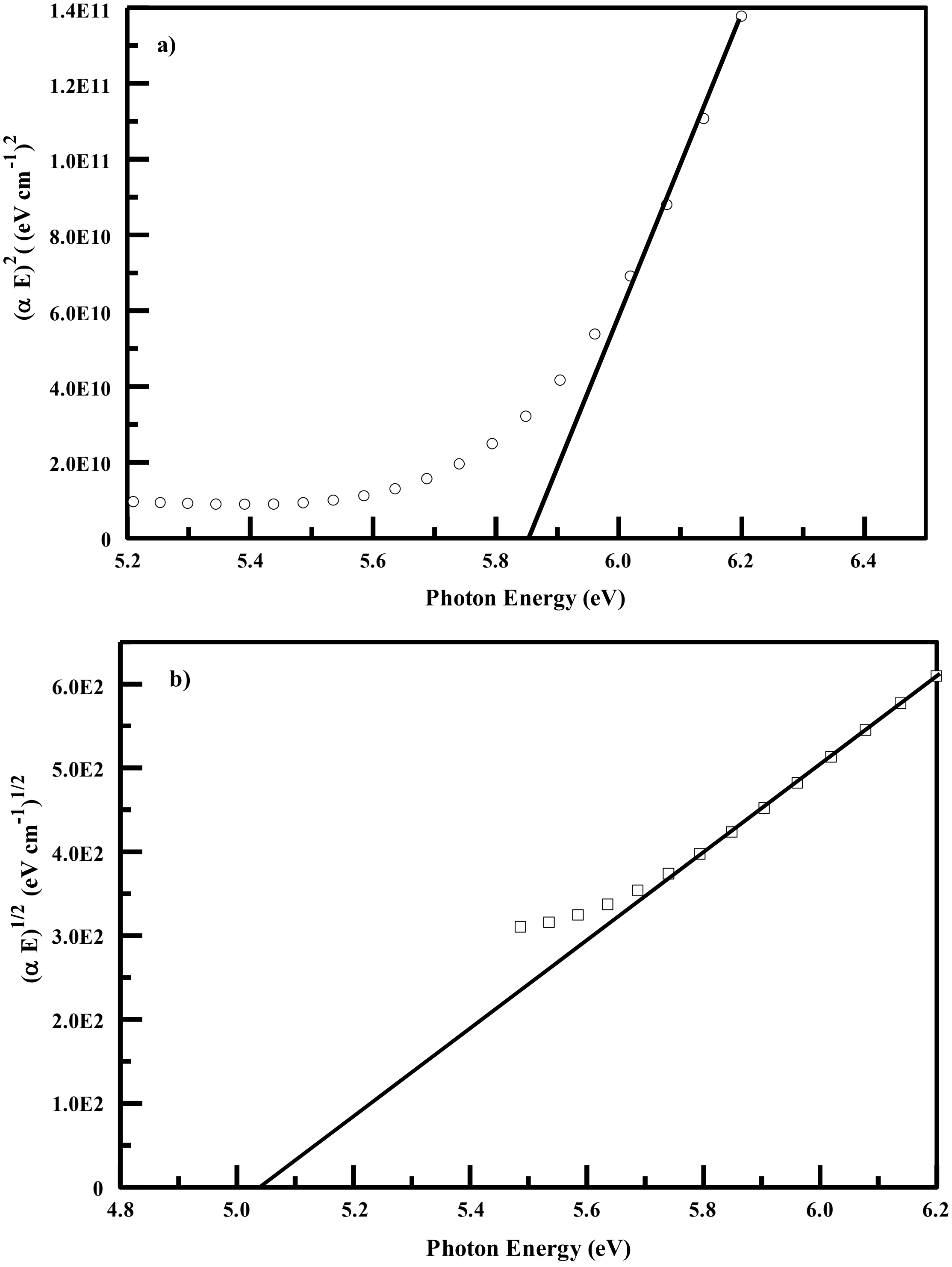

Fig 5. 13. a) Direct and b) Indirect band gap of HfO_2

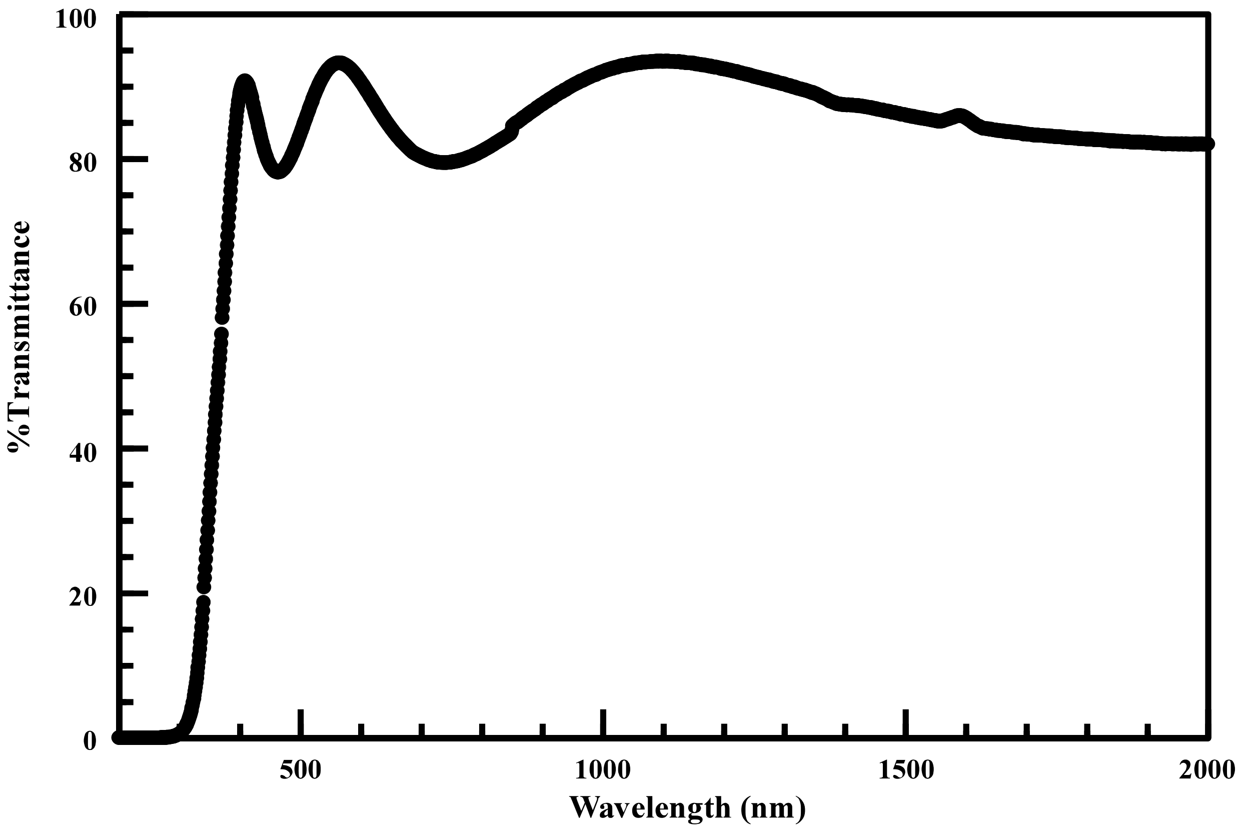

Fig 5. 14 Transmittance spectrum of MoO_3

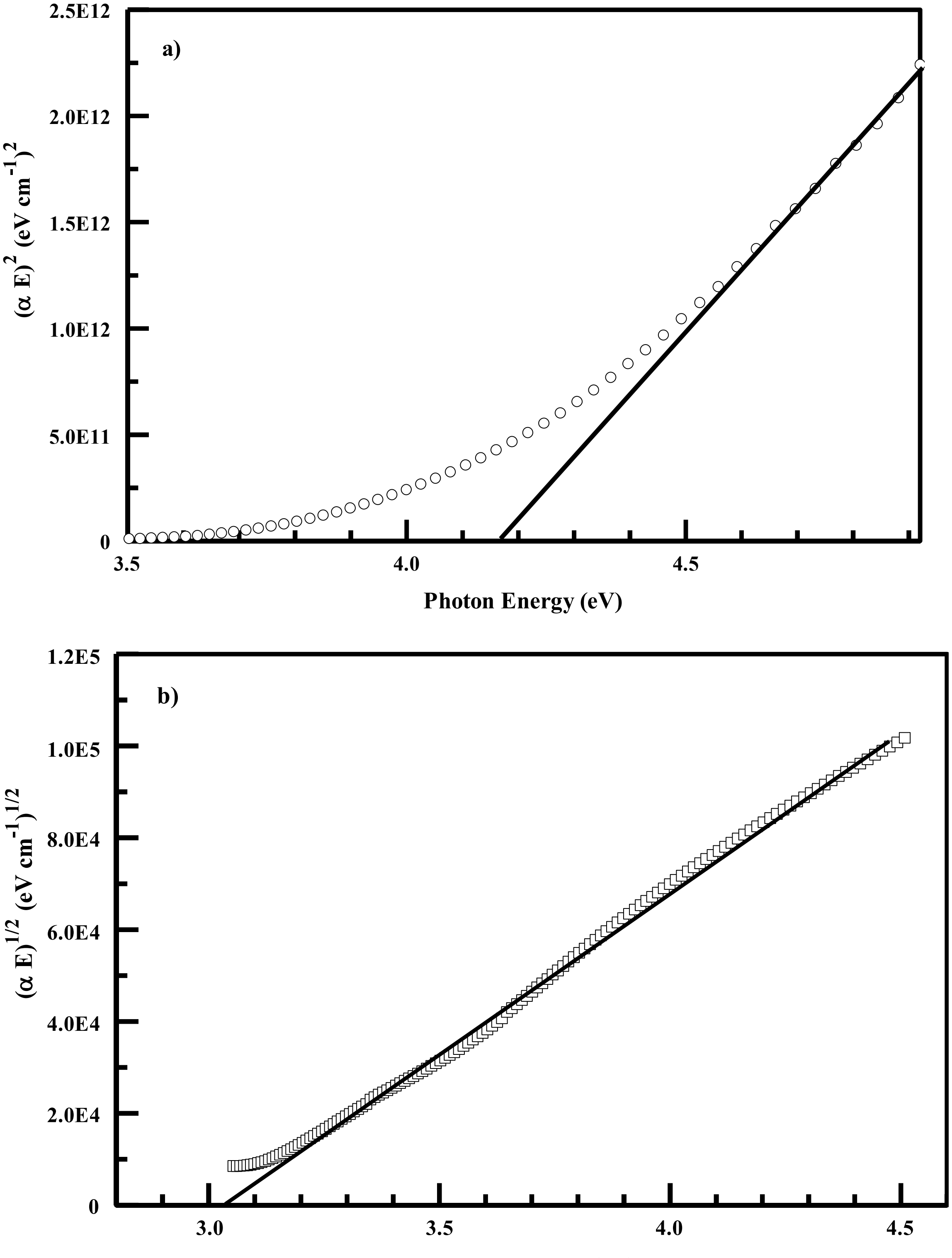

Fig 5. 15. a) Direct and b) Indirect band gap of MoO_3

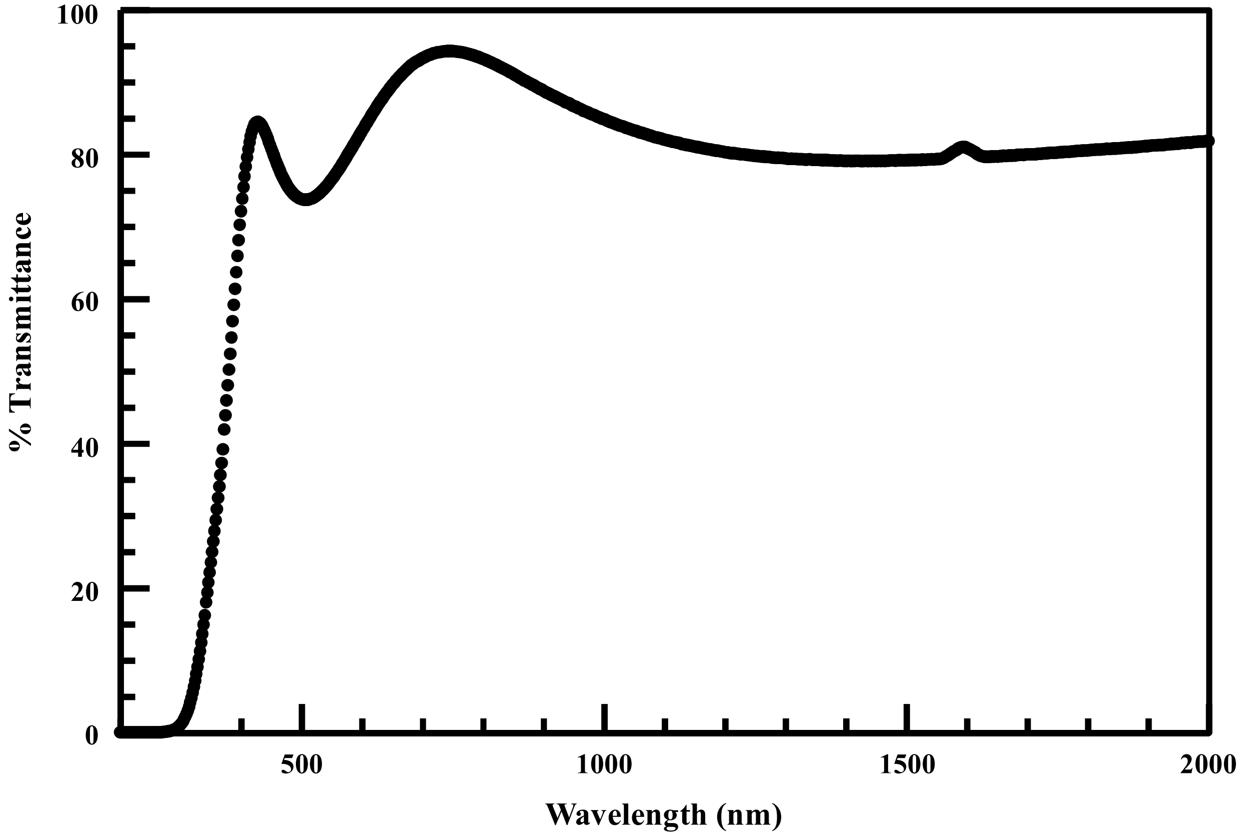

Fig 5. 16 Transmittance spectrum of SnO_2

.

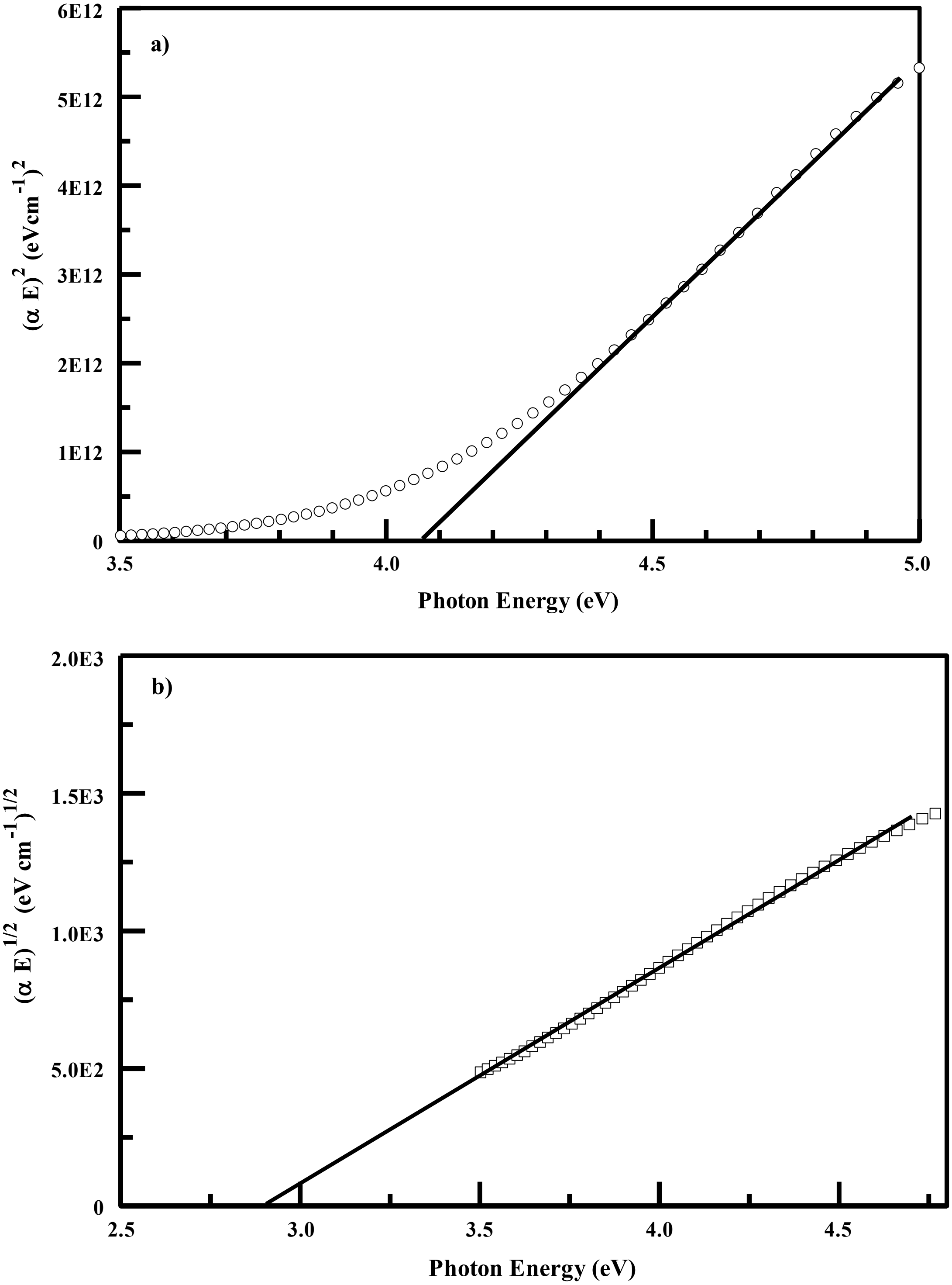

Fig 5. 17. a) Direct and b) Indirect band gap of SnO_2

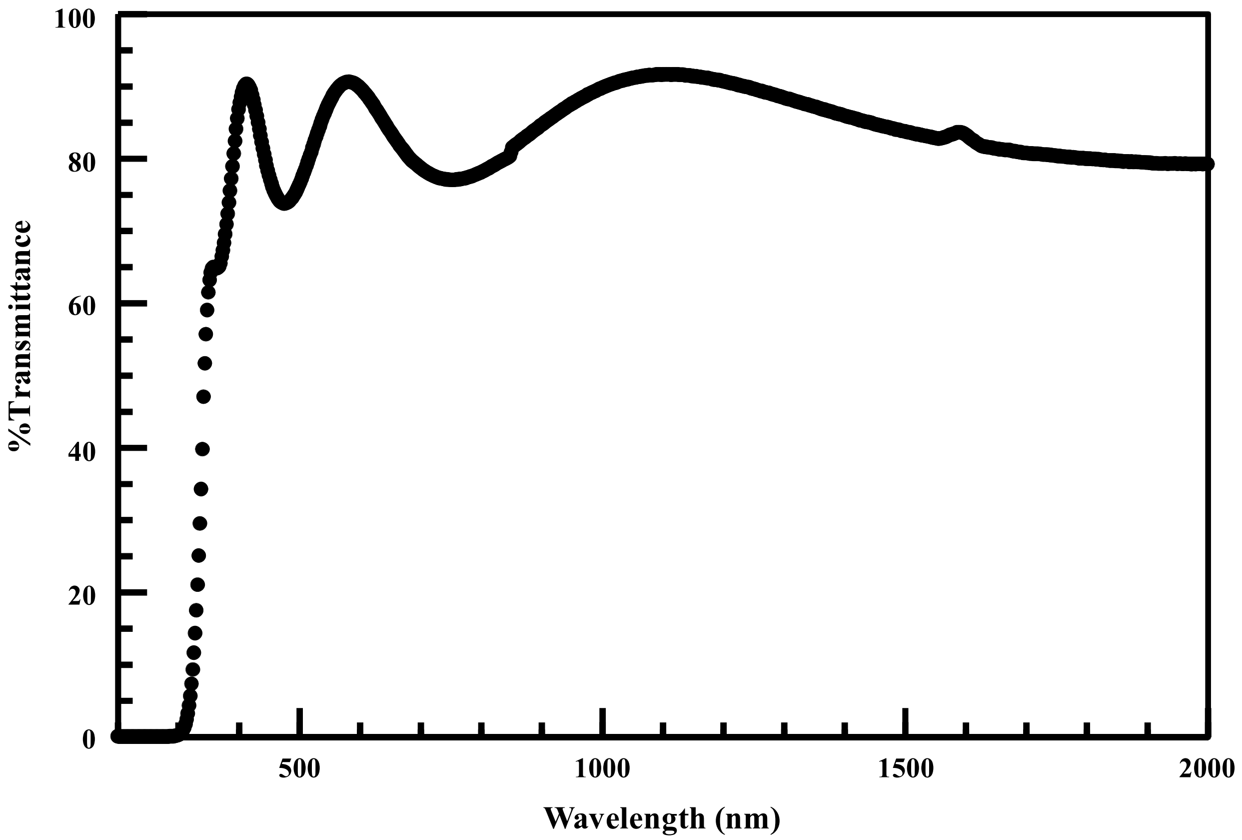

Fig 5. 18 Transmittance spectrum of TiO_2

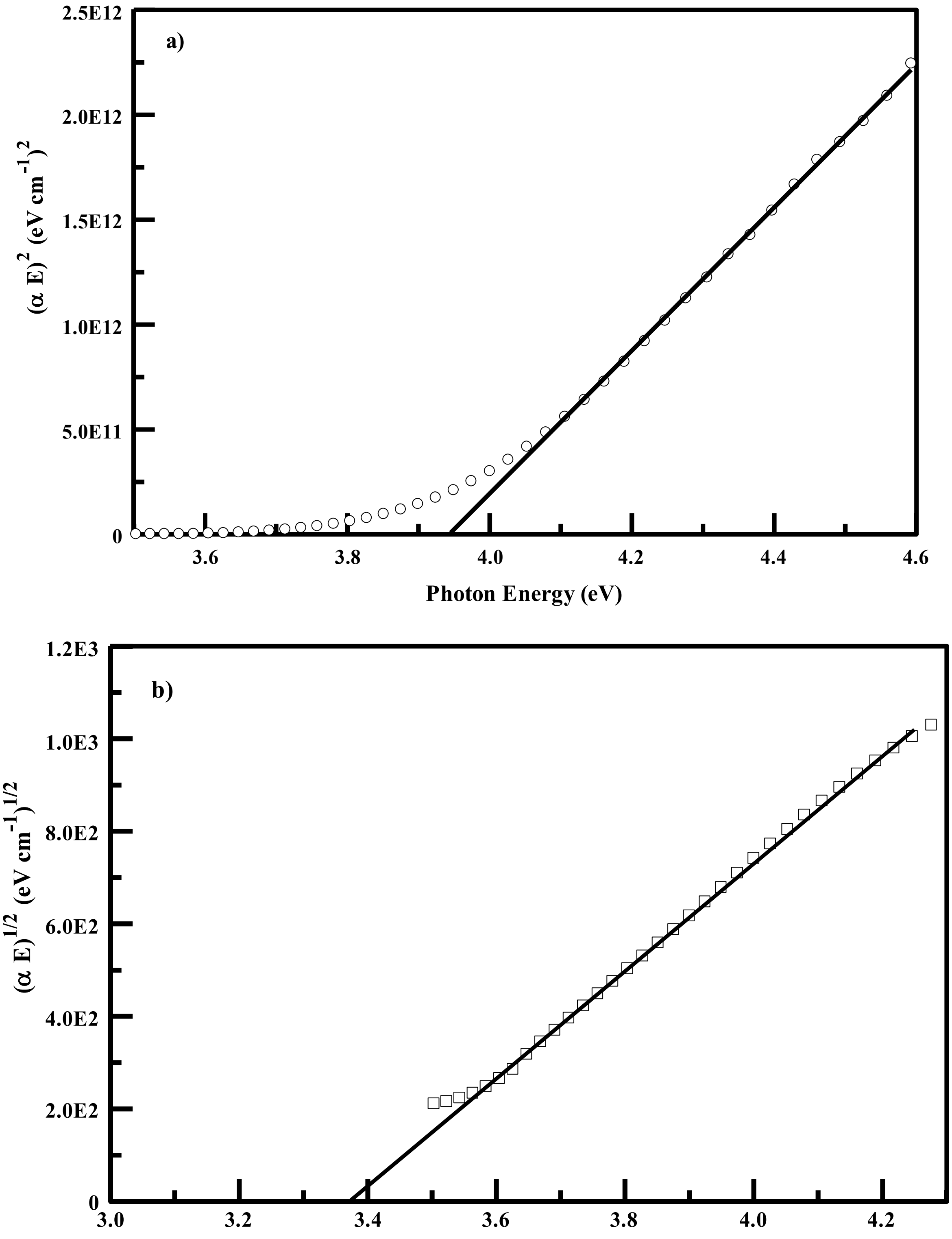

Fig 5. 19. a) Direct and b) Indirect band gap of TiO_2

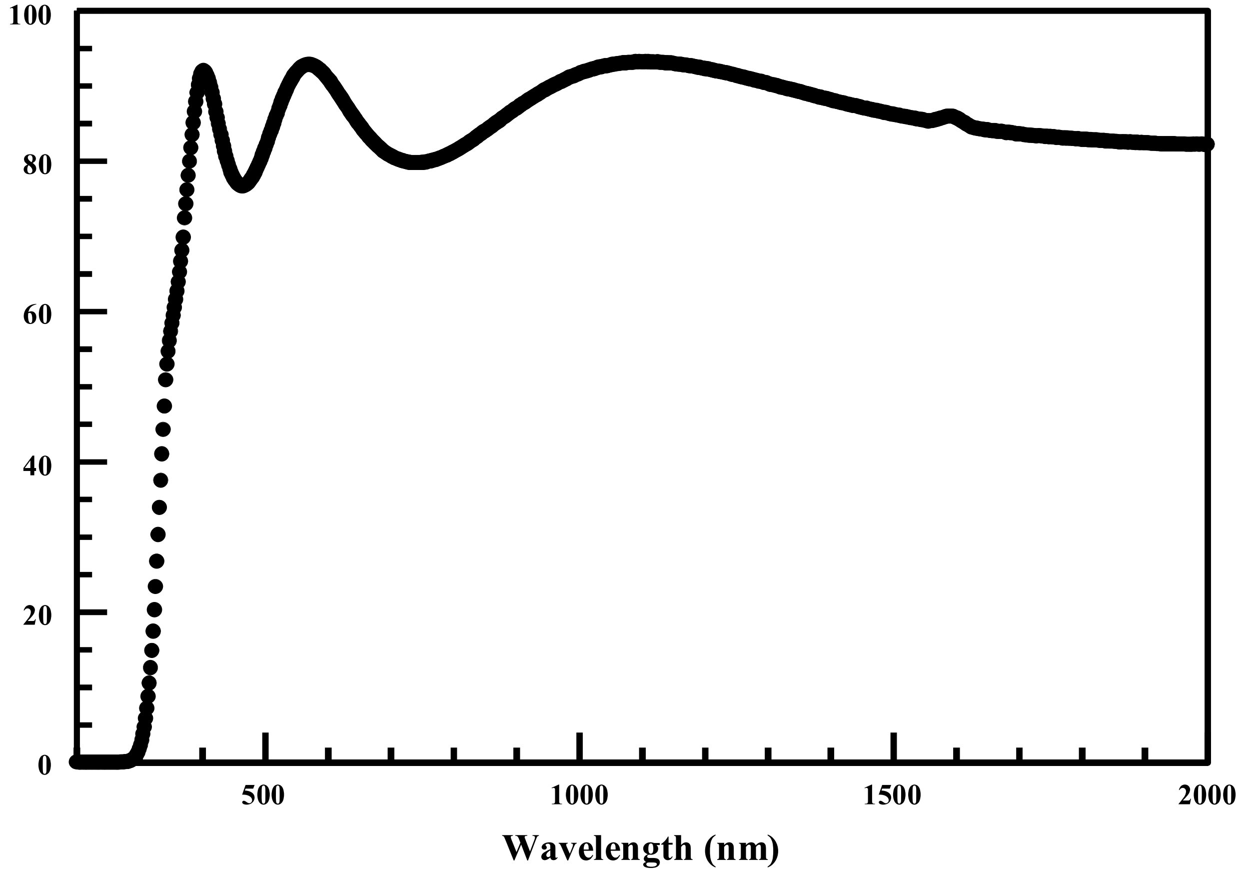

Fig 5. 20 Transmittance spectrum of WO_3

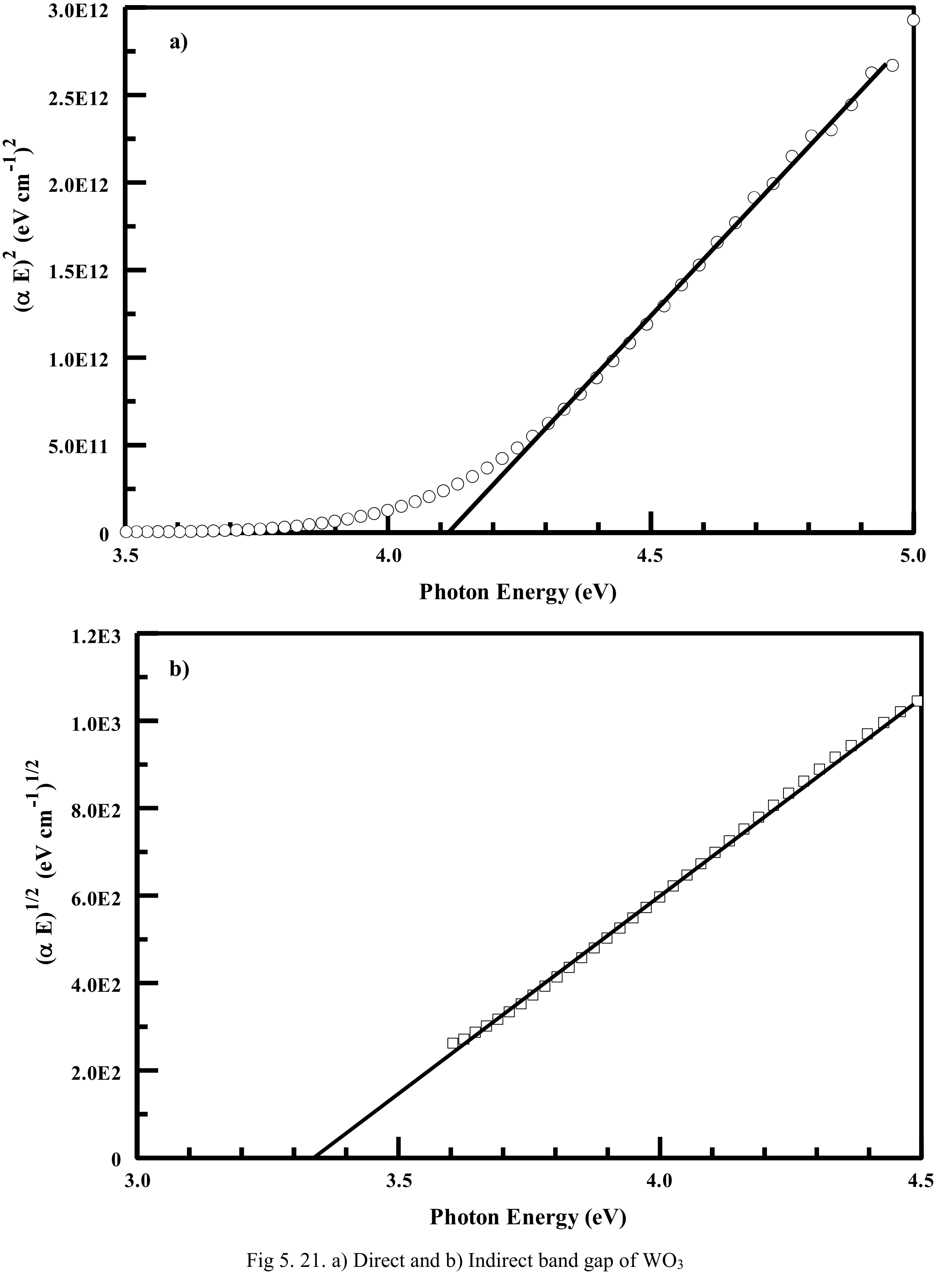

Fig 5. 21. a) Direct and b) Indirect band gap of WO_3

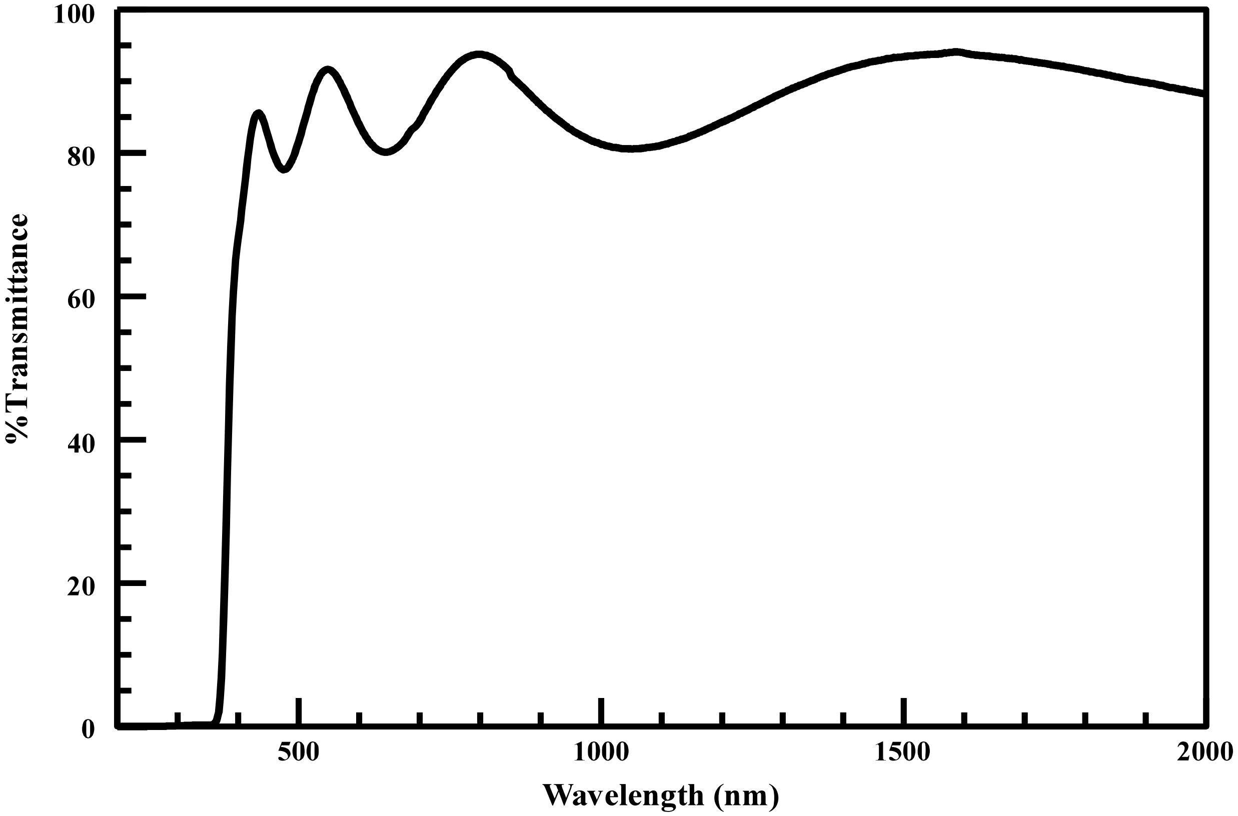

Fig 5. 22 Transmittance spectrum of ZnO

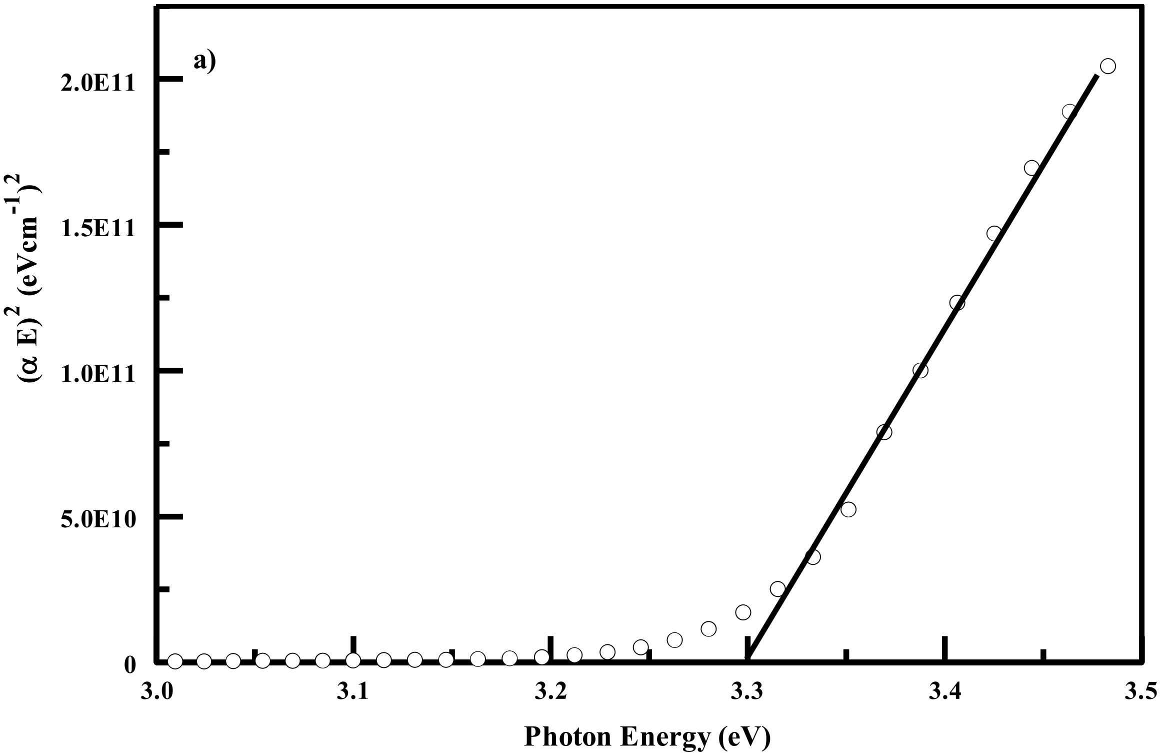

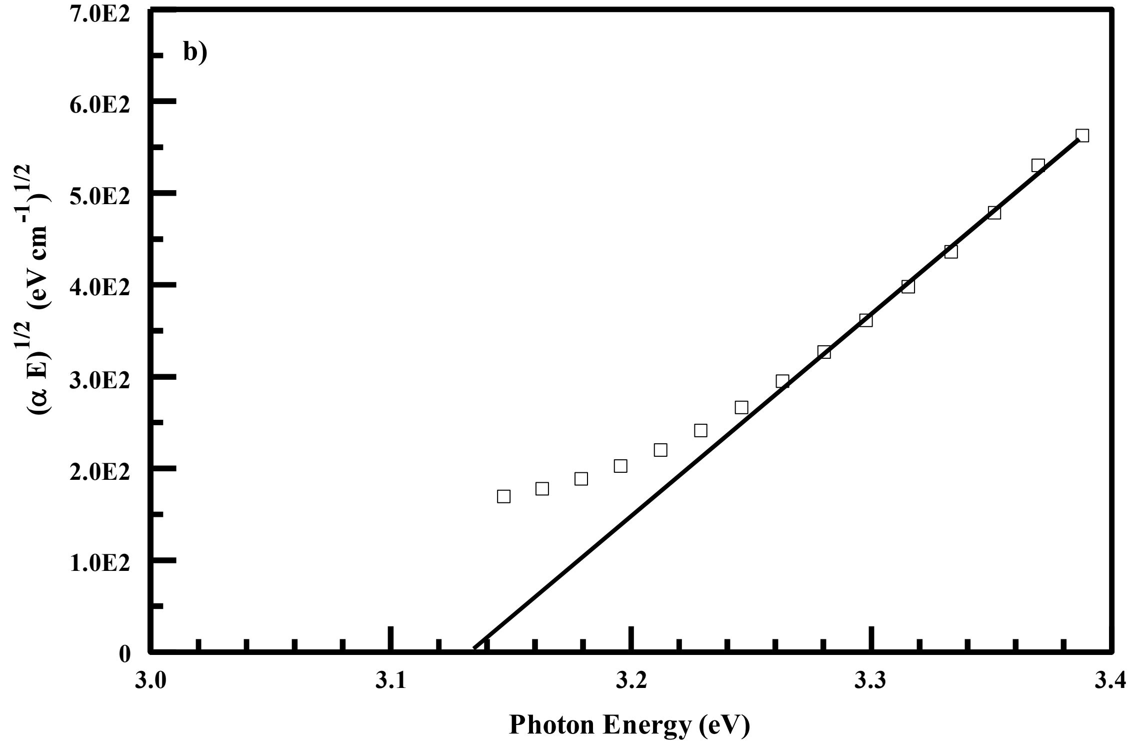

Fig 5. 23. a) Direct and b) Indirect band gap of ZnO

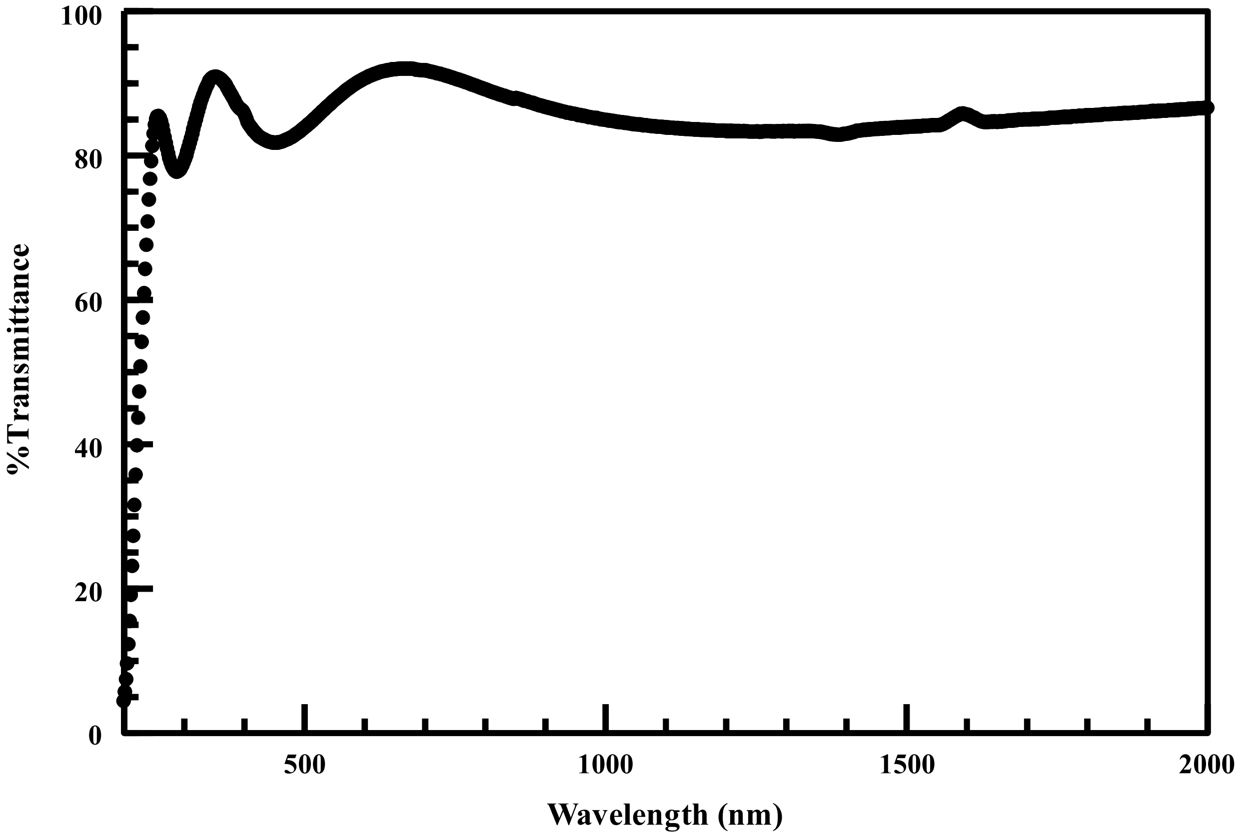

Fig 5. 24 Transmittance spectrum of ZrO_2

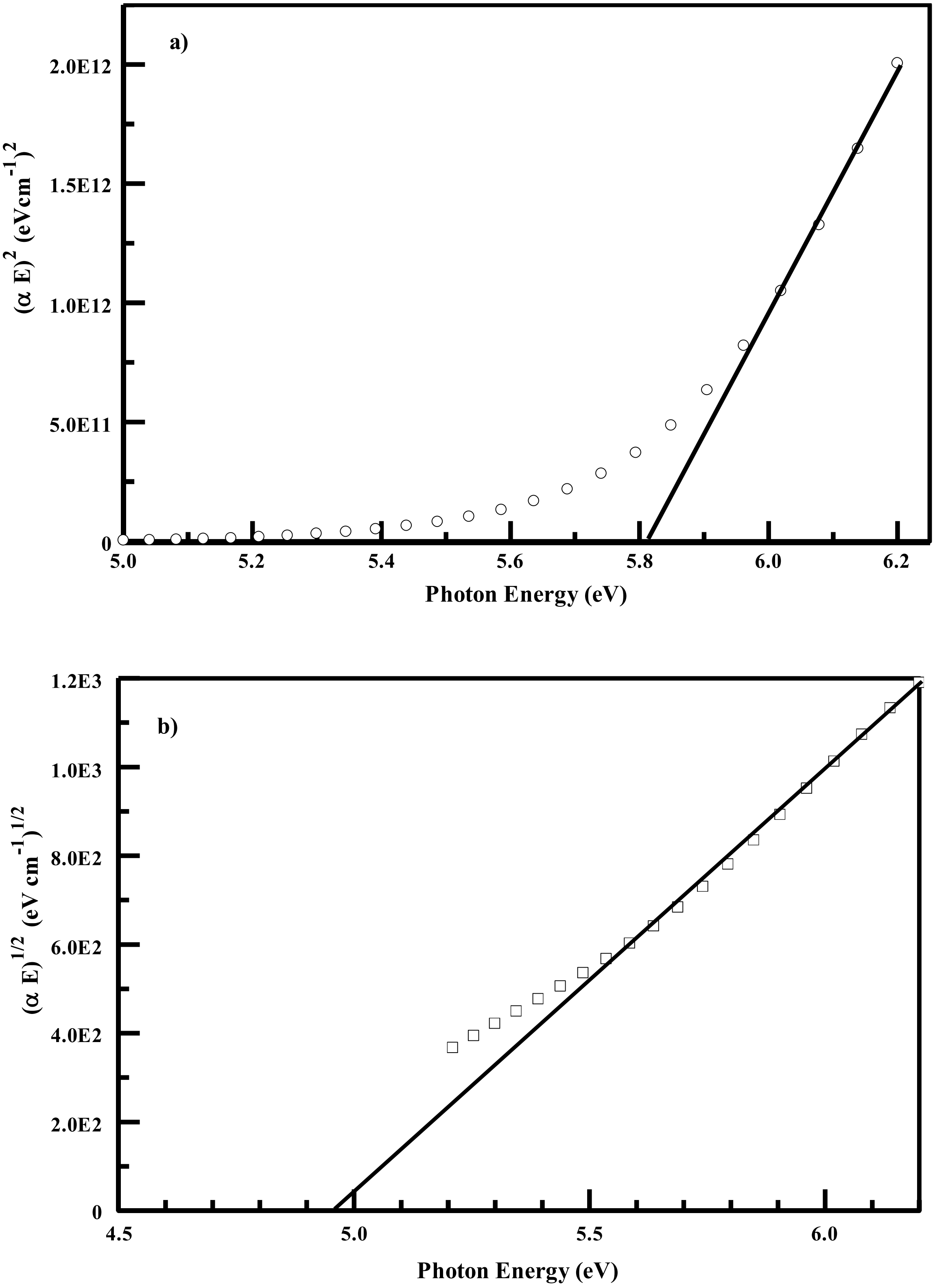

Fig 5. 25. a) Direct and b) Indirect band gap of ZrO_2

5.4 Chemical Analysis

The chemical analysis of metal oxides thin films was performed using XPS. The charge shift for all the samples was corrected using the location of C1s peak (at 284.5 eV) as the reference.

The core level spectrum of Ce 3d in cerium oxide is shown in the figure 5.26. The strong hybridization in Ce 4f and oxygen 2p gives a complex structure to CeO_2 [63]. The most dominant peak in Ce 3d spectra was the one positioned at 916.2 eV. This peak indicated the attribution of Ce^{4+} and it was absent in Ce^{+3} [184]. The other peaks associated with Ce^{+4} were the ones located at 906.8, 900.3, 897.9, 888.5 and 881.8 eV [184]. The intensity of the peaks that corresponded to Ce^{4+} was much higher as compared to Ce^{3+} peaks indicating the behavior of film deposition towards the formation of CeO_2. The presence of Ce^{3+} oxidation state was further confirmed by the positions of satellite peak at the values of 885.0 eV[184].

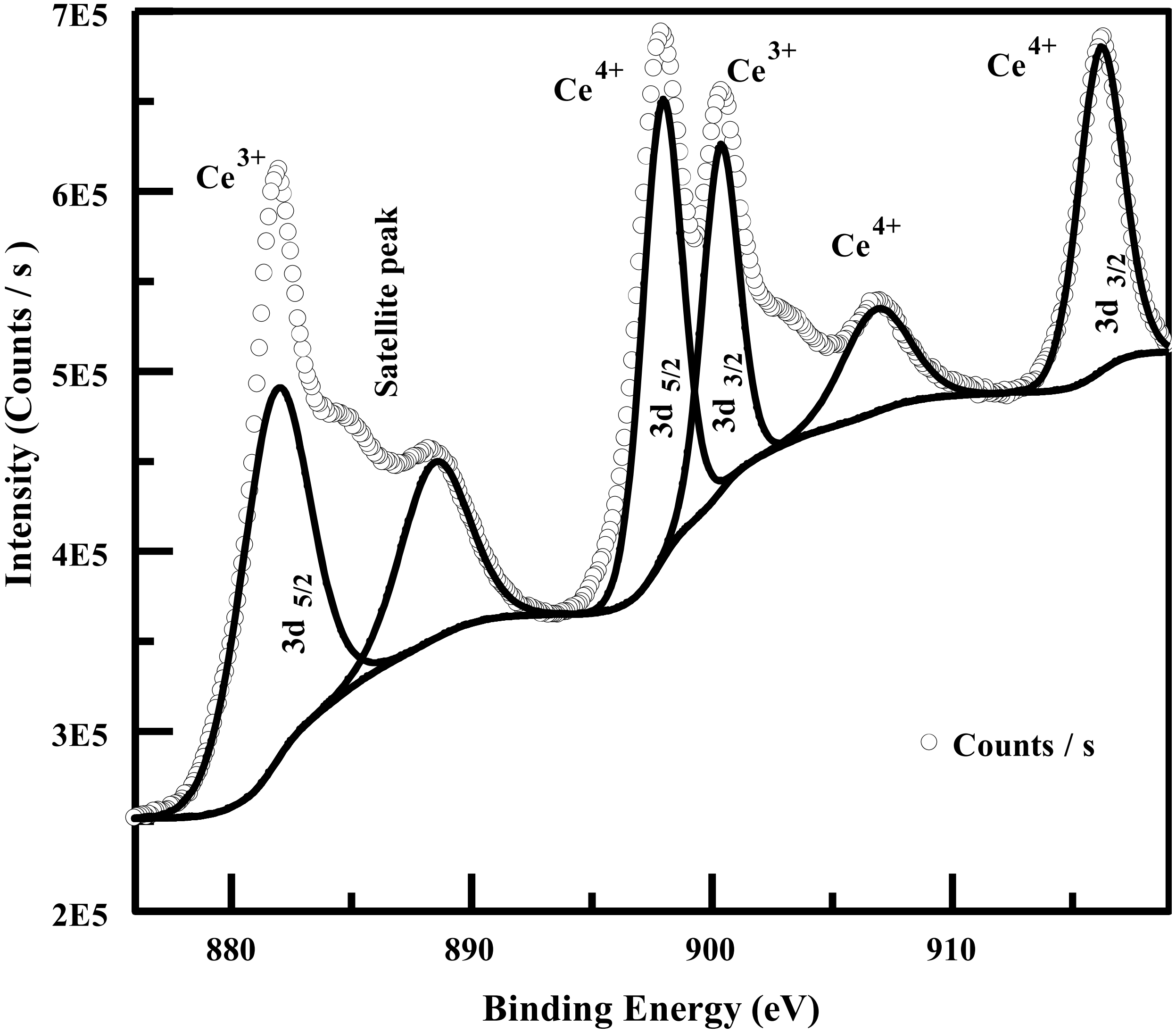

Fig 5. 26. XPS spectrum of Ce 3d core level region

The core level spectrum of Fe 2p in iron oxide is shown in the figures 5.27. It consists of spin orbit splitting of Fe 2p core levels spectra. The symmetrical peak with a binding energy of 722.9 eV was due to the Fe $2p_{1/2}$ core level. An asymmetrical peak of Fe $2p_{3/2}$ was spread over the binding energy values of 705 to 718 eV. The asymmetrical nature of this peak was due to the presence of several oxidation states of Fe. This peak was deconvoluted into three components. The component of the peak with the binding energy of 709.2 eV was due to the presence of Fe^{2+} oxidation state of iron in the Fe $2p_{3/2}$ state. Similarly, the component of the Fe $2p_{3/2}$ peak located at a binding energy value of 711.5 eV was associated with the Fe^{3+} oxidation state of iron. Its full width at half maximum value was found to be 3.4 eV. Moreover, a satellite peak was observed at a binding energy value of 715.2 eV, which was the finger print of the presence of FeO phase on the surface of the films [185]. So, the XPS analysis revealed that the iron oxide film contained both FeO and Fe_2O_3 compositions on the surface of the film.

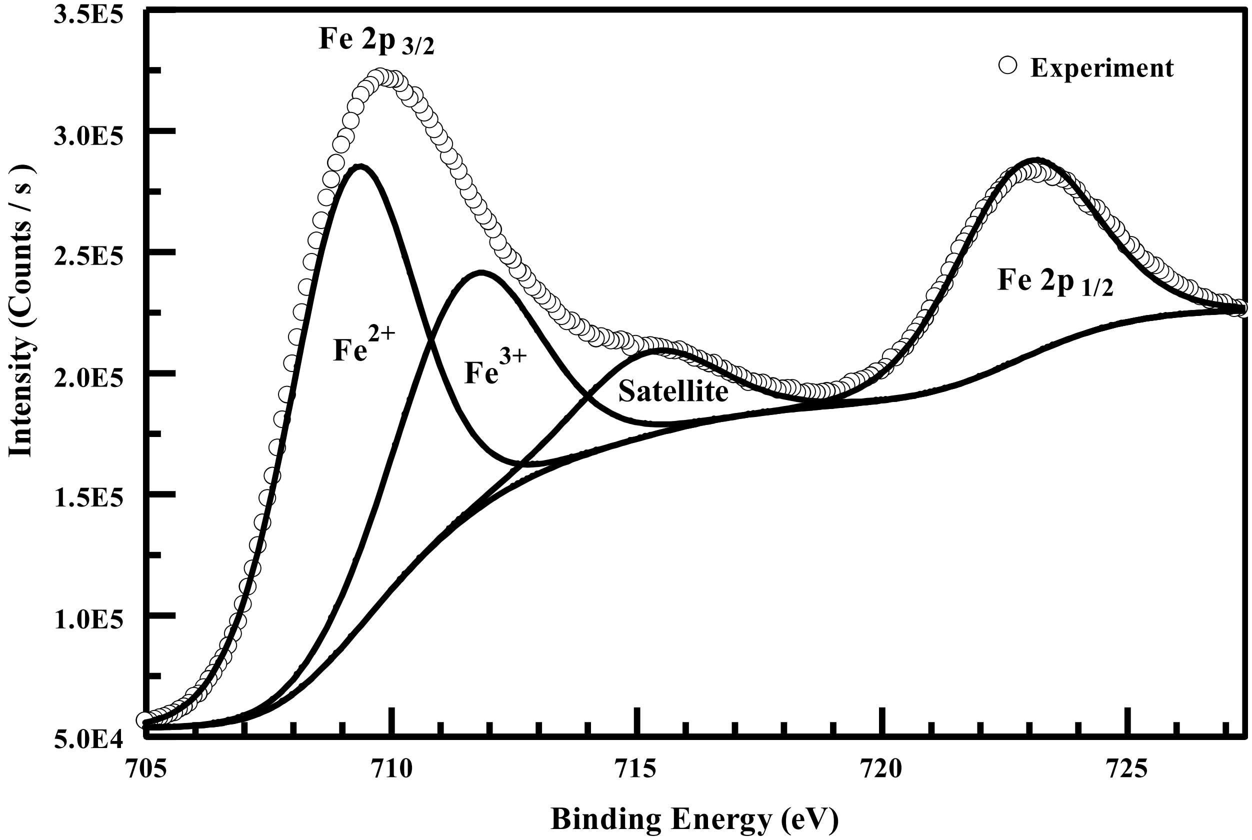

Fig 5. 27. XPS spectrum of Fe 2p core level region

The core level spectrum of Ga 2p in gallium oxide is shown in figure 5.28. Two well resolved peaks, associated with the spin orbit splitting of Ga $2p_{3/2}$ and Ga $2p_{1/2}$, were observed. The binding energies of these two peaks were found to be 1118.7 eV and 1145.5 eV, respectively, with a spin orbit splitting of 26.8 eV. The two peaks originated from the Ga-O bonding while the positions of these peaks and their splitting value confirm the Ga^{3+} oxidation state of gallium in Ga_2O_3 [75].

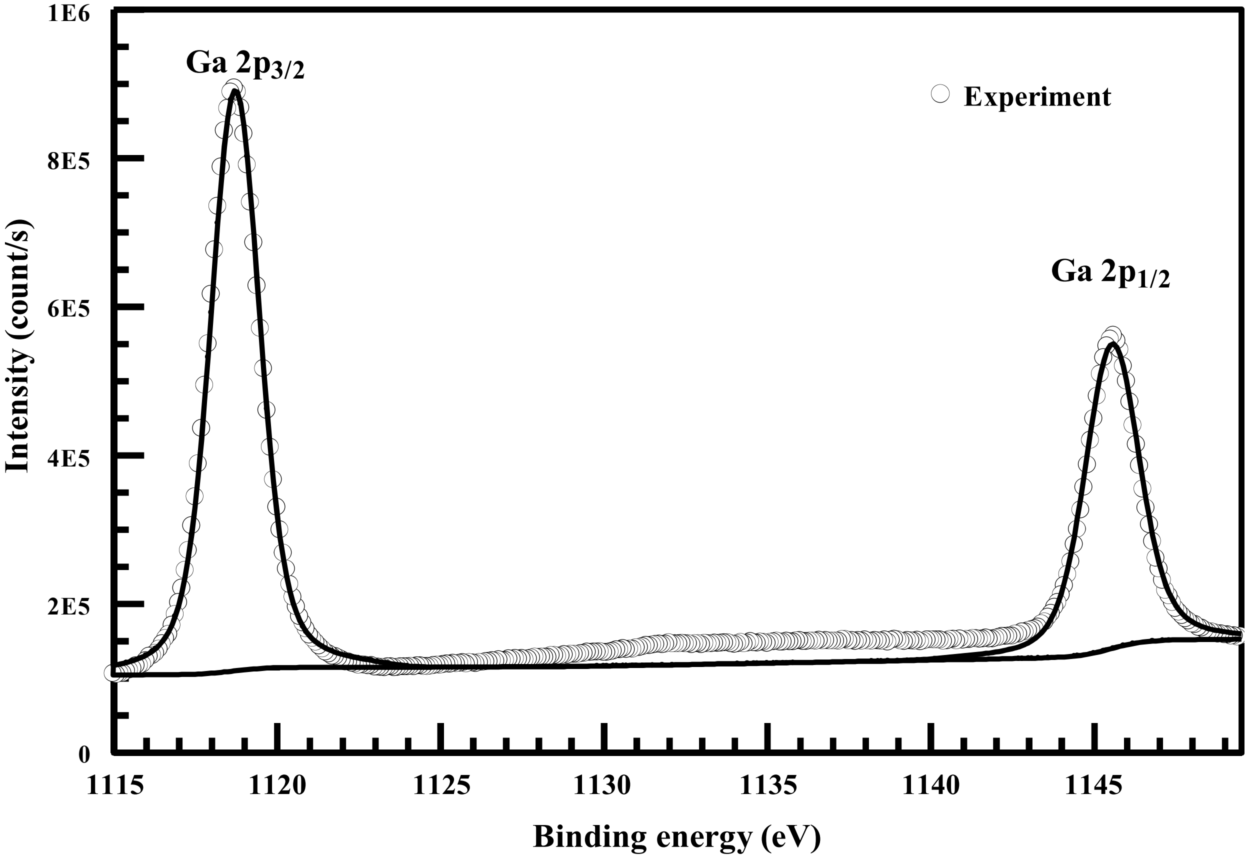

Fig 5. 28. XPS spectrum of Ga 2p core level region

The core level XPS spectrum of Hf 4f in hafnium oxide is shown in figure 5.29. The hafnium 4f spectra consist of two peaks ($4f_{5/2}$ and $4f_{7/2}$) positioned at 18.3 and 16.6 eV, respectively. The two peaks are due to the spin orbit splitting with the energy splitting value of 1.7 eV. The positions of these peaks are consistent with the values observed in previous studies within a variation of 0.1 to 0.2 eV [100–102].

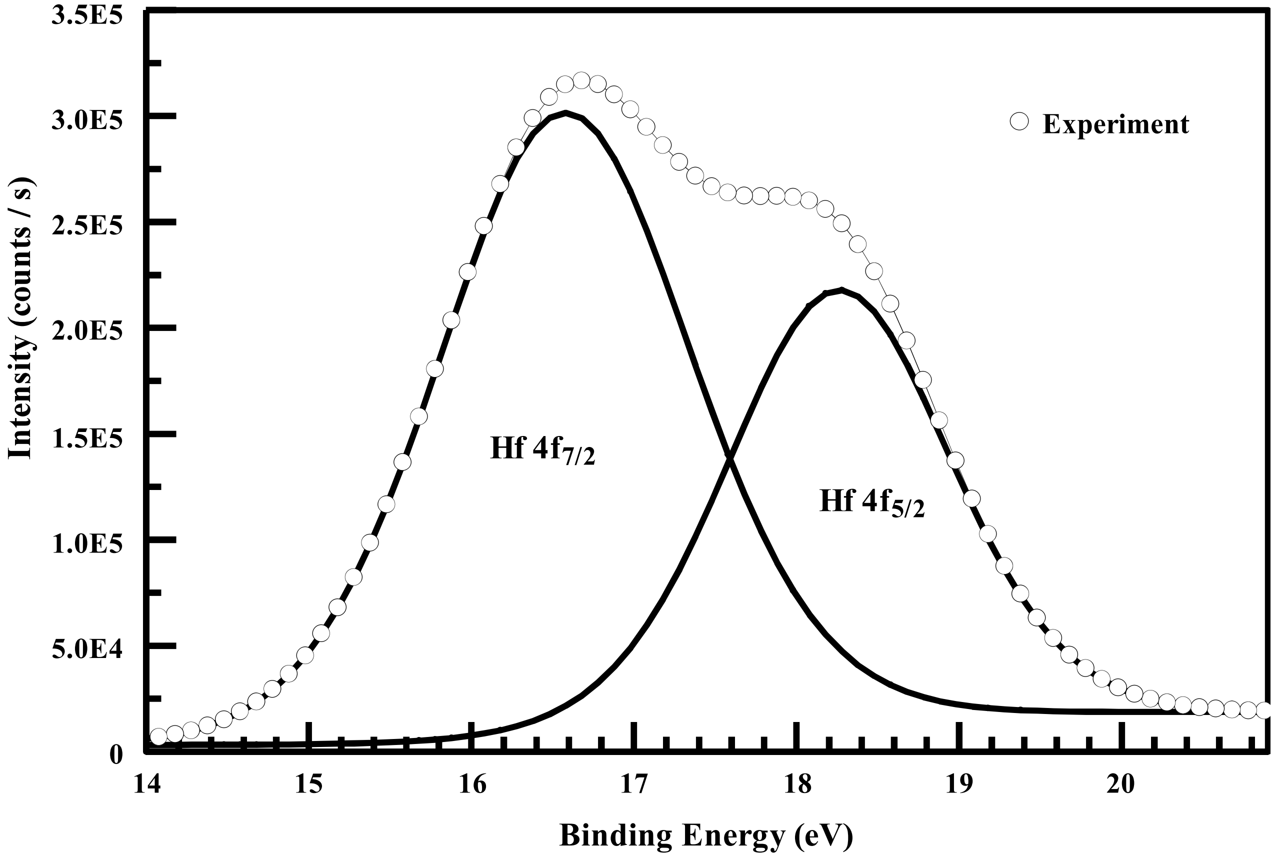

Fig 5. 29. XPS spectrum of Hf 4f core level region

The core level spectrum of Mo 3d in molybdenum oxide is shown in figure 5.30. The XPS spectrum of Mo was well resolved into two peak which were associated with the spin orbit splitting of the Mo 3d core level ($3d_{3/2}$ and $3d_{5/2}$). The value of the spin orbit splitting was calculated to be 3.2 eV which was well consistent with the value found in literature [98]. The binding energy of Mo $3d_{3/2}$ and Mo $3d_{5/2}$ were found to be 236.1 and 232.9 eV, respectively.

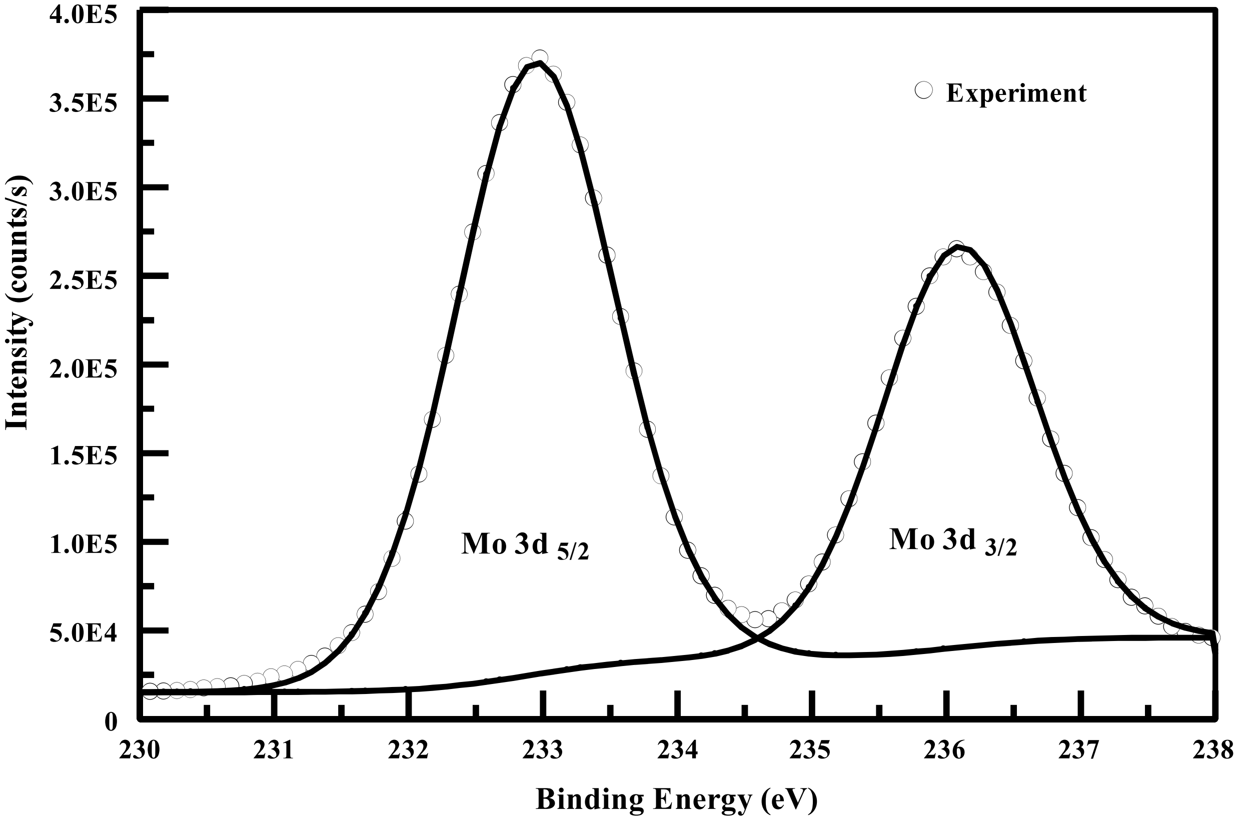

Fig 5. 30. XPS spectrum of Mo 3d core level region

The core level spectrum of Sn 3d in tin oxide is shown in figure 5.31. The spectrum consists of spin orbit components of $3d_{3/2}$ and $3d_{5/2}$ located at 495.0 and 486.6 eV, respectively. The presence of the $3d_{5/2}$ peak at 486.6 eV confirms the presence of SnO_2 [187]. The two peaks of SnO_2 were well resolved with the splitting value of 8.4 eV.

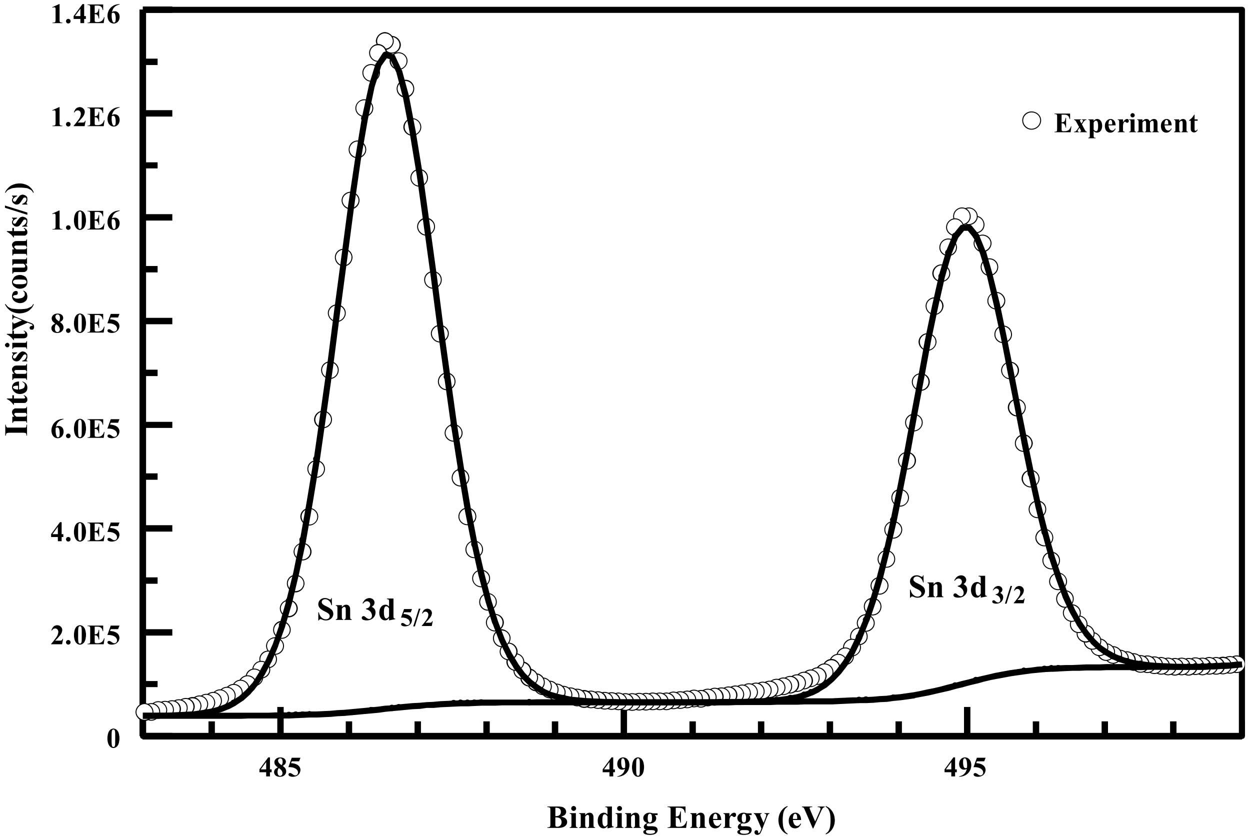

Fig 5. 31. XPS spectrum of Sn 3d core level region

The core level spectrum of Ti 2p in titanium oxide is shown in figure 5.32. It consisted of spin orbit splitting of $2p_{3/2}$ and $2p_{1/2}$ core levels of titanium. The peak position of this doublet was at 458.7eV (for $2p_{3/2}$) and 464.4 eV (for $2p_{1/2}$) with an energy splitting of 5.7 eV. The peak position of $2p_{3/2}$ was attributed to the Ti^{+4} oxidation state and it was consistent with previous studies within the variation of 0.1 to 0.4 eV [188–191].

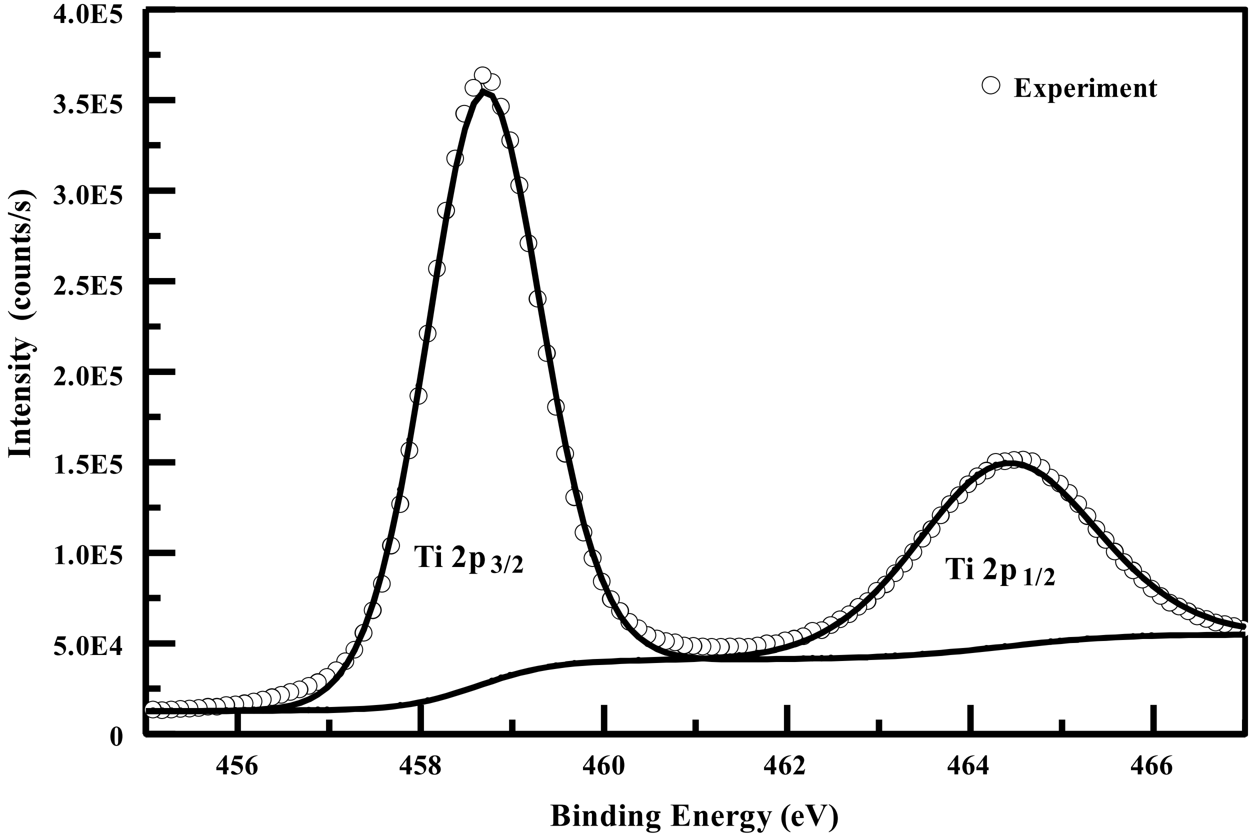

Fig 5. 32. XPS spectrum of Ti 2p core level region

The core level spectrum of W 4f in tungsten oxide is shown in figure 5.33. It consists of spin orbit splitting of 4f core level ($4f_{7/2}$ and $4f_{5/2}$), positioned at 35.7 eV and 37.8 eV, respectively. The energy splitting value of the peaks were found to be of 2.1 eV. Both $4f_{7/2}$ and $4f_{5/2}$ peaks were shifted about 4 eV towards the higher binding energies as compared to the peaks associated with elemental tungsten. This confirmed the oxide phase (WO_3) of tungsten in thin film [192,193].

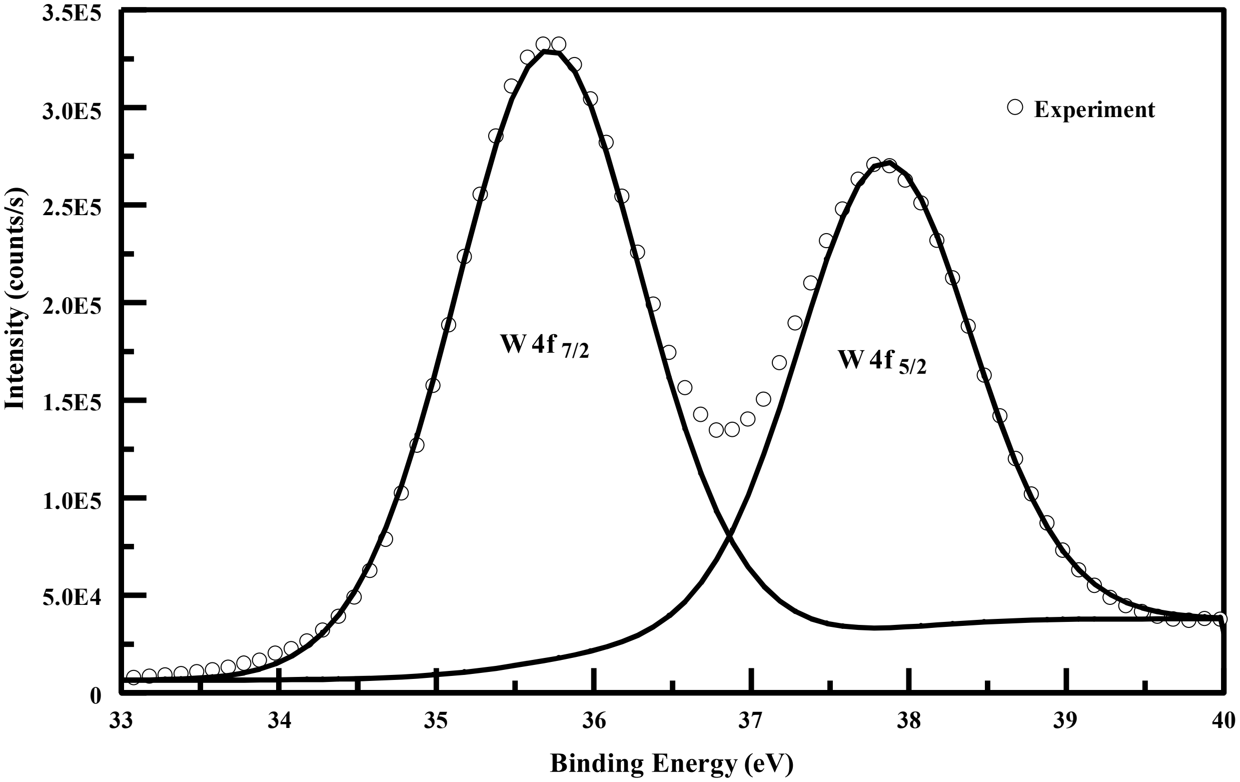

Fig 5. 33. XPS spectrum of W 4f core level region

The core level spectrum of Zn 2p in ZnO is shown in the figures 5.34. It consists of spin orbit splitting of ($2p_{3/2}$ and $2p_{1/2}$) core levels of zinc. The positions of Zn $2p_{3/2}$ and $2p_{1/2}$ peaks were found to be at 1021.8 eV and 1044.8 eV. The value of spin orbit splitting was about 23 eV which was about 0.3 eV less as compared value reported in literature [194].

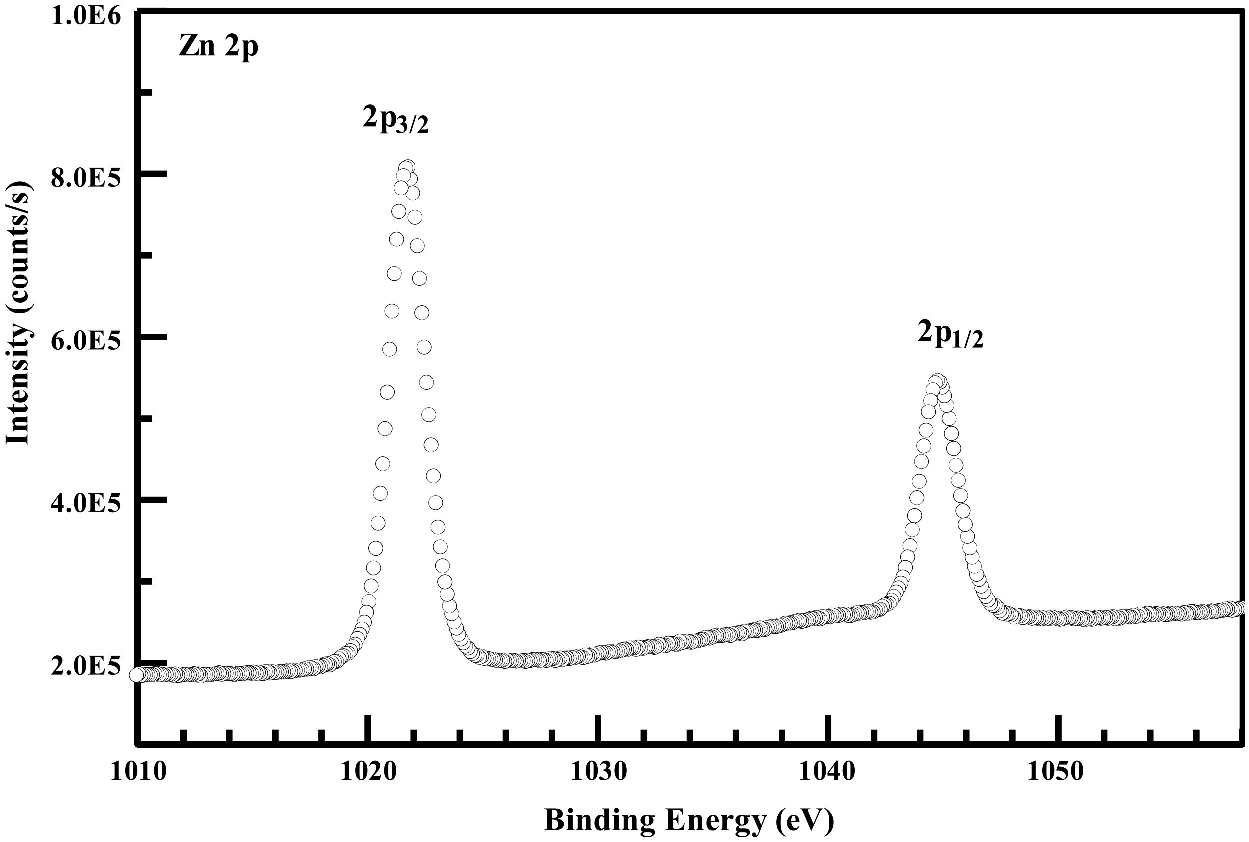

Fig 5. 34. XPS spectrum of Zn 2p core level region

The core level spectrum of Zr 3d in ZrO_2 is shown in the figures 5.35. It can be seen that the 3d spectra of Zr consist of $3d_{5/2}$ and $3d_{3/2}$ core levels located at 182.4 and 184.8 eV, respectively. The energy difference of spin orbit splitting was about 2.4 eV. It was about 0.1 less as compared to the value reported in literature, and confirms the oxidation state of zirconium to be Zr^{4+} [195].

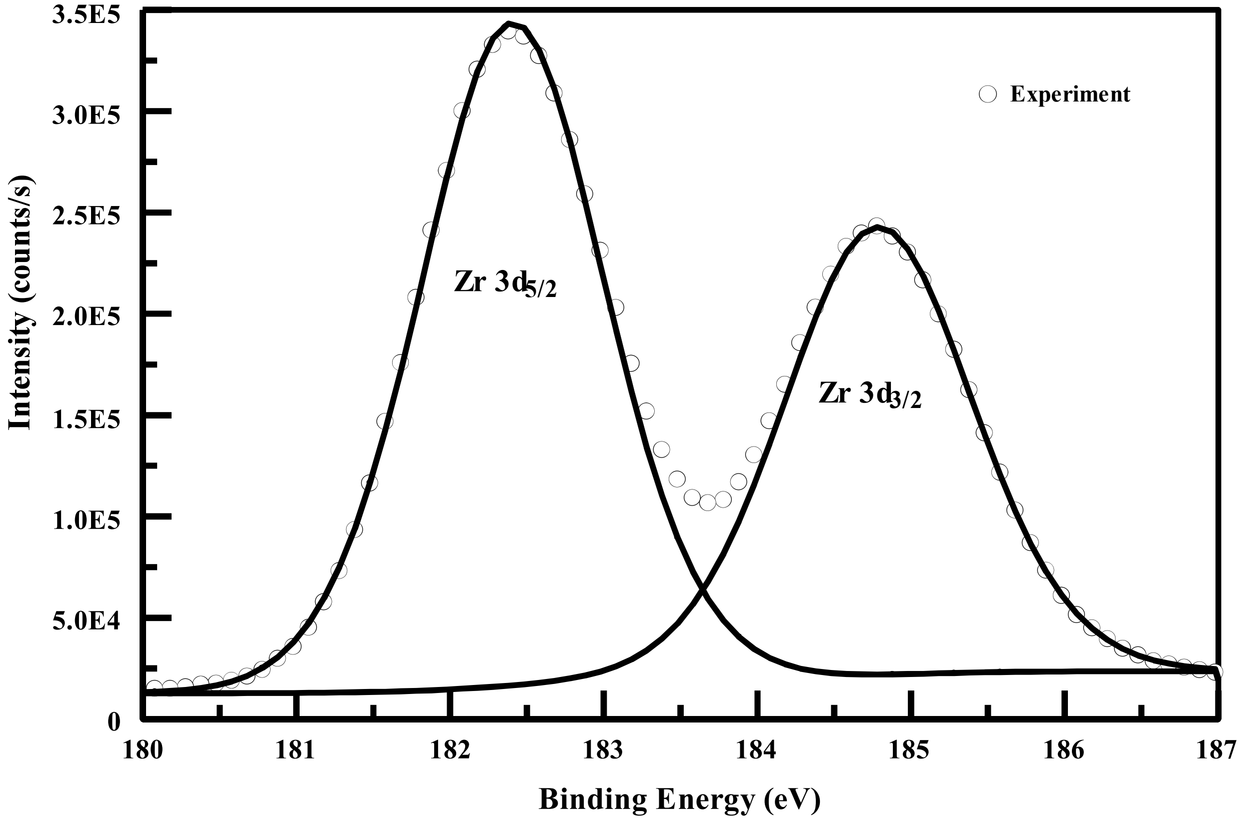

Fig 5. 35. XPS spectrum of Zr 3d core level region

In all of the metal oxide thin films, the XPS spectra of the oxygen O1s peak were deconvoluted into two components. The component associated with high binding energies was attributed to oxygen in oxygen-deficient regions (oxygen vacancies), and adsorbed oxygen. On the other hand, the component associated with the low binding energy was due to the metal oxygen bond. The XPS spectra of the films in the O 1s core level region are shown in figure 5.36. Table 5.3 shows the position of low binding energy (LBE) and high binding energy (HBE) components of oxygen 1s spectra of metal oxide thin films.

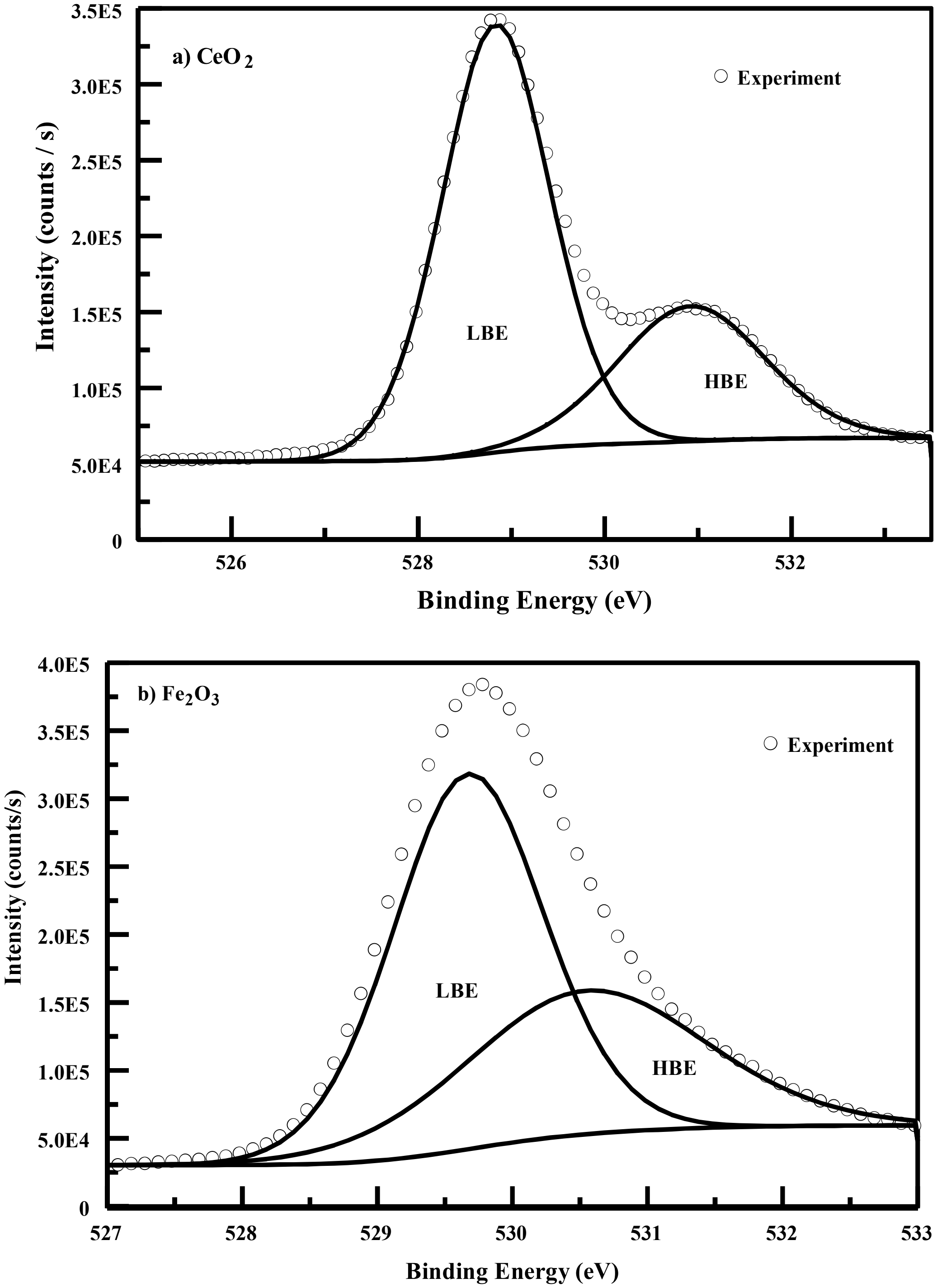
a) CeO$_2$
○ Experiment
LBE
HBE
Intensity (counts / s)
3.5E5
3.0E5
2.5E5
2.0E5
1.5E5
1.0E5
5.0E4
0
526
528
530
532
Binding Energy (eV)
b) Fe$_2$O$_3$
○ Experiment
LBE
HBE
Intensity (counts/s)
4.0E5
3.5E5
3.0E5
2.5E5
2.0E5
1.5E5
1.0E5
5.0E4
0
527
528
529
530
531
532
533
Binding Energy (eV)

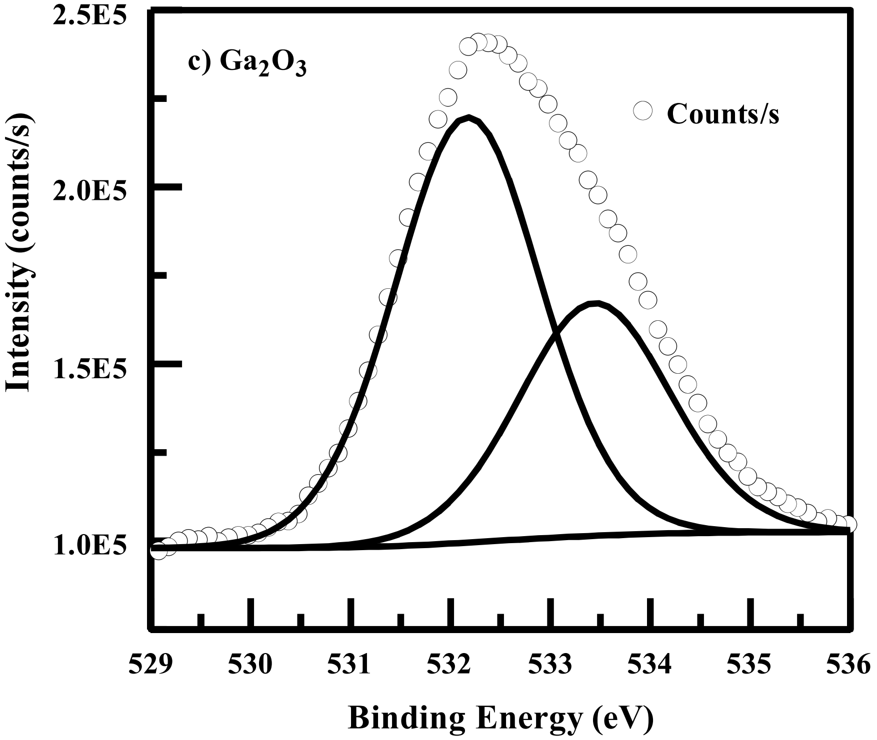
c) Ga_2O_3
Counts/s
Intensity (counts/s)
2.5E5
2.0E5
1.5E5
1.0E5
529
530
531
532
533
534
535
536
Binding Energy (eV)

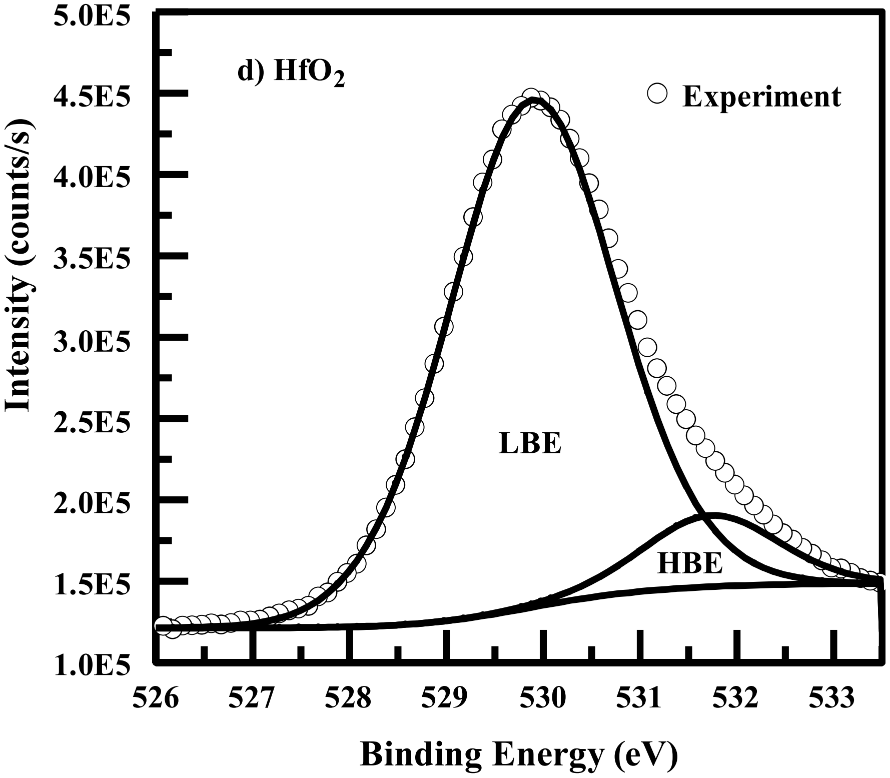
d) HfO_2
Experiment
LBE
HBE
Intensity (counts/s)
5.0E5
4.5E5
4.0E5
3.5E5
3.0E5
2.5E5
2.0E5
1.5E5
1.0E5
526
527
528
529
530
531
532
533
Binding Energy (eV)

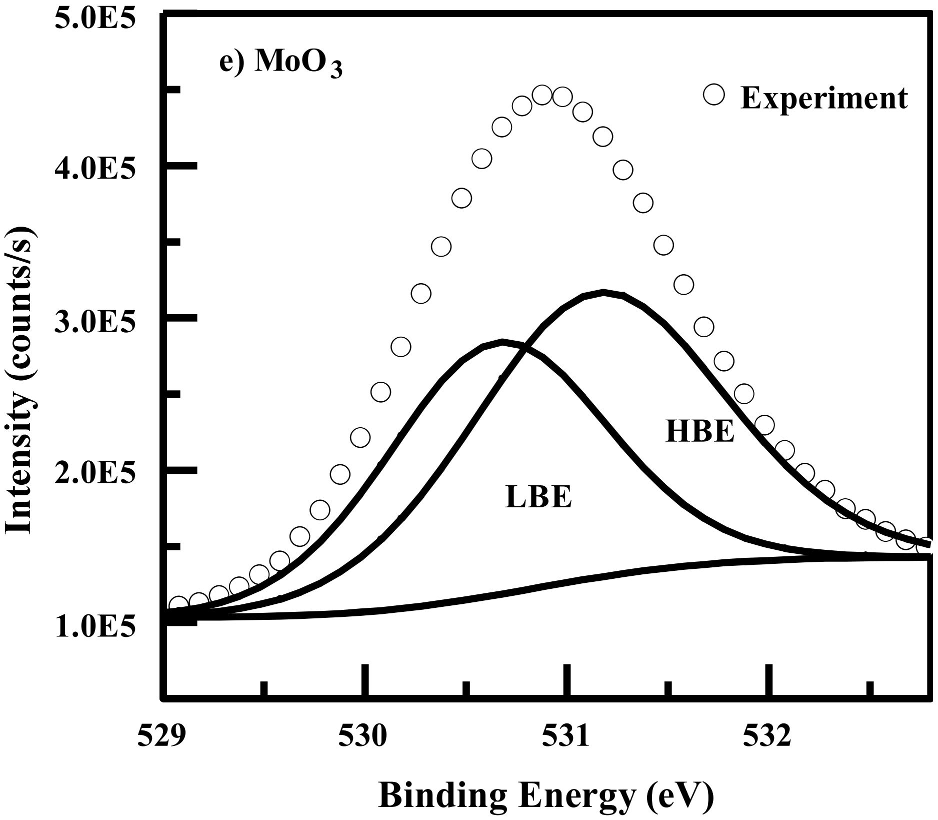
e) MoO $_3$
Experiment
HBE
LBE
Intensity (counts/s)
5.0E5
4.0E5
3.0E5
2.0E5
1.0E5
529
530
531
532
Binding Energy (eV)

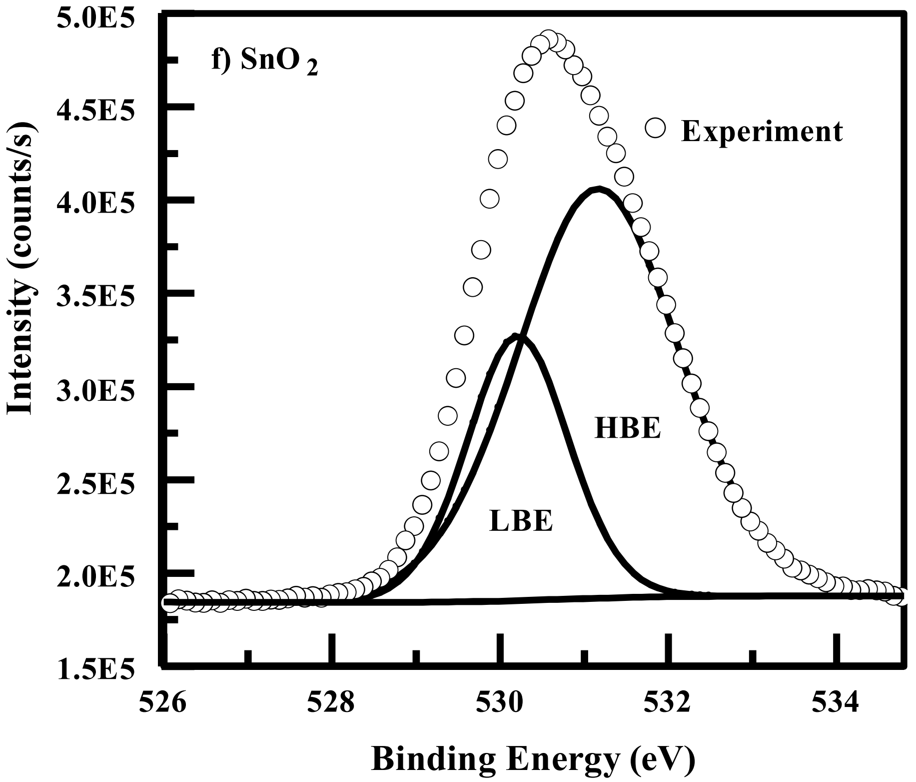
f) SnO $_2$
Experiment
HBE
LBE
Intensity (counts/s)
5.0E5
4.5E5
4.0E5
3.5E5
3.0E5
2.5E5
2.0E5
1.5E5
526
528
530
532
534
Binding Energy (eV)

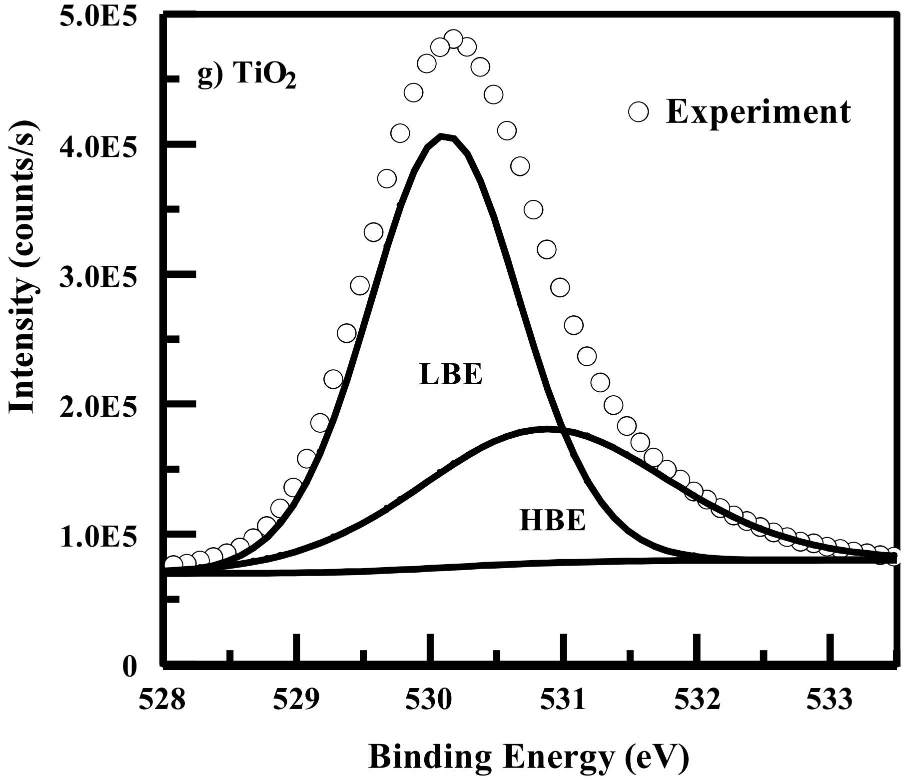
g) TiO$_2$
Experiment
LBE
HBE
Intensity (counts/s)
5.0E5
4.0E5
3.0E5
2.0E5
1.0E5
0
528
529
530
531
532
533
Binding Energy (eV)

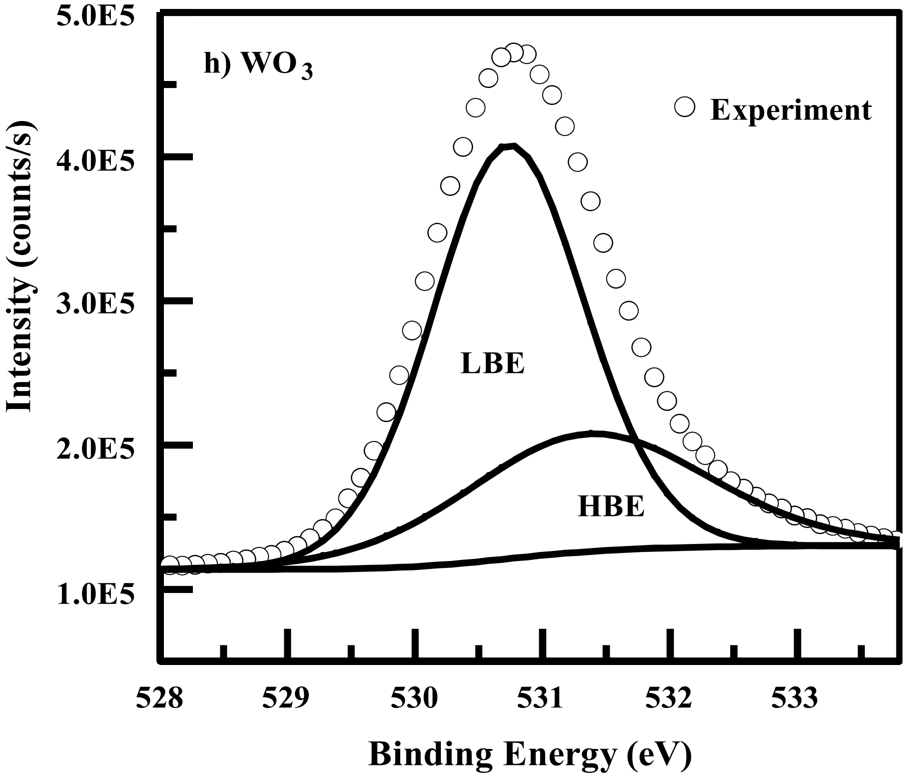
h) WO$_3$
Experiment
LBE
HBE
Intensity (counts/s)
5.0E5
4.0E5
3.0E5
2.0E5
1.0E5
528
529
530
531
532
533
Binding Energy (eV)

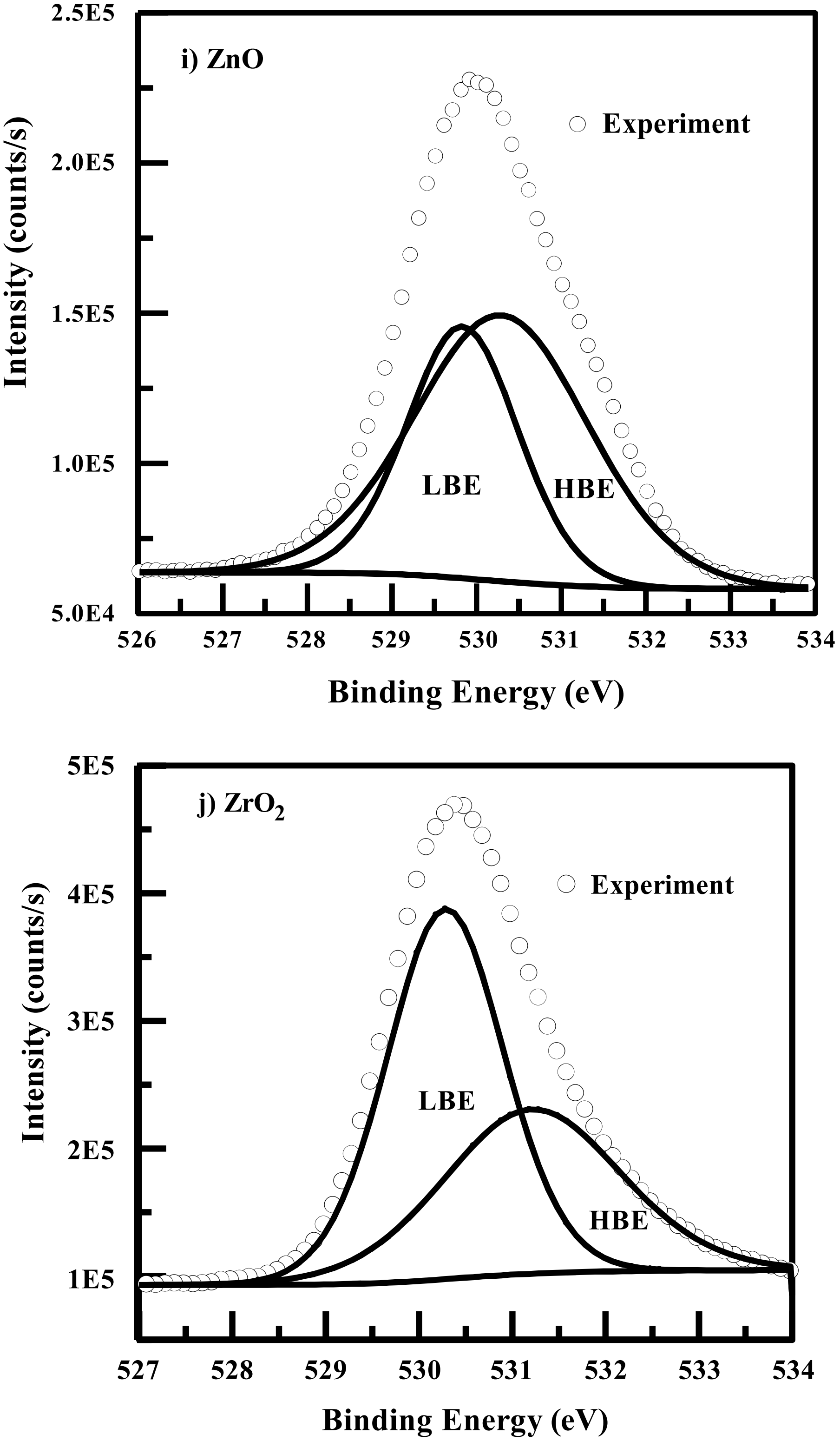

Fig 5. 36. XPS spectra of O 1s core level regions in metal oxide thin films

Metal oxide	**Low binding energy LBE (eV)**	**High binding energy HBE (eV)**
CeO_2	528.9	530.9
Fe_2O_3	529.7	530.5
Ga_2O_3	531.3	532.3
HfO_2	529.9	531.7
MoO_3	530.7	531.1
SnO_2	530.2	531.2
TiO_2	530.1	530.9
WO_3	530.7	531.3
ZnO	529.8	531.7
ZrO_2	530.3	531.2

Table 5. 3 Binding energy positions of O1s in metal oxides

CHAPTER 6

Electroreflectance Analysis

6.1 Theoretical Modeling

An important goal in performing the electroreflectance measurements is to utilize a comprehensive optical model which can successfully correlate the structures in optical spectra to critical points in the band structure. A modulated response is more precise than its absolute counterpart in a sense that it always originates in the neighborhoods of the critical points. On the other hand, the absolute spectrum spreads over the extended region of Brillouin zones. Moreover, modulation by an electric field always lowers the symmetry of the crystal [167]. So, the analysis of a modulated spectrum is more efficient in describing the optical response of the material. It requires a modulation spectroscopic model which can perform a proper line shape analysis of the spectra.

A sophisticated model, in performing the line shape analysis of the modulated spectrum, was proposed by Aspnes [150]. This model relates the change in the reflected spectra of a material, due to the applied electric field, with the critical points of the material. The mathematical form of such modulation is described by Aspnes and it is defined by [150]

$$\frac{\Delta R}{R} = \mathrm{Re}\left[\sum_{k=1}^{b} \frac{C_k e^{i\theta_k}}{\left(E - E_{gk} + i\Gamma_k\right)^p}\right] \tag{6.1}$$

where, $\frac{\Delta R}{R}$ is the normalized electroreflectance spectrum, p is associated with the movement of electron e in two dimensional or three dimensional system. The parameter C determines the amplitude of the electroreflectance (ER) spectra, E_g is the energy of the critical point, θ is a phase factor which gives the distribution of the upper and lower parts of the peak across the zero crossing, Γ is a broadening parameter related to the spectral sharpness of the peak, and b refers to the number of components for which the ER spectrum is fitted

6.2 Interpretation of Fitting Parameters

The parameters involved in eq. (6.1) have important physical significance. The value of p relies on the dimension in which free electrons move. For example, it has a value of 2.5 for a three dimensional structure while it has a value of 3 for a two dimensional structure [196].

The parameter C of equation (3.36) determines the amplitude of the resulted electroreflectance spectra. The normal value of the amplitude is typically of the order of 10^{-5} to 10^{-4}. However, it varies and strongly depends upon the crystal nature and surface properties of the material. Noises in the spectrum are below 10^{-6} [156]. The amplitude factor C only provides information about the magnitude of the intensity of the spectrum. It does not contribute the line shape analysis of the spectra.

E_g described in equation (6.1) is associated with the energy of a critical point, such as the band gap energy or exciton energy. Contrary to the consideration of local maxima or minima in the absolute spectra as the critical point locations, the positions of the modulated electroreflectance spectra are correlated with the Van Hove singularities. So, a modulated electroreflectance spectrum has basic advantage over the absolute spectrum in a way that the location of the critical point can be calculated with less uncertainty over the Brillouin zone [197]. An important advantage of using Aspnes model in calculating the critical points of a material is that, regardless of the value of other parameters involved in the model, it always provides the band gap around the extrema of the electroreflectance spectrum.

The shape of the spectra near the critical point is described by the phase factor θ. It gives the distribution of the upper and lower half of a peak across the zero crossings. It is associated with the ratio of the absolute values of maximum and minimum amplitudes of a spectrum. The important thing, in doing the line shape analysis of the electroreflectance spectrum, is to find the correct phase angle for which the line shape matches with the experimental spectrum. Once the phase factor is known, one can find the transition energies and the broadening parameter directly from the fit.

The spectral sharpness of the peaks, observed in an electroreflectance spectrum, is described in terms of the full width at half maximum value or broadening parameter Γ of eq. (6.1). It provides important pieces of information about the material structure like defects in the material, lattice strain or dislocations [198]. Normally the value of the broadening parameter in electroreflectance spectra varies from 50 meV to 100 meV for crystalline structures and greater than 100 meV for amorphous ones.

The least square fitting method was employed to fit the experimental spectrum with the Aspnes third derivative (ATD) model. The Levenberg–Marquardt Algorithm (LMA) based least square fitting method was employed, which was compatible with Mathematica software. It has the advantage over other fitting algorithm in a sense that it can find a solution even if its starting value is far from an extremum. The number of components used in the fitting depends on the number of observed peaks in the ER spectrum. Moreover, they can be increased to obtain the best-fit of the ER spectrum. However, the intensity and energy values of the components should be taken into account that they are associated with real optical transitions of a material. The energy separation value of the components should be taken into consideration during the fitting procedure. Normally, in the fitting procedure, if two components were used to resolve a peak, with the energy separation less than or close to the thermal energy, they can be considered as a single component [60], since the resolution of such peaks at room temperature is beyond the limits of ER spectroscopy. The resolution of an ER peak using more than one component might be due to its asymmetric nature.

6.3 Electroreflectance Analysis of Cerium Oxide (CeO_2)

Figure 6.1 shows the electroreflectance spectrum of CeO_2. A 5-V square wave signal of frequency 100 Hz was applied to the surface of the sample to create the necessary modulation, and the spectrum collection time was set to 10 s/nm. The amplitude of the ER spectrum was found to be of the order of 10^{-6}, which indicated the fact the obtained spectrum was with in the low field regime. The characteristics of the observed peak in the ER spectrum was found by fitting the experimental spectrum with the ATD model. A single peak was observed in the ER spectrum with the energy locations at about 3.33 eV. The rest of the fitting parameters are presented in the table below figure 6.1

The band gap of CeO_2 was calculated using both experimental and theoretical methods. Experimentally, CeO_2 was fabricated in thin film form using spray pyrolysis [60], RF sputtering [15,61], thermal oxidization [62], and e-beam evaporation [63]. In these deposition processes, the obtained structure of CeO_2 was the cubic fluorite, where the band gap values (found with the help of Tauc method [15,61,63] or scanning tunneling spectroscopy [62]) varied from 3.1 to 3.53 eV. On the other hand, the hexagonal dendrite like structure and cubic fluorite micro pillows like structure were obtained using thermal oxidation and solvo-thermal methods, respectively [61,199]. The band gaps of these structures were computed using the Tauc plot method, with values of the band gaps of 3.52 and 2.8 eV, respectively. Theoretically, the values of the band gaps were calculated using first principle calculations studies within the frame work of density functional theory. Several theoretical approaches were used in this regard. These include generalized gradient approximation (GGA), GGA with hubbard potential [200,201], GGA with PBE approximation [202,203], hybrid density functional and local spin density functional approach (LSDA) with Slater exchange correlation [203]. The value of the band gap, calculated using these approaches, varied from 1.6 to 3.3 eV. Moreover, the nature of the band gap, as found by GGA approximation, was indirect (between F and $\Gamma \rightarrow \Gamma$) [201]. The value of the band gap as found by electroreflectance analysis, that is 3.33 eV, was about 0.02 eV less than that found by Mansilla *et al.* on the basis of Tauc method [63]. Moreover, it is well matched with the value predicted by Hay *et al.* on the basis of hybrid density functional approach [203].

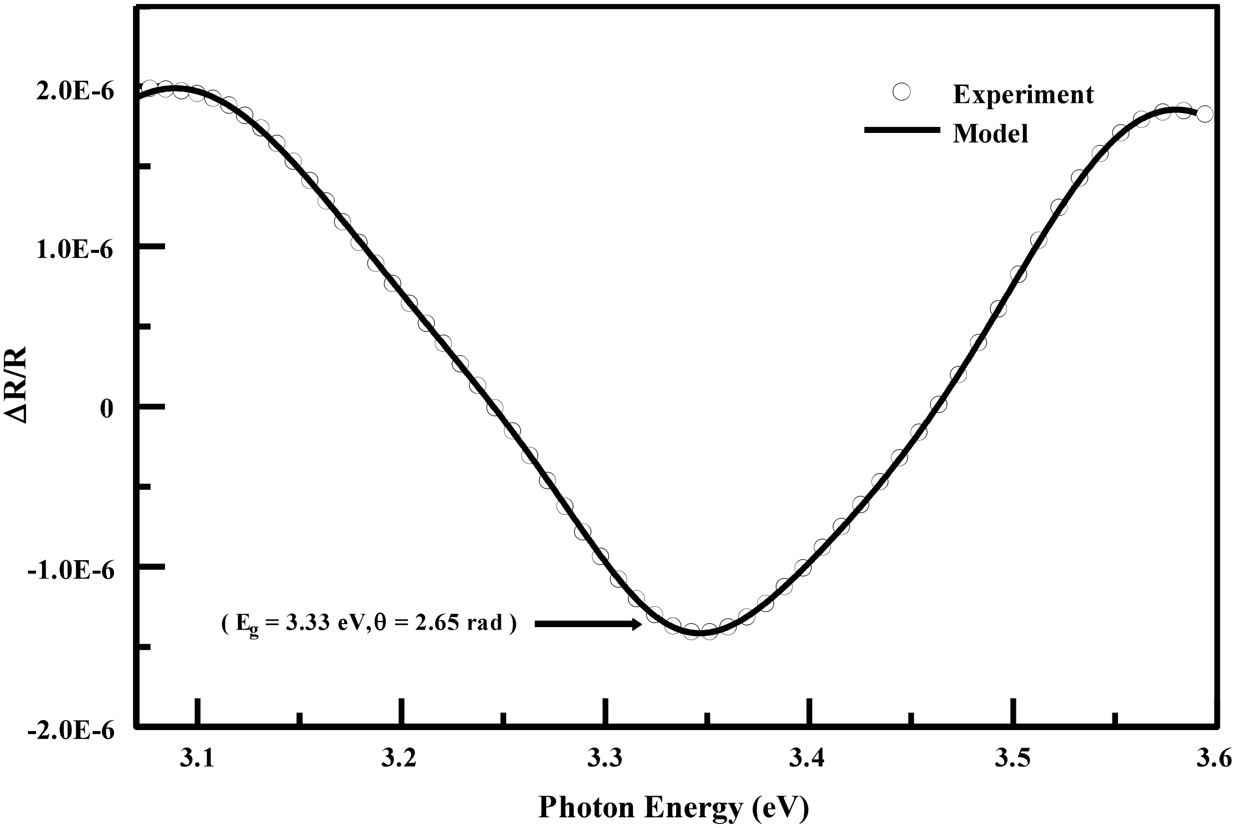

Fig 6. 1. Electroreflectance spectrum of cerium oxide thin film.

The open circles represent the experimental spectrum, and the continuous curve is the theoretical fit obtained using the ATD model. The best fit parameters are given in the table below

Best-Fit Parameters for CeO_2

C	-1.2×10^{-6}
E_g (eV)	3.33
θ (radians)	2.65
Γ (meV)	127

6.4 Electroreflectance Analysis of Iron Oxide (Fe_2O_3)

Figure 6.2 shows the electroreflectance spectrum of Fe_2O_3. A 10-V square wave signal of frequency 100 Hz was applied to the surface of the sample to create the necessary modulation, and the spectrum collection time was set to 10 s/nm. The amplitude of the ER spectrum was found to be 10^{-5} , which indicated the fact the obtained spectrum was with in the low field regime. The characteristics of the observed peak in the ER spectrum was found by fitting the experimental spectrum with the ATD model. Three peaks were observed in the ER spectrum with energy locations at 2.28 eV and 2.41 eV. The rest of the fitting parameters are presented in the table below figure 6.2

Experimentally, iron oxide thin films were fabricated by many techniques. These include e-beam evaporation [64], sol gel [65], spray pyrolysis [66], anodization [204], successive ionic layer adsorption and reaction (SILAR) [67], wet chemical method [68,69], hydrothermal [205], atomic layer deposition [206], laser ablation [207], and reactive evaporation [18]. Regarding the crystal structures, α-Fe_2O_3 and γ-Fe_2O_3 thin films showed almost the same indirect band gap values of 1.9 eV (α-Fe_2O_3) and 1.8 eV (γ -Fe_2O_3) as predicted by Emery *et al.* [206], while the maghemite phase (γ-Fe_2O_3) showed a higher direct band gap value of 2.9 eV [66]. Numerous studies were conducted on α-Fe_2O_3 because of its stable nature. The value of the band gap for α-Fe_2O_3 was calculated using the Tauc plot in these studies with a direct band gap value that varied from 2.18 to 2.97 eV [18,64–68], while the indirect band gap varied from 1.75 to 2.05 eV [57, 219, 220, 222–224]. A more precise calculation of the nature and the band gap value of α-Fe_2O_3 was performed by Gilbert *et al.*[69] on the basis of soft x-ray spectroscopy, who found an indirect nature of the band gap with a value of 2.2 eV for bulk as well as for nano scale particle of α-Fe_2O_3 [69]. Theoretically, the band gap of iron oxide was calculated on the basis of density functional approach with local density approximation [208,209], generalized gradient approximation (GGA) [210], GGA plus onsite Coulomb interaction (GGA+U) [211] and with hybrid density functional theory [212]. Different predictions were made on the nature and the band gap value of α-Fe_2O_3. For example Guo *et al.*[209] and Pozun *et al.* [212] computed the direct and indirect band gap values of α-Fe_2O_3 on the basis of screened Coulomb hybrid density functional approach. The computed band gap values in these studies were 2.56 and 2.90 eV for the direct ($\Gamma \rightarrow \Gamma$) transition, and 1.95 and 2.4 eV for the indirect (between R and $\Gamma \rightarrow$ M [209]) transitions, respectively. On the other hand, theoretical calculations on the basis of GGA+U approach were performed by Liao *et al.* [210] and Xia *et al.* [211]. They found band gap values of 2.0 eV and 2.05 eV, respectively. In the electroreflectance spectrum, the high transition at a value of 2.28 eV was close to the value of the indirect band gap of 2.2 eV as measured by Gilbert *et al*. on the basis of soft x-ray spectroscopic analysis [69]. A difference of 0.08 eV might be due to the large band gap characteristic of thin films as compared to bulk form. The low intense ER peaks located at 2.34 eV and 2.41 eV might be attributed to the transitions of electrons from valence band to the deep in the conduction band. The peak at 2.34 eV was about 0.01 eV less as compared to the deep level transition of 2.35 eV observed by Thomas *et al*.[213] on the basis of PL studies. On the other hand, the peak at 2.41 eV was about 0.15 eV less than the optical transition predicted by Pozun *et al.* [212] on the basis of hybrid density functional theory.

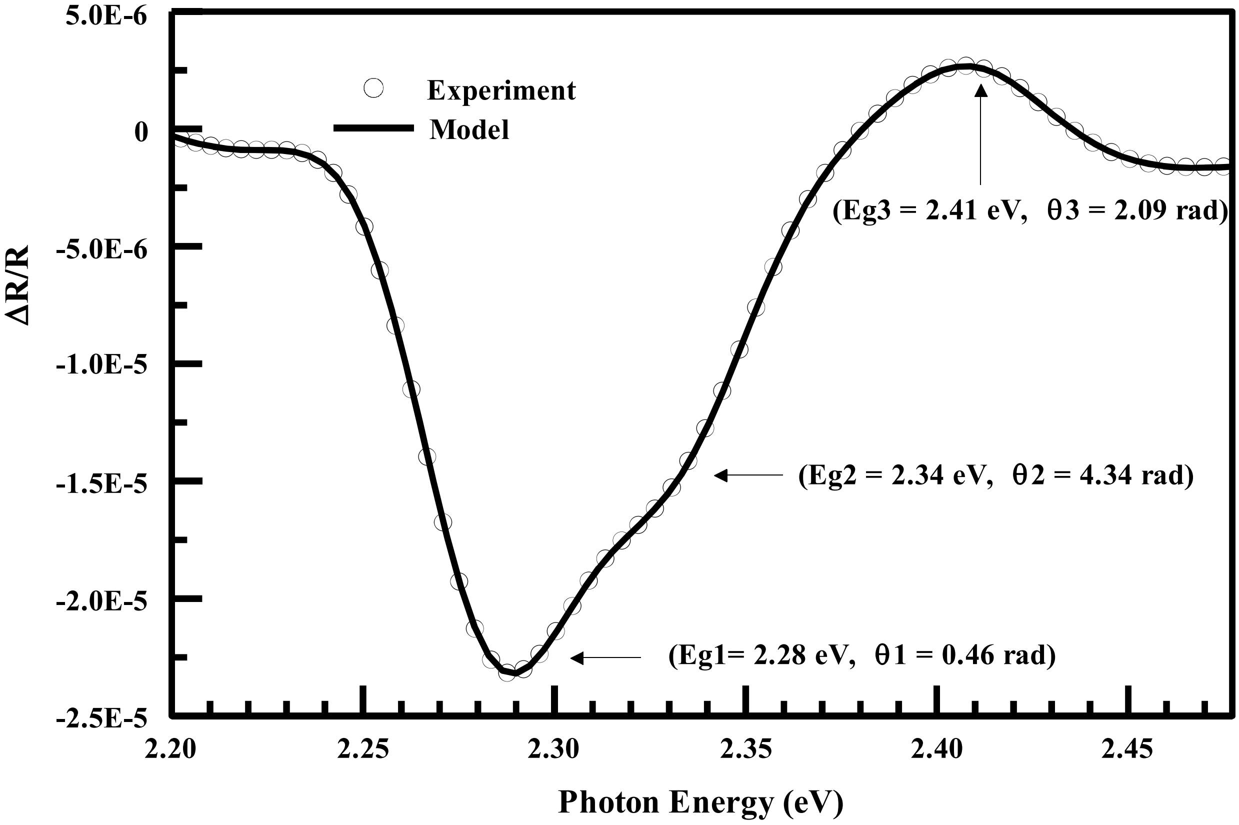

Fig 6. 2. Electroreflectance spectrum of iron oxide thin film.

The open circles represent the experimental spectrum, and the continuous curve is the theoretical fit obtained using the ATD model. The best fit parameters are given in the table below

C_1	-2.30×10^{-05}	**C_2**	-1.45×10^{-05}	**C_3**	1.80×10^{-06}
E_{g1} (eV)	2.28	**E_{g2} (eV)**	2.34	**E_{g3} (eV)**	2.41
θ_1 (radians)	0.46	**θ_2 (radians)**	4.34	**θ_3 (radians)**	2.09
Γ_1 (meV)	53	**Γ_2 (meV)**	53	**Γ_3 (meV)**	56

6.5 Electroreflectance Analysis of Gallium Oxide (Ga_2O_3)

The electroreflectance (ER) spectrum of Ga_2O_3 in shown in figure 6.3. A 10-V square wave signal of frequency 100 Hz was applied to the surface of the sample to create the necessary modulation, and the spectrum collection time was set to 10 s/nm. It can be seen from the figure that the ER signal had amplitude of $\sim 10^{-5}$, which confirms that the signal was in the low field regime. In order to find out the characteristics of the peaks observed in the ER spectrum, the experimental spectrum was fitted using the Aspnes third derivative (ATD) model. The fitting parameters are shown below figure 6.3. The fundamental absorption edge was located at the value of 4.03 eV, with a FWHM value of 346 meV. Another transition was located at 3.38 eV, with a FWHM of 197 meV.

The value of the band gap for Ga_2O_3 has been reported by many authors using both experimental and theoretical methods. Experimentally, the band gap value depends upon the fabrication technique, the nature of the synthesized product (thin films, bulk form), and the method of determining the band gap. Previously, Ga_2O_3 films were fabricated by many techniques. These include floating zone method [21,22], pulsed laser deposition [4,72], spray pyrolysis [23,73], atomic layer deposition and plasma enhanced atomic layer deposition [25,74,75], sol gel method [76], aqueous solution deposition [77], metal organic vapor phase epitaxy [78], and e-beam evaporation [79]. The nature of the band gap predicted by the Tauc plot method, in all studies, was direct. This method does not provide information about any other optical transitions involved. The value of the band gap determined for Ga_2O_3 thin films varied from 4.51 to 5.30 eV. In contrast to the experimental studies, where the direct transition was the only dominant transition predicted, the theoretical analysis of Ga_2O_3 predicted both direct (along the $\Gamma\text{–}\Gamma$ symmetry point) and indirect transitions (along the Γ-M symmetry point) in Ga_2O_3. The values of the optical transitions were different in these studies. This might be due to the different theoretical approaches. For example, the band structure calculation of β–Ga_2O_3 performed using projected augmented plane wave potential (PAW) method predicted the direct and indirect transitions at values of 4.88 and 4.84 eV, respectively [214]. On the other hand, the band structure calculation, on the basis of plane-wave pseudo potential approach within generalized gradient approximation (GGA) predicted the direct and indirect transitions at 4.40 and 4.37 eV [215]. Our value of the band gap (E_{g2}) matches closely with the experimental value determined by Chen *et al.* [216] who used the Tauc plot method and considered the direct transitions with a value of 3.99 eV. Moreover, the transition observed at 3.38 eV (Eg_1) was quite close to the gap state of 3.3 eV found by Schmitz *et al*. [71] with the help of electron energy loss spectroscopy (EELS), which was associated with the intrinsic defects in Ga_2O_3.

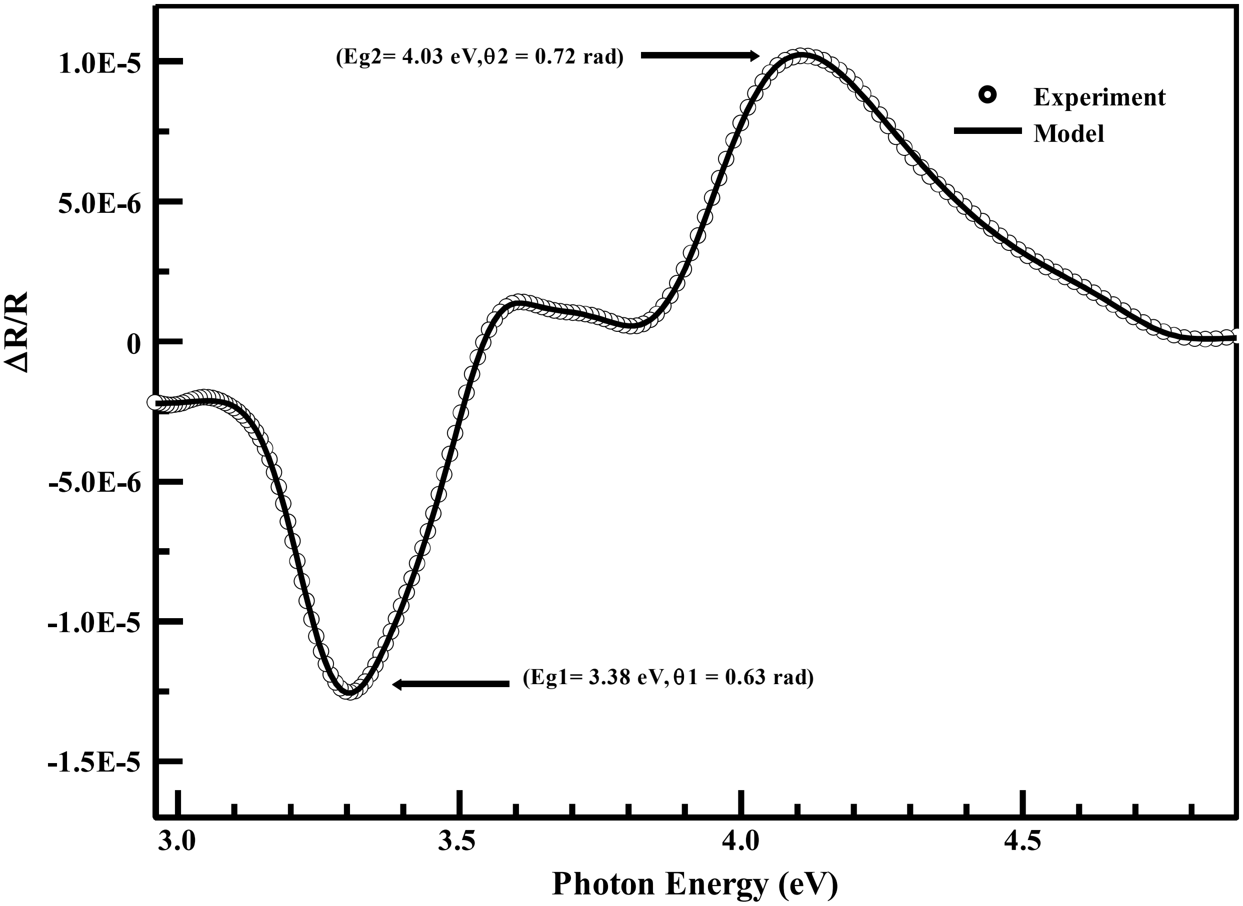

Fig 6. 3. Electroreflectance spectrum of gallium oxide thin film.

The open circles represent the experimental spectrum, and the continuous curve is the theoretical fit obtained using the ATD model. The best fit parameters are given in the table below

C_1	-1.4×10^{-6}	**C_2**	1.56×10^{-6}
E_{g1} (eV)	3.38	**E_{g2} (eV)**	4.03
θ_1 (radians)	0.63	**θ_2 (radians)**	0.72
Γ_1 (meV)	197	**Γ_2 (meV)**	346

6.6 Electroreflectance Analysis of Hafnium Oxide (HfO_2)

The ER spectrum of HfO_2 is shown in the figure 6.4. A 40-V square wave signal of frequency 100 Hz was applied to the surface of the sample to create the necessary modulation, and the spectrum collection time was set to 10 s/nm. It can be seen from figure 6.4 that the ER signal had amplitude of $\sim 10^{-5}$. Moreover, no significant oscillations were observed above the second extremum. This confirms that the ER signal was in the low field regime with no indications of Franz Keldysh oscillations. The characteristics of the observed peaks in the ER spectrum was found by fitting the experimental spectrum with ATD model. The fitting parameters are shown in the table below figure 6.4. The ER spectrum revealed a maximum at a value of 5.15 eV with a FWHM value of 242 meV. Another extremum in terms of a minimum was observed at a value of 5.49 eV with a FWHM value of 188 meV. The two peaks were associated with the transitions in HfO_2 thin films.

In literature, both experimental and theoretical techniques were employed to calculate the band gap of HfO_2 thin films. Experimentally, HfO_2 thin films were fabricated by many techniques. These include reactive molecular beam epitaxy [84,90,217], e-beam evaporation [86,218], reactive electron beam co-deposition [219], radio frequency magnetron sputtering [8,85,89,91], DC magnetron sputtering [83,220] atomic layer deposition [7,31,80,93,221–223], pulsed laser deposition [92], plasma assisted reactive pulsed laser deposition [87,88] and microwave hydrothermal method [224]. The band gaps of the films were calculated mostly using the Tauc method. In some studies, the nature of transitions were found to be direct, where the band gap values varied from 5.45 eV to 5.82 eV [84–92]. On the other hand, some studies considered the transitions to be indirect, where the band gap values varied from 3.31 eV to 5.82 eV [7,8,85,218,220,223,225–227]. Besides the Tauc technique, other experimental techniques were used to determine the band gap of HfO_2 thin films. These include electron energy loss spectroscopy (EELS), spectroscopic ellipsometry (SE), and internal photoemission (IPE) methods. The band gap determined by EELS varied from 5.15 to 5.7 eV [31,80–82]. The band gap of HfO_2 was found to be 5.82 eV with the help of SE [83], and 5.6 eV with the help of IPE [93]. In theoretical calculations, the nature of transitions and the values of the band gaps relied upon the crystal structure and the theoretical approaches used. For example, the cubic structure of HfO_2 showed a direct transitions ($X \rightarrow X$), with a band gap value of 3.65 eV predicted on the basis of generalized gradient approximation (GGA) [228], and 5.69 eV predicted on the basis of GGA plus exchange Coulomb interaction method [229,230]. On the other hand, some theoretical studies predicted an indirect nature of transitions ($X \rightarrow \Gamma$) for the cubic phase with band gap values of 3.2 and 3.16 eV [28,81]. The other phases of HfO_2, like tetragonal and monoclinic, showed an indirect nature of transitions. For the tetragonal structure, the transition was along the $A \rightarrow \Gamma$ symmetry points with band gap values of 3.44 eV and 3.75 eV [28,228], or from the $\Gamma \rightarrow M$ symmetry points with a band gap value of 3.8 eV [81]. The difference in the nature of transitions occurs due to different theoretical approximations, GGA or local density approximation (LDA), used in the studies. For the case of the monoclinic structure, the transitions were from $\Gamma \rightarrow B$ symmetry points with band gap values of 3.47 and 3.5 eV [28,81]. Yang *et al.* [231] calculated the variations in the band gap value of the cubic structure using different functional theories. They found direct transitions along $X \rightarrow X$ symmetry points, with band gap values that varied significantly from 3.8 to 6.11 eV. In the results of our ER spectrum, the component at 5.49 eV was quite close to the direct band gap value of 5.5 eV as determined by EELS [31,80] and internal photoemission [93] and was close to the value of 5.45 eV as determined by XPS spectrum analysis [222]. Moreover, it was only about 0.25 eV less than the value computed by Li *et al.* on the basis of GGA plus Coulomb exchange correlation method [229].

The component at 5.15 eV can be attributed to the indirect transition. It was only 0.1 eV less than the indirect transition computed by Cheynet *et al.* based on EELS analysis [140].

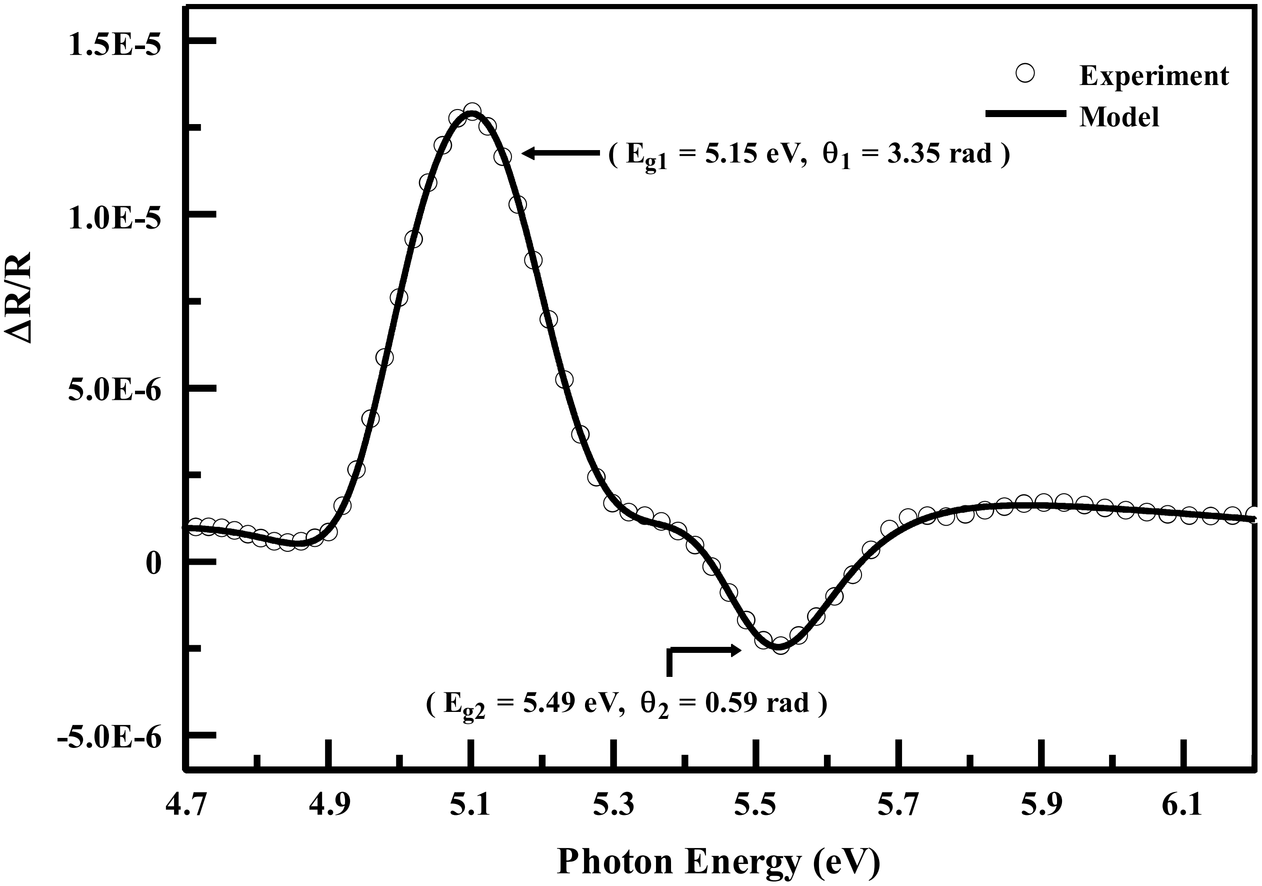

Fig 6. 4. Electroreflectance spectrum of hafnium oxide thin film.

The open circles represent the experimental spectrum, and the continuous curve is the theoretical fit obtained using the ATD model. The best fit parameters are given in the table below

C_1	1.3×10^{-5}	**C_2**	2.6×10^{-5}
E_{g1} (eV)	5.15	**E_{g2} (eV)**	5.49
θ_1 (radians)	7.71	**θ_2 (radians)**	3.05
Γ_1 (meV)	242	**Γ_2 (meV)**	188

6.7 Electroreflectance Analysis of Molybdenum Oxide (MoO_3)

Figure 6.5 shows the electroreflectance spectrum of MoO_3 thin films. It was obtained by applying a 10-V and 100 Hz square wave perturbation to the sample. The data collection time was set to 10 s/nm. The characteristics of the observed peak in the ER spectrum was found by fitting the experimental spectrum with the ATD model. The fitting parameters are shown in the table below figure 6.5. The ER spectrum revealed a single transition at an energy location of about 3.76 eV. The amplitude of transition was about 1×10^{-5}, which confirms that the spectrum was within the low field regime.

The band gap of MoO_3 thin films was calculated using both experimental as well as theoretical methods. Experimentally, the nature and value of the band gap depends upon the fabrication technique, crystal structure and the synthesized form. For example, the hexagonal crystal structure of MoO_3 obtained in the powder form showed a direct band gap of 3.14 to 3.20 eV [232,233]. On the other hand, the hexagonal structure of MoO_3 obtained in thin film form showed an indirect nature of the band gap with a value of 3.16 eV [234]. On the basis of crystal structure, the orthorhombic structure of MoO_3 (α-MoO_3) was studied extensively in both experimental and theoretical ways. Experimentally, α-MoO_3 thin films were fabricated using spray pyrolysis [94], thermal oxidation [95], laser assisted evaporation [96], thermal evaporation [97], and pulsed laser deposition [98]. The method of finding the band gap in these studies was the Tauc method with direct band gap values ranging from 3.15 to 3.98 eV, while the indirect band gap value ranged from 2.71 to 3.15 eV. The amorphous structure of MoO_3 was fabricated using sol gel dip coating [235] and RF sputtering [236]. The nature of the transition in the amorphous form of the films was direct as predicted by the Tauc method with band gap values of 3.67 and 3.73 eV. Besides the experimental studies, the theoretical analysis of the optical transitions in MoO_3 was performed using Density functional theory (DFT) with the help of full potential linearized augmented plane wave (FPLAPW) [237] and FPLAPW with modified Becke-Johnson (mBJ) functional [238], generalized gradient approximation with PBE exchange corelation functional approach [239], van der Waals functional approach [240], and tight binding linear muffin tin orbital (TB-LMTO) approach [241]. The transitions found in FPLAPW, GGA and van der Waals functional approach studies were indirect with band gap values from 0.74 to 2.81 eV. GGA with PBE functional approach predicted a direct nature of transitions ($\Gamma \rightarrow \Gamma$) with a band gap value of 2.76 eV. In our ER spectrum, the peak located at a value of 3.76 eV was close to the value of 3.67 eV as predicted by Fan [236] and can be attributed to the direct band gap transition.

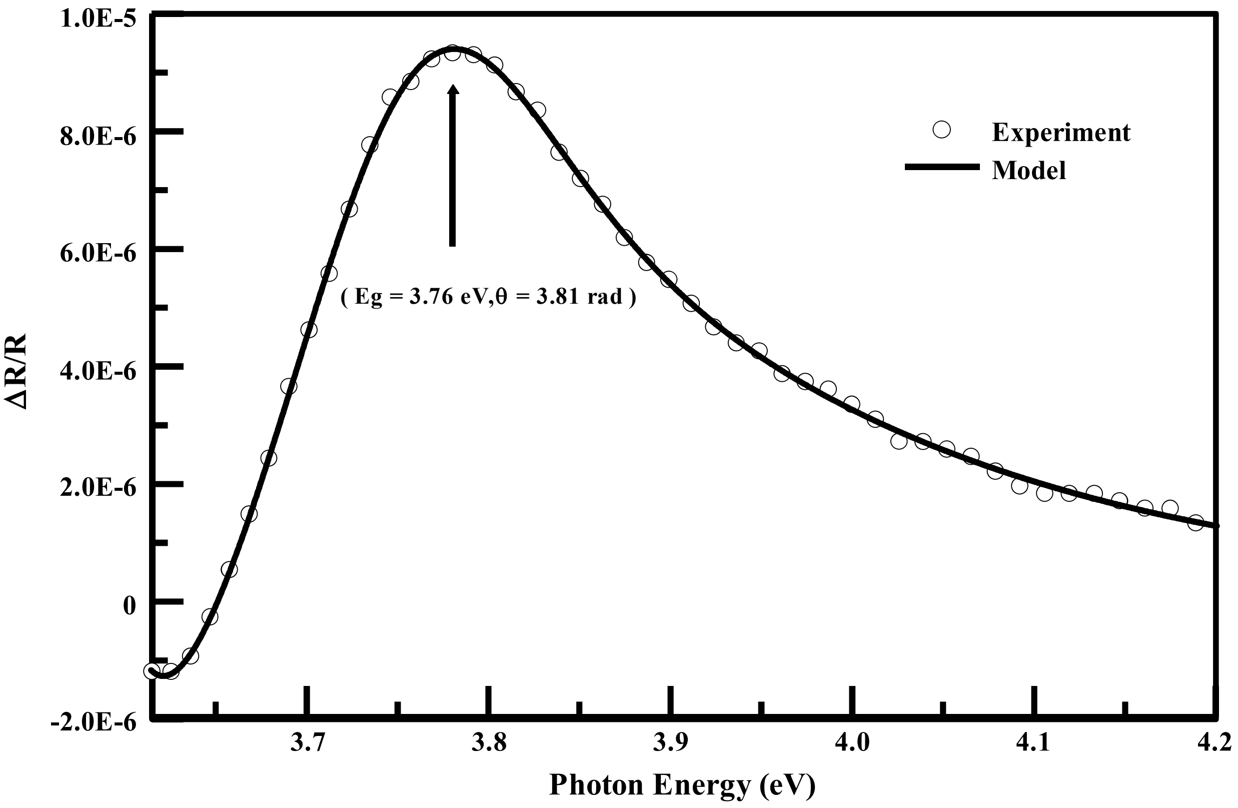

Fig 6. 5. Electroreflectance spectrum of molybdenum oxide thin film.

The open circles represent the experimental spectrum, and the continuous curve is the theoretical fit obtained using the ATD model. The best fit parameters are given in the table below

Best-Fit Parameters for MoO_3

C	9.6×10^{-6}
E_g (eV)	3.76
θ (radians)	3.81
Γ (meV)	178

6.8 Electroreflectance Analysis of Tin Oxide (SnO_2)

Figure 6.6 shows the electroreflectance spectrum of SnO_2 thin film. It was obtained by applying a 10-V and 100 Hz square wave perturbation to the sample. The data collection time was set to 10 s/nm. The characteristics of the observed peak in the ER spectrum was found by fitting the experimental spectrum with the ATD model. The fitting parameters are shown in the table below figure 6.6. The ER spectrum revealed a single transition at an energy location of 3.85 eV. The amplitude of transition was about 2×10^{-5} which confirms the spectrum was within the low field regime.

Experimentally, SnO_2 thin films were synthesized by many techniques. These include electron beam evaporation [99], chemical vapor deposition [100], chemical spray pyrolysis [101], RF sputtering [102,103], hydrothermal [104] and chemical bath deposition [105]. The band gap in these studies were found with the help of Tauc method. All of these studies predicted a direct nature of the band gap with values that varied from 3.22 to 4.22 eV. Theoretically, the band gaps of SnO_2 were found within the frame work of density functional theory using different approximations. These include generalized gradient approximations GGA [242,243], GGA+PBE [244], GGA+mbJ [243], GGA+TB+mbJ [242], coherent potential approximation (CPA) [245], or hybrid functional approaches like B3LYP [246], and HSE06 [244]. The nature of transitions in these studies depend on the crystal structure. For example, the rutile structure of SnO_2 exhibited a direct nature of transitions ($\Gamma\rightarrow\Gamma$) with band gap values that varied from 0.77 to 3.3 eV [242,243,245,246]. On the other hand, the fluorite and tetragonal structures predicted an indirect nature of transitions ($W\rightarrow\Gamma$ [243] and $k\rightarrow\Gamma$ [244], respectively). The band gap value for the fluorite structure was 2.76 eV [243]. On the other hand, the band gap value for the tetragonal crystal structure was found to be 2.55 eV with the help of

GGA+PBE, while it was found to be 4.14 eV with the help of HSE functional approach [244]. In our ER analysis, the transition at a value of 3.85 eV was 0.03 to 0.05 eV less than the value of the band gap obtained by Tauc method [100,101]. Moreover, it was about 0.18 eV higher than the band gap value computed by Ganose *et al*. [247], using PBE0 based hybrid density functional approach.

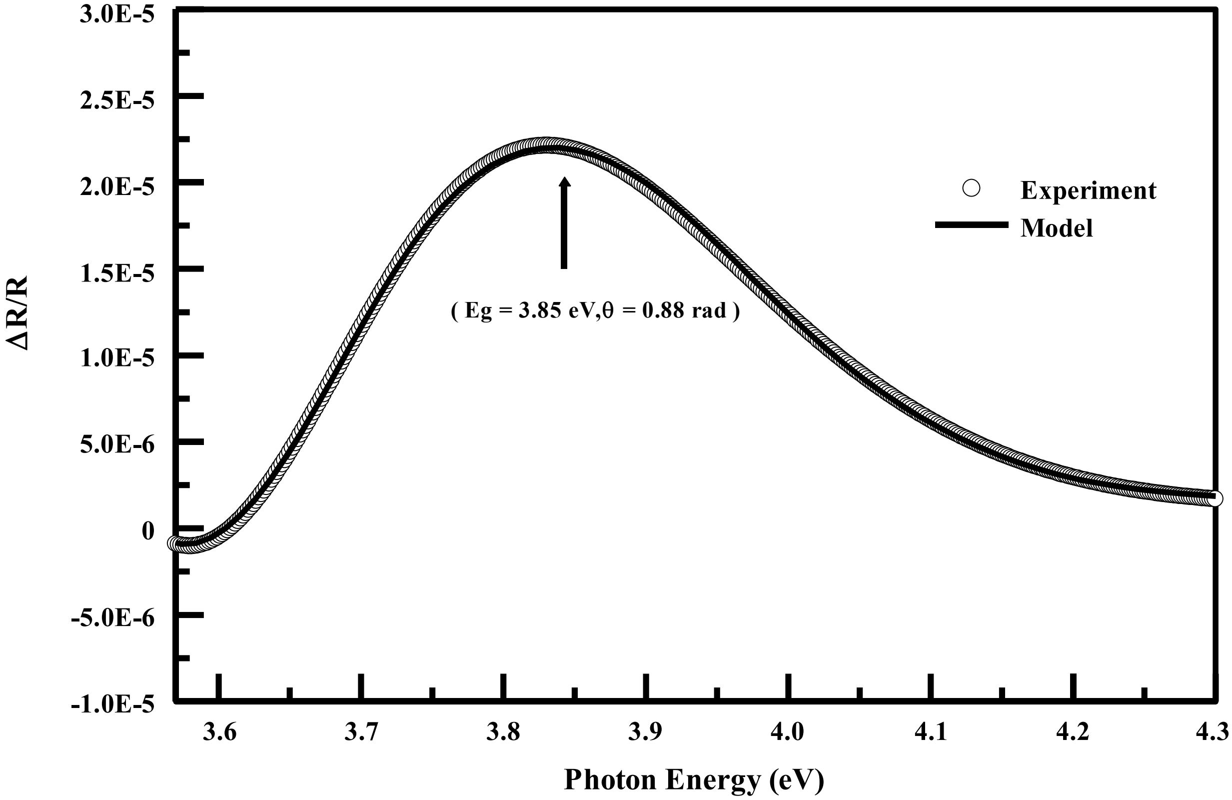

Fig 6. 6. Electroreflectance spectrum of tin oxide thin film.

The open circles represent the experimental spectrum, and the continuous curve is the theoretical fit obtained using the ATD model. The best fit parameters are given in the table below

Best-Fit Parameters for SnO_2

C	2×10^{-5}
E_g (eV)	3.85
θ (radians)	0.88
Γ (meV)	363

6.9 Electroreflectance Analysis of Titanium Oxide (TiO_2)

Figure 6.7 shows the electroreflectance spectrum of TiO_2. A 10-V square wave signal of frequency 100 Hz was applied to the surface of the sample to create the necessary modulation, and the spectrum collection time was set to 10 s/nm. It can be seen from figure 6.7 that the ER signal had an amplitude of about 10^{-5}, which indicated the fact that the obtained spectrum was with in the low field regime. The characteristics of the observed peak in the ER spectrum was found by fitting the experimental spectrum with the ATD model. The observed ER spectrum consists of two transition with the energy locations at 3.45 and 3.46 eV. The rest of the fitting parameters are presented in the table below figure 6.7

Experimentally, TiO_2 thin films were synthesized by many techniques. These include sol gel dip coating [106,248,249], RF sputtering [107,250–252], DC magnetron sputtering [108,253], plasma enhanced atomic layer deposition [254], ion assisted electron beam evaporation [255], successive ionic layer adsorption and reaction (SILAR) method [109], pulsed laser deposition [88], and spray pyrolysis deposition [110]. The method of calculating the band gap in these studies was the Tauc method with band gap values ranging from 2.95 to 3.5 eV for indirect transitions [107,108,248,249,251–256]. On the other hand, the direct band gap values varied from 3.1 to 3.7 eV [106–110]. Theoretically, the nature as well as the values of the band gap depend on the phase as well as theoretical calculation methods being employed. For example, the nature of the band gap for the rutile phase of TiO_2 was direct ($\Gamma \rightarrow \Gamma$) as predicted by PBE-GGA [257], LDA and LDA+U^d+U^p [258] approaches with the band gap values found to be 1.85, 2.0 and 3.24 eV, respectively. The nature of transitions in the anatase phase was predicted differently by different authors. For example, Landermann *et al.* found an indirect nature of transition ($\Sigma \rightarrow \Gamma$) based on DFT-PBE and PBE-HSE06 functional theories with the band gap values of 1.9 eV (DFT-PBE) and 3.60 eV (DFT-HSE06) [259]. A similar indirect nature of transition ($M \rightarrow \Gamma$) in anatase TiO_2 was found by Zhang *et al.* on the basis of DFT with Hartee Fock approximation with a band gap value of about 3.54 eV [260]. Similarly, Asahi *et al.* predicted a direct nature of transition ($\Gamma \rightarrow \Gamma$) in anatase TiO_2, with a band gap value of 2.0 eV, based on full potential linearized augmented plane wave (FP-LAPW) method [261]. In our electroreflectance analysis, the transition at a value of 3.46 eV was close to the direct band gap value of 3.50 eV as predicted by Kumar *et al*. [108]. Moreover, it was about 0.14 eV less than the direct band gap transition as predicted by More *et al.*[109]. On the other hand, the transitions located at a value of 3.45 eV was attributed to the defect transitions and consistent with the value found by Mathews *et al.*[248] on the basis of Tauc method.

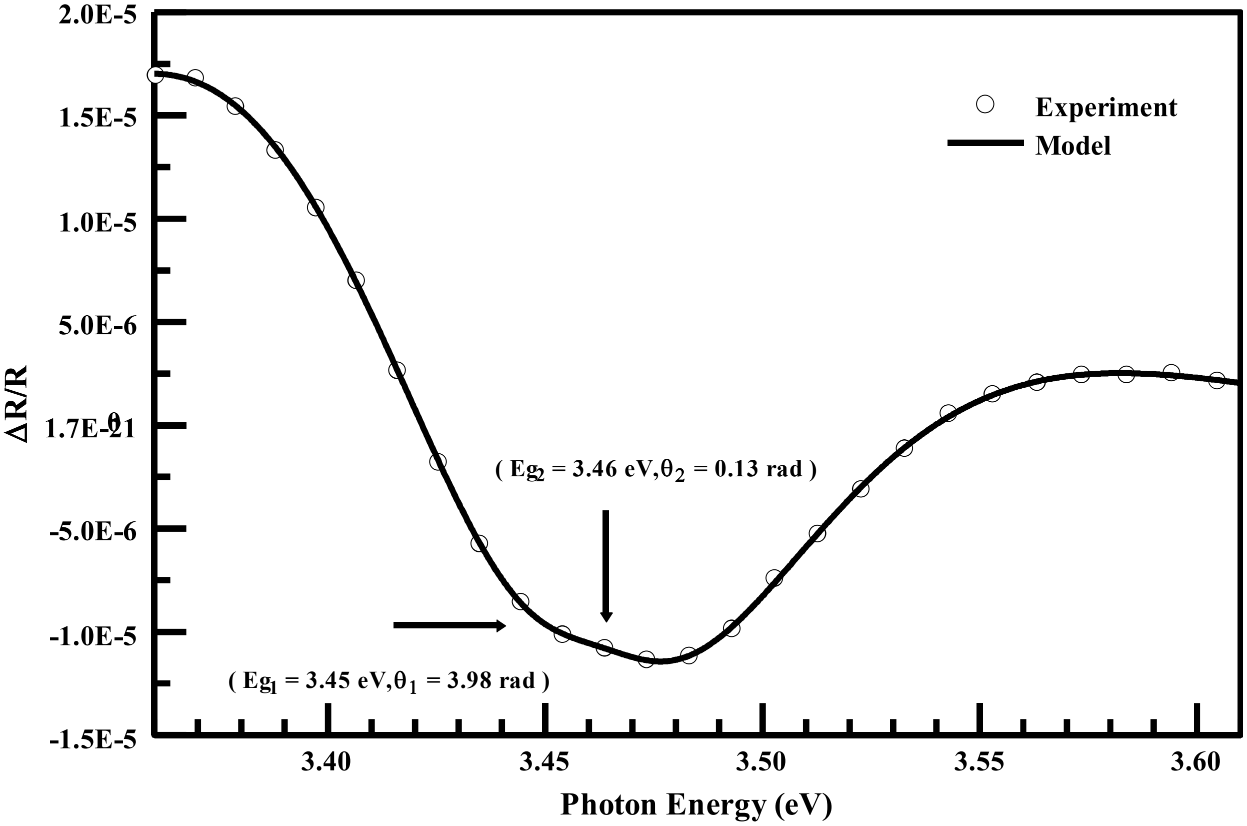

Fig 6. 7. Electroreflectance spectrum of Titanium oxide thin film.

The open circles represent the experimental spectrum, and the continuous curve is the theoretical fit obtained using the ATD model. The best fit parameters are given in the table below

C_1	-9×10^{-6}	**C_2**	-1×10^{-5}
E_{g1} (eV)	3.45	**E_{g2} (eV)**	3.46
θ_1 (radians)	3.98	**θ_2 (radians)**	0.13
Γ_1 (meV)	132	**Γ_2 (meV)**	127

6.10 Electroreflectance Analysis of Tungsten Oxide (WO_3)

The ER spectrum of WO_3 film is shown in the figure 6.8. A 5-V square wave perturbation of frequency 100 Hz was applied to the sample to achieve the ER spectrum. The collection time was fixed to 10 s/nm. The characteristics of the observed peak in the ER spectrum was found by fitting the experimental spectrum with the ATD model. The fitting parameters are shown in the table below figure 6.8. The ER spectrum revealed a single transition at an energy location of 3.61 eV. The amplitude of transition was about 1.5×10^{-5}.

Experimentally, WO_3 thins films were fabricated by RF sputtering [262-264], hydrothermal method [111], cation exchange method [112], anodisation of tungsten foils [113], thermal evaporation [47,114], glancing angle sputtering [115], pulsed DC magnetron sputtering [116], and chemical spray pyrolysis [117,118]. All of these studies used the Tauc method to find the nature of the transitions and the value of the band gap of WO_3 films. Most films showed an indirect nature of transitions except few ones where a direct nature of transitions was also observed [118]. The value of the indirect band gap varied from 2.29 eV to 3.78 eV. Besides the experimental studies, theoretical calculations were also performed to predict the nature of transitions and the correct values of the band gaps. The nature and the values of the band gap of WO_3 varied with different crystal structures. For example, the monoclinic phase of WO_3 showed a direct nature of transition ($\Gamma \rightarrow \Gamma$) where the values of the band gap varied from 1.74 to 2.78 eV [265-268]. For the cubic structure, it was indirect (from $R\rightarrow\Gamma$) with band gap values from 1.53 to 2.25 eV [265,266]. Apart from theoretical calculations and Tauc methods, spectroscopic ellipsometry was also used to find the band gap of WO_3 thin films. For example, Valuke *et al.* [119] and Szekers *et al.* [120] found band gaps of 3.15 and 3.25 eV. In our electroreflectance analysis, the peak at 3.61eV might be attributed to the indirect transition of WO_3

thin film. It was only 0.1 eV higher than the value determined by Punita *et al*.[116] on the basis of Tauc method.

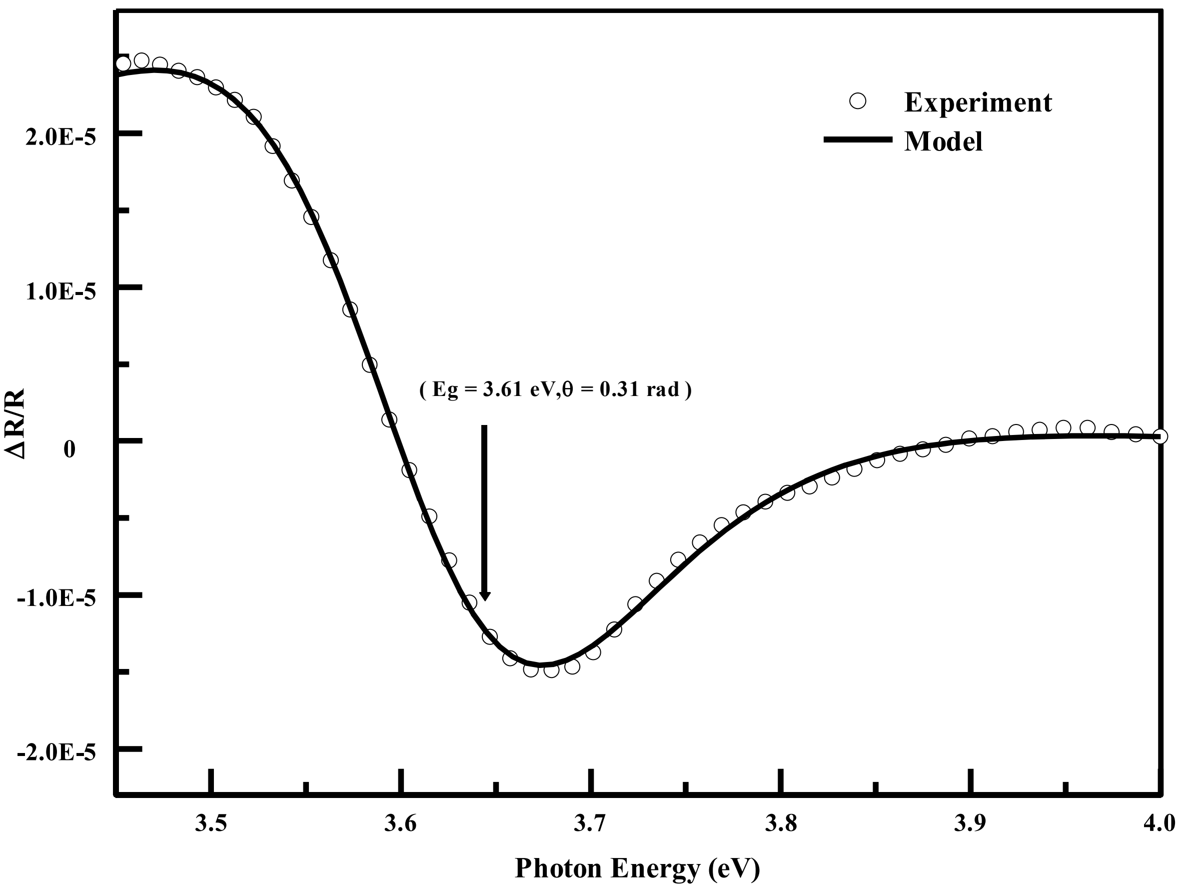

Fig 6. 8. Electroreflectance spectrum of tungsten oxide thin film.

The open circles represent the experimental spectrum, and the continuous curve is the theoretical fit obtained using the ATD model. The best fit parameters are given in the table below

Best-Fit Parameters for WO_3

C	-1×10^{-5}
E_g (eV)	3.61
θ (radians)	0.31
Γ (meV)	177

6.11 Electroreflectance Analysis of Zinc Oxide (ZnO)

Figure 6.9 shows the electroreflectance spectrum of ZnO. A 240-V square wave signal of frequency 100 Hz was applied to the surface of the sample to create the necessary modulation, and the spectrum collection time was set to 3 s/nm. The amplitude of the ER spectrum was found within the range of 10^{-5}. Moreover, the flat nature of the spectrum towards the high energy side is attributed the fact that the obtained spectrum was within the low field regime. The characteristics of the observed peak in the ER spectrum was found by fitting the experimental spectrum with the ATD model. Two prominent peaks were observed from electroreflectance spectrum. The peak located at 3.44 eV had the amplitude of 8×10^{-6} with a full width at half maximum value of 132 meV. The most intense peak was located at a value of 3.23 eV with the maximum amplitude of $\sim 6\times10^{-5}$ with a full width at half maximum value of 99 meV. The other fitted parameters are described in the table below figure 6.9.

For ZnO, the nature of the band gap was predicted to be direct by both experimental and theoretical analyses. However, the value of the band gap varied with different fabrication techniques and different theoretical methods. Experimentally, ZnO thin films were fabricated by many techniques. These include plasma enhanced atomic layer deposition [121], hydrothermal [122], sol gel [123,124], chemical vapor deposition [125], thermal oxidation [126], DC puttering [127], RF sputtering [128–130], pulsed laser deposition [130] and metal organic decomposition [131]. In these studies, the values of the band gap were either predicted by Tauc method, where the band gap values varied from 3.20 to 3.48 eV, or with the help of spectroscopic ellipsometry and Tauc Lorrentz model, where the band gap was predicted to be 3.42 eV [128]. On the other hand, the theoretical calculations on ZnO on the basis of generalized gradient approximation (GGA) [269] or GGA plus Hubbard potential (GGA+U) [270–272] predicted a direct transition ($\Gamma \rightarrow \Gamma$) with band gap values that varied from 0.77 eV to 3.42 eV. In the ER spectrum, the peak corresponding to the value of 3.44 eV might be associated with the fundamental transition in ZnO thin films. The peak location is well consistent with the values of the fundamental transitions in ZnO found in literature [123,130,131]. Similarly, the peak associated with the 3.23 eV transition might be attributed to the exciton transitions in ZnO, which was also confirmed by Welna *et al*. on the basis of room temperature Photoluminescence studies [146]

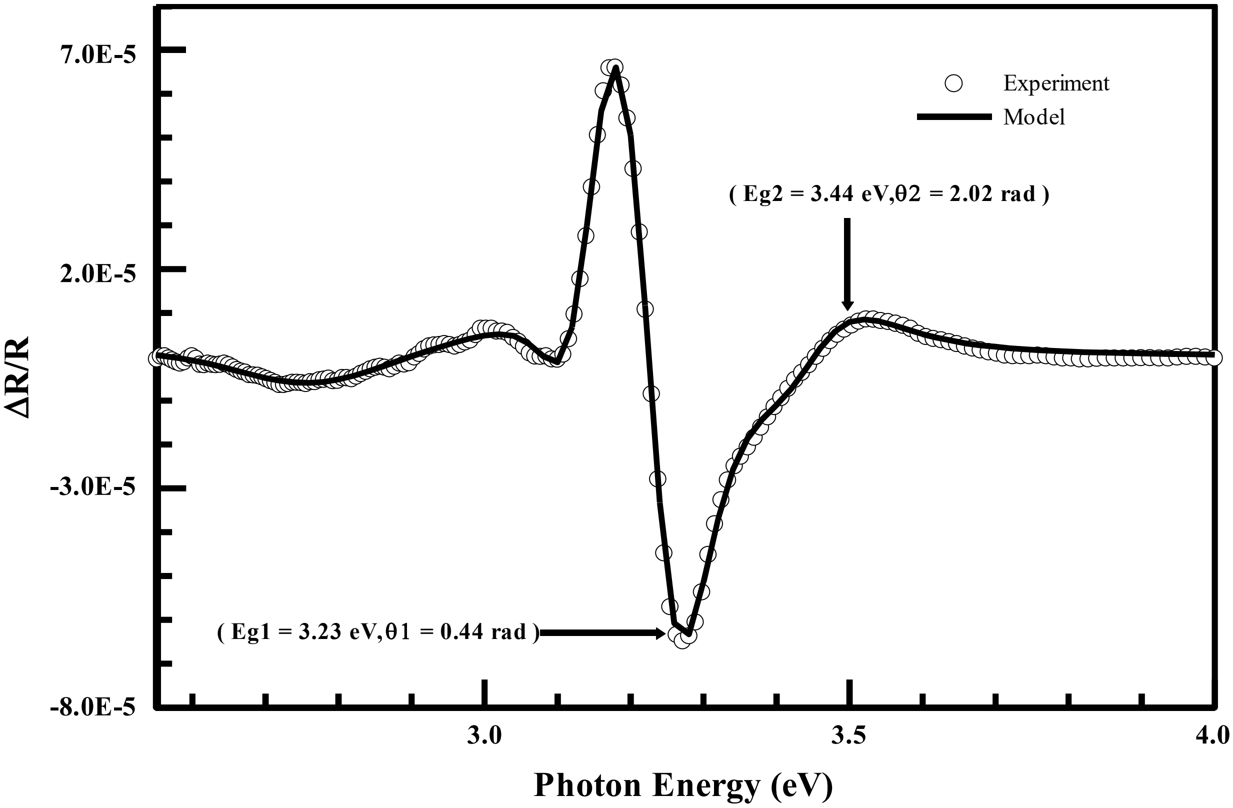

Fig 6. 9. Electroreflectance spectrum of zinc oxide thin film.

The open circles represent the experimental spectrum, and the continuous curve is the theoretical fit obtained using the ATD model. The best fit parameters are given in the table below

C_1	-6.3×10^{-5}	**C_2**	7×10^{-06}
E_{g1} (eV)	3.23	**E_{g2} (eV)**	3.44
θ_1 (radians)	0.44	**θ_2 (radians)**	2.02
Γ_1 (meV)	99	**Γ_2 (meV)**	132

6.12 Electroreflectance Analysis of Zirconium Oxide (ZrO_2)

The ER spectrum of ZrO_2 film is shown in figure 6.10. It was taken by applying a perturbation of 32-V square wave voltage at a frequency of 100 Hz. The collection time was set to 10 s/nm. The maximum amplitude of the ER spectrum was close to 10^{-5}, which confirms that the signal was within the low field regime [150]. The characteristics of the observed peak in the ER spectrum was found by fitting the experimental spectrum with the ATD model. The fitting parameters are shown in the table below figure 6.10. The spectrum revealed a single peak located at a value of 5.52 eV with a broadening of 204 meV.

Experimentally, ZrO_2 thin films were fabricated using atomic layer deposition [135,137], sol gel dip coating method [132,273], vacuum arc method [133], magnetron sputter deposition [82,134], pulsed laser deposition [195], and plasma assisted reactive pulsed laser deposition [88]. The band gap value of ZrO_2 depends on the deposition technique, crystal structure and the methods employed to determine the band gap. For example, the room-temperature monoclinic phase of ZrO_2 shows less values of band gaps, ranging from 3.85 to 5.20 eV [133,135]. On the other hand, the higher-temperature crystal structures like tetragonal and cubic phases have band gaps higher than 6 eV [56,134]. Considering the monoclinic phase, which is the stable form at room temperature, the band gaps of ZrO_2 thin films varied for different deposition techniques. For example, Adan *et al*. found the band gap of ZrO_2 film, deposited by vacuum arc technique, to be 3.85 eV [133], while Tang *et al*. found the band gap of ZrO_2 film, deposited by plasma assisted pulsed laser deposition, to be 5.96 eV [88]. Both of them calculated the direct band gap with the help of the Tauc method. The use of a graphical technique like Tauc method, for measuring the band gap, also contributes the variations in the band gap values, since the technique depends on the nature of the fitting model. For example, Al-

Kuhaili *et al*. found an additional indirect transitions with an energy value of 5.25 eV [195]. On the other hand, several other studies predicted the band gap to be direct [56,88,132–135]. The other problem involved in the Tauc technique is the spanning of the absorption data over a large dynamic range. It was found by Xu *et al.* that for an oxide with large absorption values, changing the absorption scale results in different band gap values [135]. Based upon these facts, it can be concluded that the Tauc technique determines the band gap of materials with large uncertainties. Apart from the Tauc method, some other experimental techniques were also used to calculate the band gap of ZrO_2. For example, Jeong *et al.* [137] calculated the band gap of ZrO_2 to be 4.93 eV with spectroscopic ellipsometry. Gritsenko *et al.* [82] and Dash *et al.* [136] computed the band gap of ZrO_2 to be 4.7 and 5.3 eV with the help of valence electron energy loss spectroscopy and electron energy loss spectroscopy respectively.

Besides the experimental methods, several theoretical calculations were performed to compute the band gaps of ZrO_2 thin films. These include generalized gradient approximation (GGA) [56], GGA+ exchange coulomb interaction [274] and local density approximation (LDA) [56,57,275]. In contrast to the experimental techniques, the theoretical calculations, based on the density functional theory, always underestimate the value of the band gap of a material. Moreover, the determination of the correct band gap value depends upon the theoretical aspects of calculation like the choice of a pseudo potential and the type of the functional approach used in it. For example, the band gap determined from the generalized gradient approximation (GGA) varied from 2.98 to 4.1 eV [57,231,275–277]. On the other hand, the band gap determined using the exchange Coulomb correlation and orthogonalized linear combination of atomic orbitals (OLCAO) methods predicted larger band gaps of 5.8 and 5.1 eV, respectively [56,276]. Yeng *et al.* showed the variations in the band gap value of ZrO_2 from 3.14 to 5.43 eV by employing different functional approaches [278].

Regardless of the large variations in the band gap values, the nature of transitions predicted by the theoretical calculations were indirect. That is from $X \rightarrow \Gamma$ for the cubic structure [275,278] and from $\Gamma \rightarrow B$ for the monoclinic structure [275] . In case of our electroreflectance analysis, the peak at a value of 5.52 eV was quite close to the value of 5.3 eV obtained by Dash *et al.* using EELS analysis [136] and hence, it might be attributed to the fundamental band gap transition. Moreover, the value was close to the value of 5.25 eV obtained by Al-Kuhaili *et al.* using Tauc method and consider the indirect nature of transitions [195]. Moreover, among the theoretical calculations, it was close to the predicted value of 5.2 eV obtained by French *et al.* using OLCAO approach [56].

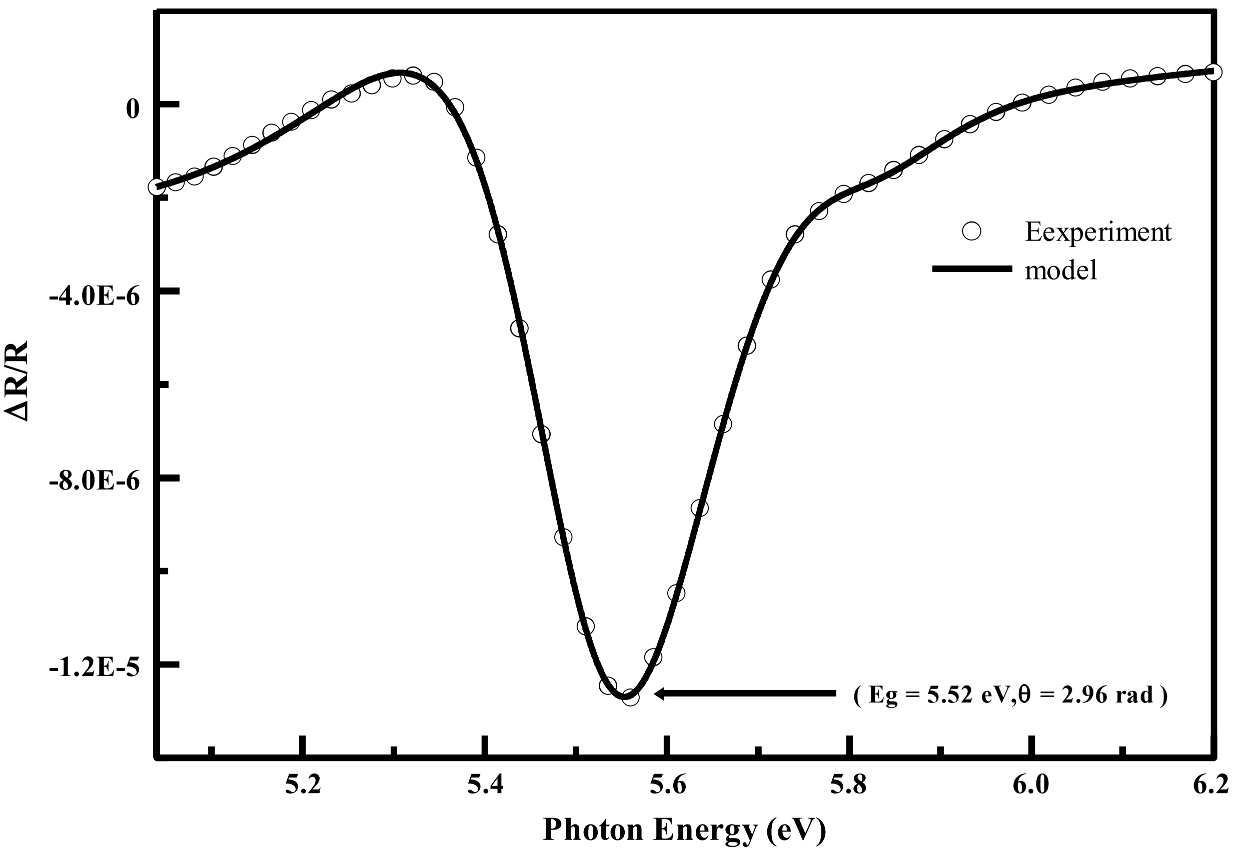

Fig 6. 10. Electroreflectance spectrum of zirconium oxide thin film.

The open circles represent the experimental spectrum, and the continuous curve is the theoretical fit obtained using the ATD model. The best fit parameters are given in the table below

Best-Fit Parameters for ZrO_2

C	-1.3×10^{-5}
E_g (eV)	5.52
θ (radians)	2.96
Γ (meV)	204

Chapter 7

Conclusion

Metal oxide thin films were fabricated using thermal evaporation and RF sputtering method. Their structural analysis showed that most of the films were amorphous except CeO_2, Fe_2O_3 and ZnO which showed some poly-crystallinity. All of the films showed columnar structure, as revealed by atomic force microscopy, with different grain size and surface roughness values. According to their optical analysis, all films showed a transmittance of greater than 80% for both visible and infrared regions. However, apart from wide band gap metal oxide thin films (Ga_2O_3, HfO_2 and ZrO_2), the transparency of the metal oxide films dropped to zero in the UV region. Moreover, it started dropping to zero for Fe_2O_3 in the lower visible region. XPS analysis of the films revealed that the prepared samples were in the oxide form. In order to perform the electroreflectance analysis, the metal oxide thin films were sandwiched between two metal electrodes and a metal- oxide- metal configuration (MOM) was obtained. The band gaps of metal oxide thin films were found by employing the electroreflectance technique. All the electroreflectance spectra of metal oxides were within the low electric field regime with no signs of Franz Keldysh oscillations. It was observed that regardless of the huge variations found in the literature in the band gap values, as predicted by spectrophotometric method, or first principle calculation studies, the electroreflectance technique provided clear optical transitions around the critical points of the metal oxide thin films. The exact energy locations and the broadening parameters of the transition peaks were found using Aspnes third derivative model. The energy locations of the optical transitions, associated with the oxides, were within the energy range of the band gaps of these oxides, reported in the literature. Keeping in view, the uncertainty caused by the spectrophotometric method, this study will prove to be an efficient substitute for the experimental determination of the band gaps of the oxides with high accuracy. Moreover, it will serve as a reference for the selection of suitable approximation techniques and a proper functional approach to compute the correct band gaps of oxides within the frame work of density functional theory.

Future Recommendations

For the better results related to the optical transitions associated with the materials, the crystalline phase of the materials should be used, and the electroreflectance analysis should be achieved at the low temperature to increase the spectral sharpness of the electroreflectance peaks. Moreover, the electromodulation can be extended in the future to observe the transitions associated with low band gap oxides, and to find the optical characteristics of alloyed films. In addition to that, the existence of high electric fields in the metal-oxide- metal configuration can be used as an efficient perturbation to engineer the band gaps of the oxides.

Appendix

A.1 Derivation of Tauc Plot

By the definition of absorption coefficient, we have

$$\alpha(\omega) = \frac{\hbar\omega\, R_t(\omega)}{I} \qquad \text{(A)}$$

where, I is the intensity of light, R_t is the transition rate of electrons, and $\hbar\omega$ is the energy of photons. The intensity of light is related to the electric filed. In order to define intensity of radiation in terms of the pointing vector S_o we have

$$S_o = \frac{c}{4\pi}\vec{E}_F \times \vec{B} \qquad \text{(A.1)}$$

Where $\vec{E}_F$ and $\vec{B}$ are the electric and magnetic component of electromagnetic radiation, and c is the speed of light. Expressing B in terms of magnetic field strength H in coulomb gauge, we can write (A.1) as

$$S_o = \frac{c}{4\pi}\vec{E}_F \times \vec{H} \qquad \text{(A.2)}$$

Since the intensity I is the time average of pointing vector S_o, we have

$$I = \langle S_o \rangle \qquad \text{(A.3)}$$

Now, using the definition of vector product

$$\mathrm{Re} < A > \cdot \mathrm{Re} < B > = \frac{1}{2}\mathrm{Re} < AB^* >$$

We can write the intensity '*I*' as

$$I = \frac{c}{8\pi} \mathrm{Re} < \vec{E}_F \times \vec{B} > \qquad \text{(A.4)}$$

For an electromagnetic radiation in the vacuum, the magnitudes of electric and magnetic components are equal. That is $\left|\vec{E}\right| = \left|\vec{B}\right|$. So, equation (3.4) can be written as

$$I = \frac{c}{8\pi} \left|E_F\right|^2 \qquad \text{(A.5)}$$

Defining the electric field in terms of vector potential $\vec{A}$ under coulomb gauge, we have

$$\vec{E}_F = -\frac{1}{c}\frac{\partial \vec{A}}{\partial t} \qquad \text{(A.6)}$$

For a given radiation frequency ω, the vector potential is described as

$$\vec{A} = \hat{e} A_o e^{i(k.r - \omega t)} + c.c \qquad \text{(A.7)}$$

So, using this relation in equation (3.6) we have

$$\vec{E}_F = \frac{i\omega}{c} \vec{A} \qquad \text{(A.8)}$$

By inserting (3.7) in to (3.5), we have

$$I = \frac{\omega^2}{8\pi c} \left|A_o\right|^2 \qquad \text{(A.9)}$$

This is expression of intensity of an electromagnetic radiation. For the electrons moving in the crystal, the transition rate from their valence bands to the conduction bands is described as

$$R_t = \frac{2\pi}{\hbar}\left(\frac{eAo}{mc}\right)^2 J_{cv}\rho_{cv} \qquad \text{(A.10)}$$

J_{cv} is the dipole matrix element or force oscillator strength, and it is equal to

$$J_{cv} = \left|\left\langle \Psi_c \left| e^{ik.r}\hat{e}.\vec{P} \right| \Psi_v \right\rangle\right|^2 = \frac{m_0^2 E_g}{2\mu} \qquad \text{(A.11)}$$

where E_g is the band gap energy of the material, m_o is the mass of the electron, and μ_r is the reduced mass of the electron. The term ρ_{cv} is defined as the joint density of states for the electros available for the transitions from their valence band to the conduction band. The expression for the joint density of states is described in equation (2.51) as

$$\rho_{cv} = \frac{1}{\left(2\pi^2\right)}\left(\frac{2\mu}{\hbar^2}\right)^{3/2}\sqrt{\hbar\omega - E_g} \qquad \hbar\omega > E_g \qquad \text{(A.12)}$$

Using (3.8) (3.9), (3.10),(2.51) in equation (2.41) we have

$$\alpha = \frac{\hbar\omega\frac{2\pi}{\hbar}\left(\frac{eAo}{mc}\right)^2 J_{cv}\rho_{cv}}{\frac{\omega^2}{8\pi c}\left|A_o\right|^2}$$

$$\Rightarrow \alpha = \frac{\hbar\omega\frac{2\pi}{\hbar}\left(\frac{eAo}{mc}\right)^2 \frac{m_0^2 E_g}{2\mu}\frac{1}{\left(2\pi^2\right)}\left(\frac{2\mu}{\hbar^2}\right)^{3/2}\left(\hbar\omega - E_g\right)^{1/2}}{\frac{\omega^2}{8\pi c}\left|A_o\right|^2} \qquad \text{(A.13)}$$

Rearranging the expression we have

$$\alpha\hbar\omega = \eta\left(\hbar\omega - E_g\right)^{1/2} \tag{A.14}$$

This is the expression for the Tauc plot with η is a constant factor defined as

$$\eta = \frac{8ce^2E_g}{\hbar}\left(\frac{2\mu}{\hbar^2}\right)^{1/2} \tag{A.15}$$

In more generalized form, the Tauc plot relation is described as

$$\left(\alpha\hbar\omega\right)^2 = \eta^2\left(\hbar\omega - E_g\right) \tag{A.16}$$

A.2 Uncertainty in the Energy Value Measured Through Electroreflectance (Case of CeO_2)

Variation in the energy values for the case of CeO_2 was measured with respect to the broadening parameter. For each fixed values of the broadening parameter, the ATD model was employed to find the energy location of the critical point. The results are summarized in table A.2

Broadening parameter Γ (eV)	**Energy of the critical point E (eV)**
0.05	3.31
0.10	3.32
0.15	3.33
0.20	3.33
0.25	3.32
0.30	3.29
0.35	3.35
0.40	3.38
0.45	3.38
0.50	3.38

Table A.2. Variations in the energy values of broadening parameter

Uncertainty in the energy values: $\frac{E_{max} - E_{min}}{2} = \frac{3.38-3.29}{2} = 0.05\ eV$

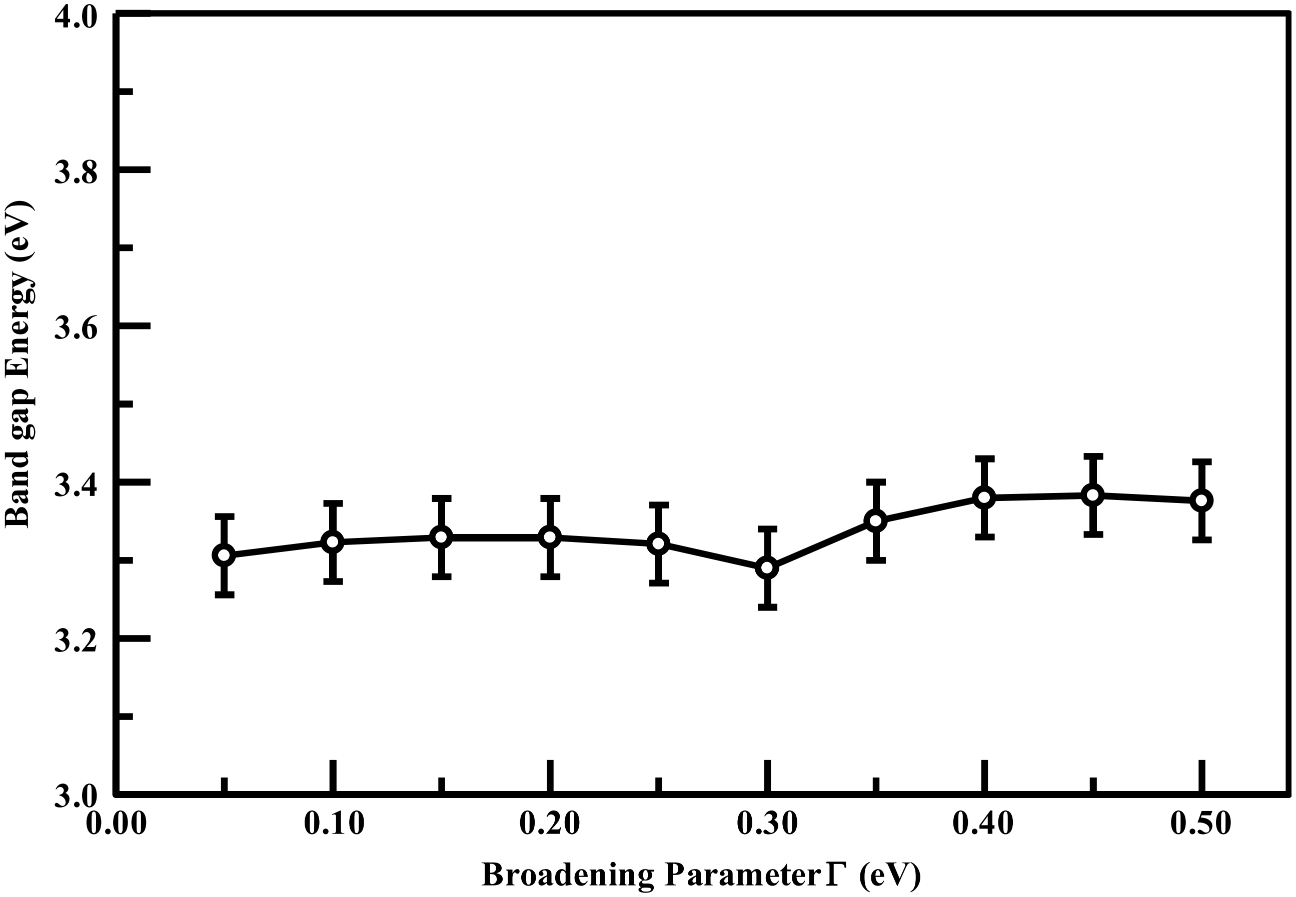

Fig A.2 Variation in the energy values with respect to the broadening parameter

References

[1] T. S. Sian, G. B. Reddy, "Optical, structural and photoelectron spectroscopic studies on amorphous and crystalline molybdenum oxide thin films," Sol. Energy Mater. Sol. Cells, vol. 82, (2004), pp. 375–386.

[2] R. S. Patil, M. D. Uplane, P. S. Patil, "Structural and optical properties of electrodeposited molybdenum oxide thin films," Appl. Surf. Sci., vol. 252, (2006), pp. 8050–8056.

[3] R. Sivakumar, R. Gopalakrishnan, M. Jayachandran, C. Sanjeeviraja, "Characterization on electron beam evaporated α-MoO_3 thin films by the influence of substrate temperature," Curr. Appl. Phys., vol. 7, (2007), pp. 51–59.

[4] K. Matsuzaki, H. Hiramatsu, K. Nomura, H. Yanagi, T. Kamiya, M. Hirano, H. Hosono, "Growth, structure and carrier transport properties of Ga_2O_3 epitaxial film examined for transparent field-effect transistor," Thin Solid Films, vol. 496, (2006), pp. 37–41.

[5] T. Takeuchi, H. Ishikawa, N. Takeuchi, Y. Horikoshi, "High resolution X-ray photoelectron spectroscopy of beta gallium oxide films deposited by ultra high vacuum radio frequency magnetron sputtering," Thin Solid Films, vol. 516, (2008), pp. 4593–4597.

[6] C.-H. Fu, K.-S. Chang-Liao, C.-C. Li, Z.-H. Ye, F.-M. Hsu, T.-K. Wang, Y.-J. Lee, M.-J. Tsai, "A higher-k tetragonal HfO_2 formed by chlorine plasma treatment at interfacial layer for metal-oxide-semiconductor devices," Appl. Phys. Lett., vol. 101, (2012), p. 032105.

[7] M. Lei, J. H. Yum, S. K. Banerjee, G. Bersuker, M. C. Downer, "Band offsets of atomic layer deposited Al_2O_3 and HfO_2 on Si measured by linear and nonlinear internal photoemission," Phys. Status Solidi B, vol. 249, (2012), pp. 1160–1165.

[8] B. Deng, G. He, X. S. Chen, X. F. Chen, J. W. Zhang, M. Liu, J. G. Lv, Z. Q. Sun, "Annealing temperature dependence on the structural and optical properties of sputtering-grown high-k

HfO_2 gate dielectrics," J. Mater. Sci. Mater. Electron., vol. 25, (2014), pp. 4163–4169.

[9] S. H. S. Chan, T. Y. Wu, J. C. Juanb, C. Y. Teha, "Recent developments of metal oxide as photocatalysts in advanced oxidation processes (AOPs) for treatment of dye waste-water," J. Chem. Technol. Biotechnol., vol. 86 , (2011), pp. 1130–1158.

[10] P. E. Batson, D. W. Johnson, J. C. H. Spence, "Resolution enhancement by deconvolution using a field-emission source in electron-energy loss spectroscopy," Ultramicroscopy, vol. 41 , (1992), pp. 137–145.

[11] F. H. Pollak, H. Shen, "Modulation spectroscopy of semiconductors: bulk/thin film, microstructures, surfaces/interfaces and devices," Mater. Sci. Eng. R Reports, vol. 10, (1993), pp. xv–374.

[12] D. E. Aspnes, N. Bottka, "Modulation Techniques," Elsevier, 1972.

[13] M. Nolan, S. Grigoleit, D. C. Sayle, S. C. Parker, G. W. Watson, "Density functional theory studies of the structure and electronic structure of pure and defective low index surfaces of ceria," Surf. Sci., vol. 576, (2005), pp. 217–229.

[14] X.-H. Lu, S.-L. Xie, T. Zhai, Y.-F. Zhao, P. Zhang, Y.-L. Zhang, Y.-X. Tong, "Monodisperse CeO_2/CdS heterostructured spheres: one-pot synthesis and enhanced photocatalytic hydrogen activity," RSC Adv., vol. 1, (2011), p. 1207.

[15] C. Libertad, "Optical and structural characterization of RF sputtered CeO_2 thin films," J. Mater. Sci., vol. 2, (1997) pp. 1861—1865.

[16] D.-E. Zhang, X.-J. Zhang, X.-M. Ni, J.-M. Song, H.-G. Zheng, "Fabrication of novel threefold shape CeO_2 dendrites: Optical and electrochemical properties," Chem. Phys. Lett., vol. 430, (2006), pp. 326–329.

[17] A. E. Hughes, J. D. Gorman, P. J. K. Patterson, R. Carter, "Unusual peak shifts in the core

levels of CeO_2 films deposited on Si(100)," Surf. Interface Anal., vol. 24, (1996), pp. 634–640.

[18] M. F. Al-Kuhaili, M. Saleem, S. M. A. Durrani, "Optical properties of iron oxide (α-Fe_2O_3) thin films deposited by the reactive evaporation of iron," J. Alloys Compd., vol. 521, (2012), pp. 178–182.

[19] P. Chauhan, S. Annapoorni, S. K. Trikha, "Preparation, characterization and optical properties of α-Fe_2O_3 films by sol-spinning process," Bull. Mater. Sci., vol. 21, (1998), pp. 381–385.

[20] A. B. F. Martinson, M. J. DeVries, J. A. Libera, S. T. Christensen, J. T. Hupp, M. J. Pellin, J. W. Elam, "Atomic layer deposition of Fe_2O_3 using ferrocene and ozone," J. Phys. Chem. C, vol. 115, (2011), pp. 4333–4339.

[21] N. Ueda, H. Hosono, R. Waseda, H. Kawazoe, "Synthesis and control of conductivity of ultraviolet transmitting β-Ga_2O_3 single crystals," Appl. Phys. Lett., vol. 70, (1997), p. 3561.

[22] N. Ueda, H. Hosono, R. Waseda, H. Kawazoe, "Anisotropy of electrical and optical properties in beta -Ga_2O_3 single crystals," Appl. Phys. Lett., vol. 71, (1997), pp. 933–935.

[23] A. Ortiz, J. C. Alonso, E. Andrade, C. Urbiola, "Structural and optical characteristics of gallium oxide thin films deposited by ultrasonic spray pyrolysis," J. Electrochem. Soc., vol. 148, (2001), pp. F26–F29.

[24] Z. Hajnal, J. Miró, G. Kiss, F. Réti, P. Deák, R. C. Herndon, J. M. Kuperberg, "Role of oxygen vacancy defect states in the n-type conduction of β- Ga_2O_3," J. Appl. Phys., vol. 86, (1999), p. 3792.

[25] F. K. Shan, G. X. Liu, W. J. Lee, G. H. Lee, I. S. Kim, B. C. Shin, "Structural, electrical, and optical properties of transparent gallium oxide thin films grown by plasma-enhanced atomic layer deposition," J. Appl. Phys., vol. 98, (2005), pp. 1–7.

[26] K. Yamaguchi, "First principles study on electronic structure of β- Ga_2O_3," Solid State

Commun., vol. 131, (2004), pp. 739–744.

[27] T. S. Böscke, J. Müller, D. Bräuhaus, U. Schröder, U. Böttger, “Ferroelectricity in hafnium oxide thin films,” Appl. Phys. Lett., vol. 99, (2011), p. 102903.

[28] T. V. Perevalov, A. V. Shaposhnikov, K. A. Nasyrov, D. V. Gritsenko, V. A. Gritsenko, “Electronic structure of ZrO_2 and HfO_2” Microelectron. Eng., (2006), pp. 423–434.

[29] M. F. Al-Kuhaili, “Optical properties of hafnium oxide thin films and their application in energy-efficient windows,” Opt. Mater. (Amst)., vol. 27, (2004), pp. 383–387.

[30] H. Y. Yu, M. F. Li, B. J. Cho, C. C. Yeo, M. S. Joo, D.-L. Kwong, J. S. Pan, C. H. Ang, J. Z. Zheng, S. Ramanathan, “Energy gap and band alignment for $(HfO_2)_x(Al_2O_3)_{1-x}$ on (100) Si,” Appl. Phys. Lett., vol. 81, (2002), p. 376.

[31] R. G. Vitchev, J. J. Pireaux, T. Conard, H. Bender, J. Wolstenholme, C. Defranoux, “X-ray photoelectron spectroscopy characterisation of high-k dielectric Al_2O_3 and HfO_2 layers deposited on SiO_2/Si surface,” Appl. Surf. Sci., vol. 235, (2004), pp. 21–25.

[32] T. He, J. Yao, “Photochromism of molybdenum oxide,” J. Photochem. Photobiol. C Photochem. Rev., vol. 4, (2003), pp. 125–143.

[33] M. T. Greiner, L. Chai, M. G. Helander, W. M. Tang, Z. H. Lu, “Metal/metal-oxide interfaces: How metal contacts affect the work function and band structure of MoO_3,” Adv. Funct. Mater., vol. 23, (2013), pp. 215–226.

[34] C. Julien, A. Khelfa, O. Hussain, G. Nazri, “Synthesis and characterization of flash-evaporated MoO_3 thin films,” J. Cryst. Growth, vol. 156, (1995), pp. 235–244.

[35] O. Hussain, K. Rao, “Characterization of activated reactive evaporated MoO_3 thin films for gas sensor applications,” Mater. Chem. Phys., vol. 80, (2003), pp. 638–646.

[36] Z. Hussain, “Optical and electrochromic properties of heated and annealed MoO_3 thin films,”

J. Mater. Res., vol. 16, (2001), pp. 2695–2708.

[37] J. M. Themlin, R. Sporken, J. Darville, R. Caudano, J. M. Gilles, R. L. Johnson, “Resonant-photoemission study of SnO_2: Cationic origin of the defect band-gap states,” Phys. Rev. B, vol. 42, (1990), pp. 11914–11925.

[38] P. Barbarat, S. F. Matar, “First-principles investigations of the electronic, optical and chemical bonding properties of SnO_2,” Comput. Mater. Sci., vol. 10, (1998), pp. 368–372.

[39] R. Larciprete, E. Borsella, P. De Padova, M. Fanfoni, M. Mangiantini, “ArF excimer laser deposited tin oxide films studied by in- situ surface diagnostics and by synchrotron radiation induced UV photoemission,” Appl. Surf. Sci.,vol. 69, (1993), pp. 59–64.

[40] L. Meng, M. dos Santos, “The influence of oxygen partial pressure and total pressure (O_2 + Ar) on the properties of tin oxide films prepared by DC sputtering,” Vacuum, vol. 45, (1994), pp. 1191–1195.

[41] M. Di Giulio, G. Micocci, R. Rella, P. Siciliano, A. Tepore, “Properties of reactively sputtered tin oxide films as CO gas sensors,” Sensors Actuators B Chem., vol. 23, (1995), pp. 193–195.

[42] A. Amtout, R. Leonelli, “Time-resolved photoluminescence from excitons in TiO_2,” Solid State Commun., vol. 84, (1992), pp. 349–352.

[43] D.-J. Won, C.-H. Wang, H.-K. Jang, D.-J. Choi, “Effects of thermally induced anatase-to-rutile phase transition in MOCVD-grown TiO_2 films on structural and optical properties,” Appl. Phys. A., vol. 73, (2001), pp. 595–600.

[44] K. Glassford, J. Chelikowsky, “Structural and electronic properties of titanium dioxide,” Phys. Rev. B, vol. 46, (1992), pp. 1284–1298.

[45] G. Wijs, P. Boer, R. Groot, G. Kresse, “Anomalous behavior of the semiconducting gap in WO_3 from first-principles calculations,” Phys. Rev. B, vol. 59, (1999), pp. 2684–2693.

[46] B. Ingham, S. V. Chong, J. L. Tallon, “Novel materials based on organic–tungsten oxide hybrid systems II: electronic properties of the W–O framework,” Curr. Appl. Phys., vol. 4, (2004), pp. 202–205.

[47] S. Keshri, A. Kumar, D. Kabiraj, “Tailoring of optical and gas sensitivity behaviors of WO_3 films by low energy Ar+ ion implantation,” Thin Solid Films, vol. 526, (2012), pp. 50–58.

[48] L. G. Teoh, J. Shieh, W. H. Lai, I. M. Hung, M. H. Hon, “Structure and optical properties of mesoporous tungsten oxide,” J. Alloys Compd., vol. 396, (2005), pp. 251–254.

[49] N. S. Gaikwad, G. Waldner, A. Brüger, A. Belaidi, S. M. Chaqour, M. Neumann-Spallart, “Photoelectrochemical Characterization of Semitransparent WO_3 Films,” J. Electrochem. Soc., vol. 152, (2005), p. G411.

[50] F. Decremps, F. Datchi, A. M. Saitta, A. Polian, S. Pascarelli, A. Di Cicco, J. P. Itié, F. Baudelet, “Local structure of condensed zinc oxide,” Phys. Rev. B, vol. 68, (2003), p. 104101.

[51] P. S. Xu, Y. M. Sun, C. S. Shi, F. Q. Xu, H. B. Pan, “The electronic structure and spectral properties of ZnO and its defects,” Nucl. Instruments Methods Phys. Res. Sect. B, vol. 199, (2003), pp. 286–290.

[52] S. Faÿ, L. Feitknecht, R. Schlüchter, U. Kroll, E. Vallat-Sauvain, A. Shah, “Rough ZnO layers by LP-CVD process and their effect in improving performances of amorphous and microcrystalline silicon solar cells,” Sol. Energy Mater. Sol. Cells, vol. 90, (2006), pp. 2960–2967.

[53] S. A. Studenikin, N. Golego, M. Cocivera, “Optical and electrical properties of undoped ZnO films grown by spray pyrolysis of zinc nitrate solution,” J. Appl. Phys., vol. 83, (1998), p. 2104.

[54] B. Szyszka, V. Sittinger, X. Jiang, R. J. Hong, W. Werner, A. Pflug, M. Ruske, A. Lopp,

“Transparent and conductive ZnO:Al films deposited by large area reactive magnetron sputtering,” Thin Solid Films, vol. 442, (2003), pp. 179–183.

[55] P. G. Neudeck, R. S. Okojie, “High-temperature electronics - a role for wide bandgap semiconductors?,” Proc. IEEE, vol. 90, (2002), pp. 1065–1076.

[56] R. French, S. Glass, F. Ohuchi, Y. Xu, W. Ching, “Experimental and theoretical determination of the electronic structure and optical properties of three phases of ZrO_2,” Phys. Rev. B, vol. 49, (1994), pp. 5133–5142.

[57] L. Soriano, M. Abbate, J. Faber, C. Morant, J. . Sanz, “The electronic structure of ZrO_2: Band structure calculations compared to electron and x-ray spectra,” Solid State Commun., vol. 93, (1995), pp. 659–665.

[58] S. Zhao, F. Ma, K. W. Xu, H. F. Liang, “Optical properties and structural characterization of bias sputtered ZrO_2 films,” J. Alloys Compd., vol. 453, (2008), pp. 453–457.

[59] Y. Isobe, M. Fuse, K. Kobayashi, “Additive Element Effects on Electronic Conductivity of Zirconium Oxide Film,” J. Nucl. Sci. Technol., vol. 31, (1994), pp. 546–551.

[60] R. Suresh, V. Ponnuswamy, R. Mariappan, N. S. Kumar, “Influence of substrate temperature on the properties of CeO_2 thin films by simple nebulizer spray pyrolysis technique”, Ceram. Int., vol 40 (2014) pp. 437–445.

[61] N.S. Arul, D. Mangalaraj, J. I. Han, “Solvothermal synthesis of three-dimensional CeO_2 micropillows and their photocatalytic property” , Phys. Status Solidi - Rapid Res. Lett., vol. 8 (2014) pp. 643–647.

[62] C. Breinlich, J.M. Essen, E. Barletta, K. Wandelt, “Growth, structure and electronic properties of ultrathin cerium oxide films grown on Pt(111),” Thin Solid Films, vol. 519 (2011) pp. 3752–3755.

[63] C. Mansilla, “Structure, microstructure and optical properties of cerium oxide thin films prepared by electron beam evaporation assisted with ion beams,” Solid State Sci., vol. 11, (2009), pp. 1456–1464.

[64] W. D. Chemelewski, O. Mabayoje, D. Tang, A. J. E. Rettie, C. B. Mullins, “Bandgap engineering of Fe_2O_3 with Cr – application to photoelectrochemical oxidation,” Phys. Chem. Chem. Phys., vol. 18 (2016) pp. 1644–1648.

[65] M. Alagiri, S.B.A. Hamid, “Sol–gel synthesis of α-Fe_2O_3 nanoparticles and its photocatalytic application,” J. Sol-Gel Sci. Technol., vol. 74 (2015) pp. 783–789.

[66] E. Parsianpour, M. Gholami, N. Shahbazi, F. Samavat, “Influence of thermal annealing on the structural and optical properties of maghemite nanoparticle thin films” Surf. Interface Anal.,vol. 47 (2015) pp. 612–617.

[67] A. U. Ubale, M.R. Belkhedkar, “Size dependent physical properties of nano-structured Fe_2O_3 thin films grown by successive ionic layer adsorption and reaction method for antibacterial application” J. Mater. Sci. Technol.,vol. 31 (2015) pp. 1–9.

[68] J. Kocher, A. Kumar, A. Kumar, S. Priya, J. Kumar, “Nickel-induced structural, optical, magnetic, and electrical behavior of α-Fe_2O_3” Phys. Status Solidi, vol. 251 (2014) pp. 1552–1557.

[69] B. Gilbert, C. Frandsen, E.R. Maxey, D.M. Sherman,”Band-gap measurements of bulk and nanoscale hematite by soft x-ray spectroscopy,” Phys. Rev. B - Condens. Matter Mater. Phys.,vol. 79 (2009) p. 035108

[70] M. H. T. Onuma, S. Saito, K. Sasaki, T. Masui, T. Yamaguchi, T. Honda, A. Kuramata, “Spectroscopic ellipsometry studies on β-Ga_2O_3 films and single crystal,” JJAP., vol. 55 (2016) p.1202B2

[71] G. Schmitz, P. Gassmann, R. Franchy, “A combined scanning tunneling microscopy and electron energy loss spectroscopy study on the formation of thin, well-ordered β-Ga_2O_3 films on CoGa (001),” J. Appl. Phys., vol. 83 (1998) p. 2533.

[72] M. Orita, H. Ohta, M. Hirano, H. Hosono, “Deep-ultraviolet transparent conductive β-Ga_2O_3 thin films,” Appl. Phys. Lett., vol. 77 (2000) p. 4166.

[73] Z. Ji, J. Du, J. Fan, W. Wang, “Gallium oxide films for filter and solar-blind UV detector,” Opt. Mater., vol. 28 (2006) pp. 415–417.

[74] G. X. Liu, F. K. Shan, W. J. Lee, B. C. Shin, S. C. Kim, H. S. Kim, C. R. Cho, “Growth temperature dependence of Ga_2O_3 thin films deposited by plasma enhanced atomic layer deposition,” Integr. Ferroelectr., vol. 94 (2007) pp. 11–20.

[75] R. K. Ramachandran, J. Dendooven, J. Botterman, S. P. Sree, D. Poelman, J. A. Martens, H. Poelman, C. Detavernier, “Plasma enhanced atomic layer deposition of Ga_2O_3 thin films,” J. Mater. Chem. A, vol. 2, (2014), pp. 19232–19238.

[76] Y. Kokubun, K. Miura, F. Endo, S. Nakagomi, “Sol-gel prepared β-Ga_2O_3 thin films for ultraviolet photodetectors,” Appl. Phys. Lett. 90 (2007) p. 31912.

[77] Y. Ohya, J. Okano, Y. Kasuya, T. Ban, “Fabrication of Ga_2O_3 thin films by aqueous solution deposition,” J. Cer. Soc. Jpn., 117 (2009) pp. 973–977.

[78] L. Kong, J. Ma, C. Luan, W. Mi, Y. Lv, “Structural and optical properties of heteroepitaxial beta Ga_2O_3 films grown on MgO (100) substrates,” Thin Solid Films, vol. 520 (2012) pp. 4270–4274.

[79] Y. Cheng, H. Liang, R. Shen, X. Xia, B. Wang, Y. Liu, S. Song, Y. Liu, Z. Zhang, G. Du, “Band gap broadening and photoluminescence properties investigation in Ga_2O_3 polycrystal,” J. Mater. Sci. Mater. Electron., vol.24 (2013) pp. 2750–2754.

[80] C. Y. Kim, S. W. Cho, M.-H. Cho, K. B. Chung, D. C. Suh, D. H. Ko, C.H. An, H. Kim, H. J. Lee, "Changes in the structure of an atomic layer deposited HfO_2 film on a GaAs (100) substrate as a function of postannealing temperature," Appl. Phys. Lett., vol. 95 (2009) p. 42903.

[81] T. V. Perevalov, V.A. Gritsenko, S.B. Erenburg, A.M. Badalyan, H. Wong, C.W. Kim, "Atomic and electronic structure of amorphous and crystalline hafnium oxide: X-ray photoelectron spectroscopy and density functional calculations," J. Appl. Phys., vol. 101 (2007) p. 53704.

[82] V. Gritsenko, D. Gritsenko, S. Shaimeev, V. Aliev, K. Nasyrov, S. Erenburg, V. Tapilin, H. Wong, M. C. Poon, J. H. Lee, J. W. Lee, C. W. Kim, "Atomic and electronic structures of amorphous ZrO_2 and HfO_2 films," Microelectron. Eng., vol. 81 (2005) pp. 524–529.

[83] N. Selvakumar, H. C. Barshilia, K. S. S. Rajam, A. Biswas, "Structure, optical properties and thermal stability of pulsed sputter deposited high temperature HfO_x/Mo/HfO_2 solar selective absorbers," Sol. Energy Mater. Sol. Cells., vol. 94, (2010), pp. 1412–1420.

[84] E. Hildebrandt, J. Kurian, M.M. Mller, T. Schroeder, H.J. Kleebe, L. Alff, "Controlled oxygen vacancy induced p-type conductivity in HfO_{2-x} thin films," Appl. Phys. Lett., vol. 99 (2011) pp. 1–4.

[85] B. Deng, G. He, J. G. Lv, X. F. Chen, J. W. Zhang, M. Zhang, Z. Q. Sun, "Modulation of the structural and optical properties of sputtering-derived HfO_2 films by deposition power," Opt. Mater. (Amst)., vol. 37 (2014) pp. 245–250.

[86] M. F. Al-Kuhaili, S. M. A. Durrani, I. A. Bakhtiari, M. A. Dastageer, M. B. Mekki, "Influence of hydrogen annealing on the properties of hafnium oxide thin films," Mater. Chem. Phys., vol. 126, (2011), pp. 515–523.

[87] Z. Ying, W. Tang, Z. Hu, W. Li, J. Sun, N. Xu, J. Wu, “Annealing behaviors of structural, interfacial and optical properties of HfO_2 thin films prepared by plasma assisted reactive pulsed laser deposition,” J. Mater. Res., vol. 25 (2010) pp. 680–686.

[88] W. T. Tang, Z. F. Ying, Z. G. Hu, W. W. Li, J. Sun, N. Xu, J. D. Wu, “Synthesis and characterization of HfO_2 and ZrO_2 thin films deposited by plasma assisted reactive pulsed laser deposition at low temperature”, Thin Solid Films, vol. 518 (2010) pp. 5442–5446.

[89] T. Tan, Z. Liu, H. Lu, W. Liu, F. Yan, W. Zhang, “Band structure and valence-band offset of HfO_2 thin film on Si substrate from photo emission spectroscopy,” Appl. Phys. A Mater. Sci. Process., vol. 97 (2009) pp. 475–479.

[90] E. Hildebrandt, J. Kurian, J. Zimmermann, A. Fleissner, H. von Seggern, L. Alff, Hafnium oxide thin films: “Effect of growth parameters on oxygen and hafnium vacancies,” J. Vac. Sci. Technol. B, vol. 27 (2009) pp. 325–328.

[91] R. Puthenkovilakam, J. P. Chang, ″An accurate determination of barrier heights at the HfO_2 ⁄ Si interfaces”, J. Appl. Phys.,vol. 96 (2004) p.2701

[92] Y. B. Zheng, S. J. Wang, C. H. A. Huan, “Microstructure-dependent band structure of HfO_2 thin films,” Thin Solid Films, vol. 504 (2006) pp. 197–200.

[93] M. Perego, G. Seguini, M. Fanciulli, ”XPS and IPE analysis of HfO_2 band alignment with high-mobility semiconductors”, Mater. Sci. Semicond. Process., vol. 11 (2008) 221–225.

[94] R. Boughalmi, A. Boukhachem, M. Kahlaoui, H. Maghraoui, M. Amlouk, “ Physical investigations on MoO_3 sprayed thin film for selective sensitivity applications,” Mater. Sci. Semicond. Process., vol. 26 (2014) pp. 593–602.

[95] V. Madhavi, P. Kondaiah, S. S. Rayudu, O. M. Hussain, S. Uthanna, “Properties of MoO_3 films by thermal oxidation: Annealing induced phase transition,” Mater. Express., vol.3 (2013) pp.

135–143.

[96] Y. A. Pastrana, J. Torres, L. D. López-Carreño, H. M. Martínez, "The Influence of Oxygen on the Structural and Optical Properties of MoO_3 Thin Films Prepared Using the Laser-Assisted Evaporation Technique," J. Supercond. Magn., vol. (2013) pp. 2475–2478.

[97] S. Park, S. J. Baik, J. S. Im, L. Fang, J. W. Jeon, K. S. Lim, "Towards a high efficiency amorphous silicon solar cell using molybdenum oxide as a window layer instead of conventional p-type amorphous silicon carbide," Appl. Phys. Lett., vol. 99 (2011) pp. 110–113.

[98] M. F. Al-Kuhaili, S. M. A. Durrani, I. A. Bakhtiari, A. M. Al-Shukri, "Optical constants and thermocoloration of pulsed laser deposited molybdenum oxide thin films," Opt. Commun., vol. 283, (2010), pp. 2857–2862.

[99] R. J. Choudhary, S. B. Ogale, S. R. Shinde, V. N. Kulkarni, T. Venkatesan, K. S. Harshavardhan, M. Strikovski, B. Hannoyer, "Pulsed-electron-beam deposition of transparent conducting SnO_2 films and study of their properties," Appl. Phys. Lett., vol. 84 (2004) p. 1483.

[100] M. R. Fadavieslam, H. Azimi-Juybari, M. Marashi, "Dependence of O_2, N_2 flow rate and deposition time on the structural, electrical and optical properties of SnO_2 thin films deposited by atmospheric pressure chemical vapor deposition (APCVD)," J. Mater. Sci. Mater. Electron. vol.27 (2016) pp. 921–930.

[101] A. A. Yadav, " Spray deposition of tin oxide thin films for supercapacitor applications: effect of solution molarity," J. Mater. Sci. Mater. Electron., vol. 27 (2016) pp. 6985–6991.

[102] S.-S. Lin, Y.-S. Tsai, K. R. Bai, "Structural and physical properties of tin oxide thin films for optoelectronic applications," Appl. Surf. Sci., vol. 2 (2016) pp. 1–7.

[103] A. Alhuthali, M. M. El-Nahass, A. A. Atta, M. M. Abd El-Raheem, K. M. Elsabawy, A. M.

Hassanien, “Study of topological morphology and optical properties of SnO_2 thin films deposited by RF sputtering technique,” J. Lumin., vol. 158 (2015) pp. 165–171.

[104] N. M. Shaalan, D. Hamad, A. Y. Abdel-Latief, M. A. Abdel-Rahim, “Preparation of quantum size of tin oxide: Structural and physical characterization,” Prog. Nat. Sci. Mater. Int., vol. 26 (2016) pp. 145–151.

[105] H. Khallaf, C. T. Chen, L. B. Chang, O. Lupan, A. Dutta, H. Heinrich, F. Haque, E. del Barco, L. Chow, “Chemical bath deposition of SnO_2 and Cd_2SnO_4 thin films,” Appl. Surf. Sci., vol. 258 (2012) pp. 6069–6074.

[106] A. Elfanaoui, E. Elhamri, L. Boulkaddat, A. Ihlal, K. Bouabid, L. Laanab, A. Taleb, X. Portier, “Optical and structural properties of TiO_2 thin films prepared by sole gel spin coating,” Int. J. Hydrogen Energy, vol. 36 (2010) pp. 4130–4133.

[107] M. M. Hasan, A.S.M.A. Haseeb, R. Saidur, H.H. Masjuki, M. Hamdi, “Influence of substrate and annealing temperatures on optical properties of RF-sputtered TiO_2 thin films,” Opt. Mater. (Amst)., vol. 32 (2010) pp. 690–695.

[108] V. Senthilkumar, M. Jayachandran, C. Sanjeeviraj, “Preparation of anatase TiO_2 thin films for dye-sensitized solar cells by DC reactive magnetron sputtering technique”, Thin Solid Films. 519 (2010) pp. 991–994.

[109] A. M. More, J. L. Gunjakar, C. D. Lokhande, O. Shim, “ Fabrication of hydrophobic surface of titanium dioxide films by successive ionic layer adsorption and reaction (SILAR) method” Appl. Surf. Sci., vol. 255 (2009) pp. 6067–6072.

[110] A. M. More, J. L. Gunjakar, C. D. Lokhande, “Liquefied petroleum gas (LPG) sensor properties of interconnected web-like structured sprayed TiO_2 films,” Sensors Actuators, B Chem., vol. 129 (2008) pp. 671–677.

[111] N. Zhang, C. Chen, Z. Mei, X. Liu, X. Qu, Y. Li, S. Li, W. Qi, Y. Zhang, J. Ye, V.A.L. Roy, R. Ma, "Monoclinic Tungsten Oxide with {100} Facet Orientation and Tuned Electronic Band Structure for Enhanced Photocatalytic Oxidations," ACS Appl. Mater. Interfaces, vol. 8 (2016) pp. 10367–10374.

[112] K. A. Newton, F. E. Osterloh, "Size and Morphology of Suspended WO_3 Particles Control Photochemical Charge Carrier Extraction and Photocatalytic Water Oxidation Activity," Top. Catal., vol. 59 (2016) pp. 750–756.

[113] N. B. D. da Costa, J. C. O. Pazinato, G. Sombrio, M. B. Pereira, H. Boudinov, A. Gündel, E. C. Moreira, I. T. S. Garcia, "Tungsten oxide thin films obtained by anodisation in low electrolyte concentration," Thin Solid Films, vol. 578 (2015) pp. 124–132.

[114] A. Arfaoui, B. Ouni, S. Touihri, T. Mannoubi, "Investigation into the optoelectrical properties of tungsten oxide thin films annealed in an oxygen air," Mater. Res. Bull., vol. 60 (2014) pp. 719–729.

[115] C. Charles, N. Martin, M. Devel, J. Ollitrault, A. Billard, "Correlation between structural and optical properties of WO_3 thin films sputter deposited by glancing angle deposition," Thin Solid Films, vol. 534 (2013) pp. 275–281.

[116] K. Punitha, R. Sivakumar, C. Sanjeeviraja, "Pulsing frequency induced change in optical constants and dispersion energy parameters of WO_3 films grown by pulsed direct current magnetron sputtering," J. Appl. Phys., vol. 115 (2014) p. 113512.

[117] V. V. Ganbavle, G. L. Agawane, A. V. Moholkar, J. H. Kim, K. Y. Rajpure, "Structural, Optical, Electrical, and Dielectric Properties of the Spray-Deposited WO_3 Thin Films," J. Mater. Eng. Perform., vol. 23 (2014) pp. 1–10.

[118] S. R. Bathe, P. S. Patil, " Electrochromic characteristics of fibrous reticulated WO_3 thin films

prepared by pulsed spray pyrolysis technique," Sol. Energy Mater. Sol. Cells, vol. 91 (2007) pp. 1097–1101.

[119] I. Valyukh, S. Green, H. Arwin, G. A. Niklasson, E. Wäckelgård, C. G. Granqvist, "Spectroscopic ellipsometry characterization of electrochromic tungsten oxide and nickel oxide thin films made by sputter deposition," Sol. Energy Mater. Sol. Cells, vol. 94 (2010) pp. 724–732.

[120] A. Szekeres, D. Gogova, K. Gesheva, "Optical properties of thin CVD-tungsten oxide films by spectroscopic ellipsometry," J. Cryst. Growth, vol. 198–199 (1999) pp. 1235–1239.

[121] L. L. Kelly, D. A. Racke, P. Schulz, H. Li, P. Winget, H. Kim, P. Ndione, A.K. Sigdel, J. Br, "Spectroscopy and control of near-surface defects in conductive thin film ZnO," J. Phys. Condens. Matter, vol. 28, (2016) p. 94007.

[122] A. R. Mcneill, A. R. Hyndman, R. J. Reeves, A. J. Downard, M. W. Allen, "Tuning the band bending and controlling the surface reactivity at polar and non-polar surfaces of ZnO through phosphonic acid binding, " ACS Appl. Mater. Interfaces, vol. 6 (2016) pp. 1–6

[123] M. R. Alfaro, O.Zarzosa, Impact of the annealing atmosphere in the electrical and optical properties of ZnO thin films, J Sol-Gel Sci Technol., vol. 79 (2016) pp. 184–189

[124] A. Talukder, J. Pokharel, M. Shrestha, Q. H. Fan, "Treatment Improving electrical properties of sol-gel derived zinc oxide thin films by plasma treatment," J. Appl. Phys.,vol. 120 (2016) p. 155303

[125] Y. Nose, T. Yoshimura, A. Ashida, T. Uehara, N. Fujimura, Novel chemical vapor deposition process of ZnO films using nonequilibrium N_2 plasma generated near atmospheric pressure with small amount of O_2, J. Appl. Phys., vol. 119 (2016) p. 175302.

[126] I. Caraman, L. Dmitroglo, I. Evtodiev, L. Leontie, D. Untila, S. Hamzaoui, M. Zerdali, G.

Bulai, S. Gurlui, " Optical properties of ZnO thin films obtained by heat treatment of Zn thin films on amorphous SiO_2 substrates" , Thin Solid Films, vol. 617 (2016) pp. 103–107.

[127] A. A. Ahmad, A. M. Alsaad, B. A. Albiss, I. A. Qattan, "Optical and structural properties of sputter deposited ZnO thin films in relevance to post annealing and substrate temperatures," Thin Solid Films, vol. 606 (2016) pp. 133-142

[128] C. Singh, S. Nozaki, S. Rath, "Spectroscopic ellipsometry study of the free-carrier and band-edge absorption in ZnO thin films," Effect of non-stoichiometry, J. Appl. Phys., vol 118, (2015) p. 195305.

[129] J. Singh, S. Ranwa, J. Akhtar, M. Kumar, " Growth of residual stress-free ZnO films on SiO_2 / Si substrate at room temperature for MEMS devices, AIP ADVANCES, vol. 6 (2015) pp. 214–208

[130] S. Vyas, P. Giri, S. Singh, "Pulsed Laser Deposition and RF Sputtering Methods for Electronic and Optoelectronic Applications," J. Electron. Mater. 44 (2015) pp. 3401–3407.

[131] S. Fujihara, Y. Ogawa, A. Kasai, "Tunable Visible Photoluminescence from ZnO Thin Films through Mg-Doping and Annealing, Chem. Mater., vol. 16 (2004) pp. 2965–2968.

[132] I. J. Berlin, V. S. Anitha, P. V. Thomas, K. Joy, "Influence of oxygen atmosphere on the photoluminescence properties of sol-gel derived ZrO_2 thin films," J. Sol-Gel Sci. Technol.,

[133] S. Korkmaz, S. Pat, N. Ekem, M. Zafer Balbağ, S. Temel, "Thermal treatment effect on the optical properties of ZrO_2 thin films deposited by thermionic vacuum arc," Vacuum, vol. 86 (2012) pp. 1930–1933.

[134] C. V. Ramana, R.S. Vemuri, I. Fernandez, A. L. Campbell, "Size-effects on the optical properties of zirconium oxide thin films," Appl. Phys. Lett., vol. 95 (2009) pp. 14–17.

[135] J. P. Xu, R.-J. Zhang, Y. Zhang, Z.-Y. Wang, L. Chen, Q.-H. Huang, H.-L. Lu, S.-Y. Wang,

Y.-X. Zheng, L.-Y. Chen, “The thickness-dependent band gap and defect features of ultrathin ZrO_2 films studied by spectroscopic ellipsometry, “ Phys. Chem. Chem. Phys., vol. 18 (2016) pp. 3316–3321.

[136] L.K. Dash, N. Vast, P. Baranek, M.-C. Cheynet, L. Reining, “Electronic structure and electron energy-loss spectroscopy of zirconia,” Phys. Rev. B, vol. 70 (2004) p. 245116.

[137] H. Jeong, “ Current transport analysis of ZrO_2 thin films: Effects of post-deposition annealing,” J. Korean Phys. Soc., vol. 65 (2014) pp. 1903–1907.

[138] Y. Feng, S. Lin, S. Huang, S. Shrestha, G. Conibeer, “Can Tauc plot extrapolation be used for direct-band-gap semiconductor nanocrystals?,” J. Appl. Phys., vol. 117,(2015) p.125701

[139] F. Hofer, F. P. Schmidt, W. Grogger, G. Kothleitner, Fundamentals of electron energy-loss spectroscopy, IOP Conf. Ser. Mater. Sci. Eng., (vol. 109) (2016) p.012007

[140] M. C. Cheynet, S. Pokrant, F. D. Tichelaar, J. L. Rouvière, ”Crystal structure and band gap determination of HfO_2 thin films,” J. Appl. Phys., vol. 101 (2007) p. 54101.

[141] D.S. Su, E. Zeitler, Background problem in electron energy-loss spectroscopy, Phys. Rev. B, vol. 47 (1993) pp. 734–740.

[142] S.C. Liou, M. W. Chu, Y. J. Lee, M. Hong, J. Kwo, C. H. Chen, “Surface exciton polariton in monoclinic HfO_2 : An electron energy-loss spectroscopy study,” New J. Phys. Vol. 11 (2009) p. 103009.

[143] P. Gimmel, K.D. Schierbaum, H.H.V.D. Vlekkert, N.F.D. Rooij, “Reduced Light Sensibility in optimized Ta_2O_5-ISFET structures, ˝ Sensors Actuators B Chem., vol. 4 (1991) pp. 135–140.

[144] M. Cardona, K. L. Shaklee, F. H. Pollak, "Electroreflectance at a Semiconductor-Electrolyte Interface," Phys. Rev., vol. 154, (1967) pp. 696–720.

[145] M.G. R. Kudrawiec, J. Misiewicz, L. Wachnicki, "Contactless electroreflectance of ZnO layers grown by atomic layer deposition at low temperature," Semicond. Sci. Technol., vol. 26 (2011) p. 075012

[146] M. Wełna, R. Kudrawiec, A. Kaminska, A. Kozanecki, B. Laumer, M. Eickhoff, J. Misiewicz, "Contactless electroreflectance studies of free exciton binding energy in Zn_{1-x} MgxO epilayers," Appl. Phys. Lett., vol. 103 (2013) p.251908

[147] K.Vos, H. J. Krusemeyer, "Low temperature electroreflectance of TiO_2," Solid State Commun., vol. 15 (1974) pp 949–952.

[148] A. I. Kulak, A. I. Kokorin, Electrolyte electroreflectance study of TiO_2 films modified with metal nanoparticles, J. Mater. Res. Vol. 16 (2011) 2357–2361.

[149] C. A. Pan, T. P. Ma, "Highly transparent conductive films of thermally evaporated In_2O_3", J. Electron. Mater., vol. 10 (1981) pp. 111–117.

[150] D. E. Aspnes, "Third-derivative modulation spectroscopy with low-field electroreflectance," Surf. Sci., vol. 37, (1973), pp. 418–442.

[151] N. D. Mermin, W. Ashcroft, "Solid State Physics," Harcourt College, 1975.

[152] H. E. Hall, J. R. Hook, "Solid state physics," 2nd Ed., Wiley, 1974.

[153] G. Grosso, G. Parravicini, "Solid State Physics, " 2nd Ed., Elsevier,1999

[154] J. H. Davies, "Physics of Low-dimensional Semiconductors: An Introduction," Cambridge University Press, 1998.

[155] R. E. Hummel, “Electronic Properties of Materials.” 4th Ed., Springer, 2000.

[156] M. Cardona, P. Yu, “ Fundamentals of Semiconductors,” 3rd Ed., Springer, 2001.

[157] N. Zettili, “Quantum Mechanics Concepts and Applications “, 2nd Ed., Wiey, 2009.

[158] X. D. Fan, J. L. Peng, L. A. Bursill, “Joint density of states of wide-band-gap materials by electron energy loss spectroscopy,” Mod. Phys. Lett. B, vol. 12, (1998), pp. 541–554.

[159] M. Fox, “OpticaI Propertles of Solids.”, Oxford, 2001

[160] J. Tauc, A. Menth, States in the Gap, J. Non. Cryst. Solids, vol. 10 (1972) pp. 569–585.

[161] J. Aarik, H. Mändar, M. Kirm, L. Pung, “Optical characterization of HfO_2 thin films grown by atomic layer deposition,” Thin Solid Films, vol. 466, (2004), pp. 41–47.

[162] B. O. Seraphin, N. Bottka, “Band Structure Analysis from Electro-Reflectance Studies,” J. Appl. Phys., vol. 145, (1966) p.721

[163] F. H. Pollack, M. Cardona, “Piezo electroreflectance in Ge, GaAs and Si,” Phys. Rev., vol. 172, (1968), p. 816.

[164] M. C. Anibal, “Modulated piezoreflectance in Semiconductors,” Phys. Rev. B, vol. 695, (1970) pp.672 –682

[165] R. R. L. Zucca, Y. R. Shen, “Wavelength-modulation spectra of some semiconductors,” Phys. Rev. B, vol. 1, (1970), pp. 2668–2676.

[166] I. Balsiev, “Influence of uniaxial stress on the indirect absorption edge in silicon and germanium,” Phys. Rev., vol. 143, (1976) pp. 636–647

[167] M. Cardona, “Modulation Spectroscopy,” Academic Press, 1969

[168] J. J. T. W. E. Engeler, M. Garfinkel, “Observation of phonon assisted indirect transitions by stress modulated optical transmission,” Phys. Rev. Lett., vol. 16, (1966) pp. 239–243

[169] H. R. Philipp, W. C. Dash, “Piezoreflectance in Ge,” Phys. Rev., vol. 127 (1962) pp. 762–

764

[170] M. Garfinkel, J. J. Tiemann, W. E. Engeler, “Piezoreflectivity of the noble metals,” Phys. Rev., vol. 148 (1966) pp. 695–706,

[171] U. Gerhardt, D. Beaglehole, R. Sandrock, “Piezo-optical constants, deformation potentials, and the electronic structure of copper,” Phys. Rev. Lett., vol. 19, (1967), pp. 309–311.

[172] P. Phillips, “Advanced Solid State Physics. Cambidge University Press,” 2nd Ed., 2012.

[173] K. Tharmalingam, “Optical absorption in the presence of a uniform field,” Phys. Rev., vol. 130, (1963), pp. 2204–2206.

[174] R. J. Elliott, “Intensity of optical absorption by excitions,” Phys. Rev., vol. 108, (1957), pp. 1384–1389.

[175] C. F. Klingshirn,” Semiconductor Optics,” Springer, 4th Ed., 2012

[176] J. Rowe, D. E. Aspnes, “Resonant nonlinear optical susceptibility: electroreflectance in the low-field limit,” Phys. Rev. B, vol. 5, (1972), pp. 4022–4030.

[177] D. E. Aspnes, “Direct verification of the third dericvative nature of electroreflactance spectra,” Phys. Rev. Lett., vol. 28, (1972), p. 168.

[178] J. A. Lahtinen, “Electroreflectance study of the Burstein-Moss shift in indium phosphide,” Phys. Rev. B, vol. 33, (1986), pp. 2550–2553

[179] L.Tan, Z. Guo, “Fundamentals and applications of nanomaterials,” Artech House, 2009.

[180] O. H. Seeck, B. Murphy, “X-Ray diffraction: modern experimental techniques,” Taylor and Francis, 2014

[181] C. D.Wagner , W. M. Riggs, L. E.Davis , J. F. Mulder, “Handbook of X-ray photoelectron spectroscopy,” Physical Electronics, 1965

[182] G.Haugstad, “Atomic Force Microscopy: understanding basic modes and advanced applications,” Wiley, 2012

[183] B. J. Clark, T. Frost, “UV Spectroscopy: techniques, instrumentation and data handling,” Springer, 4th Ed., (1993).

[184] R. Suresh, V. Ponnuswamy, R. Mariappan, “Consequence of source material on the surface properties of nebulizer spray coated cerium oxide thin films,” Vacuum, vol. 109, (2014), pp. 94–101.

[185] M. Saleem, M. F. Al-Kuhaili, S. M. A. Durrani, I. A. Bakhtiari, “Characterization of nanocrystalline α -Fe_2O_3 thin films grown by reactive evaporation and oxidation of iron,” Phys. Scr., vol. 85, (2012), p. 55802.

[186] Y.-K. Chiou, C.-H. Chang, T.-B. Wu, “Characteristics of hafnium oxide grown on silicon by atomic-layer deposition using tetrakis(ethylmethylamino) hafnium and water vapor as precursors,” J. Mater. Res., vol. 22, (2007), pp. 1899–1906.

[187] J. Szubera, G. Czempika, R. Larcipreteb, D. Kozieja, B. Adamowicz, “XPS study of the L-CVD deposited SnO_2 thin films exposed to oxygen and hydrogen,” Thin solid films, vol. 391(2001) pp. 198–203.

[188] M. Sreemany, S. Sen, “A simple spectrophotometric method for determination of the optical constants and band gap energy of multiple layer TiO_2 thin films,” Mater. Chem. Phys. 83 (2004) pp. 169–177.

[189] S.W. Ryu, E. J. Kim, S. K. Ko, S. H. Hahn, “Effect of calcination on the structural and optical properties of M/TiO_2 thin films by RF magnetron co-sputtering,” Mater. Lett. 58 (2004) pp. 582–587.

[190] N. Laidani, P. Cheyssac, J. Perri, “Intrinsic defects and their influence on the chemical and

optical properties of TiO_{2-x} films," J. Phys. D: Appl. Phys., vol. 43 (2010) p. 485402.

[191] C. Lee, J. Kim, J. Y. Son, W. Choi, H. Kim, "Environmental Photocatalytic functional coatings of TiO_2 thin films on polymer substrate by plasma enhanced atomic layer deposition," App. Cat. B, vol. 91 (2009) pp. 628–633.

[192] J. D. Reyes, R. J. D. Macuil, V. D. García, A. P. Benítez, J. A. B. López, J. A. A. Ortega, " Physical properties characterization of WO_3 films grown by hot-filament metal oxide deposition," Mater. Sci. Eng. B, vol 174 (2010) pp. 182–186.

[193] J. E. F. Mena, "Structural properties of WO_3 dependent of the annealing temperature deposited by hot-filament metal oxide deposition," Rev. Mex. Física. vol. 58 (2012) pp. 504–509.

[194] G.M. Ali, P. Chakrabarti," Performance of ZnO-based ultraviolet photodetectors under varying thermal treatment," IEEE Photonics J., vol. 2 (2010) pp. 784–793.

[195] M.F. Al-Kuhaili, S.M. A. Durrani, "Effect of annealing on pulsed laser deposited zirconium oxide thin films, " J. Alloys Compd., vol. 509 (2011) pp. 9536–9541.

[196] C. Huber, C. Krämmer, D. Sperber, A. Magin, H. Kalt, M. Hetterich, "Electroreflectance of thin film solar cells: Simulation and experiment", Phys. Rev. B. vol. 92 (2015) p. 75201.

[197] R. Sanjinés, H. Tang, H. Berger, F. Gozzo, G. Margaritondo, F. Lévy, "Electronic structure of anatase TiO_2 oxide ", J. Appl. Phys., vol.75 (1994) pp. 2945–2951.

[198] P. Capper, J. Garland, Mercury Cadmium Tellurite, Growth, Properties and Applications, Wiley, 2011.

[199] D. Zhang, Z. Tong, S. Li, X. Zhang, A. Ying, "A novel route toward fabrication of twofold-shaped CeO_2 dendrites," Eur. J. Inorg. Chem. Vol. 8 (2008) pp. 5476–5481.

[200] M. Li, H. Jia, X. Li, X. Liu, Mechanical, lattice dynamical and electronic properties of CeO_2

at high pressure: First-principles studies, Solid State Commun. 226 (2016) pp. 8–12.

[201] M. Alfredsson, C.R.A. Catlow, "A comparison between metal supported c-ZrO_2 and CeO_2," Phys. Chem. Chem. Phys., vol. 4 (2002) pp. 6100–6108.

[202] L.J. Bennett, G. Jones, "The influence of the Hubbard U parameter in simulating the catalytic behaviour of cerium oxide," Phys. Chem. Chem. Phys., vol.16 (2014) pp. 21032–21038.

[203] P. J. Hay, R. L. Martin, J. Uddin, G.E. Scuseria, "Theoretical study of CeO_2 and Ce_2O_3 using a screened hybrid density functional," J. Chem. Phys.,vol. 125 (2006) p. 34712.

[204] M.M. Momeni, Y. Ghayeb, F. Mohammadi, "Fe_2O_3 nanotube films prepared by anodisation as visible light photocatalytic" Surf. Eng., vol.31 (2015) pp. 452–457.

[205] C.S. Biju, D.H. Raja, D.P. Padiyan, "Glycine assisted hydrothermal synthesis of α-Fe_2O_3 nanoparticles and its size dependent properties," Chem. Phys. Lett., vol. 610–611 (2014) pp. 103–107.

[206] J. D. Emery, C.M. Schlepütz, P. Guo, S.C. Riha, R.P.H. Chang, A.B.F. Martinson, "Atomic layer deposition of metastable β-Fe_2O_3 via isomorphic epitaxy for photoassisted water oxidation," ACS Appl. Mater. Interfaces, vol. 6 (2014) pp. 21894–900.

[207] B. K. Pandey, A. K. Shahi, J. Shah, R. K. Kotnala, R. Gopal, "Optical and magnetic properties of Fe_2O_3 nanoparticles synthesized by laser ablation/fragmentation technique in different liquid media," Appl. Surf. Sci., vol. 289 (2014) pp. 462–471.

[208] A. Kleiman-shwarsctein, M.N. Huda, A. Walsh, Y. Yan, G. D. Stucky, Y. Hu, M. M. Al-jassim, E. W. Mcfarland, Electrodeposited aluminum-doped Fe_2O_3 photoelectrodes : experiment and theory, Chem. Mater., vol. 22 (2010) pp. 510–517.

[209] Y. Guo, S. J. Clark, J. Robertson, "Electronic and magnetic properties of Ti_2O_3 , Cr_2O_3 , and Fe_2O_3 calculated by the screened exchange hybrid density functional," J. Phys. Condens.

Matter, vol. 24 (2012) p. 325504.

[210] P. Liao, E.A. Carter, "Ab initio density functional theory + U predictions of the shear response of iron oxides," Acta Mater., vol. 58 (2010) pp. 5912–5925.

[211] C. Xia, Y. Jia, M. Tao, Q. Zhang, Tuning the band gap of hematite α- Fe_2O_3 by sulfur doping, Phys. Lett. Sect. A Gen. At. Solid State Phys., vol. 377 (2013) pp. 1943–1947.

[212] Z. D. Pozun, G. Henkelman, "Hybrid density functional theory band structure engineering in hematite," J. Chem. Phys., vol.134 (2011) p. 224706

[213] P. Thomas, P. Sreekanth, K.E. Abraham, "Nanosecond and ultrafast optical power limiting in luminescent Fe_2O_3 hexagonal nanomorphotype", J. Appl. Phys., vol. 117 (2015) pp. 1–7.

[214] H. Peelaers, C.G. Van de Walle, "Brillouin zone and band structure of β-Ga_2O_3," Phys. Status Solidi, vol. 252 (2015) pp. 828–832.

[215] H. He, M. A. Blanco, R. Pandey, "Electronic and thermodynamic properties β -Ga_2O_3," Appl. Phys. Lett., vol. 88 (2006) pp. 2006–2008.

[216] T. Chen, K. Tang, " β-Ga_2O_3 quantum dots with visible blue-green light emission property," Appl. Phys. Lett., vol. 90 (2007) pp. 70–73.

[217] E. Hildebrandt, J. Kurian, L. Alff, "Physical properties and band structure of reactive molecular beam epitaxy grown oxygen engineered HfO_{2-x} ," J. Appl. Phys.,vol.112 (2012) 1–32.

[218] A. Hakeem, M. Ramzan, E. Ahmed, a. M. Rana, N.R. Khalid, N. A.. Niaz, A. Shakoor, S. Ali, U. Asghar, M.Y. Nadeem, "Effects of vacuum annealing on surface and optical constants of hafnium oxide thin films," Mater. Sci. Semicond. Process., vol. 30 (2015) pp. 98–103.

[219] N. M. Kamble, R. B. Tokas, A. Biswas, S. Thakur, D. Bhattacharyya, N. K. Sahoo, "Determination of the optical constants of HfO_2–SiO_2 composite thin films through reverse fitting of transmission spectra," Vacuum, vol. 86 (2011) pp. 422–428.

[220] V. Dave, P. Dubey, H.O. Gupta, R. Chandra, "Influence of sputtering pressure on the structural, optical and hydrophobic properties of sputtered deposited HfO_2 coatings," Thin Solid Films, vol. 549 (2013) pp. 2–7.

[221] N. S. Bennett, K. Cherkaoui, C. S. Wong, É. O'Connor, S. Monaghan, P. Hurley, L. Chauhan, P. J. McNally, "Structural and optical properties of post-annealed atomic-layer-deposited HfO_2 thin films on GaAs," Thin Solid Films, vol. 569 (2014) pp. 104–112.

[222] M.K. Hudait, Y. Zhu, D. Maurya, S. Priya, "Energy band alignment of atomic layer deposited HfO_2 on epitaxial (110) Ge grown by molecular beam epitaxy," Appl. Phys. Lett., vol. 102 (2013) pp. 2–7.

[223] T. Wang, J. Wei, M. C. Downer, J. G. Ekerdt, "Optical properties of La-incorporated HfO_2 upon crystallization," Appl. Phys. Lett., vol. 98 (2011) p.122904.

[224] S. A. Eliziário, L.S. Cavalcante, J. C. Sczancoski, P. S. Pizani, J. A. Varela, J. W. M. Espinosa, E. Longo, "Morphology and Photoluminescence of HfO_2 Obtained by Microwave-Hydrothermal," Nanoscale Res. Lett., vol. 4 (2009) pp. 1371–1379.

[225] S. A. Elizirio, L. S. Cavalcante, J. C. Sczancoski, P. S. Pizani, J. A. Varela, J. W. M. Espinosa, E. Longo, "Morphology and photoluminescence of HfO_2 obtained by microwave-hydrothermal, " Nanoscale Res. Lett., vol. 4 (2009) pp. 1371–1379.

[226] M. Toledano-Luque, E. San Andrés, A. del Prado, I. Mártil, M.L. Lucía, G. González-Díaz, F. L. Martínez, W. Bohne, J. Röhrich, E. Strub, "High-pressure reactively sputtered HfO2: Composition, morphology, and optical properties," J. Appl. Phys., vol. 102 (2007) p. 44106.

[227] F. L. Martinez, M. Toledano-Luque, J. J. Gandia, J. Carabe, W. Bohne, J. Rohrich, E. Strub, I. Martil, "Optical properties and structure of HfO_2 thin films grown by high pressure reactive sputtering," J. Phys. D. Appl. Phys., vol. 40 (2007) pp. 5256–5265.

[228] M. Romero, R. Escamilla, "First-principles calculations of structural, elastic and electronic properties of Nb_2SnC under pressure," Comput. Mater. Sci., vol. 55 (2012) pp. 142–146.

[229] J. Li, S. Meng, L. Li, H. Lu, T. Tohyama, "First-principles generalized gradient approximation (GGA)+U^d+U^p studies of electronic structures and optical properties in cubic HfO_2," Comput. Mater. Sci., vol. 81 (2014) pp. 397–401.

[230] J. C. Garcia, L. M. R. Scolfaro, J. R. Leite, A. T. Lino, V.N. Freire, G. A. Farias, E. F. Da Silva, "Effective masses and complex dielectric function of cubic HfO_2," Appl. Phys. Lett., vol. 85 (2004) pp. 5022.

[231] A. Kaur, E. R. Ylvisaker, Y. Li, G. Galli, W. E. Pickett, "First-principles Study of Electronic and Dielectric Properties of ZrO_2 and HfO_2," Mol. Simul., vol. 34 (2003) 1016.

[232] Y. L. Yang, Y. Shen, Z. Li, "Reaction time effect of straw-like MoO_3 prepared with a facile, additive-free hydrothermal process," RSC Adv., vol. 5 (2015) pp. 255–260.

[233] P. Jittiarporn, L. Sikong, K. Kooptarnond, W. Taweepreda, " Effects of precipitation temperature on the photochromic properties of h-MoO_3," Ceram. Int., vol. 40 (2014) pp. 13487–13495.

[234] Y. Shen, Y. Yang, F. Hu, Y. Xiao, P. Yan, Z. Li, " Novel coral-like hexagonal MoO_3 thin films: Synthesis and photochromic properties," Mater. Sci. Semicond. Process., vol. 29 (2014) pp. 250–255.

[235] M. Dhanasankar, K.K. Purushothaman, G. Muralidharan, "Effect of temperature of annealing on optical, structural and electrochromic properties of sol–gel dip coated molybdenum oxide films," Appl. Surf. Sci., vol. 257 (2011) pp. 2074–2079.

[236] X. Fan, G. Fang, P. Qin, N. Sun, N. Liu, Q. Zheng, F. Cheng, L. Yuan, X. Zhao, "Deposition temperature effect of RF magnetron sputtered molybdenum oxide films on the power

conversion efficiency of bulk-heterojunction solar cells," J. Phys. D. Appl. Phys., vol. 44 (2011) p. 45101.

[237] A.D. Sayede, "An ab initio LAPW study of the α and β phases of bulk molybdenum trioxide," Chem. Phys., vol. 3, (2005) pp. 72–82.

[238] A. H. Reshak, "Specific features of electronic structures and optical susceptibilities of molybdenum oxide," RSC Adv., vol. 5 (2015) pp. 22044–22052.

[239] D. O. Scanlon, G. W. Watson, D. J. Payne, G. R. Atkinson, R. G. Egdell, D. S. L. Law, "Theoretical and Experimental Study of the Electronic Structures of MoO_3 and MoO_2," J. Phys. Chem. C, vol. 114 (2010) pp. 4636–4645.

[240] P. R. Huang, Y. He, C. Cao, Z.H. Lu, "Impact of lattice distortion and electron doping on α-MoO_3 electronic structure," Sci. Rep., vol. 4 (2014) p. 7131.

[241] C.A. Rozzi, F. Manghi, F. Parmigiani, "Ab initio Fermi surface and conduction-band calculations in oxygen-reduced MoO_3," Phys. Rev. B, vol. 68 (2003) p. 75106.

[242] M. A. Bezzerrouk, M. Hassan, R. Baghdad, S. Reguieg, M. Bousmaha, B. Kharroubi, B. Bouhafs, " Thermodynamic, structural and electronic, properties of SnO_2 by GGA and GGA+trans-blaha-modified Becke-Johnson (TB-mBJ) calculation," Superlattices Microstruct., vol. 84 (2015) pp. 80–90.

[243] F. El Haj Hassan, S. Moussawi, W. Noun, C. Salameh, A. V. Postnikov, "Theoretical calculations of the high-pressure phases of SnO_2," Comput. Mater. Sci., vol. 72 (2013) pp. 86–92.

[244] W.-Z. Xiao, G. Xiao, L.-L. Wang, " A first-principles study of the SnO_2 monolayer with hexagonal structure," J. Chem. Phys., vol. 145 (2016) pp. 174702.

[245] O. Mounkachi, E. Salmani, M. Lakhal, H. Ez-Zahraouy, M. Hamedoun, M. Benaissa, A. Kara,

A. Ennaoui, A. Benyoussef, " Band-gap engineering of SnO_2," Sol. Energy Mater. Sol. Cells, vol. 148 (2016) pp. 34–38.

[246] F.R. Sensato, R. Custódio, M. Calatayud, A. Beltrán, J. Andrés, J.R. Sambrano, E. Longo, "Periodic study on the structural and electronic properties of bulk, oxidized and reduced SnO_2(110) surfaces and the interaction with O_2," Surf. Sci., vol. 511 (2002) pp. 408–420.

[247] A.M. Ganose, D.O. Scanlon, "Band gap and work function tailoring of SnO_2 for improved transparent conducting ability in photovoltaics," J. Mater. Chem. C, vol. 4 (2016) pp. 1467–1475.

[248] N. R. Mathews, E. R. Morales, M. A. Cortés-Jacome, J. A. Toledo Antonio, "TiO_2 thin films - Influence of annealing temperature on structural, optical and photocatalytic properties," Sol. Energy, vol. 83 (2009) pp. 1499–1508.

[249] S. Munir, S. M. Shah, H. Hussain, R. Ali khan, "Effect of carrier concentration on the optical band gap of TiO_2 nanoparticles," Mater. Des., vol. 92 (2016) pp. 64–72.

[250] G. Lee, M. Kim, "Crystal Structure of TiO_2 Thin Films grown on Sapphire Substrates by RF Sputtering as a Function of Temperature", Electron. Mater. Lett., vol. 6 (2010) pp. 77–80.

[251] J. Xiong, S. N. Das, S. Kim, J. Lim, H. Choi, J. Myoung, "Photo-induced hydrophilic properties of reactive RF magnetron sputtered TiO_2 thin films," Surf. Coat. Technol., vol. 204 (2010) pp. 3436–3442.

[252] F. Meng, X. Song, Z. Sun, "Photocatalytic activity of TiO_2 thin films deposited by RF magnetron sputtering," Vacuum, vol. 83 (2009) pp. 1147–1151.

[253] B. Kınacı, B. Sarıkavak, A. Bengi, H. Altuntas, M.K. Ozt," Influence of thermal annealing on the structure and optical properties of DC magnetron sputtered titanium dioxide thin films, " Surf. Interface Anal., (2010) pp. 1247–1251.

[254] F. Wang, N.G. Kubala, C.A. Wolden, Photoelectrochemical Performance of Anatase TiO_2 Thin Films Deposited by Self-Limiting Growth Techniques, J. Electroanal. Chem., vol. 157 (2010) pp. 432–436.

[255] P. Eiamchai, P. Chindaudom, A. Pokaipisit, P. Limsuwan, " Spectroscopic ellipsometry study of TiO_2 thin films prepared by ion-assisted electron-beam evaporation," Curr. Appl. Phys., vol. 9 (2009) pp. 707–712.

[256] Z. G. Hu, W. W. Li, J. D. Wu, J. Sun, Q. W. Shu, X. X. Zhong, Z. Q. Zhu, J. H. Chu, "Optical properties of pulsed laser deposited rutile titanium dioxide films on quartz substrates determined by Raman scattering and transmittance spectra," Appl. Phys. Lett., vol. 93 (2008) pp. 23–26.

[257] G.U. Von Oertzen, A.R. Gerson," The effects of O deficiency on the electronic structure of rutile TiO_2," J. Phys. Chem. Solids, vol. 68 (2007) pp. 324–330.

[258] S. Park, B. Magyari-köpe, Y. Nishi, "Electronic correlation effects in reduced rutile TiO_2 within the LDA + U method," Phys. Rev. B, vol. 82 (2010) pp. 1–9.

[259] M. Landmann, E. Rauls, W.G. Schmidt, "The electronic structure and optical response of rutile, anatase and brookite TiO_2.," J. Phys. Condens. Matter., vol. 24 (2012) 195503.

[260] Y. Zhang, W. Lin, Y. Li, K. Ding, J. Li, "A theoretical study on the electronic structures of TiO_2: Effect of Hartree-Fock exchange," J. Phys. Chem. B, vol. 109 (2005) 19270–19277.

[261] R. Asahi, Y. Taga, W. Mannstadt, A. Freeman, " Electronic and optical properties of anatase TiO_2," Phys. Rev. B, vol. 61 (2000) pp. 7459–7465.

[262] D. Valerini, S. Hernández, F. Di Benedetto, N. Russo, G. Saracco, A. Rizzo, "Sputtered WO_3 films for water splitting applications," Mater. Sci. Semicond. Process., vol. 42 (2016) pp. 150–154.

[263] D. Nagy, D. Nagy, I. M. Szilagyi, X. Fan, “Effect of the morphology and phases of WO_3 nanocrystals on their photocatalytic efficiency,” RSC Adv., vol. 6 (2016) pp. 33743–33754.

[264] H. Simchi, B. E. McCandless, T. Meng, W. N. Shafarman, ” Structural, optical, and surface properties of WO_3 thin films for solar cells,” J. Alloys Compd., vol. 617 (2014) pp. 609–615.

[265] W. Wang, A. Janotti, C. G. Van de Walle, “ Role of oxygen vacancies in crystalline WO_3,” J. Mater. Chem. C, vol. 4 (2016) pp. 6641–6648.

[266] C. Di Valentin, F. Wang, G. Pacchioni, “Tungsten Oxide in Catalysis and Photocatalysis: Hints from DFT,” Top. Catal., vol. 56 (2013) pp. 1404–1419.

[267] N. L. Heda, B. L. Ahuja, “Electronic properties and electron momentum density of monoclinic WO_3,” Comput. Mater. Sci., vol. 72 (2013) pp. 49–53.

[268] Y. Ping, D. Rocca, G. Galli, “Optical properties of tungsten trioxide from first-principles calculations,” Phys. Rev. B, vol. 87 (2013) p. 165203.

[269] Y. Wang, W. Tang, J. Zhu, J. Liu, “ Strain induced change of band structure and electron effective mass in wurtzite ZnO : A first-principles study,” Comput. Mater. Sci., vol. 99 (2015) pp. 145–149.

[270] Q. Wang, C. Zhou, J. Wu, T. Lü, K. He, “ GGA + U study of the electronic and optical properties of hexagonal BN phase ZnO under pressure,” Comput. Mater. Sci., vol. 102 (2015) pp. 196–201.

[271] R. Farooq, T. Mahmood, A.W. Anwar, G. N. Abbasi, “ First-Principles Calculation of Electronic and Optical Properties of Graphene like ZnO (G-ZnO),” Superlattices Microstruct., vol. 90 (2016) pp. 165–169

[272] J. Lei, D. Zhu, M. Xu, S. Hu, “First-principles simulations of two dimensional electron gas near the interface of ZnO / GaN (0001) superlattice,” Phys. Lett. A, vol. 379 (2015) pp.

2384–2387.

[273] S. M. Hwang, S. M. Lee, K. Park, M. S. Lee, J. Joo, J. H. Lim, H. Kim, J. J. Yoon, Y. D. Kim, "Effect of annealing temperature on microstructural evolution and electrical properties of sol-gel processed ZrO_2/Si films," Appl. Phys. Lett. 98 (2011) p. 22903.

[274] J.-H. Hur, S. Park, U.-I. Chung, "First principles study of oxygen vacancy states in monoclinic ZrO_2: Interpretation of conduction characteristics," J. Appl. Phys., vol. 112 (2012) p. 113719.

[275] M. Grüning, R. Shaltaf, G.-M. Rignanese, " Quasiparticle calculations of the electronic properties of ZrO_2 and HfO_2 polymorphs and their interface with Si," Phys. Rev. B, vol. 81 (2010) p. 35330.

[276] J. Li, H. Lu, Y. Li, S. Meng, Y. Zhang, "First-principles generalized gradient approximation (GGA) +U studies of electronic structure and optical properties in cubic ZrO_2", Solid State Commun., vol. 211 (2015) pp. 38–42.

[277] Q. J. Liu, Z. T. Liu, L. P. Feng, "Elasticity, electronic structure, chemical bonding and optical properties of monoclinic ZrO_2 from first-principles," Phys. B Condens. Matter., vol. 406 (2011) pp. 345–350.

[278] Y.-L. Yang, X.-L. Fan, C. Liu, R.-X. Ran, " First principles study of structural and electronic properties of cubic phase of ZrO_2 and HfO_2," Phys. B Condens. Matter., vol. 434 (2014) pp. 7–13.

VITAE

HAFIZ ADIL QAYYUM

Ph.D Physics

Address: R # 116, B # 826 Nationality: Pakistani

Graduate Housing KFUPM, Dhahran Saudi Arabia Date of Birth: Oct 7, 1986

Cell# +966-53032563692 **Email:** hadilq09@gmail.com

EDUCATION

Ph.D Physics Jan 2013 – Nov 2017

King Fahd University of Petroleum & Minerals, Saudia Arabia

CGPA: 3.52/4.00

M.S. Energetic Materials Oct 2009 - August 2011

National University of Sciences and Technology, Pakistan

CGPA: 3.55/4.00

BSc. (Hons.) Computational Physics Oct 2005 - August 2009

University of the Punjab, Pakistan

CGPA: 3.71/4.00

AREAS OF EXPERTISE

- **Materials Fabrication**
  - Fabrication of thin films
  - Multi layered hetero-structures

- Metal-Oxide based capacitor geometries
- RF & DC Sputtering
- Resistive thermal Evaporation
- Electron beam evaporation

➢ Materials Characterization

- Electro-optical Measurements using Electroreflectance
- Chemical Analysis using XPS
- Optical Characterization using Photoluminescence
- Optical Characterization using Spectrophotometry
- Electrical Characterization using Hall effect & Electrometer.
- Structural characterization XRD
- Surface Morphology using AFM

➢ Experimental Setup Designing

- High voltage electroreflectance setup

➢ DFT Calculations

- Band structure and density of states calculation using Quantum Espresso
- Effect of external perturbation on the optical parameters using Materials Studio

➢ Scientific Computing

- Modeling and Simulations using Mathematica, C# and C++
- Nonlinear curve fitting using Origin, Mathematica, PSI Plot, Avantage

THESIS AND PROJECTS

- Determination of band gaps of metal oxide thin films through electroreflectance. **PhD thesis**
- Electrical characterization of iron doped ZnO thin films for solar cells applications, **National Science, Technology and Innovation Plan (NSTIP) project, KSA**
- Mathematical modeling and simulations of Single stage gas permeation, **MS thesis, NUST funded project**
- Monte Carlo simulation of quantum ideal gas and its implementation on Bose Einstein Condensation Phenomena, **BSc (Hon's) project**

PUBLICATIONS

- **H. A. Qayyum**, M. F. Al-Kuhaili, S. M. A. Durrani, T. Hussain, M. Ikram, Blue shift in the optical transitions of ZnO thin film due to an external electric field, Journal of Physics and Chemistry of Solids, 112 (2018) 94–99.
- **H. A. Qayyum**, M. F. Al-Kuhaili, S. M. A. Durrani, Investigation of fundamental and high order optical transitions in α-Fe2O3 thin films using surface barrier electroreflectance, Superlattices and Microstructures, 110 (2017), 98–107
- T. Hussain, M. F. Al-Kuhaili, S. M. A. Durrani, A. Qurashi, **H. A. Qayyum**, Enhancement in the Solar Light Harvesting Ability of Tungsten Oxide Thin Films by Annealing in Vacuum and Hydrogen, International journal of Hydrogen Energy, 42 (2017), 28755–28765

- Hassan Younas, Ishtiaq A. Qazi, Imran Hashmi, M. Ali Awan, Asif Mahmood**, Hafiz Adil Qayyum**, Visible light photocatalytic water disinfection and its kinetics using Ag-doped titania nanoparticles, Environmental Science and Pollution Research, 21(2014), 740–752
- **Qayyum, A**. Hussain, Coupling Model for multi-component Gas Permeation Process, International Journal of Mathematical Modelling & Computations, 4 (2014), 223-241
- **H. A. Qayyum**, M.F. Al-Kuhaili, S.M.A. Durrani, T. Hussain, Determination of band gap of metal oxide thin films using Electromodulation, Under Review, Journal of Alloys and Compounds.

EXPERIENCE

- **Lecturer** January 2013 – November 2017

  King Fahd University of Petroleum & Minerals Dhahran, Saudi Arabia

  Major Courses: Physics 101, Phys102

  Responsibilities: Labs and Recitations

- **Research Assistant** August 2010 – September 2011

  National University of Sciences and Technology, Pakistan

ACHIEVEMENTS

- Merit Scholarship holder in National University of Science and Technology (NUST), Islamabad, Pakistan.
- Achieved two times study scholarship for best CGPA holder in Centre for High Energy Physics, (CHEP), University of the Punjab, Lahore.